Het overbruggen van spatiotemporele schalen in biomechanische modellen voor levende weefsels: van de contracterende slokdarm tot hartgroei

Bridging Spatiotemporal Scales in Biomechanical Models for Living Tissues: From the Contracting Esophagus to Cardiac Growth

Mathias Peirlinck

Promotoren: prof. dr. ir. P. Segers, dr. ir. M. De Beule, em. prof. dr. ir. B. Verhegghe
Proefschrift ingediend tot het behalen van de graad van
Doctor in de ingenieurswetenschappen: biomedische ingenieurstechnieken

UNIVERSITEIT
GENT

Vakgroep Elektronica en Informatiesystemen
Voorzitter: prof. dr. ir. K. De Bosschere
Faculteit Ingenieurswetenschappen en Architectuur
Academiejaar 2018 - 2019

ISBN 978-94-6355-258-5
NUR 954
Wettelijk depot: D/2019/10.500/66

Supervisors:

Prof. dr. ir. Patrick Segers
Prof. dr. ing. Matthieu De Beule
Prof. dr. ir. Benedict Verhegghe

Research lab:

Biofluid, Tissue and Solid Mechanics for Medical Applications (bioMMeda)
Institute Biomedical Technology
Ghent University
Corneel Heymanslaan 10 - Blok B (ing. 36), 9000 Gent, Belgium

Members of the exam committee:

Chairman:

Prof. dr. ir. Luc Taerwe	Faculty of Engineering and Architecture, UGent

Secretary:

Prof. dr. ir. Wim Van Paepegem	Faculty of Engineering and Architecture, UGent

Reading committee:

Prof. dr. ir. Nele Famaey	Faculty of Engineering Technology, KULeuven
Prof. dr. ir. Stéphane Avril	Center for Biomedical and Healthcare Engineering, Ecole Nationale Supérieure des Mines de Saint-Etienne
Prof. dr. Martijn van den Broek	Faculty of Engineering and Architecture, UGent
Prof. dr. ir. Wim Van Paepegem	Faculty of Engineering and Architecture, UGent

Other members:

Prof. dr. ir. Pascal Verdonck	Faculty of Engineering and Architecture, UGent
Prof. dr. ir. Patrick Segers	Faculty of Engineering and Architecture, UGent
Prof. dr. ing. Matthieu De Beule	Faculty of Engineering and Architecture, UGent
Prof. dr. ir. Benedict Verhegghe	Faculty of Engineering and Architecture, UGent

This research was funded by the Flemish Agency for Innovation and Entrepreneurship (strategic basic research grant IWT/141014).

Alternative title

Modeling the Space-Time Continuum
Mechanics of Soft Living Matter

Contents

Contents vii

Abbreviations and Symbols xiii

Samenvatting xvii

Summary xxiii

Introduction 1

1 Continuum Mechanics and FEA 9
- 1.1 Kinematics . . . 10
- 1.2 Strain . . . 12
- 1.3 Stress . . . 13
- 1.4 The finite element method . . . 15
  - 1.4.1 Equilibrium equations . . . 16
  - 1.4.2 The strong and weak formulation . . . 17
  - 1.4.3 Solution strategy . . . 19
  - 1.4.4 Finite elements . . . 20
  - 1.4.5 Nonlinear solution schemes . . . 23
    - 1.4.5.1 Implicit . . . 24
    - 1.4.5.2 Explicit . . . 25
    - 1.4.5.3 Implicit vs explicit vs quasi-static . . . 26
  - 1.4.6 Geometric discretization . . . 27

2 Soft Tissue Biomechanics 29
- 2.1 Passive behavior . . . 29
  - 2.1.1 Modeling constitutive behavior . . . 30
    - 2.1.1.1 (Non)linearity . . . 31
      - 2.1.1.1.1 Linear elasticity . . . 31
      - 2.1.1.1.2 Strain energy function . . . 32
      - 2.1.1.1.3 Hyperelasticity . . . 33

2.1.1.1.4 Incompressibility 35
2.1.1.2 Viscoelasticity 36
2.1.1.3 (An)isotropy 38
2.1.1.4 Heterogenity 38
2.1.1.5 Residual stress 40
2.1.1.6 FEA implementation 40
2.1.2 Measurement of passive behavior 41
2.1.2.1 Ex vivo methods 41
2.1.2.2 In vivo methods 45
2.2 Active behavior 46
2.2.1 Modeling active behavior 48
2.2.1.1 Active stresses 49
2.2.1.2 Active strains 49
2.2.2 Measurement of active behavior 50
2.3 Growth and remodeling 51
2.3.1 Kinematics-based growth 52
2.3.2 Constrained mixture modeling 54

I Gastro-Intestinal Biomechanics 57

Clinical rationale 59

3 The 'virtual esophagus' 61
3.1 Esophageal function, structure and histology 61
3.2 Esophageal mechanics 64
3.2.1 Constitutive behavior 64
3.2.1.1 Invariants 65
3.2.1.2 Strain energy function 66
3.2.1.2.1 Volumetric bulk material 66
3.2.1.2.2 Non-collagenous ground matrix 67
3.2.1.2.3 Collagen fibers 67
3.2.1.2.4 Smooth and striated muscle cells 68
3.2.1.2.5 Layer-specific equations 69
3.2.1.3 Evaluation of the constitutive parameters . 70
3.2.2 Geometry 72
3.2.3 Buckling 74
3.2.4 In vivo stress state 75
3.2.5 External tissue support 78
3.2.6 Peristalsis 78
3.3 Results 79
3.3.1 In vivo stress state 79

3.3.2 Peristalsis . . . 80
3.4 Discussion . . . 82
3.5 Future work . . . 84

4 Esophageal stenting **87**
4.1 Introduction . . . 87
4.2 Methods . . . 91
4.2.1 In vitro experimental testing stent samples . . . 92
4.2.2 Finite element PBFS model . . . 94
4.2.3 Modeling the implantation procedure . . . 95
4.3 Results . . . 95
4.3.1 Degradation through time . . . 95
4.3.2 Friction calibration and stent model validation . . . 97
4.3.3 Virtual stent implantation . . . 98
4.4 Discussion . . . 100
4.4.1 Mechanical behavior of the (biodegradable) PBFS . . . 100
4.4.2 Stent-esophagus interaction . . . 102
4.5 Limitations and future work . . . 103

II Cardiac Biomechanics **107**

Clinical rationale **109**

5 The 'virtual heart' **113**
5.1 Cardiac structure and function . . . 113
5.1.1 Anatomy and cardiac cycle . . . 114
5.1.2 Cardiac wall structure . . . 116
5.1.3 Structure of the myocardium . . . 118
5.1.4 Cardiac muscle fibers . . . 119
5.2 Cardiac electrophysiology . . . 121
5.3 Cardiac mechanics . . . 123
5.3.1 Passive myocardial mechanics . . . 123
5.3.1.1 Invariants . . . 124
5.3.1.2 Strain energy function . . . 125
5.3.1.2.1 Ground matrix . . . 125
5.3.1.2.2 Collagen-muscle fiber structure 126
5.3.1.2.3 Volumetric bulk material . . . 127
5.3.1.2.4 Passive myocardium . . . 127
5.3.1.3 Evaluation constitutive parameters . . . 127
5.3.1.4 Viscoelasticity . . . 129
5.3.2 Active myocardial mechanics . . . 130

5.4 Heart modeling . . . 133
5.4.1 Subject-specific geometry . . . 133
5.4.2 Myocardial muscle fiber orientation . . . 136
5.4.3 Boundary conditions . . . 137
5.4.3.1 Hemodynamic loading during cardiac cycle 137
5.4.3.2 Surrounding tissue . . . 137
5.5 Heart failure . . . 138

6 Kinematic BCs in ventricular modeling 145
6.1 Introduction . . . 145
6.2 Currently used kinematic constraints . . . 146
6.3 Methods . . . 147
6.3.1 In vivo imaging analysis . . . 149
6.3.1.1 Quantification of myocardial strain . . . 149
6.3.1.2 Subject-specific ventricular geometry . . . 150
6.3.2 Kinematic boundary conditions . . . 151
6.3.3 Hemodynamic pressure loading conditions . . . 153
6.3.4 Cardiac tissue behavior . . . 155
6.3.4.1 Myocardial muscle architecture . . . 155
6.3.4.2 Passive and active constitutive modeling . 156
6.3.5 Experimental design . . . 159
6.4 Results . . . 160
6.4.1 In vivo strain analysis . . . 160
6.4.2 Model validation . . . 160
6.4.3 Comparison of BC cases . . . 162
6.5 Discussion . . . 165
6.5.1 Limitations . . . 168
6.6 Conclusion . . . 169

7 Heart failure modeling validity across the scales 171
7.1 Introduction . . . 171
7.2 Methods . . . 172
7.2.1 Animal model . . . 173
7.2.2 Multiscale model of cardiac growth . . . 173
7.2.2.1 Growth law . . . 175
7.2.2.2 Myocardial tissue response . . . 175
7.2.2.3 Computational model . . . 175
7.2.2.4 Identification of elastic parameters . . . 176
7.2.3 Sensitivity analysis of growth speed . . . 176
7.2.4 Uncertainty quantification using Bayesian inference 177
7.2.5 Uncertainty propagation using Gaussian process regression . . . 178

7.3 Results . . . 179
7.3.1 End-diastolic volumes increase with volume overload 179
7.3.2 Myocyte lengths increase with volume overload . . . 180
7.3.3 Elastic behavior in vivo is softer than ex vivo 182
7.3.4 Growth displays temporal and regional variations . . 183
7.3.5 Growth model correctly predicts myocyte lengthening 186
7.4 Discussion . . . 189
7.4.1 Discrepancy between in vivo and ex vivo elastic tissue behavior . . . 190
7.4.2 Growth displays temporal and regional variations . . 191
7.4.3 Bayesian inference reveals chronic dilation and myocyte lengthening . . . 192
7.4.4 Uncertainty propagation provides quantitative insight into the quality of our model . . . 193
7.4.5 Limitations . . . 194
7.5 Conclusion . . . 195

III Inverse elastostatics **197**

8 Pressure-induced in vivo stress state **199**
8.1 Motivation . . . 200
8.2 Problem description . . . 201
8.3 A modified modular inverse elastostatics method . . . 201
8.4 Accuracy . . . 206
8.4.1 Arterial tube . . . 206
8.4.2 Porcine biventricular model . . . 208
8.5 Applications . . . 209
8.5.1 The in vivo stress state of a patient-specific AAA . . 209
8.5.2 The in vivo stress state of the human heart . . . 211
8.6 Discussion . . . 213

Conclusion **219**

List of Tables **227**

List of Figures **229**

Bibliography **233**

Abbreviations and Symbols

Abbreviations

	2D	Two-dimensional
	3D	Three-dimensional
	4D	Four-dimensional (3D including the time domain)
A		
	AAA	Abdominal aortic aneurysm
	AHA	American Heart Association
	ANOVA	Analysis of variance
	ATP	Adenosine triphosphate
	AV	Atrioventricular
B		
	BC	Boundary condition
	BI	Backward Incremental method
	BV	Biventricular
C		
	CT	Computed tomography
	CVD	Cardiovascular disease
D		
	DOFs	Degrees of freedom
	DT-MRI	Diffusion tensor magnetic resonance imaging
E		
	ECG	Electrocardiogram
	EDP	End-diastolic pressure
	EDV	End-diastolic volume
	EF	Ejection fraction
	EP	Electrophysiology
	ESV	End-systolic volume
	EU	European Union
F		
	FC	Friction coefficient

	FDA	U.S. Food and Drug Administration
	FE	Finite element
	FEA	Finite element analysis
	FEM	Finite element method
	FRR	Foreshortening recovery ratio
G		
	G&R	Growth and remodeling
	GI	Gastro-intestinal
H		
	HF	Heart failure
I		
	IE	Inverse elastostatics
	IVC	Inferior vena cava
L		
	LA	Left atrium
	LDRB	Laplace-Dirichlet Rule-Based
	LES	Lower esophageal sphincter
	LHHM	Living Heart Human Model
	LPN	Lumped parameter network
	LV	Left ventricle
	LVLS	Left ventricular long axis shortening
M		
	MR	Magnetic resonance
	MRI	Magnetic resonance imaging
O		
	ODE	Ordinary differential equation
P		
	PBFS	Polymeric braided fiber stent
	PDE	Partial differential equation
	PDS	Polydioxanone
	PV	Pressure-volume
R		
	R&D	Research and development
	RA	Right atrium
	RV	Right ventricle
	RVE	Representative volume element
S		
	SA	Sinoatrial
	SEF	Strain energy function
	SEMS	Self-expanding metal stent
	SEPS	Self-expanding plastic stent
	SMC	Smooth muscle cell

SV	Stroke volume
SVC	Superior vena cava

T

TMRI	Tagged magnetic resonance imaging

U

US	Ultrasound

SYMBOLS

%	Percentage
$\boldsymbol{\sigma}$	Cauchy or 'true' stress tensor
Ψ	Strain energy function
κ	Structural fiber dispersion parameter
λ	Stretch
λ_L	Second Lamé constant
μ	Mean
μ_L	First Lamé constant
ψ	Strain energy function per unit of mass
ρ	Mass density
$\mathbb{C}$	Stiffness tensor / tangent moduli tensor / Jacobian matrix
$\boldsymbol{\varepsilon}^{\boldsymbol{G}}$	Green-Lagrange strain tensor
ϕ	Potential energy function from Laplace equation
$\boldsymbol{\varphi}$	Non-linear kinematic deformation map
ς^*	Pooled standard deviation
ς	Standard deviation
$\vartheta^{\parallel}$	Longitudinal cardiac growth multiplier
$\vartheta^{\perp}$	Transverse cardiac growth multiplier
$\boldsymbol{b}$	Left Cauchy-Green deformation tensor
$\boldsymbol{C}$	Right Cauchy-Green deformation tensor
d	Cohen's d size effect
E	Modulus of elasticity / Young's Modulus
$\boldsymbol{F}$	Deformation gradient
$\boldsymbol{f}$	Body force
$\boldsymbol{f}_0$	Myocardial fiber direction
$\boldsymbol{I}$	Second-order identity tensor
J	Jacobian / the third invariant of strain
K	Bulk modulus
M	Shear modulus
$\boldsymbol{n}_0$	Myocardial sheet-normal direction
ν	Poisson ratio
$\boldsymbol{P}$	First Piola-Kirchoff stress tensor
$\boldsymbol{R}$	Rotation tensor

$\boldsymbol{S}$	Second Piola-Kirchoff stress tensor
$\boldsymbol{s}_0$	Myocardial sheet direction
$\boldsymbol{t}$	Traction force per unit area
$\boldsymbol{U}$	Right stretch tensor
$\boldsymbol{V}$	Left stretch tensor

SAMENVATTING

INLEIDING

Gastrointestinale en cardiovasculaire aandoeningen hebben een alsmaar toenemende impact op de maatschappij, zowel op sociaal als op economisch vlak. Om de morbiditeit en mortaliteit van deze pathologieën naar beneden te halen is het essentieel meer inzicht te verschaffen in het (patho)fysiologisch functioneren van het onderliggende weefsel. Aan de hand van mechanotransductie conformeert biologisch weefsel zich steeds aan wijzigende mechanische belastingen die het weefsel impacteren. Door middel van biochemische signalen worden cellulaire reacties opgewekt die tot interne structurele wijzigingen van de weefselsamenstelling kunnen leiden, wat zowel positief als negatief kan zijn voor de orgaanfunctie. Aangezien mechanische stimuli deze weefselhermodelleringsproces mede aansturen is het in kaart brengen van het biomechanisch functioneren van het weefsel essentieel om nieuwe inzichten te verwerven in weefsel(patho)fysiologie. Aan de hand van alsmaar beter wordende beeldvormingstechnieken kan men tegenwoordig alsmaar preciezer 'zien' welke vervormingen zich voltrekken in deze weefsels, zowel bij een gezond als een pathologisch functioneren van het orgaan. Om echter de spanningstoestand te karakteriseren die cellen 'voelen' moeten we mathematische modellen opstellen die het samenspel van rekken en spanningen binnen het orgaan kunnen kwantificeren.

Met als hoofddoel het ontwikkelen van *gepersonaliseerde* gastrointestinale en cardiovasculaire modellen, willen we tot nieuwe accurate karakterisering komen van het biomechanisch gedrag van levend weefsel binnen een in vivo setting. Zulk een evaluatie heeft een groot klinisch potentieel, zowel op diagnostisch als prognostisch vlak.

Hoofdstuk 1 - Continuümmechanica en de eindige elementen methode

Dit hoofdstuk introduceert het continuümmechanica-onderzoeksdomein aan de hand van enkele kinematische basisbeginselen die het raamwerk vormen om mechanische problemen te beschrijven en op te lossen. In dit doctoraatswerk plannen we biomechanische problemen op te lossen

waarbij complex constitutief materiaalgedrag wordt geïntegreerd met patient-specifieke geometriën, weefselstructuren en randvoorwaarden. Aangezien het behoud van massa, momentum en energie voor zulke modellen niet analytisch opgelost kan worden zonder grove vereenvoudigen door te voeren, bespreken we welke numerieke methoden ingezet kunnen worden om tot een oplossing te komen. Een korte introductie tot de eindige elementenmethode is voorzien.

Hoofdstuk 2 - Weefselmechanica

Om levend weefsel mathematisch te beschrijven moeten we gebruiken maken van constitutieve materiaalwetten. In dit hoofdstuk leggen we uit hoe deze constitutieve modellen opgesteld en ingezet worden om verscheidene aspecten van weefselmechanica te kwantificeren. Zo bespreken we hoe vervormingsenergiefuncties afgestemd worden om hyperelasticiteit, (on)samendrukbaarheid, viscoelasticiteit, anisotropie, heterogeniteit en viscoelasticiteit te beschrijven. Daaropvolgend beschrijven we hoe deze functies geimplementeerd worden in de gebruikte eindige elementen analyse software. Ook de verscheidene experimentele methodes die frequent gebruikt worden om dit passief multiaxiaal weefselgedrag in vitro te karakteriseren komt aan bod.

Aangezien gastrointestinaal en cardiovasculair weefsel niet enkel passief gedrag vertoont, focussen de daaropvolgende secties op het actieve contractiegedrag en het groei- en hermodelleringsgedrag van levend weefsel. Om actieve contractie binnen het continüummechanisch raamwerk van hoofdstuk 1 te beschrijven, kunnen er verschillende methodologieën gebruikt worden De twee meest gebruikte methodologieën, 'actieve' spanningen en 'actieve' rekken', worden uitgewerkt. Om de hieruit voortvloeiende actieve constitutieve model parameters te kalibreren moet de actieve contractie van weefsel experimenteel bestudeerd worden. De meest courante methodes om dit te doen worden daarom kort overlopen. Ten slotte formuleren we de twee courante theorieën die gebruikt worden om het groei- en hermodelleringsgedrag van biologisch weefsel te modelleren binnen het hiervoor vermelde raamwerk: de 'kinematics-based growth' en de 'constrained mixture modeling' theorie.

DEEL I - GASTROINTESTINALE BIOMECHANICA

In dit deel schetsen we allereerst de klinische achtergrond die ons motiveerde om het gastrointestinaal systeem, en meer bepaald de slokdarm, biomechanisch te bestuderen. Hieropvolgend beschrijven we de ontwikkeling van een patiënt-specifiek, actief contracterend, op zichzelf plooiend slokdarmmodel onder in vivo spanningen. Daaropvolgend gaan we dieper in op de interactie tussen de slokdarm en een nieuwe generatie van biodegradeerbare slokdarmstents.

Hoofdstuk 3 - De 'virtuele' slokdarm

In dit hoofdstuk beschrijven we allereerst de rol die de slokdarm heeft binnen het gastrointestinaal syteem en hoe dit orgaan is opgebouwd. Daaropvolgend gaan we die informatie integreren met experimentele data uit de literatuur (histologie en multiaxiale spanning-rek kwantificatie) om tot een gepaste gekalibreerde constitutieve rek energie functie te komen. Hierbij breiden we de gangbare passieve materiaalwet voor arterieel weefsel uit met een actieve spiercelconstituent die ons toelaat de actieve tonus en contractie van de slokdarmwand te simuleren. Op basis van CT beelddata bouwen we vervolgens geometrisch eindig elementen model op met behulp van eigenhandig ontwikkelde geometrische modelleringsscripts opgesteld in *pyFormex* en de *Mimics* segmentatie software. Aangezien een slokdarm in rust op zichzelf plooit ten gevolge van residuele spanningen en de actieve tonus van het spierweefsel, werd de in vivo spanningstoestand van de patient-specifieke slokdarm berekend aan de hand van de 'Backward Incremental' methodologie. Dit leidt tot een patient-specifiek, op zichzelf plooiend slokdarmmodel met een realistische in vivo spanningstoestand. Om de functionele en biomechanische subtiliteiten van slokdarmperistaltiek te bestuderen, simuleren we finaal ook een multispatiale en multitemporale activatie van het spierweefsel conform het neurologisch prikkelpatroon beschreven in de literatuur.

Hoofdstuk 4 - Slokdarmstenting

Slokdarmvernauwing of achalasie kan de slokdarmfunctie sterk belemmeren, wat tot (potentieel gevaarlijke) ondervoeding en ongemak leidt voor de patiënt. Een mogelijke behandelingsmethode voor deze patienten omvat het plaatsen van een slokdarmstent die het lumen openhoudt. Gedurende de laatste twee decennia werden er hiervoor verscheidene nieuwe slokdarmstents ontwikkeld en op de markt gebracht. De jongste innovatie, biodegradeerbare slokdarmstents, vervullen een functie van 'tijdelijke aard' waardoor het stenten van de slokdarm in de toekomst eventueel ook wordt toegepast bij goedaardige slokdarmpathologieën. Er wordt echter geopperd dat deze eerste generatie biodegradeerbare slokdarmstents niet voldoende radiale kracht heeft om het slokdarmlumen open te houden. Om deze aanklacht en de kans op typische slokdarmstenting complicaties (bvb migratie, slokdarmruptuur, bloedingen, fistels of misselijkheid) te onderzoeken, ontwikkelen we in dit hoofdstuk een state-of-the-art stentmodel dat het mechanisch gedrag van biodegradeerdbare polymere gevlochten vezelstents numeriek simuleert. Dit stentmodel wordt ontwikkeld, gecalibreerd en gevalideerd op basis van een experimenteel degradatieprotocol met compressieproeven en trektesten. Eens gevalideerd, laat het in hoofdstuk 3-ontwikkelde numeriek slokdarm model ons toe om de stent virtueel ontplooien in een virtuele patient-specifieke

slokdarm onder in vivo spanningen. Dit gecombineerd framework vormt een ongeziene virtuele testomgeving die toegang verleent tot onmeetbare data die met de stent-slokdarm interactie gepaard gaat.

DEEL II - HARTBIOMECHANICA

Hart- en vaatziekten zijn wereldwijd de belangrijkste doodsoorzaak en brengen heel wat morbiditeit met zich mee. Vooral hartfalen speelt hier een grote rol in. Aan de hand van gepersonaliseerde hartmodellen ontwikkeld op basis van een minimum aan klinisch patient-specifieke data (hoofdstuk 5) en systematisch geanalyseerde modelleringsaannames (hoofdstuk 6) , trachten we in hoofdstuk 7 de accuraatheid van bepaalde groeimodellen voor het hart te kwantificeren. Deze modellen hebben veel prognostisch potentieel maar werden tot nog toe onvoldoende gevalideerd in correlatie met experimentele data.

Hoofdstuk 5 - Het 'virtuele' hart

In dit hoofdstuk beschrijven we allereerst de rol die het hart heeft binnen het cardiovasculair systeem en hoe dit orgaan is opgebouwd. Hiervoor overlopen we de anatomie, de wandstructuur, de microstructuur van het myocardium en de complexe myocardiale vezelstructuur. Hierna bespreken we de elektromechanische hartfysiologie, waarbij we focussen op de constitutieve beschrijving van het myocardium. Passieve en actieve materiaalmodellen worden geïmplementeerd en een nieuwe dubbele calibratieprocedure wordt voorgesteld om zowel passief als actief materiaalgedrag te tunen op basis van het patient-specifiek in vivo gedrag. Daaropvolgend wordt de opbouw van subject-specifieke geometrische hartmodellen, de reconstructie van de myocardiale vezelstructuur en de hemodynamische en omliggende weefsel randvoorwaarden uiteengezet. Ten slotte overlopen we de uitdagingen die aangepakt moeten worden om de accuraatheid van groeimodellen te bestuderen.

Hoofdstuk 6 - Randvoorwaarden voor realistiche ventriculaire modellering

Omwille van de beperkte beschikbaarheid en resolutie van beelddata binnen een klinische context, worden hartmodellen vaak beperkt tot het modelleren van de ventrikels. Bij het mechanisch verankeren van deze ventrikels in de virtuele ruimte moet het effect van het niet-expliciet-gemodelleerde omliggende weefsel op de hartfunctie zo realistisch mogelijk benaderd worden. Een literatuurstudie naar courante kinematische ventriculaire randvoorwaarden brengt een grote variëteit in verankeringsstrategieën naar voren. Om systematisch tot een nieuwe consensus rond geschikte

randvoorwaarden te komen, stellen we een zo accuraat mogelijk patiënt-specifiek biventriculair model op aan de hand van 4D Tagged MR beelddata. Dit model wordt dan op basis van vijf verschillende strategieën verankerd. Daaropvolgend wordt het gesimuleerde gedrag en het in vivo gekakteriseerde gedrag op een globale (a.d.h.v. klinische hartfunctie metrieken) en lokale (o.b.v. lokale rek- en spanningsconcentraties) schaal vergeleken. Hieruit blijkt dat een zwakke gedistribueerde penalty-based verankeringsmethodologie beter geschikt is dan de meer gangbare volledige verankering van bepaalde delen van het computationeel domein.

Hoofdstuk 7 - Multispatiale en multitemporale modelering van hartfalen

Binnen biomechanische wetenschapskringen vormen 'kinematics-based growth' modellen een algemeen aanvaard prognostisch paradigma om de invloed van mechanische overbelasting van het hart te linken aan de structurele hermodellering van de hartwand. Deze modellen zijn echter nog niet klinisch aanvaard omwille van een gebrek aan validatie. Om de accuraatheid van deze modellen te kwantificeren in correlatie met experimentele data, hebben we allereerst een dierenstudie opgezet waarbij enkele chordae werden doorknipt om hogere vulbelastingen in de hartkamer te induceren. De experimentele resultaten van deze studie (tweewekelijkse biopten ter karakterizatie van de subcellulaire en cellulaire weefselevolutie en tweewekelijkse US beeldvorming en drukmetingen ter karakterisatie van de orgaanvorm en -functie) werden vervolgens systematisch vergeleken met een parallelle computationele 'stretch-driven multiscale heart modeling' studie, om tot een predictieve nauwkeurigheid te komen van 52.7%. Belangrijk hier is de probabilistische uitvoering van deze studie, waarbij statistische 'machine learning' technieken werden ingezet om enerzijds onzekerheid in experimentele data te karakteriseren en anderzijds onzekerheid in model input te propageren doorheen het model om zo de onzekerheid op gesimuleerde output te kwantificeren.

DEEL III - INVERSE ELASTOSTATICA

Aangezien patient-specifieke gastro-intestinale en cardiovasculaire modellen steeds opgebouwd worden op basis van in vivo beeldvormingstechnieken, mag niet uit het oog verloren worden dat het gevisualiseerde orgaan onder een in vivo spanningstoestand functioneert. Om dit gedrag in gepersonaliseerde orgaanmodellen te implementeren moet een invers probleem opgelost worden, wat op twee manieren kan gebeuren: direct invers of iteratief voorwaarts benaderend. Iteratieve voorwaartse benaderingsmethodieken zijn populair aangezien deze makkelijk te implementeren zijn in (commerciële) eindige elementensoftware. Deze oplossingsmethode is vaak echter nogal

rekenintensief en niet altijd even robuust. Als antwoord hierop zetten we in dit hoofdstuk een modulaire inverse elastostatische methodologie uiteen afgestemd op een relatief eenvoudige implementatie in de commerciële eindige elementensoftware *Abaqus*. Vervolgens berekenen we de in vivo spanningstoestand van enkele complexe patient-specifieke cardiovasculaire modellen om de accuraatheid, robuustheid en efficiëntie van deze oplossingmethode te toetsen.

CONCLUSIE

De conclusie vat de belangrijkste verwezenlijkingen en bevindingen van dit werk samen, en beschouwt de *weg naar klinische translatie* die nog afgelegd moet worden om gepersonalizeerde gastrointestinale en cardiovasculaire orgaanmodellen tot bij de patiënt te brengen.

Summary

Introduction

Gastrointestinal and cardiovascular disease have an ever increasing impact on society, both on a social and economical level. To bring down the associated mortality and morbidity, an increased understanding of the (patho)physiological tissue function is vital. Through mechanotransduction processes cells sense and respond to mechanical stimuli by converting them to biochemical signals that induce specific cellular, and thus structural, responses. These responses can lead to an improvement or deterioration of organ function. As mechanical stimuli thus play a role in the pathophysiological adaptation of tissue, we focus our attention towards an accurate biomechanical description of gastrointestinal and cardiovascular tissue behavior. Therefore, our key objective is the development of personalized computational organ models that characterize the mechanical environment that is being 'felt' by the tissue. This quantification holds immense diagnostic and prognostic potential.

Chapter 1 - Continuum mechanics and the finite element method

This chapter introduces the branch of mechanics that deals with the mechanical behavior of materials modeled as a continuous mass rather than as discrete particles. We set out the fundamental principles needed to set up a continuum mechanics problem. Given that this research work will set up models that integrate complex constitutive material laws with patient-specific geometries, intricate 3D tissue microstructures and boundary conditions, an analytic solution to the partial differential equations derived from the conservation of mass, momentum and energy will not exist. Therefore, a short introduction to numerical solution techniques, and more specifically the finite element method, is provided.

Chapter 2 - Soft tissue mechanics

To describe the mechanical behavior of soft living tissue, we need appropriate constitutive material models. In this chapter, we disclose how these material laws are set up and deployed to quantify different intrinsic aspects of soft

tissue mechanics. More specifically, we describe how strain energy density functions take into account hyperelasticity, (in)compressibility, anisotropy and viscoelasticity. Consequently, we explain how these functions are implemented in the utilized finite element analysis software. Also the different experimental methodologies used to experimentally characterize the multiaxial response of soft tissue to physiological loading conditions are discussed.

Given that gastrointestinal and cardiovascular tissue also generate substantial amounts of active contraction, we describe two prevailing methodologies to bring active force generation into the continuum mechanics description of chapter 1. To subsquently tune the associated active constitutive parameters, we need to characterize this soft tissue behavior experimentally. The commonly used experimental protocols to do this are shortly summarized. As tissue also undergoes structural changes on a long term, we outline the 'kinematics-based growth' and 'constrained mixture modeling' framework that are frequently used to incorporate such behavior in biomechanical organ models.

PART I - GASTROINTESTINAL BIOMECHANICS

In the first place, this part provides the clinical context that motivated us to study the biomechanical behavior of the gastro-intestinal system, and more specically the esophagus. Consequently, we describe the realization of a patient-specific, actively contracting, buckling and in vivo stresses esophagus model. Next, we further develop our framework to include a realistic numerical stent model to study the stent-esophagus interaction in more detail.

Chapter 3 - The 'virtual' esophagus

This chapter outlines the role that the esophagus has to fulfill within the gastrointestinal system and how this organ is structured. Consequently, this information is further integrated with tissue histology and multiaxial stress-strain descriptions from literature to come to an accurate, calibrated strain energy function. In doing so, we expand the prevailing passive constitutive law for arterial tissue to include an active muscle cell constituent that allows us to simulate active tone and contraction of esophageal tissue. Based on CT imaging data, we subsequently construct a patient-specific finite element mesh using *pyFormex*-based geometrical modeling and image segmentation protocols in *Mimics*. Given that the esophagus buckles in response to the residual stresses and active tone present in the esophageal wall, the in vivo stress state is computed using a double 'Backward Incremental'-methodology. This leads to a patient-specific in vivo stressed esophagus models. To deepen

our understanding of the biomechanical subtleties of peristaltic contractions, we also simulate a multispatial and multitemporal muscle cell activation conform the neurological stimulus pattern described in literature.

Chapter 4 - Esophageal stenting

Esophageal strictures or achalasia can strongly impede the esophageal food transport, leading to considerable malnutrition and discomfort for the patient. Esophageal stenting provides a potential treatment strategy to restore lumen patency. Over the last two decades, continuous technological innovations brought different esophageal stent designs to the market. The latest innovation, biodegradable esophageal stents, could however bring a wind of change to the esophageal stenting market due to its 'temporary character' which could potentially open up the list of indications for esophageal stenting to include benign esophageal pathologies. To systematically assess the ability of these stents to restore esophageal lumen patency and estimate the risk for adverse events (such as migration, rupture, bleeding, fistula formation, nausea), we develop a new state-of-the-art numerical stent model that captures the intrinsic mechanical behavior of (biodegradable) poylmeric braided fiber stents. This model is developed, calibrated and validated based on an in vitro degradation study including radial compression and tensile testing procedures. Once validated, the in chapter 3 developed numerical esophagus model allows us to virtually deploy this stent in a virtual patient-specific, in vivo stressed esophagus. Such a combined framework comprises an unprecedented virtual testing environment which allows us to compute unmeasurable mechanical metrics related to the stent-esophagus interaction.

PART II - CARDIAC BIOMECHANICS

Cardiovascular diseases are a major cause of mortality worldwide, which is strongly related to heart failure. Through the development of personalized heart models based on clinical patient-specific data (chapter 5) and the systematic analysis of different modeling assumptions, we quantify the accuracy of cardiac growth models in chapter 7.

Chapter 5 - The 'virtual' heart

This chapter outlines the role that the esophagus has to fulfill within the cardiovascular system and how this organ is structured. More specifically, we discuss the anatomy and cardiac cycle, the cardiac wall structure, the microstructure of the myocardium and the complex 3D organization of cardiomyocytes throughout the heart wall. Consequently, we describe the electromechanical functioning of the heart, where focus on the constitutive description of myocardial tissue. Passive and active material laws are

implemented and a novel two-stage calibration procedure is used to correct for the mismatch between subject-specific in vivo and ex vivo characterized passive and active tissue behavior. Consequently we outline how subject-specific heart geometries are build from imaging data, how the myocardial fiber structure is reconstructed in these models and how hemodynamic loading conditions and surround tissue is accounted for in our personalized heart models. Lastly, we summarize the challenges that are currently impeding clinical adoption of cardiac growth modeling.

Chapter 6 - Accounting for surrounding tissue in ventricular modeling

Due to the absence of relevant imaging data or sub-optimal imaging resolution in the clinical context, personalized heart models are typically confined to modeling the ventricular behavior. For these models, it is important to appropriately account for the (not explicitly modeled) surrounding tissue that tether and/or constrain the mechanical functioning of the ventricles. A literature study on ventricular models brought forward a large variety of commonly used kinematic boundary conditions, which shows that the appropriateness of these anchoring strategies remains relatively investigated. Therefore, a patient-specific biventricular model based on 4D Tagged MR imaging data is developed, which will be used to systematically investigate the role of a subset of current boundary conditions on the modeled ventricular behavior at a global and local scale. In vivo measured strains are used as a reference to quantify and determine the more appropriate anchoring strategy to be used for ventricular modeling.

Chapter 7 - Heart failure modeling validity across the scales

In the biomechanics community, 'kinematics-based growth modeling' represents a well-accepted paradigm to link cardiac overload to hypertrophic tissue responses in the heart. These models have not been adopted clinically, however, due to lack of validation. To quantify the predictive capacity of these models in correlation with experimental data, we set up an animal study where the chordae were disrupted to induce volume overload in the heart. The experimental results of this study (biweekly biopsies taken to characterize the cell scale and biweekly ultrasound and pressure measurements to characterize the organ scale) were systematically correlated with a parallel computational 'stretch-driven' cardiac growth model which resulted in an overlap of 52.7% between the experimental and the simulation results. Important here is the probabilistic conduct applied in this study, where statistical 'machine learning' techniques were employed to quantify the uncertainty of sparse and noisy experimental data collection and to propagate uncertainty on model input through the modeling pathway to quantify uncertainty on the simulated output.

PART III - INVERSE ELASTOSTATICS TO COMPUTE THE IN VIVO STRESS STATE

Patient-specific biomechanical modeling of the gastro-intestinal and cardiovascular system is complicated by the constant presence of a physiological pressure load due to which the imaged tissue is in a pre-stressed and -strained state. To incorporate this deformed and loaded tissue state into our personalized organ models, an inverse problem needs to be solved, which can be done in two ways: through direct inverse methodologies or iterative forward approximation procedures. Iterative methodologies are popular given that they can be easily implemented in (commercial) finite element analysis software. However, these methodologies often suffer from high computational costs and are not always robust. Therefore, this chapter formulates a modular inverse elastostatics method attuned to a straightforward implementation in the commercial finite element analysis software *Abaqus*. Consequently, we compute the in vivo stress state of some complex patient-specific cardiovascular models to study the method's accuracy, robustness and computational efficiency.

CONCLUSION

The conclusion summarizes the major achievements and findings of this work, and outlines the remaining obstacles on the *road to clinical translation* that need to be overcome to bring personalized gastrointestinal and cardiovascular models to the patient.

Introduction

Should we consider the human body to be a well-engineered machine or system? In *The Creation of Adam*, Michelangelo portrayed the human body as a *perfect* physical specimen. Charles Darwin's theory of evolution on the other hand raised quite some imperfections in the anatomic structures and functions of the human body.

So who was right? Well, they both are. Anthropologists have shown that evolution does not produce perfection, it produces function [45]. A panel of anatomists and biologists can easily come up with a whole list of design flaws and sound propositions on how to improve our body. But if you look more closely at these *evolved functions* from an engineering perspective, we have to admit that even the best scientists and engineers cannot come close to replicating their intricate performance and complexity. The body's computer, the brain, is by far the most sophisticated, finest constructed and most efficient computer that has ever existed. With a memory of 2.5 million gigabytes and 10 quadrillion (which equals a billion billion) calculations per second, comprised in a volume of 1450 cubic centimeters only using 20W of power (which is equivalent to one light bulb), the fastest supercomputer to date is still far from the efficiency portrayed by the human brain. The human heart works tirelessly, for the many years of our lives, to pump vitality through our body. This organ pumps 7500 liters of blood through our blood vessels each day. Starting to beat the 4th week into pregnancy with an average 100.000 beats a day, your heart will have beaten 2.5 billion times by the time you are 70 years old. Weighing only 300 grams, this pump creates enough energy to drive a truck 30 kilometers a day. In a lifetime, that is equivalent to driving that same truck to the moon and back. It is difficult to imagine a mechanical pump anywhere near as good in operating so well over so long as the human heart.

Understanding the beauty of biology and how it functions has defied our understanding for many millennia now, from the writings of ancient philosophers to our advanced and hyper-technified methods of today. For a long time, scientists have been convinced that mechanics play an

extremely important role in governing biological and physical interactions. Mid-20th century, this hypothesis was confirmed by the discovery of mechanotransduction in cells [41, 236, 334], the fundamental structural and functional units of *life*, where different genes, and thus functions, are expressed in response to mechanical stimuli. In other words, the importance of mechanics in biology and medicine cannot be underestimated and forms a very interesting field of study: biomechanics.

BIOMECHANICS

Biomechanics combines biology, the study of living things with mechanics, the study of motions and the applied loads that cause them. Therefore, a very simple and dry definition for biomechanics could be the study of the motions experienced by living things to applied loads. A better and more complete definition however enholds [155]:

> *Biomechanics is the development, extension, and application of mechanics for the purposes of better understanding the influence of mechanical loads on the structure, properties and function of living things.*

The field can be dated back to essays by Aristotle (384-322 BC) on the movement of animals, in which he uses the mechanical concept of 'ground action force' as a starting point to deliberate where movement comes from. Later, this field has been further shaped by scientists including da Vinci (1452-1519), Galilei (1564-1642), Hooke (1635-1703), Euler (1707-1783), Young (1773-1829), Poiseulle (1799-1869), von Helmholtz (1821-1894), ... The field however really came into its own starting the mid 1960s due to the concurrency of the post World War II renaissance in continuum mechanics, the birth of modern biology, the 'Space Race' (how will the human body react to the different environments when traveling to the moon) and the technological developments leading to ever-increasing computational power needed to solve many important but complex non-linear problems.

Today, biomechanics encompasses a broad range of topics, and tons of examples can be found where biomechanics plays a central role in health care applications (see Figure 0.1). Humphrey and Delange [155] listed some of the various applications where mechanics play a role: "from understanding why abdominal aortic aneurysms rupture, to identifying the failure strength of the anterior cruciate ligament in an elite athlete, which must be protected during training and competition; from designing an artificial heart valve that must open and close over 30 million times per year, to understanding why artificial hip implants loosen over time and cause pain; from understanding

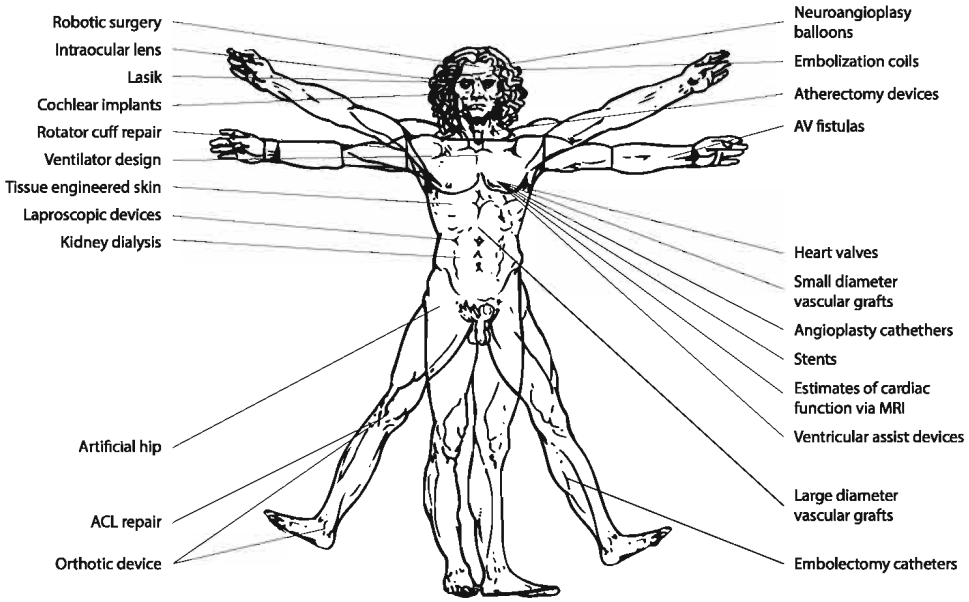

Figure 0.1: A scheme of Da Vinci's *Visuvian Man* depicting some aspects of human physiology, pathophysiology, and injury that can be addressed using biomechanics. Adapted from [155].

what pressure must be applied to an angioplasty balloon to open a diseased artery, to understanding how deep and how many incisions should be made to modify the curvature of the cornea to correct for visual problems; from understanding the role of stresses in biological growth for the purpose of engineering tissue replacements, to designing a mechanical ventilator for those in respiratory distress; from using computer-aided modeling to guide robotic-assisted surgery, to designing needles that induce less damage to the arterial or venous wall; from designing an orthotic device for supporting an injured limb, to specifying a rehabilitation schedule that promotes tissue healing".

MOTIVATION

Even though the aforementioned evolved functions in the human body are quite impressive from an engineering point of view, these systems can and do also fail. In the gastro-intestinal system, structural remodeling of the esophageal wall impedes food transport to the stomach leading to considerable discomfort and problems for the patient. In the cardiovascular system, cardiomyopathy deteriorates the heart's pump function which eventually results in sudden death. To address these system failures, an improved understanding of the comprising tissue's biomechanical behavior

is essential. Therefore, this work set out to obtain more insights into the mechanisms responsible for the development and progression of pathological gastro-intestinal and cardiovascular conditions.

Nowadays, the affluence and quality of available medical imaging data in fundamental research offers interesting opportunities to study and characterize soft tissue behavior through comprehensive information on anatomy and the kinematics of deformation. Even though this evolution provides an ever clearer view on gastro-intestinal and cardiovascular function and pathology, it remains difficult to connect what we 'see' with what is physiologically 'happening' in the tissue [118, 129]. The physiological mechanisms in the tissue are governed by cells that constantly sense (and adapt their structure to) the tissue's mechanical environment. Quantification of the biomechanical environment thus has the potential to resolve the missing link between imaging-deduced tissue kinematics and the underlying physiological mechanisms. To quantify the tissue's biomechanics, we developed mathematical models describing the biomechanical tissue behavior. This is challenging for two reasons. First, gastro-intestinal and cardiac tissue exhibits, similar to any other soft biological tissue, non-linear, pseudo-elastic, inhomogeneous and anisotropic behavior and tends to perform under large physiological deformations. Secondly, these tissues are metabolically active when alive; their mechanical behavior varies with time, both on the short term (e.g. a peristaltic contraction, a heart beat) and the long term (e.g. disease, aging). Consequently, it is difficult to model this behavior with *analytical* closed-form expressions without assuming idealized geometries and simplified mechanical behavior (e.g. based on Laplace's law (physics) or the axisymmetric membrane theory). Given that such assumptions and simplifications undermine the diagnostic and prognostic power of soft tissue modeling [76, 118, 202, 335, 375], this work employed the finite element method to *numerically* solve mass, moment and energy equilibrium of a certain body (of tissue).

Using the recent advances in image processing and computational infrastructure, this dissertation integrates medical image data and finite element models of tissue function with the key objective to develop accurate, efficient, robust and reliable *personalized* esophagus and heart models. The accurate representation of these highly complex multiscale organs with a mathematical structure involves careful consideration of multiple modeling decisions. Therefore, important modeling aspects (e.g. appropriate constitutive laws including passive and active tissue behavior, subject-specific material calibration, boundary conditions, reference geometry, residual stress) are carefully selected and/or resolved throughout this work. Given that the accuracy of personalized soft tissue organ models will always be restricted by the quantity and quality of the data at hand, the developed

modeling pathway continuously takes into account the limited availability of clinical data and its limitations.

With these models, we aim to faithfully represent observed physiology and function, but also to study the underlying mechanistic disease- and/or age-induced mechanisms degrading organ function. As such, these models hold immense diagnostic and prognostic potential for clinical decision-making and surgical planning. For instance, a personalized simulation approach will facilitate the identification of clinically relevant individual patient characteristics that serve as biomarkers to discriminate between health and disease. Likewise, we will be able to virtually assess the safety, efficacy and success rate of a certain procedure (device implantation, surgery) for each and every patient prior to the actual intervention. Additionally, quantification of biomechanical metrics can also bring forward increased understanding of the underlying (patho)physiological mechanisms that progressively deteriorate esophageal and cardiac function. As such, these insights can guide the evolution towards more effective, subject-specifically tailored and mechanism-targeted treatment strategies. Overall, the objective of this research fits in the broader global incentive to bring computational soft tissue modeling technology from the engineering research lab to the patient.

This dissertation was conducted at the lab for Biofluid, Tissue and Solid Mechanics for Medical Applications (bioMMeda) at Ghent University, where in silico tools for the development and validation of numerical stent models and arterial bifurcation models have been established in the past, e.g. [49, 52, 57, 159, 233]. This project further expanded these tools towards personalized esophageal and cardiac modeling. Moreover, this project implemented the kinematics-based cardiac growth framework and a novel inverse elastostatics methodology in commercial FEA software (*Abaqus*). Additionally, accurate numerical models describing the mechanical behavior of biodegradable polymeric braided wire stents were developed. During this PhD project, successful collaborations were set up with the University of Cape Town, South Africa (dr. ir. Kevin Leigh Sack) and Stanford University, USA (dr. ir. Francisco Sahli Costabal and prof. dr. ir. Ellen Kuhl).

STRUCTURE

Chapter 1 provides the reader with a brief introduction into the field of continuum mechanics. Like many other fields of science, solving a continuum mechanics problem involves finding a solution to a set of differential equations deduced from the physical laws governing the body of interest (i.e. conservation of mass, moment and energy) and a set of boundary

and/or initial values. The complexity of the mechanical problems to be solved in this work (due to a.o. complex material models, geometries and boundary conditions needed to mechanically describe soft living matter) required a numerical approach to solve the system of differential equations deduced from the continuum mechanics formulations (kinematics, kinetics and constitutive laws). Therefore, chapter 1 also gives a short summary on the theoretical background of the finite element method, the numerical solution approach used throughout the remainder of this dissertation. Next, chapter 2 outlines how we experimentally measure and constitutively model passive, active, growing and remodeling soft biological tissue behavior.

Part I, *Gastro-Intestinal Biomechanics*, exposes the impact that highly prevalent and costly gastro-intestinal diseases have on the patient's quality of life and productivity. Following a short overview on the current state-of-the-art in gastro-intestinal biomechanics, and more specifically esophageal biomechanics, chapter 3 develops a biomechanical 'virtual esophagus' model which transcends the current state of the art in mathematical and constitutive modeling of esophageal function in health and disease. As stated in this dissertation's motivation, the developed patient-specific tissue models can eventually be used to virtually study potential treatment strategies prior to intervention. To this end, chapter 4 develops a validated biodegradable esophageal stent model which gets virtually implanted into the patient-specific in vivo stressed esophagus model developed in the previous chapter. This combined framework provides both clinicians and device manufacturers with detailed quantitative mechanical insights in the interaction between device design on the one hand and patient-specific anatomy and (patho)physiology on the other hand.

Part II, *Cardiac Biomechanics*, focuses on the growing clinical and economical burden that cardiovascular disease, and more specifically heart failure, forms to society. To assist the detection, diagnosis and treatment of cardiac disease in the clinical practice, chapter 5 first discusses the model-based interpretation of cardiac structure and function, and how this interpretation leads to cardiac computational models that allow diagnostic and prognostic personalized modeling of heart mechanics. In this chapter, we carefully address important modeling attributes that, due to the typical absence of relevant data in the clinical practice, need to be based on assumptions which need to be thoroughly studied (e.g. patient-specific reference geometry, fiber distribution, boundary conditions to account for not explicitly modeled surrounding structures tethering and constraining the movement of the developed computational cardiac models). As it turns out that different common strategies to mechanically anchor ventricular models in space remained insufficiently studied in the literature, chapter 6 systematically

investigates the role and suitability of a subset of current boundary conditions on the modeled ventricular behavior at a global and local scale. Concluding our work on cardiac biomechanics, we eventually address the current challenges that hinder an accurate assessment of the predictive power of cardiac growth models in tight correlation with experimental data. To overcome this impediment, chapter 7 sets forth a novel approach to quantify the predictive power of cardiac growth modeling using a unique chronic volume overload study, multiscale subject-specific kinematics-based growth modeling and machine learning techniques to quantify and propagate uncertainty on experimentally sparse data through the models.

Finally, in our objective to develop accurate, efficient, robust and reliable patient-specific gastro-intestinal and cardiovascular tissue models that need to correct for the pressure-induced in vivo stress state present during image acquisition, *Inverse Elastostatics* (part III) further extends the developed set of mathematical tools developed and implemented in this research work with a novel modular inverse elastostatics approach that turns out to be an interesting computationally efficient and robust alternative for the iterative methodology used to compute the pressure-induced in vivo stress state in chapter 3.

LIST OF PUBLICATIONS

First author peer-reviewed papers

- M. Peirlinck, F. Sahli Costabal, K. L. Sack, J. S. Choy, G. S. Kassab, J. M. Guccione, M. De Beule, P. Segers, and E. Kuhl, "Using machine learning to characterize heart failure across the scales", *Biomechanics and Modeling in Mechanobiology*, 2019, in press

- M. Peirlinck, K. L. Sack, P. De Backer, P. Morais, P. Segers, T. Franz, and M. De Beule, "Kinematic boundary conditions substantially impact in silico ventricular function", *International Journal for Numerical Methods in Biomedical Engineering*, vol. 35, no. 1, e3151, 2019

- M. Peirlinck, M. De Beule, P. Segers, and N. Rebelo, "A modular inverse elastostatics approach to resolve the pressure-induced stress state for in vivo imaging based cardiovascular modeling", *Journal of the Mechanical Behavior of Biomedical Materials*, vol. 85, pp. 124–133, 2018

- M. Peirlinck, N. Debusschere, F. Iannaccone, P. D. Siersema, B. Verhegghe, P. Segers, and M. De Beule, "An in silico biomechanical analysis of the stent–esophagus interaction", *Biomechanics and Modeling in Mechanobiology*, vol. 17, no. 1, pp. 111–131, 2018

Co-author peer-reviewed papers

- A. Caenen, M. Pernot, M. Peirlinck, L. Mertens, A. Swillens, and P. Segers, "An in silico framework to analyze the anisotropic shear wave mechanics in cardiac shear wave elastography", *Physics in Medicine and Biology*, 2018

- M. Hirdes, M. Peirlinck, M. De Beule, and P. D. Siersema, "Can we develop self-expandable metallic stents without consideration of mechanical properties? Reply", *Endoscopy*, vol. 46, no. 8, p. 716, 2014

- J. Ochola, M. Peirlinck, I. Peeters, B. Malengier, M. De Beule, L. Daelemans, J. Githaiga, L. De Wilde, and L. Van Langenhove, "Feasibility of reinforcing suture repaired tendon using a tubular braided fabric", in preparation

Book chapter

- S. Levine, T. Battisti, B. Butz, K. D'Souza, F. Sahli Costabal, and M. Peirlinck, "Modeling congenital heart disease - engineering a patient-specific therapy", in, G. Butera, S. Schievano, G. Biglino, and D. B. McElhinney, Eds. Springer Nature, 2019, ch. Dassault Systèmes' Living Heart Project, under review

CHAPTER 1

CONTINUUM MECHANICS AND THE FINITE ELEMENT METHOD

Continuum mechanics forms a specific subbranch of mechanics in which we hypothesize that the gross (macroscropic) response of a body (e.g. a soft tissue slab), which at a nanoscale will be very inhomogeneous and discontinuous, can macroscropically be approximated by assuming locally averaged properties, defined at every point in the body [154]. This hypothesis has been shown to be justified and useful to study soft tissue behavior as long as a characteristic length of the body of interest is at least 100 times larger than a characteristic length in that tissue's microstructure. Consequently, continuum mechanics allows us to describe quantities of interest (such as the stress and strain state of tissue) by continuous, or at least piece-wise continuous, functions that exist at each point within a locally homogenized body [154]. This aspect of continuum mechanics merges symbiotically with the finite element method (FEM) where we solve for (mechanical) unknowns at discrete number of points over the domain of interest.

In this chapter, we provide the reader with a brief introduction into the field of continuum mechanics, with a focus on soft tissue biomechanics. We also briefly describe how the finite element method is set up and how this method is used to solve complex continuum mechanics problems. This chapter has been assembled through study of the following books and documents, to which we refer the interested reader who wants a more in depth description of continuum mechanics and the finite element method: [17, 46, 57, 69, 77, 84, 143, 152, 154, 361, 378].

1.1 KINEMATICS

Consider a solid body $\mathscr{B}$, which gets transformed from its base configuration $\mathcal{B}_0$ to the current configuration $\mathcal{B}_t$ at time $t \in \mathbb{R}_+$. In order to describe the kinematics of this transformation, we can choose to work in two different kinematic description frameworks: the *Lagrangian* or *Eulerian* description. In the *Lagrangian* (or material) description the initial configuration of the body at time t_0 is considered the reference configuration which means that the position and physical properties of the particles are described in terms of the material or referential coordinates and time. In the *Eulerian* (or spatial) description the current configuration is considered the reference configuration.

In order to describe the motion of a solid body $\mathscr{B}$ (see Figure 1.1), it is common practice to introduce a non-linear *deformation map* $\boldsymbol{\varphi}$ which maps the material point $\boldsymbol{p}$ with coordinates $\boldsymbol{X}$ in the reference configuration $\mathcal{B}_0$ onto spatial points $\boldsymbol{x} = \boldsymbol{\varphi}(\boldsymbol{X}, t)$ at time $t \in \mathbb{R}_+$ in the deformed configuration $\mathcal{B}_t$. Note the used notation here using upper case $\boldsymbol{X}$ and lower case $\boldsymbol{x}$ to denote the position of material point $\boldsymbol{p}$ in the reference configuration and current configuration respectively. This convention will be kept throughout this

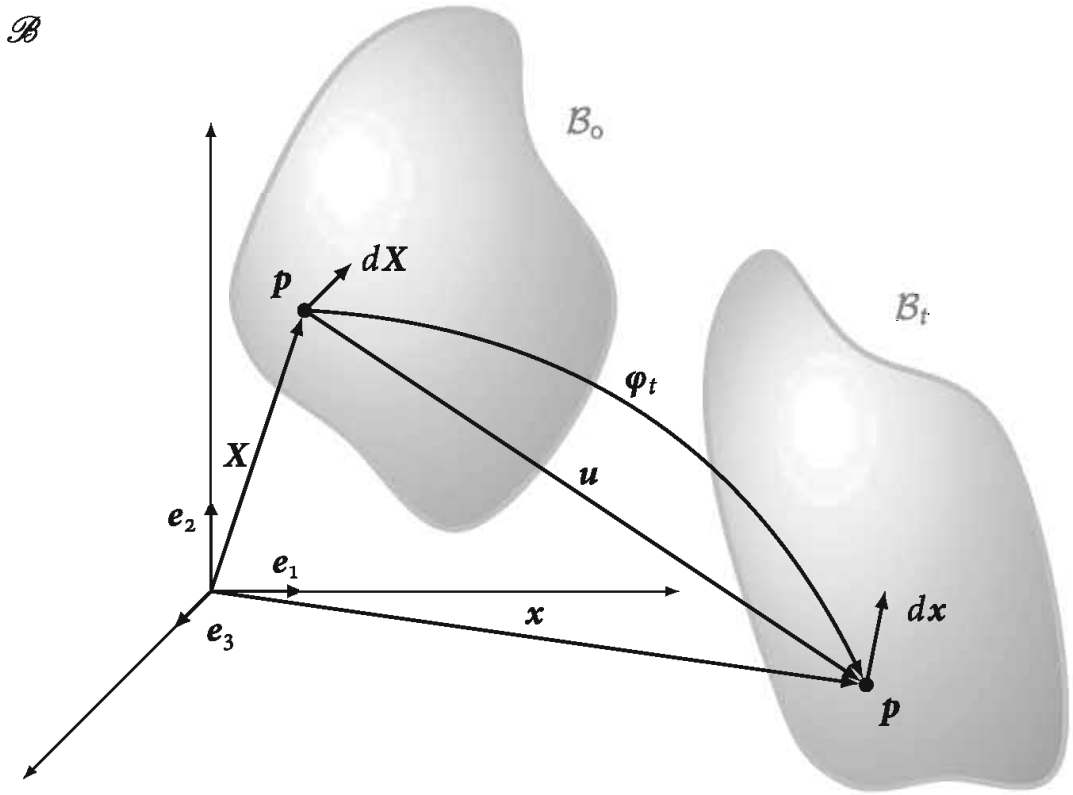

Figure 1.1: Deformation of a solid body from the reference geometry $\mathcal{B}_0$ to the deformed geometry $\mathcal{B}_t$ through the mapping function $\boldsymbol{\varphi}$ which maps the position $\boldsymbol{X}$ of a material point $\boldsymbol{p}$ onto the current coordinates $\boldsymbol{x}$. Image adapted from [57].

dissertation to denote other kinematic measures in different configurations, e.g. dS and ds respectively describe an infinitesimal surface in the reference configuration and current configuration. The displacement of material point $\boldsymbol{p}$ is described by $\boldsymbol{u} = \boldsymbol{x} - \boldsymbol{X}$, so

$$\boldsymbol{\varphi}(\boldsymbol{X}, t) : \mathcal{B}_0 \subset \mathbb{R}^3 \rightarrow \mathcal{B}_t \subset \mathbb{R}^3 \tag{1.1}$$

As the material behavior depends on the straining of the material and not on its rigid body motion, those parts of the motion in the vicinity of a material point must be distinguished. Characterizing this local material deformation with respect to the reference configuration requires the introduction of the *deformation gradient tensor* $\boldsymbol{F}$ which is defined as

$$\boldsymbol{F} := \partial_{\boldsymbol{X}} \boldsymbol{\varphi}(\boldsymbol{X}) = \frac{\partial \boldsymbol{x}}{\partial \boldsymbol{X}} \tag{1.2}$$

The polar decomposition theorem states that any motion can be represented as a pure stretch of three orthogonal directions followed by a pure rigid body rotation or a pure rigid body rotation followed by a pure stretch of three orthogonal directions (see Figure 1.2):

$$\boldsymbol{F} = \boldsymbol{R}\boldsymbol{U} = \boldsymbol{V}\boldsymbol{R} \tag{1.3}$$

where $\boldsymbol{R}$ is the orthogonal rotation tensor depicting the pure rigid body rotation and $\boldsymbol{V}$ and $\boldsymbol{U}$ are the positive definite symmetric left and right

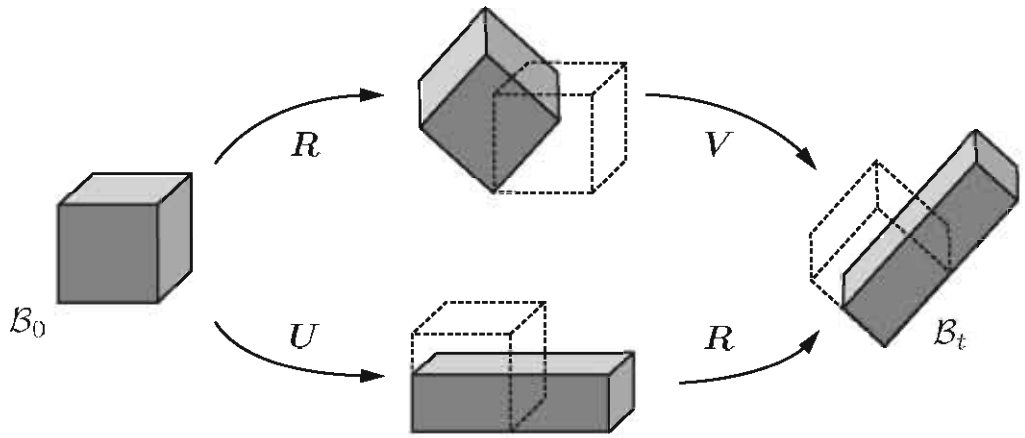

Figure 1.2: The deformation gradient $\boldsymbol{F}$ can be decomposed, using the polar decomposition theorem, into a product of two second-order tensors: a pure rigid body rotation $\boldsymbol{R}$ followed by a pure stretch of three orthogonal directions $\boldsymbol{V}$; $\boldsymbol{F} = \boldsymbol{V}\boldsymbol{R}$ or a pure stretch of three orthogonal directions $\boldsymbol{U}$ followed by a pure rigid body rotation $\boldsymbol{R}$; $\boldsymbol{F} = \boldsymbol{R}\boldsymbol{U}$.

stretch tensors, respectively. The polar decomposition theorem is important because it allows us to distinguish the straining part of the motion from the rigid body rotation.

Useful measures of deformation or stretch can be found by

- solving an eigenvalue problem to describe the left or right stretch tensor in terms of its principal eigenvalues and eigenvectors, which correspond to the *principal stretches* and *directions*:

$$\boldsymbol{U} = \lambda_I \boldsymbol{N}_I \boldsymbol{N}_I{}^T + \lambda_{II} \boldsymbol{N}_{II} \boldsymbol{N}_{II}{}^T + \lambda_{III} \boldsymbol{N}_{III} \boldsymbol{N}_{III}{}^T \tag{1.4}$$

  where $\boldsymbol{N}_I$, $\boldsymbol{N}_{II}$ and $\boldsymbol{N}_{III}$ are an orthonormal set of base vectors in the reference configuration.

- elimination of the pure rigid body rotation tensor $\boldsymbol{R}$. By left and right side tensor multiplication of $\boldsymbol{F}$ with its transpose $\boldsymbol{F}^T$, we get the so-called left and right *Cauchy-Green tensors* $\boldsymbol{b}$ and $\boldsymbol{C}$:

$$\boldsymbol{b} = \boldsymbol{F}\boldsymbol{F}^T, \boldsymbol{C} = \boldsymbol{F}^T\boldsymbol{F} \tag{1.5}$$

  These tensors have the benefit that the polar decomposition, which is computationally expensive in practice, does not need to be computed to express the relative motion of neighboring points in the solid body. As will be seen later on, these tensors are often used to describe hyperelastic tissue behavior (see paragraph 2.1.1.1.3). Both tensors are independent of rigid body rotation, but they describe the deformation in two different coordinate systems. The right Cauchy-Green tensor $\boldsymbol{C}$ is a *material tensor*, describing the deformation in the material coordinate system, while the left Cauchy-Green tensor $\boldsymbol{b}$ is a *spatial tensor*, describing the deformation in the spatial coordinate system.

1.2 STRAIN

Strain ε is a description of deformation in terms of relative displacement of particles in the body that excludes rigid-body motions. Even though *stretch* λ can be considered the true deformation, different equivalent choices can be made for the expression of a strain field, depending on the application and whether we work in a Lagrangian or Eulerian description. These alternative measures are typically a function of stretch, $\varepsilon = f(\lambda)$, for which it is required that $f(1) = 0$ (strain is zero in the unstretched state), $\partial f/\partial\lambda = 1$ when $\lambda = 1$ (to ensure small strain is defined as the change in length per unit length), and $\partial f/\partial\lambda > 0$ for all λ (which means we set the convention in this work that positive direct strains represent tension when $\lambda > 1$). Some common strain measures include:

- Nominal (or Biot or Engineering) strain: $f(\lambda) = \lambda - 1$
- Logarithmic (or True) strain: $f(\lambda) = \ln \lambda$
- Green-Lagrange strain: $f(\lambda) = \frac{1}{2}[\lambda^2 - 1]$

The Green-Lagrange strain is one of the more convenient strain measures, given that it can directly be calculated from the deformation gradient $\boldsymbol{F}$. In 3D, the generalized Green-Lagrange strain tensor $\boldsymbol{\varepsilon}^{\boldsymbol{G}}$ is defined by.

$$\boldsymbol{\varepsilon}^{\boldsymbol{G}} = \frac{1}{2}\left(\boldsymbol{F}^T\boldsymbol{F} - \boldsymbol{I}\right) \tag{1.6}$$

where $\boldsymbol{I}$ depicts the second-order identity tensor. When the deformations become infinitely small, the Green-Lagrange strain tensor $\boldsymbol{\varepsilon}^{\boldsymbol{G}}$ translates to the classical definition of infinitesimal strain

$$\varepsilon_{ij} = \frac{1}{2}\left(\frac{\partial u_j}{\partial X_i} + \frac{\partial u_i}{\partial X_j}\right) \tag{1.7}$$

The volumetric change ratio in the vicinity of a material point $\boldsymbol{p}$ is typically expressed by computing the *Jacobian*, which is the determinant J of the deformation gradient

$$J = det(\boldsymbol{F}) \tag{1.8}$$

This Jacobian, or third invariant of strain, is a measure for local material compression ($J < 1$) or expansion ($J > 1$). For an incompressible material (ex infra), $J := 1$ in all material points of $\mathscr{B}$ for any configuration $\mathcal{B}_t$. This volumetric change ratio is correlated to the Poisson ratio ν, which expresses a material's expansion in directions perpendicular to the direction of compression or, vice versa, its contraction in the directions transverse to the direction of stretching.

1.3 STRESS

Stress expresses the internal forces that neighboring particles of a continuous material exert on each other. To better understand this mechanical concept, consider an infinitely small surface area dS in the vicinity of the material point $\boldsymbol{p}$ at an intersection of the solid body $\mathscr{B}$ with current configuration $\mathcal{B}_t$ as shown in Figure 1.3. With $\boldsymbol{t}$ the traction force per unit area acting on $\boldsymbol{p}$ and $\boldsymbol{n}$ the normal unit vector characterizing the intersection ds, the 'true' stress or Cauchy stress $\boldsymbol{\sigma}$ at $\boldsymbol{p}$ satisfies:

$$\boldsymbol{t} = \boldsymbol{n} \cdot \boldsymbol{\sigma} \tag{1.9}$$

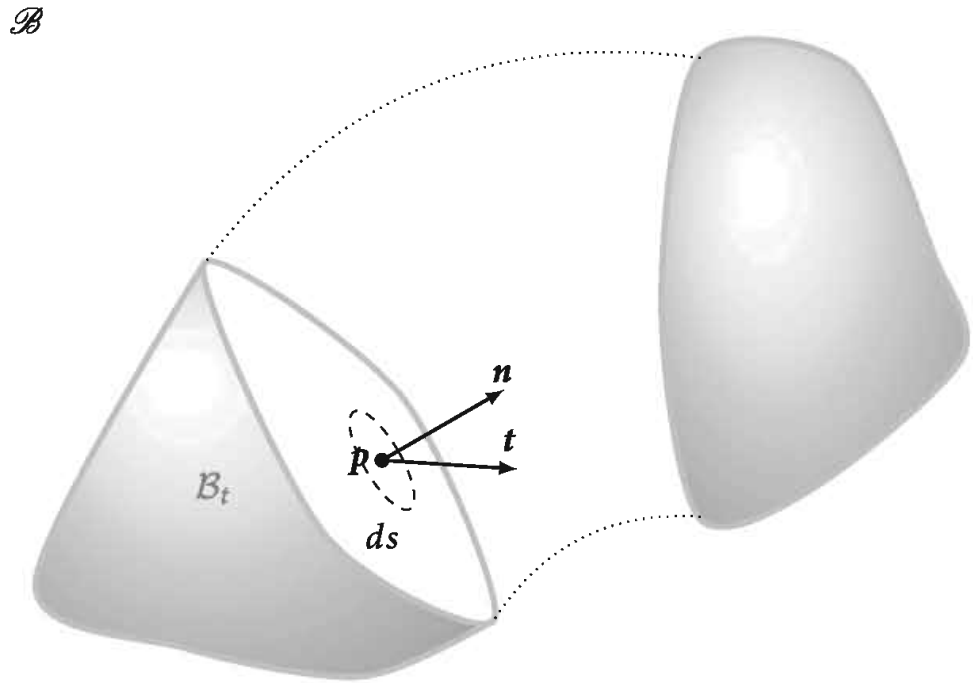

Figure 1.3: Definition of stress inside a solid body $\mathscr{B}$. The Cauchy stress tensor $\boldsymbol{\sigma}$ characterizes the traction force $\boldsymbol{t}$ at a material point $\boldsymbol{p}$ that is acting on an arbitrary intersection surface ds through $\boldsymbol{p}$ with normal unit vector $\boldsymbol{n}$, within the current configuration $\mathcal{B}_t$. Image adapted from [57]

Similar to strain, different stress measures exist. The Cauchy-stress $\boldsymbol{\sigma}$ is the most commonly used stress measure and relates internal forces caused by deformation to the current configuration. If we multiply the Cauchy-stress $\boldsymbol{\sigma}$ with the determinant of the deformation gradient $\boldsymbol{F}$, the Jacobian J, we get the Kirchoff stress tensor $\boldsymbol{\tau} = J\boldsymbol{\sigma}$. Different from the Cauchy stress tensor, the first Piola-Kirchoff stress tensor $\boldsymbol{P}$ defines the internal stresses with respect to the reference configuration. So in comparison, this gives:

$$\boldsymbol{\sigma}^T = \frac{df}{\boldsymbol{n}ds} \quad , \quad \boldsymbol{P} = \frac{df}{\boldsymbol{N}dS} \tag{1.10}$$

with $df = \boldsymbol{t} \cdot ds$. Given that one index of $\boldsymbol{P}$ is attached to the reference configuration and one to the deformed configuration, this leads to a non-symmetric tensor. Therefore, we can pull back df to the reference configuration through a *pull-back* operation which leads to the symmetric second Piola-Kirchoff stress tensor $\boldsymbol{S}$

$$\boldsymbol{S} = \frac{\boldsymbol{F}^{-1}df}{\boldsymbol{N}dS} \tag{1.11}$$

These *pull-back* ($\boldsymbol{F}^{-1}\cdot$) and *push-forward* ($\boldsymbol{F}\cdot$) operations allow us to switch between different stress measures by switching the configurations we are defining the traction force and the infinitesimal surface in. For example

$$\boldsymbol{P} = J\boldsymbol{\sigma}\boldsymbol{F}^{-T} \quad , \quad \boldsymbol{S} = \boldsymbol{F}^{-1}\boldsymbol{P} = J\boldsymbol{F}^{-1}\boldsymbol{\sigma}\boldsymbol{F}^{-T} \quad , \quad \boldsymbol{\sigma} = J^{-1}\boldsymbol{P}\boldsymbol{F}^T = J^{-1}\boldsymbol{F}\boldsymbol{S}\boldsymbol{F}^T \tag{1.12}$$

The stress tensor $\boldsymbol{\sigma}$ can be decomposed into a hydrostatic pressure term $\boldsymbol{\sigma}_{hyd} = -p\boldsymbol{I}$ caused by local volume deformations, and the remaining so-called deviatoric stress $\overline{\boldsymbol{\sigma}}$.

$$\boldsymbol{\sigma} = \overline{\boldsymbol{\sigma}} + \boldsymbol{\sigma}_{hyd} = \overline{\boldsymbol{\sigma}} - p\boldsymbol{I} \ , \ p = -\mathrm{tr}\,(\boldsymbol{\sigma})/3 \tag{1.13}$$

Here $\mathrm{tr}\,(\bullet)$ stands for the trace of a tensor, $\mathrm{tr}\,(\boldsymbol{\sigma}) = \sum \sigma_{ii}$. Hydrostatic stress causes volume changes only, wehereas deviatoric stress causes angular distortion only. The hydrostratic pressure p is the product of the bulk modulus of the material K and the volumetric strain

$$p = -K \cdot \varepsilon_{vol} \ , \ \varepsilon_{vol} = \mathrm{tr}\,(\boldsymbol{\varepsilon}) \tag{1.14}$$

1.4 THE FINITE ELEMENT METHOD

In order to solve a biomechanics problem, we have to obey the laws of physics. The description of these laws for space- and time-dependent problems are usually expressed in terms of partial differential equations (PDEs). Given that these PDEs can only be solved analytically for idealized geometries and problems, we need an alternative solution scheme to solve these equations numerically for complex biomechanical problems where the geometries are complex, as are the material laws. This can be done using finite element, finite difference or finite volume approaches. All three methods convert the continuous problem represented by the PDEs into a discrete algebraic problem in the form of a matrix equation system. Each method has its own advantages and disadvantages, but for describing the behavior of soft biological tissue, the finite element method (FEM) is the most appropriate given its generality to solve arbitrary PDEs, its compatibility with mixed formulations and its ease to increase the order of the elements which is necessary for accurate local approximations of the physics field (e.g. local stress concentrations).

To apply the FEM, we need to set up a finite system of equations which, when numerically solved, leads to an approximated solution. Therefore we first need to set up the governing PDEs for the physics problem at hand. Subsequently, we need to establish the strong formulation which, intrinsically for a finite element analysis (FEA) approach needs to be reformulated in an equivalent form, the weak formulation. The implementation of an approximation scheme for the unknown solution and the weight functions, allows us to set up the equations which can be solved using numerical methods. In the following subsections, we will discuss each of these steps in more detail.

1.4.1 Equilibrium equations

A solid continuum mechanics problem, just like any other mechanics problem, is governed by Newton's laws of motion (and the conservation of mass). The conservation of linear momentum (Newton's second law of motion) states that the rate of change of linear momentum should equal the net applied force. For a deformable solid body $\mathscr{B}$, these forces can be contact forces or body forces. Contact forces arise from the body's contact with its surrounding and act per unit of area of the body's boundary $\partial\mathcal{B}$. Body forces act per unit of mass of the body $\mathcal{B}$. By assuming that the mass is conserved (balance of mass), that Newton's second law of motion holds for any subpart (e.g. an arbitrary volume V and its boundary surface ∂V, see Figure 1.4) and that the stress field is continuously differentiable, we can write the equilibrium equations as follows

$$\nabla\boldsymbol{\sigma} + \rho\boldsymbol{f} = \rho\boldsymbol{a} \tag{1.15}$$

where ρ is the density, $\boldsymbol{\sigma}$ is the Cauchy stress tensor, $\boldsymbol{f}$ is the body force per unit of mass and $\boldsymbol{a}$ is the acceleration per unit of mass. For a static state of equilibrium (Eq. 1.15 at $t \in \mathbb{R}_+$), this equation simplifies to

$$\nabla\boldsymbol{\sigma} + \rho\boldsymbol{f} = \mathbf{0} \tag{1.16}$$

Based on the constitutive relation between $\boldsymbol{\sigma}$ and $\nabla\boldsymbol{u}$ (see Eq. 2.3 in section 2.1.1.1), we can rewrite this as follows

$$\nabla \cdot (\mathbb{C} : \nabla\boldsymbol{u}) + \rho\boldsymbol{f} = \mathbf{0} \tag{1.17}$$

Apart from the balance of linear momentum, the balance of angular momentum also needs to be conserved. This conservation law states that the rate of change of angular momentum should equal the net applied torque. From this balance of angular momentum, it can be derived [143] that the Cauchy stress tensor $\boldsymbol{\sigma}$ is symmetric. This result is also referred to as Cauchy's second equation of motion:

$$\boldsymbol{\sigma} = \boldsymbol{\sigma}^T \tag{1.18}$$

Boundary conditions are needed to truncate the computational domain. They represent interactions with the surrounding structures, which are not included in the analysis. To complete the description of the mechanical problem, we include the boundary constraints on the considered domain:

$$\boldsymbol{u} = \boldsymbol{u}_d \quad \text{on} \quad \partial V_d \tag{1.19a}$$

$$\boldsymbol{n} \cdot (\mathbb{C} : \nabla\boldsymbol{u}) = \boldsymbol{t}_n \quad \text{on} \quad \partial V_n \tag{1.19b}$$

where we decomposed the boundary ∂V in two parts, ∂V_d and ∂V_n. ∂V_d represents the boundary constrained by Dirichlet or essential boundary conditions (Eq. 1.19a) while ∂V_n represents the boundary constrained by Neumann or natural boundary conditions (Eq. 1.19b). A third type of boundary condition, named Robin-type boundary conditions exists as well, and can be seen as a generalization of the Neumann boundary condition:

$$\alpha \nabla \boldsymbol{u} + \beta \boldsymbol{u} = \tilde{\boldsymbol{t}} \quad \text{on} \quad \partial V_r \tag{1.20}$$

where α and $\beta \in \mathbb{R}$ and ∂V_r represents the part of the domain constrained by this condition. The essential boundary conditions are needed to make sure that the solution to the mechanical problem is not just a pure rigid body transformation, i.e. the body needs a minimum set of 'external support'.

Since this dissertation focuses on the mechanical behavior of soft biological tissues, we will not focus on other conservation laws (e.g. thermodynamics, electromagnetism) for now.

1.4.2 The strong and weak formulation

If we consider an arbitrary volume V around the material point $\boldsymbol{p}$ enclosed by the boundary surface ∂V (see Figure 1.4), the static state of equilibrium at $t \in \mathbb{R}_+$ states that the body forces $\boldsymbol{f}$ acting on V and the traction forces interacting with ∂V must add up to zero.

$$\int_V \boldsymbol{f} dV + \int_{\partial V} \boldsymbol{t} d\partial V = \boldsymbol{0} \tag{1.21}$$

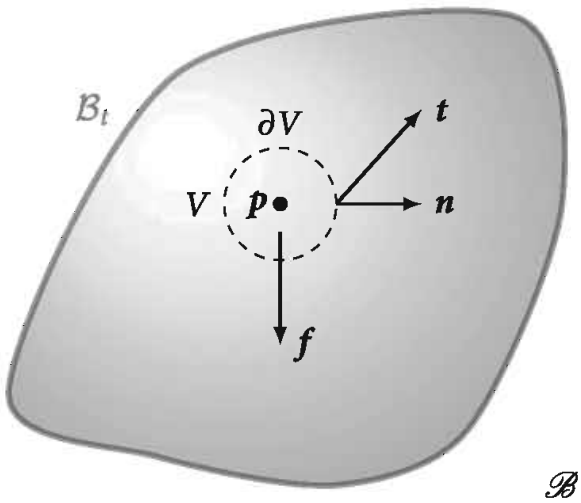

Figure 1.4: Force equilibrium inside a solid body $\mathcal{B}$ with current configuration $\mathcal{B}_t$. Body forces $\boldsymbol{f}$ and traction forces $\boldsymbol{t}$ are acting upon an arbitrary volume V and its boundary surface ∂V around the material point $\boldsymbol{p}$. The surface ∂V is characterized by its unit normal vectors $\boldsymbol{n}$. Image adapted from [57]

The volume integral terms in this equation describe what is stored inside the domain or added by sources (e.g. internal stresses originating from prior deformations, body forces, thermal loading, friction, etc.) whilst the surface integrals describe the interaction with the neighboring environment. Using the divergence theorem by Gauss and Eq. 1.9, the surface integral can be converted into volume integrals as follows

$$\int_V \boldsymbol{f} dV + \int_{\partial V} \boldsymbol{n}.\boldsymbol{\sigma} d\partial V \overset{Gauss}{=} \int_V \left(\boldsymbol{f} + \nabla.\boldsymbol{\sigma}\right) dV = \mathbf{o} \tag{1.22}$$

Since we used an arbitrary domain in this derivation, and these conditions must be valid at every point individually, we obtain the so-called *strong formulation* of static force equilibrium inside a solid body $\mathscr{B}$.

$$\overset{\forall V}{\Longrightarrow} \boldsymbol{f} + \nabla.\boldsymbol{\sigma} = \mathbf{o} \tag{1.23}$$

The divergence theorem by Gauss can however only be applied provided that all involved functions are smooth enough, which is often not the case for practical engineering problems. Imagine for example the description of layered soft tissue where layers with differing material properties lead to discontinuities in the stress distributions. Consequently, for most geometries and problems the strong formulation cannot be solved analytically (because the application of Gauss's theorem cannot be justified).

The *weak formulation* partially reverses the above derivation procedure to return an integral formulation which is less strict on the solution than the strong formulation because it relaxes the requirement that the PDE must be well defined in all points. This formulation forms the first step in developing a *finite element* approximation of the solution. By multiplying Eq. 1.23 with an arbitrary smooth weight/test function $\boldsymbol{w}$ and integrating over the volume V, we get the weak formulation of static force equilibrium:

$$\int_V \left(\boldsymbol{f} + \nabla \cdot \boldsymbol{\sigma}\right) \cdot \boldsymbol{w} dV = \mathrm{o} \tag{1.24}$$

Using the chain rule and Gauss's theorem on the weight functions, we can rewrite Eq. 1.24 as follows

$$\int_V \left(\boldsymbol{f} \cdot \boldsymbol{w} + \nabla \cdot (\boldsymbol{\sigma} \cdot \boldsymbol{w}) - \boldsymbol{\sigma} : \nabla \boldsymbol{w}\right) dV = \mathrm{o} \quad \forall \boldsymbol{w} \tag{1.25a}$$

$$\int_{\partial V} \boldsymbol{n} \cdot \boldsymbol{\sigma} \cdot \boldsymbol{w} d\partial V + \int_V \left(\boldsymbol{f} \cdot \boldsymbol{w} - \boldsymbol{\sigma} : \nabla \boldsymbol{w}\right) dV = \mathrm{o} \quad \forall \boldsymbol{w} \tag{1.25b}$$

Reshuffling this equation and using the constitutive relation between $\boldsymbol{\sigma}$ and $\nabla \boldsymbol{u}$ (see Eq. 2.3 in section 2.1.1.1), we get

$$\int_V (\mathbb{C} : \nabla \boldsymbol{u}) : \nabla \boldsymbol{w} dV = \int_{\partial V} \boldsymbol{n} \cdot (\mathbb{C} : \nabla \boldsymbol{u}) \cdot \boldsymbol{w} d\partial V + \int_V \boldsymbol{f} \cdot \boldsymbol{w} dV \quad \forall \boldsymbol{w} \tag{1.26}$$

Applying the Neumann boundary condition (Eq. 1.19a) on ∂V_n and choosing the test function $\boldsymbol{w}$ to vanish on ∂V_d (i.e. we do not need to test the integral on the boundary ∂V_d where the solution is known to be $\boldsymbol{u} = \boldsymbol{u}_d$), the above equation can be simplified to:

$$\underbrace{\int_V (\mathbb{C} : \nabla \boldsymbol{u}) : \nabla \boldsymbol{w} dV}_{\text{internal}} = \underbrace{\int_V \boldsymbol{f} \cdot \boldsymbol{w} dV + \int_{\partial V_n} \boldsymbol{t}_n \cdot \boldsymbol{w} d\partial V}_{\text{external}} \quad \forall \boldsymbol{w}, \boldsymbol{w} = \mathbf{o} \text{ on } \partial V_d \tag{1.27}$$

In solid mechanics problems like these, these weight/test functions can be seen as a virtual velocity field. Consequently, Eq. 1.24 expresses that the total virtual work done over the volume V must be zero. Therefore, the weak formulation is also called the *principle of virtual work*. Eq. 1.27 was organized in such a way that, in a virtual work sense, the left hand side can be seen as the rate of work done by the internal stresses, whilst the right hand side can be seen to represent the rate of work done by the external body forces $\boldsymbol{f}$ and traction forces $\boldsymbol{t}$ subjected to the virtual velocity field $\boldsymbol{w}$.

It is possible to show that the weak formulation is equivalent to the solution from the strong formulation together with the boundary conditions. Even though we initially claimed that the weight/test functions $\boldsymbol{w}$ were arbitrary, this not entirely true since our manipulations towards the weak formulation should be meaningful. Therefore we define these functions to belong to an infinite-dimensional (Hilbert) functions space H^1, where all functions are bounded (quadratic integrable). We want these functions to be well-behaved so we can define operations on them within the rules of (say) integration. In Eq. 1.27, we applied the essential boundary conditions by further limiting the test functions to belong to a subspace of H^1 where $\boldsymbol{w} = \mathbf{o}$ on ∂V_d. As can be seen from comparing Eq. 1.22 and Eq. 1.27, the strong form requires $\boldsymbol{u}$ to be continuously differentiable until at least a second partial derivative, while the new weak formulation lowered this requirement to only first partial derivatives.

1.4.3 Solution strategy

The weak formulation allows us to discretize the mathematical model equations to obtain numerical model equations. A solution is found by requiring Eq. 1.27 to hold for all weight/test functions in the test function space. More precisely, not just one test function is considered, rather a whole class of test functions where each one corresponds to an equation. Of course, we could never consider all possible test functions as this would result in an infinite amount of equations. In practice, we need a finite number of well-chosen test functions. This is where finite elements come into play. We first approximate the volume V_0 belonging to the reference configuration $\mathcal{B}_0$

by a discrete number of cells called *elements*, of which the vertices, i.e. the *nodes* form the equilibrium integration points. Looking for an approximate solution for the displacement field $\boldsymbol{u}$, we express the approximate solution $\boldsymbol{u}_h$ as a linear combination of a set of i *basis* or *shape* functions that belong to the aforementioned subspace H^1:

$$\boldsymbol{u}_h = \sum_i u_i \psi_i \ , \ \boldsymbol{u}_h \approx \boldsymbol{u} \tag{1.28}$$

In practice, this approximation is carried out over each of the smaller *finite elements* and these results are reassembled for the entire region (see section 1.4.4). For the next step, different FEM approaches are available, but the original solution scheme, which is still mostly used for solving mechanical problems, is the so-called *Galerkin* method. In this method, the solution's shape functions and the aforementioned weight/test functions are assumed to belong to the same Hilbert function space H^1. Consequently, the discretized version of Eq. 1.26 for every test function ψ_j becomes:

$$\sum_i u_i \int_V \left(\mathbb{C} : \nabla\psi_i\right) : \nabla\psi_j dV = \sum_i u_i \int_{\partial V} \boldsymbol{n}\cdot\left(\mathbb{C} : \nabla\psi_i\right)\cdot\psi_j d\partial V + \int_V \boldsymbol{f}\cdot\psi_j dV \tag{1.29}$$

Imposing the boundary conditions on Eq. 1.29, we get the following system of equations for a static displacement finite element analysis written in matrix form:

$$\boldsymbol{K}\boldsymbol{u} = \boldsymbol{P} \tag{1.30}$$

where $\boldsymbol{u}$ is the vector of (displacement) unknowns, $\boldsymbol{K}$ is the *stiffness matrix* (also called the *system matrix*) and $\boldsymbol{P}$ represents the external load vector. For a dynamic finite element problem, we also have to take into account the inertial forces and (potential) damping forces into the system equations, which leads to

$$\boldsymbol{M}\ddot{\boldsymbol{u}} + \boldsymbol{C}\dot{\boldsymbol{u}} + \boldsymbol{K}\boldsymbol{u} = \boldsymbol{P} \tag{1.31}$$

with *mass matrix* $\boldsymbol{M}$ and *damping matrix* $\boldsymbol{C}$.

This discretized system of equations can be solved numerically using variational methods to approximate the solution by minimizing an associated error function. Usually, this is done in an iterative approach and several commercial and open-source FEA-software packages are available for this purpose. In this research, the commercial finite element solver *Abaqus* (Dassault Systemes - Simulia Corp.) was used.

1.4.4 Elementwise approximation, integration and reassembly

In the previous section, we mentioned that the approximation of the solution is carried out over each of the smaller *finite elements* and these results are

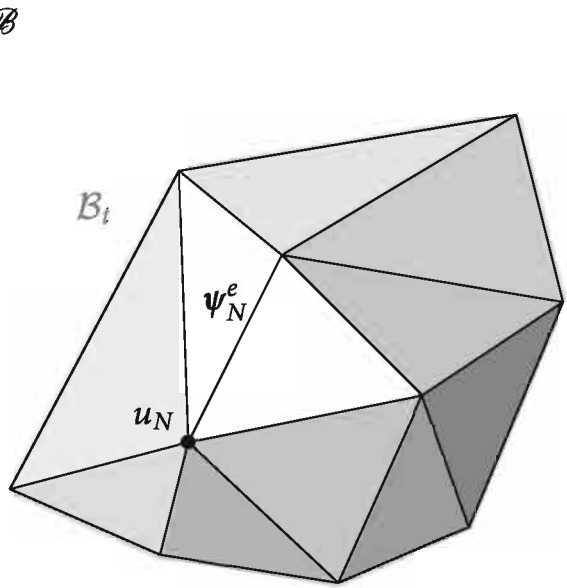

Figure 1.5: Finite element approximation of the solid body $\mathcal{B}$. The volume is subdivided into a discrete number of simple geometrical shapes, called the elements. The element shape functions $\boldsymbol{N}_N$ couple the nodal variables u^N. Image adapted from [57]

reassembled for the entire region. Whereas it is pretty difficult to find appropriate test functions for the whole domain, a piecewise approximation of the physical field (using a discrete number of simple geometrical shapes, called the elements, see Figure 1.5) allows for a good precision of the approximate solution even with simple shape functions. Consequently, the problem of finding appropriate test functions is shifted towards a geometrical problem where the choice of partitions and the position of vertices becomes more important (see section 1.4.6). Simply increasing the number of elements can achieve increasing precision. Once the geometrical partitioning is done, the system of equations for each element can be generated automatically and reassembled to end up with the full system of equations of Eq. 1.30 or Eq. 1.31. Moreover, the subdivision of the whole domain into simpler parts allows for an accurate representation of complex geometries, the inclusion of dissimilar material properties (see section 2.1.1) and capturing local effects.

In a static displacement finite element analysis (Eq. 1.30), for each element the following has to be valid:

$$\boldsymbol{k}_e \boldsymbol{u}_e = \boldsymbol{P}_e \quad \forall e \tag{1.32}$$

where $\boldsymbol{k}_e$ represents the *element stiffness matrix*:

$$\boldsymbol{k}_e = \int_{V_e} \boldsymbol{B}^T \mathbb{C} \boldsymbol{B} dV_e \tag{1.33}$$

with the incremental constitutive tensor $\mathbb{C}$ (see paragraph 2.1.1.1.1) and the matrix of shape function derivatives $\boldsymbol{B}$. The form of the element stiffness matrices and the associated shape functions depends on the dimension of the problem, the order of the element (e.g. linear, quadratric) and the choice of integration procedure (e.g. reduced, full). Given that it is difficult to depict shape functions in 3D, we consider a simple 2D example: a bilinear quadrilateral element (see Figure 1.6 a). The nodal variables are interconnected by the following isoparametric element shape functions:

$$\psi_1^e = \frac{1}{4}(1-\xi)(1-\eta) \tag{1.34a}$$

$$\psi_2^e = \frac{1}{4}(1+\xi)(1-\eta) \tag{1.34b}$$

$$\psi_3^e = \frac{1}{4}(1+\xi)(1+\eta) \tag{1.34c}$$

$$\psi_4^e = \frac{1}{4}(1-\xi)(1+\eta) \tag{1.34d}$$

where ξ and η represent the nodal coordinates in the element coordinate system. This element coordinate system ξ and η is chosen such that the coordinates of nodes 1, 2, 3, and 4 are: (-1,-1), (1,-1), (1,1), and (-1,1) respectively. The i shape functions each have a value of 1 at point i, but 0 at other the other points. These shape functions are also depicted in Figure 1.6 b. If we would decide to use quadratic elements, with extra mid-edge nodes and a central node, the principle stays the same but the shape functions intrinsically become more complex, as depicted in Figure 1.6 c.

As can be seen from Eq. 1.33, the computation of the stiffness matrix and load vectors requires the evaluation of integrals. Numerical integration approximation schemes are preferred given that solving these integrals analytically is not always feasible, takes too much time to compute, has no guarantee that numerical issues are removed (division by zero, floating point errors, etc.) and that post-processing requires numerical evaluation of quantities. Using the Gaussian quadrature, the integrals can be approximated by performing a weighted sum of function values at specified points within the domain of integration (the elements). This weighted sum yields exact results for polynomials of a degree 2n-1 where n is equal to the amount of sampling points. For this reason, using elements with reduced integration schemes must be done with caution, making sure that we avoid inaccurate results and so-called hourglassing effects. More information on shape functions and amount of integration points for each element type in Abaqus can be found in [46].

In finite element codes, the sub-matrices $\boldsymbol{K}_e$ and sub-vectors $\boldsymbol{P}_e$ are typically computed at the element level and then combined together to

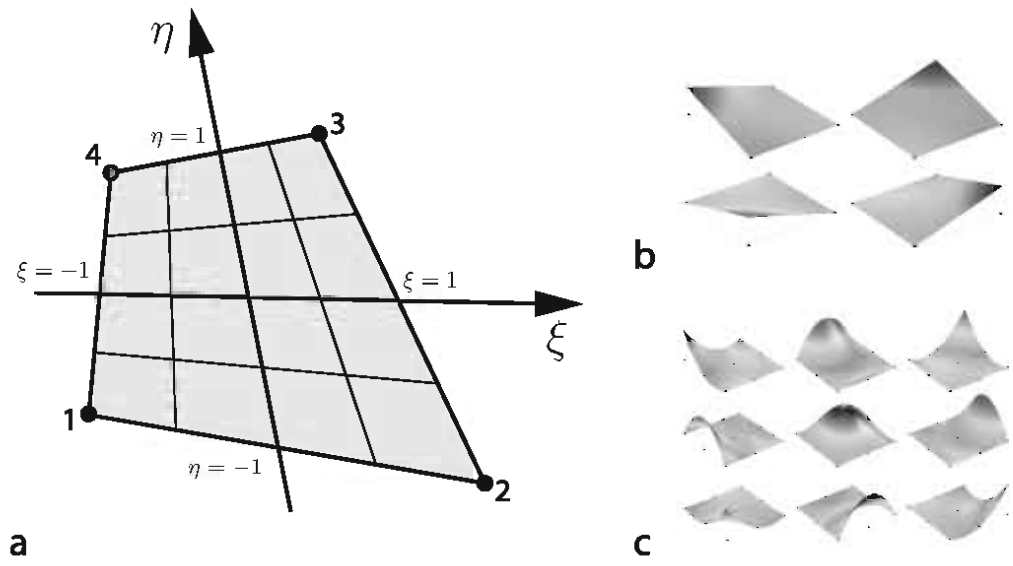

Figure 1.6: The quadrilateral finite element. (a) isoparametric representation, (b) visualization of the bilinear shape functions, (c) visualization of quadratic shape functions. The gray shading in (b) and (c) depicts the shape function's evolution from zero (light gray) to unity (dark gray) at each node of the considered element.

produce $\boldsymbol{K}$ and $\boldsymbol{P}$. During the assembly to the global system of equations, we have to account for the degrees of freedom that appear in the displacement vector of multiple elements (neighboring elements). Introducing the essential boundary conditions leads to a set of equations which can be taken out of the global system of equations, given that the solution in these nodes is already set.

1.4.5 Nonlinear solution schemes

Up to this point, we have always assumed the stiffness matrix to be constant during loading and deformation. This assumption typically does not hold for most applications due to the following sources of nonlinearity:

- *Material nonlinearity*: Soft tissue typically shows nonlinear, inelastic, anisotropic and heterogenic material behavior (see section 2.1.1.1), which is often related to the gradual recruitment of (elastin and) collagen fibers during stretching (see Figure 1.7).
- *Boundary nonlinearity*: When structures start to interact with each other during deformation (e.g. self-contact of the contracting ventricular endocardium), the response of the structure changes very instantaneously.

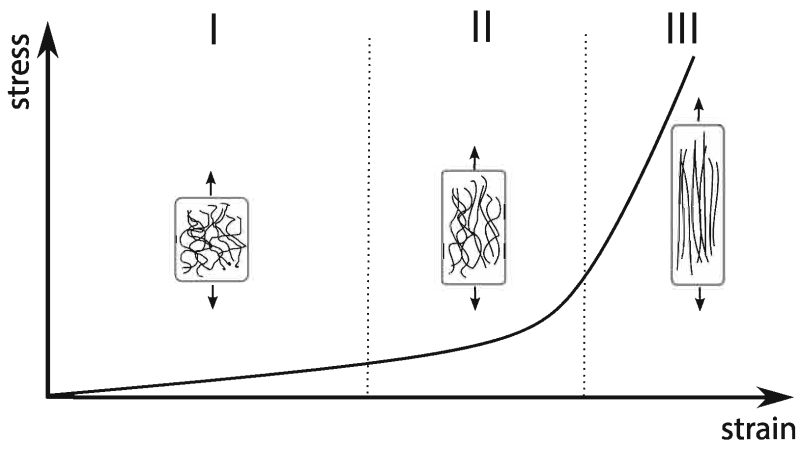

Figure 1.7: Illustration of material nonlinearity of soft tissue associated with the gradual recruitment of collagen fibers. In phase I, the collagen fibers embedded in the elastin matrix are curled up and consequently do not contribute much to the stiffness. In phase II, the tissue is stretched further and the collagen fibers begin to straighten as they reach a taut state, causing a stiffening effect. In the third phase, almost all fibers are contributing to the material stiffness. Figure reproduced from [69].

- *Geometric nonlinearity*: Soft tissue typically undergoes large deformations, where the magnitude of the displacement might affect the response of the structure (e.g. buckling of a thin-walled tube under external pressure).

In all these cases, a linear FEA procedure, where the calculations are based on the initial geometry, is no longer capable to produce meaningful results. Therefore, non-linear FEA procedures have been developed where the code keeps track of the changing element size, shape, position and loading conditions throughout the analysis by iteratively updating the (element) geometry at each load increment. Based on the integration and solution scheme, these iterative computational approaches to solve the (often very large) system of equations (see Eq. 1.30 and Eq. 1.31) can be categorized as *implicit* or *explicit*.

1.4.5.1 *Implicit*

In an implicit solution scheme, the solution to the current mechanical state is obtained through an iterative solution of the equilibrium equations. In other words, a solution is found by applying the loads gradually to incrementally compute the final solution. In Abaqus/Standard, the Newton-Raphson method is used to successively find better estimations of the k-incremental solution $\Delta \boldsymbol{u}_k^i$ at iteration i. At increment k, the equilibrium equations can be written as follows:

$$\boldsymbol{K}_k \Delta \boldsymbol{u}_k = \Delta \boldsymbol{P}_k \tag{1.35}$$

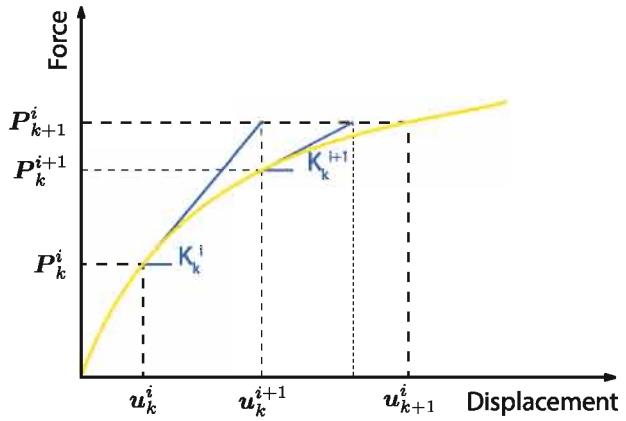

Figure 1.8: Graphical representation of the iterative Newton-Raphson process in an implicit solution scheme. Adapted from [46].

which can be rewritten using a Taylor-series expansion as follows:

$$\boldsymbol{K}^i_k \Delta \boldsymbol{u}^i_k - \Delta \boldsymbol{P}^i_k + \frac{\partial \boldsymbol{K}^i_k \Delta \boldsymbol{u}^i_k}{\partial \Delta \boldsymbol{u}_k} (\Delta \boldsymbol{u}_k - \Delta \boldsymbol{u}^i_k) + \ldots = 0 \tag{1.36}$$

The first two terms of this Taylor expansion form a linear set of equations that is used to update the correction term $\boldsymbol{c}^{i+1}_k = \Delta \boldsymbol{u}^{i+1}_k - \Delta \boldsymbol{u}^i_k$ for every iteration.

$$\boldsymbol{K}^i_k \boldsymbol{u}^i_k + \boldsymbol{K}^i_k \boldsymbol{c}^{i+1}_k = \Delta \boldsymbol{P}^i_k \;\rightarrow\; \boldsymbol{c}^{i+1}_k = \left(\boldsymbol{K}^i_k\right)^{-1} \left(\Delta \boldsymbol{P}^i_k - \boldsymbol{K}^i_k \boldsymbol{u}^i_k\right) \tag{1.37}$$

Per increment, the iterations are repeated until a certain convergence criterion is reached, which typically implies that the displacement corrections $\boldsymbol{c}^{i+1}_k$ have to be small enough compared to the incremental displacements $\Delta \boldsymbol{u}^i_k$, contact conditions are satisfied, and the force and moment equilibirum were obtained, for each and every node of the model. This method is graphically depicted in Figure 1.8. The increment size $\Delta \boldsymbol{u}_k$ is chosen by the solver internally based on the ease of iterative convergence of the prior increment.

1.4.5.2 *Explicit*

In contrast to the implicit solution scheme, the explicit solution scheme does not require solving the system of equations and inverting the tangent stiffness matrix in each iteration. Instead, the solution uses the dynamic equilibrium equations in Eq. 1.31 to kinematically extrapolate the solution at a time increment $t + \Delta t$ from time increment t. In other words, the equations of motion are explicitely solved through time. If we consider Eq. 1.31 and assume, for simplicity, that no damping forces occur in this system, we need to solve for the following dynamic equilibrium:

$$\boldsymbol{M}\ddot{\boldsymbol{u}} = \boldsymbol{P} - \boldsymbol{K}\boldsymbol{u} \tag{1.38}$$

If we suppose we obtained a solution at time increment t, we can solve for the accelerations at time t:

$$\ddot{\boldsymbol{u}}|_t = (\boldsymbol{M})^{-1} (\boldsymbol{P} - \boldsymbol{K}\boldsymbol{u})\big|_t \tag{1.39}$$

Given that the explicit solution scheme always uses a diagonal, or lumped mass matrix, no equations need to be solved simultaneously to compute these accelerations, which renders the increment relatively inexpensive to solve. Each node's acceleration is determined by its mass and the net force acting on it. Using the central difference integration scheme, the accelerations $\ddot{\boldsymbol{u}}$, velocities $\dot{\boldsymbol{u}}$ and the displacements $\boldsymbol{u}$ are integrated through time as follows

$$\dot{\boldsymbol{u}}|_{t+\frac{\Delta t}{2}} = \dot{\boldsymbol{u}}|_{t-\frac{\Delta t}{2}} + \left(\frac{\Delta t|_{t+\Delta t} + \Delta t|_t}{2} \right) \ddot{\boldsymbol{u}}|_t \tag{1.40a}$$

$$\boldsymbol{u}|_{t+\Delta t} = \boldsymbol{u}|_t + \Delta t|_{t+\Delta t}\, \dot{\boldsymbol{u}}|_{t+\frac{\Delta t}{2}} \tag{1.40b}$$

From the displacement field, we can compute the strains and the accompanying stresses (using the constitutive relations). Once these are computed, the internal forces can be computed, which allows us to compute $(\boldsymbol{K}\boldsymbol{u} - \boldsymbol{P})\big|_{t+\Delta t}$ and move to the next increment, to repeat this whole process again, and again, until the set end time is reached.

Given that this explicit solution scheme solves the state at the end of the increment solely based on the displacements, velocities and accelerations at the beginning of the increment, the increment time needs to be chosen small enough to produce accurate results. A typical rule of thumb, mentioned in the Abaqus Theory Manual [46], is to limit the time increment to be smaller or equal to

$$\Delta t_{stable} = \min \left(\frac{L_e}{c_d} \right) \tag{1.41}$$

where L_e and c_d are the characteristic element length and the dilatational wave speed, a material characteristic which e.g. for a linear elastic material (see paragraph 2.1.1.1.1) can be defined as $c_d = \sqrt{(\lambda + 2\mu)/\rho}$ with λ and μ the Lamé constants and ρ the material density. From this it naturally follows that a stable solution requires smaller increments and thus longer simulation times if the total simulation time increases, if the tissue stiffness increases, if the material density decreases and the smallest element size decreases.

1.4.5.3 *Implicit vs explicit vs quasi-static*

For many static problems, the implicit solution scheme provided by Abaqus/Standard will be able to come to an accurate solution within a reasonable amount of increments, and is therefore often the best choice. However, for highly nonlinear static FE-problems (e.g. models

incorporating highly nonlinear tissue behavior and/or involving complex contact conditions), the amount of increments and iterations might rapidly increase, even to the point that an explicit solution technique (with more inexpensive time increments) becomes more desirable. In such a case, special considerations have to be taken to assure that the explicit solution provided by Abaqus/Explicit, which is inherently dynamic, remains a quasi-static solution. Therefore, the contributions of $\boldsymbol{M\ddot{u}}$ need to remain negligible. In a quasi-static analysis, a good balance between simulation time and computational cost (where it is often computationally impractical to simulate the model behavior in its natural time scale) needs to be found. Mass scaling, the concept of artificially increasing the mass of the entire model or a subset of the model, impacts the stable increment size (see Eq. 1.41) and can potentially speed up the simulation, but this can lead to increased non-physical inertial effects which, again, need to be kept to a minimum.

1.4.6 Geometric discretization

As mentioned in section 1.4.5, soft tissue typically undergoes large deformations. This can eventually lead to an excessive distortion of the finite elements in the model, which leads to numerical convergence issues. In order to avoid excessive mesh distortion, a significant amount of attention and effort has to be given to the quality of the geometric domain discretizations. In this dissertation, we often used and further developed our in-house open-source geometrical and finite element analysis preprocessor *pyFormex* (`http://pyformex.org`) to come to stable geometric discretizations of the computational domain.

CHAPTER 2

SOFT TISSUE BIOMECHANICS

The computation of soft biological tissue behavior (both short and long term) and its interaction with (minimally invasive) devices and/or its reponse to surgery is challenging due to its complex material behavior. This chapter gives the reader a rundown on each aspect of soft tissue behavior and the current state of the art in describing its acute and chronic response.

2.1 PASSIVE BEHAVIOR

As stated by Fung [84], the key to successfully study the biomechanical behavior of (soft) biological tissues is the identification of robust constitutive relations. A *constitutive model* describes the material response to external stimuli, usually applied loads or forces, under specific conditions of interest. This response depends on the material's internal makeup, or constitution, and the conditions of interest themselves. In order to describe a material through a constitutive formulation, the general characteristics of the material behavior first need to be delineated.

Linearity describes whether or not the material responds with proportionate or disproportionate increases in extension upon applying increasingly greater loads. Whereas bone typically exhibits a linear stress-strain response under small strains, soft tissues tend to exhibit disproportionate changes in strain to increasing stress (see Figure 2.1). This renders these nonlinear materials of course more complex to describe constitutively. The *elasticity* of a material expresses the material's dissipation of energy through deformation.

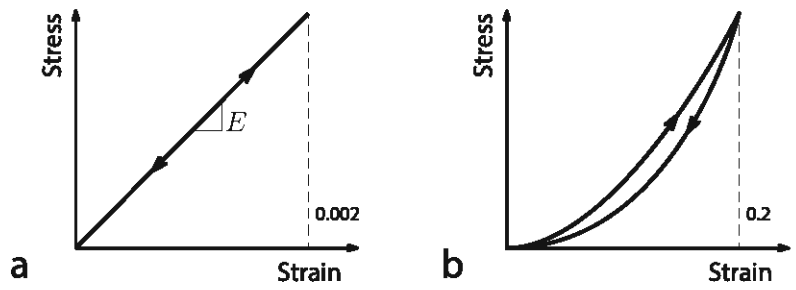

Figure 2.1: Qualitative comparison of the stress-strain behavior of two classes of materials: hard linear elastic (a) versus soft nonlinear pseudoelastic (b) tissues. Note the different order of magnitude of the associated strains (from 0.002 to 0.2) and that the soft tissues showcase noncoincident loading and unloading curves, related to the material's pseudoelastic behavior. Image inspired by [154].

An elastic material (e.g. the response of bone under small strains) will follow the same path in the stress-strain plot during loading and unloading, and thus no hysteresis (i.e. energy dissipation) is seen. Soft tissues, however, can be called pseudoelastic, given the characteristic differences seen between the loading and unloading curves due to energy dissipation within the tissue during such a loading and unloading procedure (see Figure 2.1). When the material does not return to its original starting point after a loading-unloading procedure, the material is said to have shown plastic behavior under those loading conditions (e.g. metals, concrete, bone under larger strains). In that case, the material has undergone non-reversible shape changes in response to the applied forces. *Isotropy* represents the material behavior's independence of orientation within the material body. Most tissues exhibit anisotropic behavior where the tissue response is different in one or more directions (see Figure 2.2). Again, anisotropy complicates the constitutive description of the material. Finally, *homogeneity* describes the material behavior's independence of the position within the material body. If this is not the case, the material is said to be inhomogeneous. In this section, we focus on the descriptors of passive tissue behavior and how this theoretically translates to constitutive equations (ex infra) expressed through strain energy functions (SEFs).

2.1.1 Modeling constitutive behavior

Looking at soft tissues, we typically encounter nonlinear responses to tissue deformation, viscoelasticity, pronounced anisotropy and heterogenity. As mentioned before, a constitutive equation, which describes the material response (stress) to external stimuli (strain), depends on the material's internal make-up itself. The material behavior showcased by these materials typically is a consequence of the constituents present in the tissue matrix

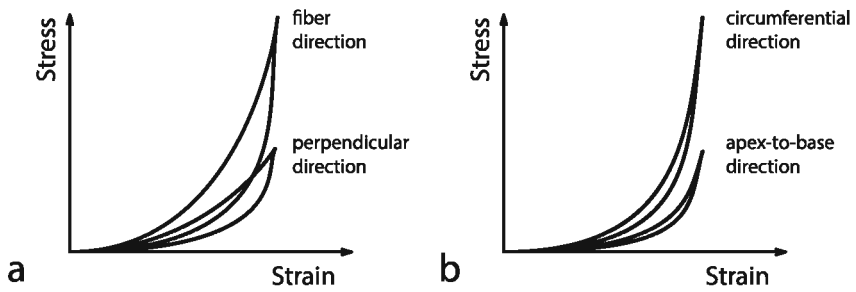

Figure 2.2: Qualitative stress-strain relationship illustration from a thin slab of noncontracting myocardium (a) and associated epicardium (b). Note the nonlinear anisotropic response of both tissues, where the epicardium shows a stronger nonlinear response due to its higher collagen content. Also shown is the hysteresis due to internal energy dissipation upon loading and unloading for these tissues, where muscle tissue tends to exhibit greater hysteresis than for example epicardial tissue. Image inspired by [154].

and how these interact. The complexity of this behavior still renders the formulation of appropriate constitutive relations for these tissues one of the most important and challenging areas within biomechanics. Here, we start from a standard linear elastic material model and establish the framework for describing hyperelasticity, whereby stresses are derived from a SEF. These hyperelastic material models then form the basis to gradually build up increasingly more complex constitutive relations accounting for each of the aforementioned descriptors of material behavior.

2.1.1.1 *(Non)linearity*

2.1.1.1.1 *Linear elasticity.* If we look at bone and teeth, these hard biological tissues typically show a linear, nearly elastic material response prior to yield, as depicted in Figure 2.1 a. Therefore, these tissues can easily be assumed to behave according to Hooke's law (note that this assumption entails that we consider them to be part of a class of materials that are linear, elastic, homogeneous and isotropic). If we would perform a tensile test on a rod of any elastic material, the tensile stress σ is linearly proportional to the strain by the modulus of elasticity E:

$$\sigma = E\varepsilon \tag{2.1}$$

which is the classic form of Hooke's law for a linear spring. To describe the stresses and strains in a continuous 3D elastic media, Hooke's law becomes:

$$\sigma_{ij} = \lambda_L tr(\boldsymbol{\varepsilon})\delta_{ij} + 2\mu_L \varepsilon_{ij} \tag{2.2}$$

where μ_L and λ_L are two scalar parameters called the Lamé constants, which are related to the modulus of elasticity E and the Poisson ratio ν. In tensor

notation, we can write this as follows:

$$\boldsymbol{\sigma} = \mathbb{C} : \boldsymbol{\varepsilon} = \mathbb{C} : \nabla \boldsymbol{u} \tag{2.3}$$

where $\mathbb{C}$ is a fourth-order *material stiffness tensor* or *constitutive tensor* with 81 elastic constants, reducing to 21 constants (for anisotropic materials) due the symmetry of the strain tensor, the stress tensor and $\mathbb{C}$. Hooke's law is sufficient to describe the mechanical behavior of hard tissue (e.g. bone and teeth) and common engineering materials undergoing small deformations. Soft biological tissues, however, undergo large elastic deformations, which limits the realism of linear elastic material models to describe its behavior. Nonlinear material models are needed to increase the realism of our models.

2.1.1.1.2 Strain energy function. Given that soft biological tissues typically exhibit a nonlinear hyperelastic response, we need a theoretical framework to describe this material behavior. A common method relies on the introduction of a *strain energy function (SEF)* Ψ, which is a scalar function describing the elastic potential (strain) energy per unit of volume that is stored inside a volume when subjected to deformation. The strain energy is always greater than or equal to zero and should be equal to zero when there is no deformation.

From the SEF, the first Piola-Kirchoff stress tensor for isotropic hyperelastic materials can be shown [84] to be given by

$$\boldsymbol{P} = \frac{\partial \Psi(\boldsymbol{F})}{\partial \boldsymbol{F}} \tag{2.4}$$

which, using Eq. 1.12 leads to the following Cauchy stress:

$$\boldsymbol{\sigma} = \frac{1}{J} \frac{\partial \Psi(\boldsymbol{F})}{\partial \boldsymbol{F}} \boldsymbol{F}^T \tag{2.5}$$

Dependent on the complexity of the strain energy function Ψ, different features such as hyperelasticity (paragraph 2.1.1.1.3) and anisotropy (section 2.1.1.3) can be included in the model. Of course, a linear elastic material leads to the most simple SEF. Take for example the stress-strain curve taken from a uniaxial tensile test on a simple linear elastic rod as depicted in Figure 2.1; the surface under the stress-strain curve depicts the amount of energy stored inside the volume. Consequently the strain energy function can easily be calculated as the surface underneath the $\sigma(\varepsilon) = E\varepsilon$ curve (see Eq. 2.1), which leads to:

$$\Psi(\varepsilon) = \frac{1}{2} E \varepsilon^2 \tag{2.6}$$

2.1.1.1.3 Hyperelasticity. Before we dive into different hyperelastic strain energy functions, we have to take into mind the (nearly-)incompressible behavior of hyperelastic materials (see paragraph 2.1.1.1.4). Therefore, it is often convenient to decompose the SEF $\Psi(\boldsymbol{F}) = \bar{\Psi}(\bar{\boldsymbol{F}}) + \Psi_{vol}(J)$ into a deviatoric/isochoric part $\bar{\Psi}$ and a volume-dependent part Ψ_{vol}. To do so, the volumetric deformation can be filtered out of the deformation gradient [254], so we get the isochoric deformation gradient

$$\bar{\boldsymbol{F}} = det(\boldsymbol{F})^{\frac{-1}{3}}\boldsymbol{F} = J^{\frac{-1}{3}}\boldsymbol{F} \tag{2.7}$$

To allow for realistic results, these models need to produce results which are invariant under superposed rigid body motions. Therefore, a hyperelastic strain energy functions Ψ is typically formulated in terms of strain combination which are invariant under coordinate transformations. These *invariants* are based on the right or left Cauchy-Green tensors [329] (see Eq. 1.5). Consequently, the principal invariants of deformation become:

$$\bar{I}_1 = \mathrm{tr}\,\bar{\boldsymbol{b}} = \mathrm{tr}\,\bar{\boldsymbol{C}} \tag{2.8a}$$

$$\bar{I}_2 = \frac{1}{2}\left(\left(\mathrm{tr}\,\bar{\boldsymbol{b}}\right)^2 - \mathrm{tr}\,\bar{\boldsymbol{b}}^2\right) = \frac{1}{2}\left(\left(\mathrm{tr}\,\bar{\boldsymbol{C}}\right)^2 - \mathrm{tr}\,\bar{\boldsymbol{C}}^2\right) \tag{2.8b}$$

$$\bar{I}_3 = \det\bar{\boldsymbol{b}} = \det\bar{\boldsymbol{C}} = J^2 \tag{2.8c}$$

where $\bar{\boldsymbol{b}} = J^{\frac{-2}{3}}\boldsymbol{b}$, $\bar{\boldsymbol{C}} = J^{\frac{-2}{3}}\boldsymbol{C}$ are the isochoric left and right Cauchy-Green tensors respectively. For an isotropic hyperelastic material, with a deviatoric SEF written in terms of the first two invariants of deformation

$$\Psi(\boldsymbol{F}) = \bar{\Psi}(\bar{I}_1, \bar{I}_2) + \Psi_{vol}(J) \tag{2.9}$$

the hyperelastic stress state can be deduced (based on Eq. 2.5) as follows:

$$\boldsymbol{\sigma} = \frac{2}{J}\mathrm{dev}\left[\left(\frac{\partial\bar{\Psi}}{\partial\bar{I}_1} + \bar{I}_1\frac{\partial\bar{\Psi}}{\partial\bar{I}_2}\right)\bar{\boldsymbol{b}} - \frac{\partial\bar{\Psi}}{\partial\bar{I}_2}\bar{\boldsymbol{b}}^2\right] + \frac{\partial\Psi_{vol}}{\partial J}\boldsymbol{I} \tag{2.10}$$

Here, $\mathrm{dev}(\bullet)$ represents the deviatoric projection tensor operator, $\mathrm{dev}(\bullet) = \bullet - 1/3\mathrm{tr}(\bullet) = \mathbb{P} : \bullet$, with $\mathbb{P}$ a fourth order deviatoric projection tensor, $\mathbb{P} = \mathbb{I} - 1/3\boldsymbol{I} \otimes \boldsymbol{I}$. In order to compute the mechanical response of a material with the hypothetical SEF of Eq. 2.9 in an implicit finite element analysis (FEA) framework, the exact or (numerically) approximated *stiffness tensor* $\mathbb{C}$, also known as the *tangent moduli tensor* or the *Jacobian matrix*, needs to be computed (see section 1.4.5.1 and section 2.1.1.5). Similar to Eq. 2.10, the Jacobian matrix, i.e. the derivative of the Cauchy stress with

respect to the strain increment $\Delta\boldsymbol{\varepsilon}$, can be defined as

$$\begin{aligned}\mathbb{C} = \frac{1}{J}\mathbb{P} : \Bigg[4 \Bigg[\Bigg(\frac{\partial^2 \bar{\Psi}}{\partial \bar{I}_1^2} + \frac{\partial \bar{\Psi}}{\partial \bar{I}_2} + 2\bar{I}_1 \frac{\partial^2 \bar{\Psi}}{\partial \bar{I}_1 \partial \bar{I}_2} + \bar{I}_1^2 \frac{\partial^2 \bar{\Psi}}{\partial \bar{I}_1^2} \Bigg) \bar{\boldsymbol{b}} \otimes \bar{\boldsymbol{b}} \\ - \Bigg(\frac{\partial^2 \bar{\Psi}}{\partial \bar{I}_1 \partial \bar{I}_2} + \bar{I}_1 \frac{\partial^2 \bar{\Psi}}{\partial \bar{I}_1^2} \Bigg) (\bar{\boldsymbol{b}} \otimes \bar{\boldsymbol{b}}^2 + \bar{\boldsymbol{b}}^2 \otimes \bar{\boldsymbol{b}}) \\ + \frac{\partial^2 \bar{\Psi}}{\partial \bar{I}_2^2} \bar{\boldsymbol{b}}^2 \otimes \bar{\boldsymbol{b}}^2 - \frac{\partial \bar{\Psi}}{\partial \bar{I}_2} \mathbb{H}_{\bar{\boldsymbol{b}}} \Bigg] \\ - \frac{2}{3} \Bigg(\frac{1}{J} \bar{\boldsymbol{F}} \bar{\boldsymbol{\sigma}} \bar{\boldsymbol{F}}^T \otimes \boldsymbol{I} + \boldsymbol{I} \otimes \frac{1}{J} \bar{\boldsymbol{F}}^T \bar{\boldsymbol{\sigma}} \bar{\boldsymbol{F}} \Bigg) + \mathbb{H}_{\bar{\boldsymbol{\sigma}}} \Bigg] : \mathbb{P} \\ + \Bigg(\frac{\partial \bar{\Psi}_{vol}}{\partial J} + J \frac{\partial^2 \bar{\Psi}_{vol}}{\partial J^2} \Bigg) \boldsymbol{I} \otimes \boldsymbol{I}\end{aligned} \tag{2.11}$$

where the term $\mathbb{H}_{\bar{\boldsymbol{\sigma}}}$ was defined as $\mathbb{H}_{\bar{\boldsymbol{\sigma}}_{ijkl}} = (\bar{\sigma}_{ik}\bar{\sigma}_{jl} + \bar{\sigma}_{il}\bar{\sigma}_{jk})/2$. More information on the derivation of this tangent moduli tensor can be found in [57, 70].

Over the past few decades, several models (and thus strain energy functions) have been proposed to represent the nonlinear response of soft tissue undergoing large deformations. Several *phenomenological* hyperelastic material models actually emerged from earlier research on rubber-like materials, such as polymers, due to the behavioral similarity in *strain hardening*, the effect where a material strengthens (increasing elastic modulus) with increasing deformation. These SEFs can be categorized into two main families, the power law models and the limited-chain extensibility models. (*Microstructurally-based* material models are further discussed in section 2.1.1.4).

Focusing on the *power law models*, several variants can be traced back to material models for rubber-like materials proposed 50 years ago. The generalized polynomial form given by

$$\bar{\Psi}_P\left(\bar{I}_1, \bar{I}_2\right) = \sum_{i+j=1}^{N} c_{i,j} \left(\bar{I}_1 - 3\right)^i \left(\bar{I}_2 - 3\right)^j \tag{2.12}$$

can easily be deduced from Ogden's power law model expressed in terms of the principal stretch ratios [255]. Two very common variants from this generalized polynomial form are the Neo-Hookean model and the Mooney-Rivlin model. The neo-Hookean deviatoric strain energy function is defined as

$$\bar{\Psi}_{NH}\left(\bar{I}_1\right) = \frac{M}{2}\left(\bar{I}_1 - 3\right) \tag{2.13}$$

which has been used by Holzapfel et al. to describe the non-collagenous ground matrix of arterial tissue [142]. Here, M describes the shear modulus of the material. Another commonly used derivative from Ogden's model, is the Mooney-Rivlin material, which is given by

$$\bar{\Psi}_{MR}\left(\bar{I}_1\right) = \frac{M_1}{2}\left(\bar{I}_1 - 3\right) + \frac{M_2}{2}\left(\bar{I}_2 - 3\right) \tag{2.14}$$

where M_1 and M_2 are empirically determined material constants. This material model has been used to model a.o. porcine brain tissue and the liver and kidneys [227].

Another source of power-law variants can be traced back to Fung's material model which generally reads

$$\bar{\Psi}_{Fung} = \frac{1}{2}\left[q + c\left(e^Q - 1\right)\right] \tag{2.15}$$

with

$$q = a_{ijkl}\varepsilon^G_{ij}\varepsilon^G_{kl}\ , \quad Q = b_{ijkl}\varepsilon^G_{ij}\varepsilon^G_{kl} \tag{2.16}$$

quadratic polynomial forms of the Green-Lagrange strain $\boldsymbol{\varepsilon}^G$ coefficients in the Einstein notation and a_{ijkl}, b_{ijkl}, c material constants. This model has been, and still is, widely used by different research groups to develop constitutive models describing the behavior of ovine, porcine, bovine, human, ... arterial, myocardial, gastrointestinal, skin, ... tissues (see [69]).

Different from the power law models, the *limited-chain extensibility models* limit the maximal achievable length of the polymeric molecular chains composing the material, and can be linked to the prototype SEF by Gent et al. [100]. An important derivative limited-chain extensibility model is the Arruda-Boyce model [5], which has been used for modeling skin and myocardial tissue, and will be used in this dissertation for incorporating the nearly-incompressible tissue response of soft tissue (see paragraphs 2.1.1.1.4, 3.2.1.2.1 and 5.3.1.2.3).

2.1.1.1.4 Incompressibility. Many hyperelastic materials show (nearly) incompressible behavior, meaning they do not change volume during deformation and have a Poisson's ratio tending or equal to 0.5. If we consider the stress decomposition in Eq. 1.13 into deviatoric and hydrostratic stress, we saw that the hydrostatic pressure is the product of the material's bulk modulus and the volumetric strain. Taking the definition of the bulk modulus of a linear elastic material:

$$K = \frac{E}{3(1-2\nu)} \tag{2.17}$$

we can clearly see that K tends to infinity as the Poisson's ratio tends to 0.5. At the same time ε_{vol} tends to zero. Such conditions typically result in numerical difficulties. To avoid such issues, two modeling choices can be taken:

- a hybrid/mixed displacement-pressure formulation can be set up, in which the hydrostratic pressure p is treated as an additional degree of freedom. Given that the pressure terms are kept in the assembled stiffness matrix (ex infra), this matrix becomes non-symmetric. Consequently, such a mixed formulation can only be solved by direct solvers due to the ill-conditioned matrix (see section 1.4.5.1). In constitutive terms, the volumetric SEF term in Eq. 2.9 then reads $\Psi_{vol}(J) = -p(J-1)$ where p is a Lagrange multiplier.
- a minimal amount of compressibility can be modeled, where the bulk modulus is chosen to be significantly greater than the shear modulus. For example, for a nearly-incompressible neo-Hookean material, we can set $\Psi_{vol} = \frac{\kappa}{2}(J-1)^2$, where $K >> \mu$ in Eq. 2.13.

2.1.1.2 *Viscoelasticity*

Even though the previous models already took into account the nonlinear response of soft tissues, a classic hyperelastic material model does not account for the strain rate-, frequency-, or time-dependent mechanical behavior of soft tissue. Soft tissue typically shows *viscoelastic* behavior which can experimentally be observed in the hysteresis loops during cyclic loading and unloading, in stress relaxation at constant strain and in preconditioning during repeated deformation cycles (see Figure 2.2). This viscoelastic behavior can be attributed to the interstitial fluid flow, the inherent dissipation of the solid phases and the viscous interaction between the tissue phases [348]. This combined viscous fluid and elastic solid behavior results into a stress-strain response which is a function of the rate of deformation. Classic rheological viscoelasticity models use a combination of spring (elastic behavior) and dashpot (viscous behavior) elements to characterize this dependency on deformation rate, as described by the Voigt, Maxwell and 3 parameter model (see Figure 2.3). Looking at the mechanical behavior of each of these models, the Maxwell model shows a sudden extension, corresponding to the spring stretching immediately, followed by a linear increase caused by the dashpot slowly extending. For the Voigt model there is a gradual increase in the deformation. For the 3 parameter model, these is a sudden extension followed by a gradual extension [150].

The most straightforward isotropic implementation of a generalized Maxwell model in *Abaqus* relies on a Prony series expansion of the shear

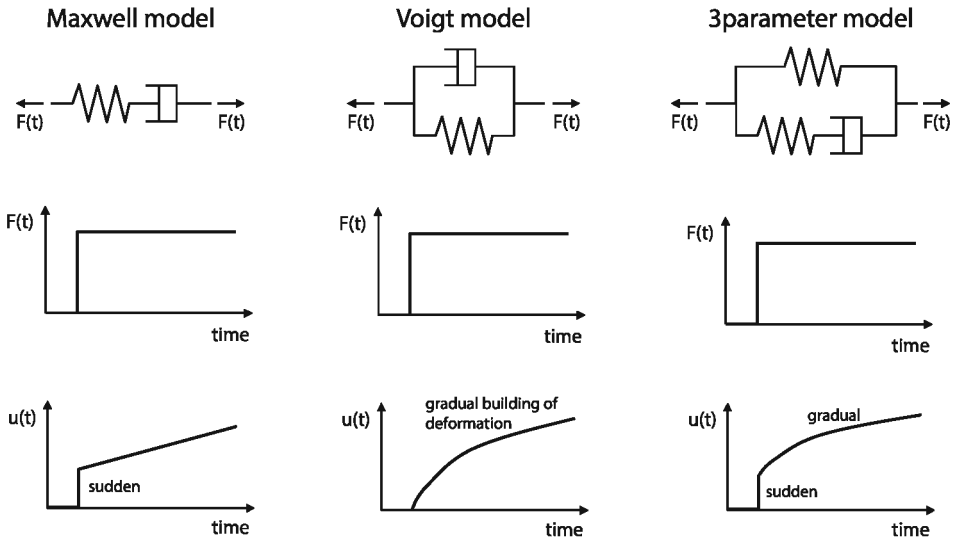

Figure 2.3: Three standard viscoelastic models, namely the Maxwell, Voigt and 3 parameter models. Image inspired by [150].

modulus M and bulk modulus K versus time t with n_G terms, as follows:

$$M(t) = M_0 \left[1 - \sum_{i=1}^{n_G} g_i \left(1 - e^{-\frac{t}{\tau_i}} \right) \right] \tag{2.18a}$$

$$K(t) = K_0 \left[1 - \sum_{i=1}^{n_G} g_i \left(1 - e^{-\frac{t}{\tau_i}} \right) \right] \tag{2.18b}$$

where M_0 and K_0 represent the instantaneous value of the shear and bulk modulus, respectively, coefficient g_i represent the ratio of the considered and instantantaneous modulus and τ_i are the material time constants. The unknown parameters g_i and τ_i can then be determined from experimental creep or relaxation test data [46]. Recently, the increasing complexity of experimental testing facilities allowed for experimental evidence of an anisotropic nature of the viscoelastic response of various tissues. In the believe that the non-equilibrium response is governed by a combined action of the different soft tissue constituents, anisotropic viscoelastic material models are on the rise. For example, recently a generalized Maxwell model formed by connecting Maxwell elements and one spring in parallel has recently been proposed for arterial tissue [145] and myocardial tissue [128]. Therein, each Maxwell element corresponds to a distinct response of the extracellular matrix, the collagen fibers, the myocytes/smooth muscle cells, etc. For more information on viscoelastic material models, we refer to [155, 348]. Tissue damage mechanics, another subsection of soft tissue biomechanics, was considered beyond the scope of this dissertation. The interested reader can find more information on that subject in [69, 144].

2.1.1.3 *(An)isotropy*

For biological tissues, mechanical properties typically vary according to different material orientations. This anisotropic material behavior complicates the description of the constitutive behavior. For isotropic linear elastic materials, the material stiffness tensor $\mathbb{C}$ (Eq. 2.3) could be described by just two constants (the Lamé constants λ and μ, see Eq. 2.2). For anisotropic materials, we need 21 constants to describe the constitutive tensor $\mathbb{C}$. However, by assuming biological tissue to behave *orthotropically*, where each material point has three mutually-orthogonal twofold axes of rotational symmetry, we keep three symmetry planes and reduce the elastic tensor $\mathbb{C}$ to 9 constants. Another frequently used approximation is *transverse isotropy*, a special class of orthotropy and the simplest form of anisotropy. A transversely isotropic material is one with physical properties that are symmetric about an axis that is normal to a plane of isotropy. This transverse plane has infinite planes of symmetry and thus, within this plane, the material properties are the same in all directions. Such materials are described by 5 independent elastic constants, instead of 9 for fully orthotropic.

Some phenomenological constitutive material models describe the tissue's anisotropic behavior through appropriate tuning of their constitutive parameters, e.g. Fung's material parameters in Eq. 2.16. Another means of imposing material anisotropy relies on using multiphasic models, where fibers are embedded in an isotropic matrix [69]. This approach is discussed in the next paragraph on heterogeneity.

2.1.1.4 *Heterogenity*

Human soft tissues, especially muscle and arterial tissue, are complex materials that, next to their nonlinear, time dependent and anisotropic behavior also express quite some heterogenity. Using a *phenomenological* approach to model these tissues would enforce a homogeneous material response. To incorporate the heterogenity, one could use a *multiphasic* approach, a *microstructural* approach or use *representative volume elements (RVEs)* [15, 69]. The dominant approach in biomechanics, and the approach followed in this manuscript, is to adopt a *microstructurally-based phenomenological approach* where the tissue is considered to be a structure of different constituents. Moving from a basic phenomenological (e.g. through one of the derived SEFs from the Fung's constitutive equation for preconditioned soft tissues, see Eq. 2.15) to a more microstructurally-based approach in constitutive modeling has been a focus in recent years in order to provide model parameters with a more natural physical interpretation[132]. Setting up a microstructurally-based constitutive relation encompasses a couple of steps to be taken [154]. First, the histology of the tissue (e.g. collagen, elastin, smooth muscle cell content

and structure) needs to be studied to delineate the underlying constituents of importance which are used to formulate a hypothesized constitutive relation. Subsequently, well-designed experimental tests (which are informed by the established theoretical framework, see section 2.1.2) should be set up and performed to test the proposed hypothesis. Based on these experiments, we can calibrate the values of the corresponding material parameters. Finally, the predictive capability of the final constitutive relation should be evaluated to study the validity and robustness of the constitutive relation. The strain energy function Ψ can take many forms and can span various levels of complexity to model the mechanical behaviour of a wide range of materials. Nowadays, the most commonly used microstructurally-based constitutive relation to generally describe soft tissue behavior is the Holzapfel-Gasser-Ogden material model initially developed for arterial tissue [89, 142]. This constitutive equation describes the biomechanical response of the aortic wall as the sum of an isotropic contribution, i.e. the matrix material (and for example the non-organized elastin content), and an anistropic contribution, i.e. two collagen fiber families embedded in the matrix material. This gives

$$\bar{\Psi}_{HGO}\left(I_1, I_4', I_6'\right) = \frac{c}{2}\left(I_1 - 3\right) + \frac{k_1}{2k_2}\sum_{i=4,6}\exp\left[k_2\langle I_i' - 1\rangle^2\right] - 1 \qquad (2.19)$$

where $c > 0$ and $k_1 > 0$ are stress-like parameters, $k_2 > 0$ is a dimensionless parameter, I_1 is the first invariant of the Cauchy-Green tensor (see Eq. 2.8a) and I_i' is the invariant related to the (collagen) fiber direction of a fiber family and can be written as

$$I_i' = \kappa I_1 + \left(1 - 3\kappa\right) I_i, \quad I_i = \lambda_\theta{}^2 \cos^2\alpha + \lambda_z{}^2 \sin^2\alpha \qquad (2.20)$$

where I_i, $i = 4, 6$ are fiber family invariants depicting the stretch in each of the fiber directions, α is the angle between the (average) fiber direction and the circumferential direction of the luminal tube, and $\kappa \in [0, 1/3]$ is a parameter related to the dispersion of the fibers. $\langle\rangle$ stands for the Macauley brackets making sure the collagen fibers only contribute to the strain energy potential when they are stretched (they are assumed not to lead to any additional strain energy in compression).

In this dissertation, we will consider human soft tissue behavior in the esophagus (see part I), the myocardium (see parts II and III) and arterial tissue (see part III). The histology and proposed or used constitutive relations for all the studied tissues will be discussed in the corresponding parts. It is important to note that *a constitutive relation is but a mathematical descriptor of particular behaviors exhibited by a material under conditions of interest; it is not a descriptor of a material per se* [154]. For the implementation of these constitutive models in Abaqus' finite element analysis framework, please refer to section 2.1.1.6.

2.1.1.5 *Residual stress*

When a soft tissue sample (e.g. an artery) is taken out of the body, and thus removed from a pressurized environment (see chapter 8), some stresses are typically still present in the sample's unloaded configuration. Such a situation is different from a standard continuum mechanics approach, where the reference configuration is assumed to be stress free. The exact origin of these *residual stresses* is still unknown, where some believe they arise from inhomogeneous tissue growth patterns in pressurized environments, or they are induced by the constant synthesis and breakdown of matter within the tissues and associated remodeling, cell death, and renewal, etc. [83, 154]. The first experimental evidence of these stresses was provided by Bergel et al. [19], who noticed that if an artery is split open longitudinally, it will unroll itself. This observation was confirmed by Chuong and Fung [37] who systematically cut rabbit arteries along their symmetry axis. Later experiments on left ventricles showed the same behavior [258], indicating that residual stress not only exists in arteries, but more generally in unloaded soft tissues.

To computationally account for these stresses in a continuum mechanics framework, two approaches can be found in literature. The first approach is embedded in the continuum theory of fictitious configurations (see section 2.3.1) and uses a fixed-point iteration on the geometry itself to find the residual stress state in the tissue (e.g. [99]). The second approach introduces residual stress in the invariant-based constitutive model through additional pseudo-invariants which bring 'residual deformation' parameters into the equation which can be tuned to fit experimental data [318] (e.g. [352]). More information on these procedures can be found in the cited literature.

2.1.1.6 *FEA implementation*

Even though some basic constitutive material models, e.g. the Neo-Hookean material model, are inherently built in to *Abaqus*, more complex and more tissue-specific constitutive material models are not. Moreover, pre-programmed material models do not allow the user to modify the material description. Therefore, the implementation of such material models requires the user to write their own Fortran-coded material subroutines. *UMAT*s and *VUMAT*s comprise the most flexible implicit and explicit user material subroutines, respectively. These subroutines provide the deformation gradient (at the beginning and the end of each increment) as input passed in for information, and require the developer to update the stresses and solution-dependent state variables to their values at the end of the increment for which it is called. In the implicit *Abaqus/Standard UMAT* subroutine, the material Jacobian matrix $\delta\boldsymbol{\sigma}/\delta\boldsymbol{\varepsilon}$ also needs to be fed back to the FEA solver for the Newton-Raphson iterations mentioned in section 1.4.5.1. Dependent

on the needed complexity, the user can also use *UANISOHYPER_INV* and *VUANISOHYPER_INV* subroutines to implement invariant-based material formulations. These subroutines only require the user to provide the first and second derivatives of the SEF w.r.t. the (provided) invariants to compute the loads $\boldsymbol{P}$ needed to compute the residuals in each iteration (see Figure 2.4). More information on the implementation of (material) user subroutines can be found in [46, 70].

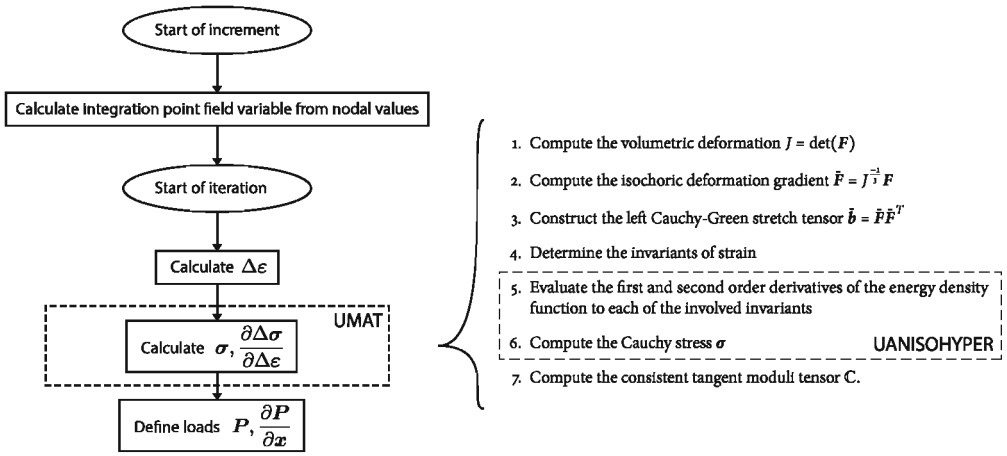

Figure 2.4: Hypothetical flow chart depicting where (user) material subroutines fit in the computational flow of an *Abaqus/Standard* increment. The enumeration (right) generally describes the steps to be taken when writing a *UMAT* (or *UANISOHYPER_INV*). For a hyperelastic material model that depends only on the first invariant $\bar{I}_1$, the second invariant $\bar{I}_2$ and the Jacobian J, step 4, 6 and 7 can be referred to Eq. 2.8, Eq. 2.10 and Eq. 2.11 respectively. Image partly inspired by [46].

2.1.2 Measurement of passive behavior

Several methods and types of mechanical tests have been developed and used to estimate the mechanical properties of soft biological tissues. These methodologies allow comparison of diseased versus control samples to provide important insights into the progression of the disease, but also allow translation of patient- and tissue-specific mechanical behavior into constitutive models, and thus in FEA models. Here, we will provide the reader with a short overview of different approaches to mechanically characterize the passive behavior of soft tissue, both ex vivo and in vivo.

2.1.2.1 Ex vivo methods

Ex vivo, also called in vitro, mechanical tests all work based on the same principle. Excised tissue is subjected to a certain stress causing them to stretch.

By recording the corresponding deformation (being it from the actuators or using optical means), the strain in the testing sample can be computed. The resulting stress-strain correlation can subsequently be used to characterize the tissue's mechanical behavior and to fit constitutive parameters related to the tissue's (hyper)elasticity and/or viscoelasticity. The different methods can be subdivided into categories based on the number of directions on which loads are independently imposed: uniaxial, biaxial or triaxial tests. The complexity of the material and the properties of interest dictate which test needs to be performed.

Uniaxial tests. Uniaxial tests constitute in vitro tests where a load is applied in one direction. These tests are typically used to describe isotropic materials or determine when a material fails (e.g. ultimate tensile stress). For anisotropic materials, these tests do not suffice. Different uniaxial tests are available. The uniaxial *strip extension* test streches a rectangular or dogbone shaped sample in one direction. In the uniaxial *ring* test a cylindrical (tube-like) sample is stretched by gradually moving two parallel rods on which the sample is mounted apart. A more local test compared to the previous tests is the *indentation* test, where an indentor indents the tissue in one direction. Such a test often does not comprise a physiological loading state of the tissue, but has its use for specific case studies (e.g. probing the stiffness of (non-)fibrotic liver tissue). In order to approximate the physiological loading conditions better, one could consider performing a strip extension test to a

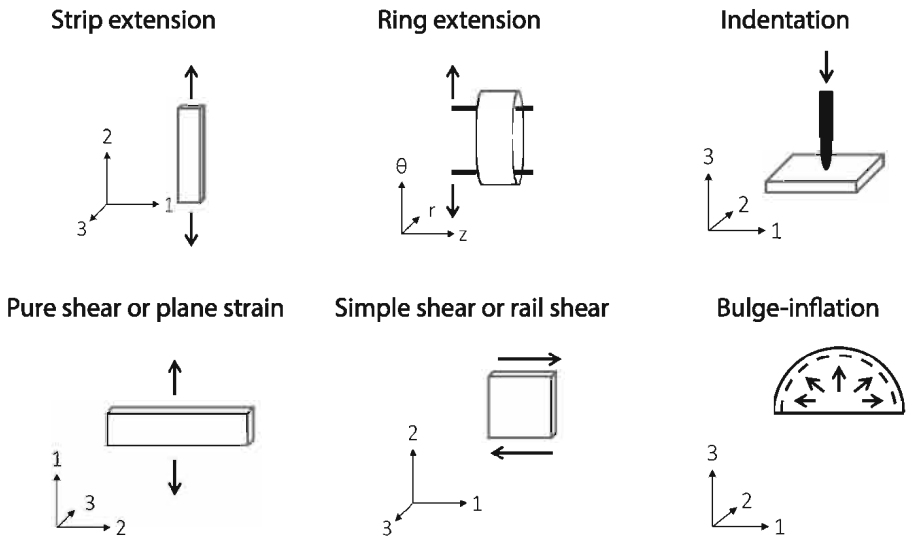

Figure 2.5: Uniaxial tests: conceptual sketches describing the deformation applied on the tissue sample in a uniaxial strip extension test, a uniaxial ring test, an indentation test, a pure shear or plane strain test, a simple shear or rail shear test and a bulge-inflation test. Image adapted from [73].

sample with a high width-to-length ratio, where the load can be applied in the circumferential or axial direction (if we are considering tubular tissue samples, e.g. arterial or esophageal tissue). Such a test, called a *pure shear* or *plane strain* test applies pure shear to the sample transformed under 45° to characterize the tissue's shear properties. Another uniaxial test to characterize the shear properties is the *simple shear* or *rail shear* test, where a simple shear deformation is obtained by applying a shear force on the surface with the normal in the circumferential or axial direction. Finally, in order to produce a 3D deformation with only one load, one can consider a *bulge-inflation* test, where a membrane-like sample is clamped into the testing device and the sample is pressurized from below using air or fluid. Figure 2.5 summarizes these different tests using conceptual sketches. More information on these tests can be found in [73].

Biaxial tests. In biaxial tests two loads are applied simultaneously but independently, which is consistent with the physiological loading of most soft biological tissues, e.g. gastro-intestinal ducts or arteries. The most common biaxial mechanical test to describe soft tissue is the *planar biaxial test*, a methodology which has been extensively studied by Fehervary et al. [73]. This test involves stretching in two perpendicular directions, where both loads can be varied independently, resulting in different deformations. Contradictory to the uniaxial tests, this experimental procedure allows the characterization of some anisotropic soft biological tissues. Another biaxial test is the *extension-shear test*, a combination of a strip extension and simple shear test. An *extension-inflation test* involves the inflation of a tubular tissue or vessel sample under a controlled pressure whilst this sample is simultaneously stretched in the axial direction. The resulting deformational change is then measured optically. This method has the advantage that the tubular sample maintains the same overall shape it had in the body, including any residual stresses (see section 2.1.1.5), which renders this setup more similar to the in

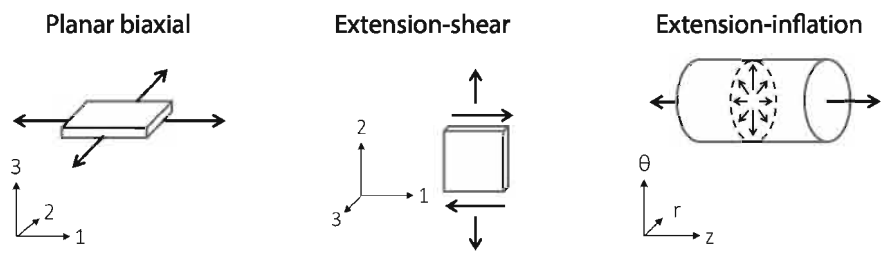

Figure 2.6: Biaxial tests: conceptual sketches describing the deformation applied on the tissue sample in a planar biaxial test, an extension-shear test and an extension-inflation test. Image adapted from [73].

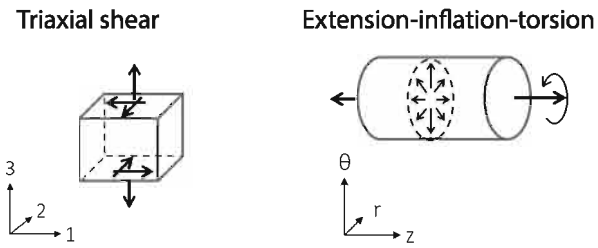

Figure 2.7: Triaxial tests: conceptual sketches describing the deformation applied on the tissue sample in a triaxial shear test and an extension-inflation-torsion test. Image adapted from [73].

vivo configuration than other tensile testing methods. Figure 2.6 summarizes these different tests using conceptual sketches. More information can again be found in [73].

Triaxial tests. Some soft biological tissues, e.g. myocardial tissue (see section 5.3.2), experience such a complex loading that we need to apply three independent loads, i.e. a triaxial test, to characterize its behavior. The *triaxial shear* test, also called the biaxial extension-shear test, comprises a simple shear loading applied in two orthogonal directions, whilst being pulled in the perpendicular direction. By combining an extension-inflation test with a rotation about the axial direction, we get an *extension-inflation-torsion* test. Figure 2.7 summarizes these two tests using conceptual sketches. More information can be found in [73].

Opening angle experiment. Classically, the residual stress in soft pressurized tissues is experimentally characterized by measuring the so-called *opening angle*. Therefore, one takes a ring-shaped segment of the tissue and cuts it open, after which the opening angle θ is measured, as illustrated in Figure 2.8. The axial residual stresses of tube-like samples can be derived from comparing the in vivo length of the sample to its length after excision (see also Figure 3.9).

General considerations. Given that it is often easier to acquire enough sample data from animals, rather than humans, animal models have long been use in medical research. Each animal model (being it of mouse, rat, rabbit, feline, canine, porcine or bovine origin) has its own specific considerations and specific attention has to be given when these models are to be used for translational research. Ideally, prior to and during testing, the samples have to be kept viable and in a condition as close as possible to that in vivo [83]. Given that ex vivo mechanical tests often cannot be performed immediately after excision, strict attention must be given to how the tissue samples are stored,

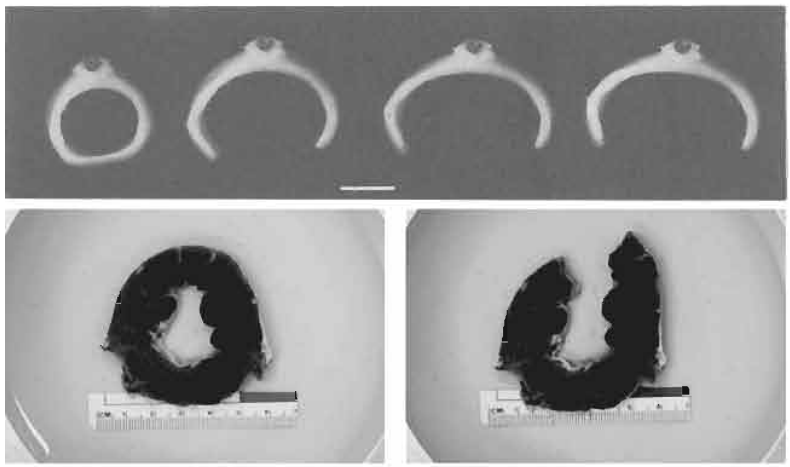

Figure 2.8: Opening angle experiment. Top: cutting open a ring-shaped segment of a feline thoracic aorta slice (from left to right: before cut, 15s after cut, 15min after cut, 30 min after cut). Bottom: Isolated porcine mid ventricular heart slice before (left) and after (right) radial cutting in the middle of the left ventricular free wall. Images taken from [37, 99].

frozen and thawed prior to testing. A short overview of the importance of all these steps can be found in [73]. To characterize the mechanical behavior of soft biological tissues, the experimental protocols typically include a *preconditioning* step. In this procedure, the tissue sample is subjected to a series of loading-unloading cycles until a repeatable curve is obtained. The data collected during these preconditioning cycles can be extremely valuable if one wishes to identify the history-dependent behavior of the tissue itself. Even though it is clear that the softening during preconditioning occurs due to internal changes in the structure of the tissue, the specific mechanisms of these changes remain under debate. In the case that an instantaneous and irreversible softening of the stress–strain curve occurs when the load increases beyond its prior all-time maximum value, we speak of the so-called *Mullins effect*. After the ex vivo mechanical testing procedures disclosed in this section, the tissue morphology can further be studied by fixing the tissue in physiological fixative solution. Dependent on the desired biological component in the tissue to be visualized, different stains can be used [65].

2.1.2.2 *In vivo methods*

Given that soft biological tissues behave differently when tested in vivo and ex vivo (e.g. nerve control responses, neighboring organs, connective tissue effects, metabolic activity, perfusion, pressurized environment, residual stresses) [24, 83], several approaches have been developed to study the properties of soft tissue in vivo. These approaches include *pressure wave*

analysis for vessels (e.g. pulse wave velocity [343], augmentation index [252]), *imaging data* (e.g. pressure-wall motion measurements in arteries and the heart (pressure-volume (PV) loops)) and *elastography* [25]. Apart from its potential use in a clinical setting [63], these measurements typically cannot grasp the anisotropic behavior of soft tissue, therefore the mechanical properties are not fully characterized. Consequently, both ex vivo and in vivo methods complement each other in assessing the tissue's mechanical passive behavior [83] and current and future work on residual stress (section 2.1.1.5) and pressure-induced stress state characterization (see also section 3.2.4 and chapter 8) could be the key to explain the current discrepancies between in vivo and ex vivo measurements and computational simulations in the literature.

2.2 ACTIVE BEHAVIOR

Apart from its complex *passive* behavior, biological tissues are *living matter* which means that internal processes also lead to certain *anelastic* behavior of the material [221]. In this dissertation, we will focus on two main manifestations of anelasticity in soft tissue: active mechanical processes and growth and remodeling. We distinguish between these two phenomena by stating that active processes only affect the reference configuration temporarily (this section), whilst growth and remodeling has a lasting effect (see section 2.3). Moreover, both anelastic phenomena typically operate at different time scales. Active processes take seconds or minutes whereas growth and remodeling effects take days or months to affect the tissue's mechanical behavior.

The active mechanical processes in the human body are regulated by three kinds of muscle tissue: skeletal, cardiac and smooth muscle tissue (see Figure 2.9). *Skeletal* muscle tissue, packed in connective tissue sheets into organs called skeletal muscles, are responsible for general body movement. The skeletal muscle fibers are long, cylindrical cells containing many nuclei, with a very precise alignment of myofilaments, which is reflected in their banded, or 'striated' appearance. Given that skeletal muscle contraction is under conscious control, it is typically called voluntary muscle. *Cardiac* muscle cells, like skeletal muscle cells, are striated but differ structurally because they are generally uninucleate and branching cells fit together at unique junctions called intercalated discs. These involuntary regulated muscle cells are, as intrinsically suggested by their name, only found in the walls of the heart. The third and final type of muscle tissue is *smooth* muscle tissue. The nomenclature for this muscle tissue was based on the fact that smooth muscle cells (SMCs) have no visible striations. Individual SMCs are spindle-shaped and contain one centrally located nucleus. Smooth

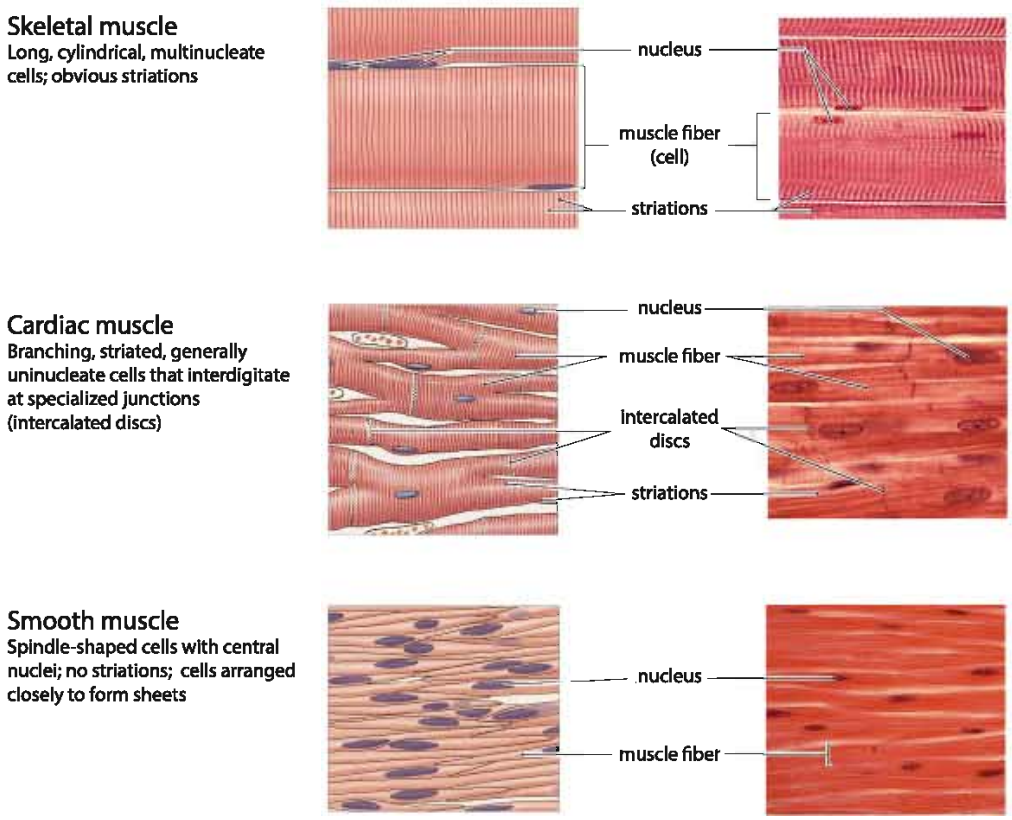

Figure 2.9: Muscle tissues; schematic representation and photomicrographs showing the most important structural features of each muscle tissue type; (top) skeletal muscle tissue, (mid) cardiac muscle tissue, (bottom) smooth muscle tissue. Image adapted from [220].

muscle is mostly found in the walls of hollow organs other than the heart (e.g. blood vessels, digestive and urinary tract organs, uterus) acting to squeeze substances through these organs by alternately contracting and relaxing involuntarily.

Each of these contractile biological tissues/cells have the ability to produce internal displacements and shape modifications leading to active internal stresses and deformation generation, even in the absence of external loads. This ability is detectable at different spatial (from the cellular to the full organ scale) and time scales (fractions of seconds to hours). All muscle cells possess *myofilaments*, elaborate versions of *actin* (thin) and *myosin* (thick) filaments which govern most active processes at the cellular level. These filament networks contain molecular motors which consume energy (adenosine triphosphate (ATP)) to change their molecular configurations resulting in the relative sliding and tensioning of these filaments [321]. Dependent on the type of muscle tissue, the interaction itself is different. Specifically, contraction of smooth muscle is thick filament regulated and requires an alteration in myosin before it can interact with actin, whereas contraction of striated

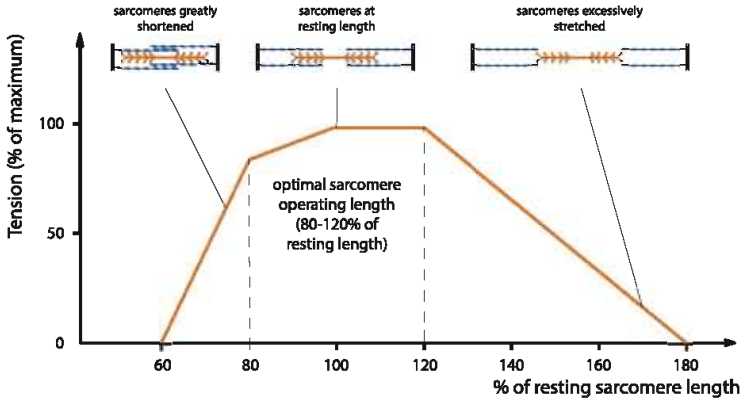

Figure 2.10: Length-tension relationships of sacromeres in skeletal muscles. Maximum force is generated when the muscle is between 80 and 120 % of its optimal resting length. Increases and decreases beyond this optimal range result in decreased force and inability to generate tension. Image adapted from [220].

muscle is thin filament regulated and requires movement of the troponin-tropomyosin complex on the actin filament before myosin can bind to actin. For a detailed description of the mechanochemical process of smooth and striated muscle contraction, the interested reader is referred to [238, 330]. Here, in a larger (tissue) scale continuum mechanics framework, we focus our attention to the generated active force. This force is affected by the number of stimulated muscle cells, their relative size, the frequency of stimulation and the degree of muscle stretch. Each of these factors can be very different for each type of muscle tissue, but overall it should be noted that muscle cells present optimal operating lengths or stretches for active force generation. Such an ideal *length-tension* relationship occurs when a muscle is slightly stretched so the filaments overlap optimally, which permits relative filament sliding along nearly the entire possible length. Stretching beyond this optimal stretch ratio results in increasing amounts of molecular motors that do not longer overlap across filaments, thus can no longer attach to the other filament and consequently cannot generate tension. This typical parabolic length-tension relationship is depicted for sarcomeres (the smallest contractile unit of a muscle fiber) in skeletal muscles in Figure 2.10. Introducing these active forces in our aforementioned kinematic framework can be done in multiple ways, as discussed in section 2.2.1. Once kinematically implemented, successful active tissue modeling required accurate calibration of the active constitutive parameters based on experimental data, which is discussed in more detail in section 2.2.2.

2.2.1 Modeling active behavior

The very first description of the mechanical behavior of muscle tissue was proposed by Hill in 1938 [134, 135], which was extended to the three-element

Hill model by Fung in 1970 [82]. This model consists of a contractile element in series with a spring element, representing the contractile unit. Another spring in parallel represents the surrounding material (see Figure 2.11). Since then, the inclusion of internal active force generation in the governing equations of the nonlinear theory of elasticity has taken many forms. By introducing active forces at different levels in the governing equations, we can discriminate between *active forces*, *active stresses*, *active strains*, *active metrics* and *active fibers* approaches. Here, we will focus on two of the most used approaches: active stresses and active strains. For a mini-review of the other approaches, we refer the interested reader to [112].

2.2.1.1 *Active stresses*

In order to model the contractile tissue response with the active stress formalism, the stress tensor is supplemented with a tensional contribution generated by the contraction of active fibers $\boldsymbol{f}$ [154]. Expressed in the Cauchy stress tensor (Eq. 2.5), this gives:

$$\boldsymbol{\sigma} = J^{-1}\frac{\partial \Psi(\boldsymbol{F})}{\partial \boldsymbol{F}}\boldsymbol{F}^T - p\boldsymbol{I} + \boldsymbol{\sigma}_{act} \text{ with } \boldsymbol{\sigma}_{act} = \sigma_{act}(\boldsymbol{F}, \beta)\boldsymbol{f}_0 \otimes \boldsymbol{f}_0. \tag{2.21}$$

where the active stress generation σ_{act} is dependent on the kinematics of deformations $\boldsymbol{F}$ (e.g. the length-tension relationship as depicted in Figure 2.10) and non-mechanical factors β (e.g. electrophysiogical (ionic) currents). Apart from the active production of strain, the nonmechanical factors β can also affect the mechanical properties of the tissue itself, which would lead to:

$$\boldsymbol{\sigma} = J^{-1}\frac{\partial \Psi(\boldsymbol{F}, \beta)}{\partial \boldsymbol{F}}\boldsymbol{F}^T - p\boldsymbol{I} + \boldsymbol{\sigma}_{act}(\boldsymbol{F}, \beta) \tag{2.22}$$

Practically however, it is difficult to identify $\Psi(\boldsymbol{F}, \beta)$ experimentally, so it is customary to include all the activation-driven changes of the material in the active stress term only:

$$\boldsymbol{\sigma} = J^{-1}\frac{\partial \Psi_{pass}(\boldsymbol{F})}{\partial \boldsymbol{F}}\boldsymbol{F}^T - p\boldsymbol{I} + \boldsymbol{\sigma}_{act}(\boldsymbol{F}, \beta) \tag{2.23}$$

where Ψ_{pass} depicts the passive SEF [112, 256].

2.2.1.2 *Active strains*

The active strain approach considers muscular contraction as a temporary internal remodeling of the continuum. Similar to the kinematic-based growth method (see section 2.3.1), the deformation gradient is decomposed multiplicatively:

$$\boldsymbol{F} = \boldsymbol{F}_e\boldsymbol{F}_a(\beta) \tag{2.24}$$

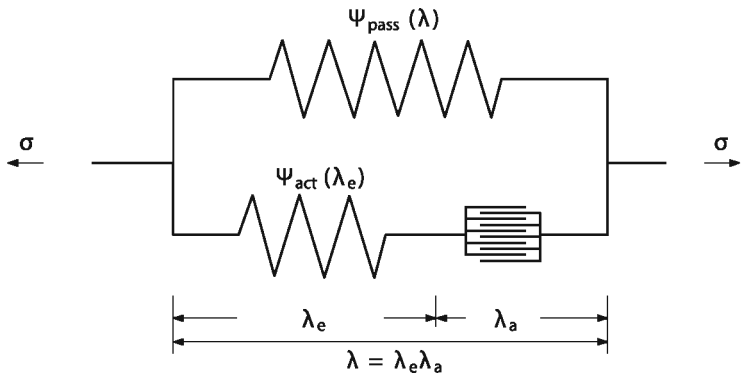

Figure 2.11: Schematic illustration of the active-strain approach implemented on the generalized Hill model where a passive element in the upper branch (with SEF $\Psi_{pass}(\lambda)$) is connected to the lower active branch in parallel. The lower branch is composed of an active element (characterized by the SEF $\Psi_{act}(\lambda_e)$) and a contractile element that generates active contraction λ_a upon its excitation through the action potential β . The total stretch λ is the product of the elastic stretch λ_e and the active stretch λ_a. Image inspired by [111].

where $\boldsymbol{F}_e$ and $\boldsymbol{F}_a$ represent the elastic and active deformation gradients, respectively. In this approach, the SEF Ψ is often broken up in a passive term $\Psi_{pass}(\boldsymbol{F})$ and an active contribution $\Psi_{act}(\boldsymbol{F}_e, \beta)$, so using Eq. 2.5, we get:

$$\boldsymbol{\sigma} = J^{-1}\frac{\partial \Psi_{pass}(\boldsymbol{F})}{\partial \boldsymbol{F}}\boldsymbol{F}^T + J^{-1}\frac{\partial \Psi_{act}(\boldsymbol{F}_e, \beta)}{\partial \boldsymbol{F}}\boldsymbol{F}^T - p\boldsymbol{I} \tag{2.25}$$

This principle is summarized in Figure 2.11, where a nonlinear spring in the upper branch representing $\Psi_{pass}(\lambda)$ is coupled in parallel with an active spring $\Psi_{act}(\lambda_e)$ equipped with a contractile element $\lambda_a(\beta)$ dictated by the eletrophysiological field β. More information can be found in [111, 112, 256].

2.2.2 Measurement of active behavior

To quantify the activation of smooth muscle cells in soft biological tissue, one typically performs isometric ((electrically) stimulating the muscle to generate force while keeping the length fixed) or isotonic ((electrically) stimulating the muscle to contract and shorten against a fixed afterload) uniaxial or biaxial tensile tests, similar to the tests discussed in section 2.1.2.1. By adding potassium chloride (KCl) to the buffer solution in which the samples are contained, the SMC membrane can be depolarized, which influences the intracellular calcium concentration [Ca^{2+}] which is known to activate the myosin motors in the cell [237]. By gradually increasing [Ca^{2+}] at different tissue stretch levels, the aforementioned $\sigma_{act}(\boldsymbol{F}, \beta)$ (Eq. 2.21) or $\Psi_{act}(\boldsymbol{F}_e, \beta)$ (Eq. 2.25) can be quantified experimentally (see Figure 2.12 which depicts

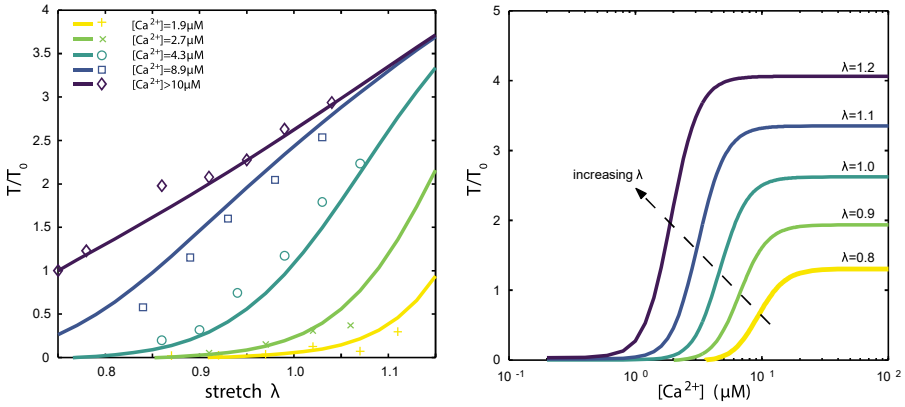

Figure 2.12: Normalized stress ratio (T/T_o) versus stretch for selected $[Ca^{2+}]$ concentrations (left) or versus $[Ca^{2+}]$ concentrations for selected stretches λ (right), where T_o is the minimum value of the stress at the maximally activated state. Image adapted from [330]

.

the isometric normalized active stress dependence on stretch λ and calcium concentration $[Ca^{2+}]$ for cardiac tissue). For more complex experiments, we refer the interested reader to [327] who developed an experimental framework to study active muscle behavior over a wide range of combined loading conditions.

2.3 Growth and remodeling

Beyond living soft tissues' passive and active behavior (time scale: milliseconds to hours), these tissues also comprise the remarkable ability to grow and remodel in health and disease, typically while exposed to complex biochemomechanical loads (time scale: weeks to months to years). Before we dive into the different theoretical frameworks for growth and remodeling (G&R), we first have to consider how G&R impacts our constitutive equations from the previous sections.

In a standard elasticity problem, Eq. 2.5 defines the constitutive (hyper)elastic material relation between stress and deformation, where the mass density ρ does not change over time. If we define this in terms of a strain energy function per unit of mass ψ, the total strain energy function Ψ becomes:

$$\Psi = \rho_o \psi \tag{2.26}$$

where the reference mass density ρ_o does not change over time, nor does ψ. In G&R however, this is no longer the case. Growth implies, in general, a temporal change in tissue mass, thus mass density $\rho(t)$, whilst remodeling in general implies a temporal change in material properties, that is stored

strain energy $\psi(t)$. Consequently, G&R goes beyond the transitional stress-strain relations discussed in the previous sections and calls for additional mechanobiological constitutive equations that define ρ and ψ over time. A general postulate of mechanobiology is that the biological processes of G&R are driven by mechanical stimuli, with stress and strain often used as convenient metrics for remodeling. Therefore, mechanobiological constitutive equations typically define the evolution of ρ and ψ in terms of mechanical stresses or strains [44].

This third section will introduce two common theoretical frameworks which propose such equations and are believed to eventually lead to a better understanding of tissue development (morphogenesis), adapation (homeostasis), and change in disease (pathogenesis). Most of this section was based on [44], to which we refer the interested reader who wants more information on or some applied examples of these theoretical G&R frameworks (e.g. G&R in arterial, cardiac, skin, skeletal muscle and eye tissue).

2.3.1 Kinematics-based growth

In 1994, Rodriguez et al. [295] proposed the three-dimensional theory of kinematic growth. In this theory, similar to Eq. 2.24, the total deformation gradient $\boldsymbol{F}$ is decomposed into an elastic part $\boldsymbol{F}_e$ and an inelastic part $\boldsymbol{F}_g$:

$$\boldsymbol{F} = \boldsymbol{F}_e \boldsymbol{F}_g \tag{2.27}$$

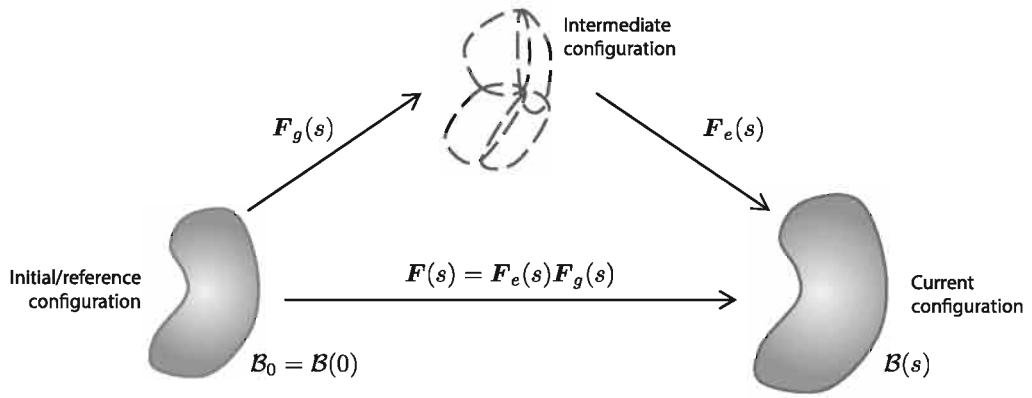

Figure 2.13: Kinematic growth models assume a multiplicative deposition of the total deformation gradient $\boldsymbol{F}$ into the inelastic part $\boldsymbol{F}_g$ and the elastic part $\boldsymbol{F}_e$. The growth deformation gradient $\boldsymbol{F}_g$ deforms the initial reference configuration $\mathcal{B}(0)$ into an intermediate configuration, which, in general, is geometrically incompatible. The elastic deformation gradient $\boldsymbol{F}_e$ results from mechanical equilibrium under a given load and enforced geometrical compatibility due to each volume element's elastic connection to its neighboring volume elements. Image adapted from [44].

The permanent changes of the volume and the microstructure due to G&R are incorporated in this inelastic $\boldsymbol{F}_g$, which deforms the body into a hypothetical intermediate configuration which (in general) is not geometrically compatible (see Figure 2.13). This intermediate configuration simply describes a state, in which, after a certain G&R process, each separate volume element would be stress free if it would not be elastically constrained to neighboring volume elements [44]. The elastic deformation gradient $\boldsymbol{F}_e$ thus results from the condition that the final deformation $\boldsymbol{F}$ has to ensure both mechanical equilibrium under a given load and geometric compatibility. Assuming that elastic deformations of soft tissue are isochoric ($\det(\boldsymbol{F}_e) = 1$, see paragraph 2.1.1.1.4), we can conclude from Eq. 2.27 that

$$\det(\boldsymbol{F}) = \det(\boldsymbol{F}_e)\det(\boldsymbol{F}_g) = \det(\boldsymbol{F}_g) \tag{2.28}$$

Coupling this back to the mechanobiological constitutive equations for ρ and ψ, we can state, by assuming soft tissue to have a constant spatial mass density [295], that at time point $s \in \mathbb{R}_+$:

$$\rho(s) = \det(\boldsymbol{F}_g)\rho(0) \tag{2.29}$$

Based on the experimental observations that a preferred homeostatic state (being it defined by stress or strain) exists in living soft tissues, at which no net growth occurs, and that disturbing this homeostatic state initiates growth which will change the volume and the stress-free state of the tissue, a mechanical G&R stimulus can be defined as $\Delta\boldsymbol{G}$, the difference between a mechanical quantity $\boldsymbol{G}$ and its homeostatic value $\boldsymbol{G}_h$. This quantity can be stress- or strain-based. The growth deformation gradient $\boldsymbol{F}_g$ can then, informed by experimental data, be indirectly defined based on an evolution equation for $\dot{\boldsymbol{F}}_g$ which is a function of $\Delta\boldsymbol{G}$ or composed of different direction tensors $\boldsymbol{B}^j$ (accounting, for example, for $m \in \mathbb{N}$ preferred growth directions) scaled by time-dependent factors $\beta^j(s)$

$$\boldsymbol{F}_g = \sum_{j=1}^{m} \beta^j(s)\boldsymbol{B}^j \tag{2.30}$$

which are typically computed from evolution equations for $\dot{\beta}^j(\Delta\boldsymbol{G})$ that are defined on the basis of experimental observations (see chapter 7), with $\dot{\beta}^j(\Delta\boldsymbol{G} = \boldsymbol{0}) = 0$.

Since the introduction of Rodriguez et al.'s three-dimensional theory of kinematic growth [295], growth laws have been successfully applied in different soft tissues (e.g. cardiac, arterial, skin tissue). Yet, few studies have used kinematic growth models in a truly predictive way (see chapter 7). The kinematic growth theory provides a phenomenological description of

the G&R processes in the tissue, but lacks a strong micromechanical and mechanobiological basis [153]. To address this issue, constrained mixture models arose which, in general, account for the different material properties, rates of synthesis and degradation, and natural configurations for individual structurally significant constituents that constitute a typical soft tissue.

2.3.2 Constrained mixture modeling

The basis of constrained mixture models is based on the following experimental observations [44]:

- Cells continually synthesize and break down individual structurally significant constituents, which can have different material properties, different rates of turnover, and different natural (stress-free) configurations.
- Despite possessing in general different natural configurations, all structurally significant constituents are assumed to deform together with the whole tissue (i.e., they form a so-called *constrained mixture*).
- Turnover of constituents (production and removal) is balanced in a so-called homeostatic state.
- If the state is perturbed from homeostatic, turnover need not be balanced and G&R processes can change the mass (geometry) and structure (properties) of the tissue.
- New constituents are deposited under stress, but this stress need not equal that of the extant constituents.

By discriminating between nonstructurally significant and diffusible (e.g. cytokines, growth factors, proteases and vasoactive molecules) and structurally significant and nondiffusible (e.g. elastin, collagen, muscle fibers) constituents, we can consider the balance of linear momentum only for the latter class of constituents (see Eq. 1.16). Given that these constituents are assumed to deform together, a simple rule-of-mixtures relation can be used for the stored energy, where the total strain energy per unit volume Ψ is assumed to equal the sum of the strain energies of all n structurally significant constituents, including their evolution (see Figure 2.14). During G&R, the constrained mixture's theoretical framework states that the body is assumed to evolve through different configurations $\mathcal{B}(0), ..., \mathcal{B}(\tau), ..., \mathcal{B}(s)$ at G&R times $0, ..., \tau, ..., s$. The evolving geometry is described by the general concepts of continuum mechanics, in particular the deformation gradient $\boldsymbol{F}$. In each configuration at each time, constituent-specific increments of mass may be deposited and/or removed in each volume element. For each

constituent i, the contribution to Ψ is based on the standard forms for energy storage (from section 2.1-section 2.2) augmented with micromechanically informed relations for constituent production and degradation/survival rate $\dot{\rho}_o^i$ which is dependent on mechanical growth stimuli $\Delta \boldsymbol{G}$. Here, any new constituent mass deposit takes place in an extant matrix with some elastic prestress, which can be described by an elastic deformation gradient $\boldsymbol{F}_{pre}^i(\tau)$ relative to their natural stress-free configuration $\mathcal{B}_n^i(\tau)$. Recall that, once the constituent is incorporated within the extant matrix, it deforms together with the matrix. Thus, at time s, the elastic deformation gradient $\boldsymbol{F}_e^{i(\tau)}(s)$ of a mass increment deposited at time τ depends on the elastic *deposition stretch* $\boldsymbol{F}_{pre}^i(\tau)$ and subsequent deformation of the whole tissue $\boldsymbol{F}(s)\boldsymbol{F}^{-1}(\tau)$. This yields

$$\boldsymbol{F}_e^{i(\tau)}(s) = \boldsymbol{F}(s)\boldsymbol{F}^{-1}(\tau)\boldsymbol{F}_{pre}^{i(\tau)} \tag{2.31}$$

Constrained mixture models assume that the elastic energy (per unit mass) ψ^i for individual mass increments depends only on their elastic deformation relative to their individual natural configuration [44].

The total strain energy of the whole mixture is the sum of strain energies of all mass increments, taking into consideration their individual elastic stretch, as well as degradation since deposition. Taking into account the deposition stretches of the previous time steps and taking into account the history of all the constituents makes the implementation in a FEA framework much more involved and computationally expensive than implementing the

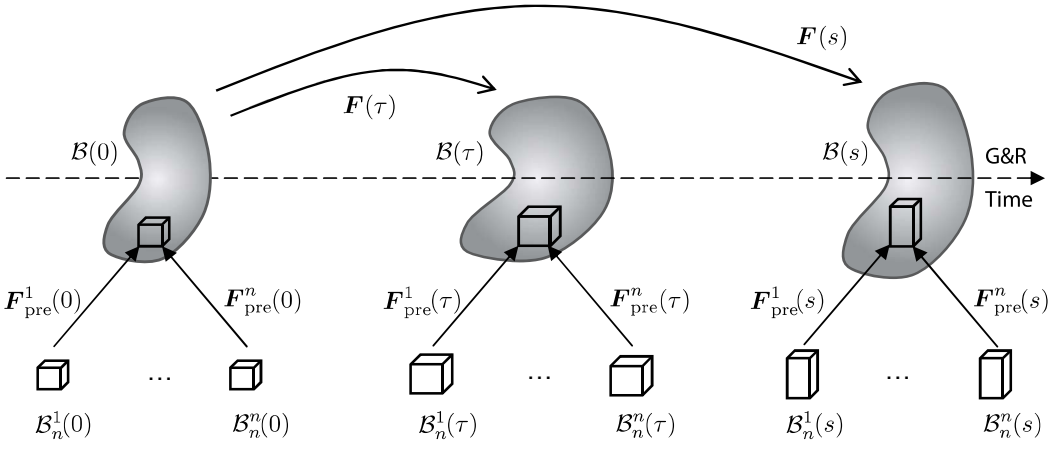

Figure 2.14: Constrained mixture models assume an, in general, continuous deposition of mass (increments) into the body. At time τ, the mass increment is deposited into the current configuration $\mathcal{B}(\tau)$ with a prestress that can be accounted for via an elastic *deposition stretch* (deformation gradient) $\boldsymbol{F}_{pre}^i(\tau)$ relative to the individual natural (stress-free) configuration $\mathcal{B}_n^i(\tau)$ for each constituent. Image adapted from [44].

kinematic based growth theory. Consequently, only recently the first steps towards constrained mixture theory implementation in Abaqus were taken by [71, 235].

Comparing constrained mixture models to kinematic growth models, the biggest difference lies in the microstructural-mechanobiological versus mechanistic kinematics-based approach between both frameworks. Constrained mixture models can often be directly related to physiological or experimental parameters (e.g. half-life of collagen or elastin in soft tissue), which simplifies a physiologically realistic model definition. Nevertheless, most of these parameter values used nowadays are still mostly extracted from different, although related, experiments, not single well-controlled experiments. Thus, as for kinematic growth models, true evaluations of specific constrained mixture G&R predictions are still largely missing and assessment of the theory's predictive power remains a largely open challenge.

I

Gastro-Intestinal Biomechanics

Chapters

Clinical rationale 59

3 **The 'virtual esophagus'** 61

4 **Esophageal stenting** 87

Clinical rationale

Gastro-intestinal diseases affecting patients' quality of life and productivity are highly prevalent, costly and lead to substantial health care utilization worldwide [265]. The gastro-intestinal tract is primarily a self-regulating organ responsible for the transport of the liquids and solids to be taken in. Heterogeneous food materials received from the esophagus and stomach are propelled further down the intestine and mixed with secreted fluids to digest and absorb the food constituents. Given that these operations mostly constitute moving heterogeneous food materials in various complex ways and/or following special flow patterns (for fermentation and/or absorption), it is clear that the gastro-intestinal function is, to an important degree, mechanical. The gastrointestinal peristaltic food transport is a neuromuscular function where the autonomous nervous system controls contraction frequency of contractions governed by length-tension-velocity muscle mechanics. Whilst the nervous system of the gastrointestinal tract has been extensively studied [117], the understanding of these tissues' biomechanical behavior is lagging far behind. Overall, it can be stated that biomechanics and bioengineering have only to a small degree entered the thinking of researchers and clinicians in gastroenterology [118]. Consequently, the mechanical deformation and movement of the gastro-intestinal (GI) tract continues to be perhaps the least rationally developed subject in physiology, which results in limited understanding of how disturbed GI mechanics cause alimentary problems for many patients. Studying the biomechanical behavior of the GI tract will lead to an improved understanding of the mechanics of alimentation, which will surely benefit those who suffer from insufficiently understood GI disorders.

This part focuses on the biomechanical behavior of the human esophagus, a very common source of gastro-intestinal problems (e.g. achalasia, ulcers, strictures, carcinomas, gastro-esophageal reflux disease, swallowing disorders). Given that any malfunctioning of this gastro-intestinal organ can easily lead to considerable discomfort and problems for the patient, knowledge of the esophageal wall mechanics has been proven crucial in the understanding of esophageal physiology and pathophysiology, depending on both passive

and active wall properties. Structural remodeling of the esophagus, leading to diseases such as achalasia or systemic sclerosis, can only be studied considering the large deformations and transmural stress and strain distributions in the esophageal wall [201]. Such information is also central to address problems in surgery, in medical-device applications, and for the optimal design of prostheses [117, 203].

Therefore, we will develop a biomechanical 'virtual esophagus' framework which transcends the current state of the art in mathematical and constitutive modeling of esophageal function in health and disease in chapter 3. Such a framework can lead to new and improved understanding of esophageal function and (patient-specific) treatment planning. One of the possible treatment strategies for a number of esophageal disorders, esophageal stenting, still suffers from considerable complications. Therefore, chapter 4 combines the power of the developed virtual esophagus framework with sophisticated numerical models that capture the time-varying behavior of biodegradable polymeric braided fiber stents. The virtual implantation procedure of such a stent in a patient-specific, actively contracting and buckling esophagus provides stent developers and clinicians with a state-of-the-art in silico bench testing environment to optimize the current generation of (biodegradable) esophageal stents.

The long-term goal of this work is to develop biomechanical insights in the human esophagus's function in health and disease and to improve current treatment strategies. Through exploring the anatomy, morphology and physiology of the esophagus and introducing this knowledge into continuum mechanics descriptions of the considered tissue, we hope to contribute to a better understanding of the esophagus as a biomechanical system. Such an integrated approach can help to understand esophageal disorders whose pathophysiology has hitherto, from a bioeningeering point of view, remained an enigma [118]. We strongly believe that the integration of the developed patient-specific computer models in gastro-intestinal clinical sciences can lead to improved disease management, especially considering the patient-specific nature of simulating disease-specific physiological and mechanical processes [120].

CHAPTER 3

THE 'VIRTUAL ESOPHAGUS'

In this chapter, we describe the development of a virtual esophagus framework to set up actively contracting, patient-specific, buckling and in vivo stressed esophagus models that allow us to study the mechanical behavior of the esophagus during normal and pathological functioning in more detail.*

3.1 ESOPHAGEAL FUNCTION, STRUCTURE AND HISTOLOGY

The esophagus is a 20-to-25 cm long multi-layered muscular tube in the alimentary canal which takes a fairly straight downward course through the mediastinum of the thorax connecting the throat (pharynx) to the stomach (see Figure 3.1). Its single digestive function is food propulsion, which is done through peristaltic contractions. In healthy subjects, peristalsis is a well-coordinated passive and active mechanism to propel the food bolus downward. The circularly arranged muscle cells behind the food bolus contract together with the longitudinally arranged muscle cells ahead of the food bolus, whilst the muscle cells around the food bolus relax (see Figure 3.2).

*This chapter is based on the appendix materials to be found in M. Peirlinck, N. Debusschere, F. Iannaccone, P. D. Siersema, B. Verhegghe, P. Segers, and M. De Beule, "An in silico biomechanical analysis of the stent–esophagus interaction", *Biomechanics and Modeling in Mechanobiology*, vol. 17, no. 1, pp. 111–131, 2018

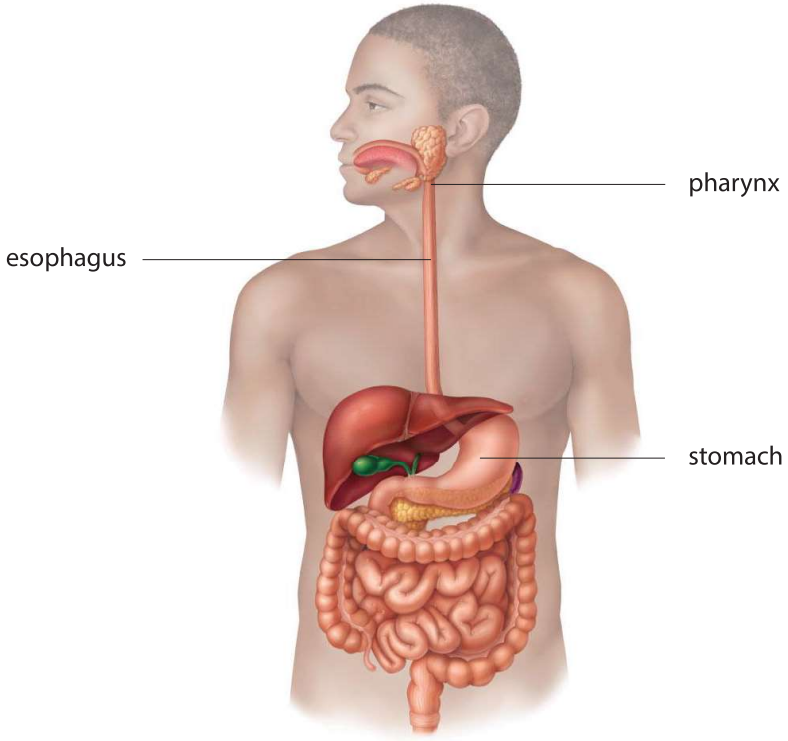

Figure 3.1: The digestive system showing the alimentary canal and all the related accessory digestive organs, including the esophagus. Image reproduced from [220].

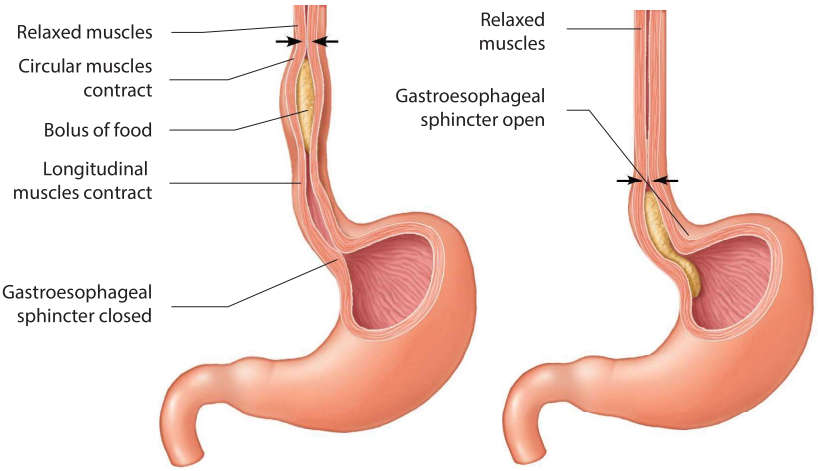

Figure 3.2: Peristalsis propels a food bolus along the length of the digestive tract (esophagus here) by coordinated contractions of the circular and longitudinal layers. Image adapted from [220].

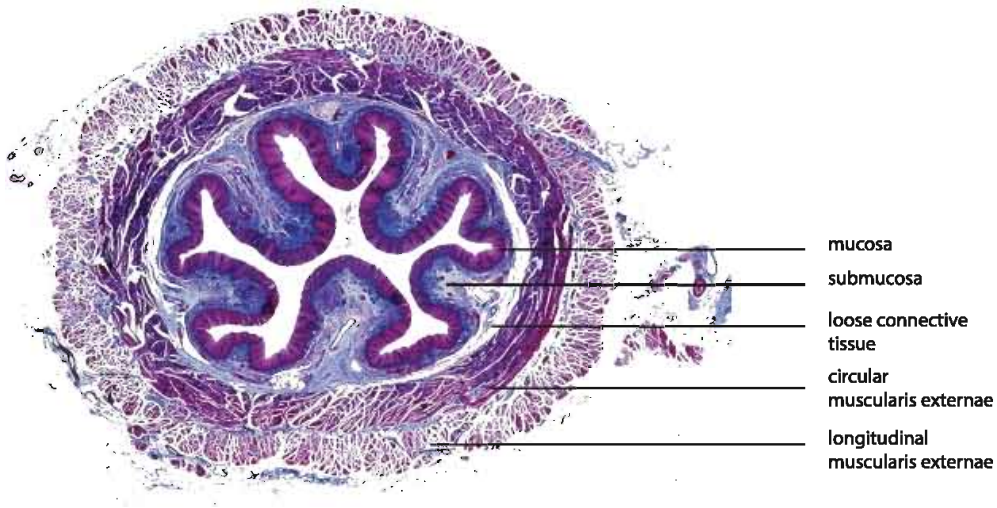

Figure 3.3: Light micrograph of a cross section through the human esophagus depicting the mucosa, submucosa, the loose connective tissue in between the submucosa and the muscle layers, the circular and the longitudinal muscle layers. Image credit: biophoto associates/science photo library

The esophagus shows an almost cylindrical shape with a lumen of variable diameter surrounded by the esophageal wall which is composed of four well-defined layers: the mucosa, the submucosa, the muscularis externa and the adventitia [117, 118, 242], see Figure 3.3. The mucosal layer is composed of connective tissue and can be subdivided in the epithelium, the lamina propria, and the muscularis mucosa. Contrary to the mucosa, where very fine collagen fibrils are loosely and randomly organized, collagen fibrils in the submucosa are organized in thick aligned fibers arranged in a criss-cross pattern which runs helically down the esophagus. In this criss-cross pattern, we can distinguish two groups of collagen fibers, one running in a clockwise helix down the esophagus and the other running in a counterclockwise helix (Figure 3.4). Due to this difference in constituents and internal architecture, the submucosa plays a stronger mechanical role than the mucosa in offering resistance to the deformation of the esophageal wall. The submucosa is loosely interconnected [325] with the muscularis externa which is mainly composed of smooth and striated muscle cells (the transition from striated to smooth muscle is spread throughout the middle third of the esophagus). This muscle layer can be subdivided in two layers, the inner one having muscle cells arranged in the circumferential and the outer one arranged in the longitudinal (axial) direction (see Figure 3.3). The muscle layer is surrounded by a thin layer of soft connective tissue rich in blood and lymph vessels and adipose tissue, the adventitia. This layer supports the flexibility of the esophagus and its integration in the thorax [118]. Even though collagen is much more prevalent and forms the predominant fibrous element conferring stiffness and strength to the tissue, elastin is also present in some layers [331].

For the submucosa and muscle layers, the elastin content constitutes up to 10% and 3% of the matrix respectively. There is minimal elastin in the mucosa and adventitia [324]. These elastin fibers typically assume the form of wavy fibers and are less organized than the aforementioned collagen fibers.

From a biomechanical perspective, the esophagus can thus be summarized as an actively contracting multilayered composite structure mainly consisting of the inner mucosa-submucosa layers loosely interacting (soft connective tissue interfacial layer) with two outer muscle layers. This heterogeneity in layer-specific material behavior requires determination of layer-specific tissue characterization for a sound biomechanical understanding of the esophagus' (patho)physiology [325]. Moreover, it motivated our choice for a geometrically five-layered esophagus model, see further section 3.2.2.

3.2 ESOPHAGEAL MECHANICS

3.2.1 Constitutive behavior

The esophagus exhibits, as most other biological soft tissues (see chapter 2), a large deformability, together with non-linear, pseudo-elastic and anisotropic material properties for each of its composing layers [72, 365]. To characterize the mechanical behavior of esophageal tissue, a functional relationship between stress and stretch is needed. As described in paragraph 2.1.1.1.3, anisotropic hyperelastic material properties can be adequately represented constitutively by means of a strain energy function (SEF) [83]. The histological and anatomical features of the esophagus make it evident that the esophageal wall, from a biomechanical point of view, should be treated as a heterogeneous/multi-layered anisotropic composite material [203, 242]. As shown in multiple animal and clinical investigations, each layer is characterized by its own (an)isotropic behavior due to the specific orientation of reinforcing fibers and variations in residual stretch, opening angle, and stress-stretch relationships [72, 118, 205]. Over the past 15 years, multiple research groups have studied the passive response of the esophagus (e.g. [203, 242, 323–325, 331, 369]). However, the neurologically incited active tissue response, which is the most important feature of the peristaltic movement of the esophagus, remains insufficiently studied. Including the active contractile behavior of the smooth (and striated) muscle cells is therefore considered an essential factor to come to a better understanding of the mechanical functioning of the esophagus in physiology and pathophysiology[206].

To overcome the currently missing active material behavior in constitutive esophageal tissue modeling, we propose and apply a general constitutive material model which describes both *passive* and *active* esophageal tissue.

Given that it was recently shown that, compared with a purely phenomenological Fung-type model, a microstructure-motivated model seemed to offer better approximation of the actual behavior of esophageal tissue with even fewer parameters [206], we chose to follow such a microstructure-motivated approach. Consequently, the proposed constitutive model was additively decomposed in three constituents: an isotropic matrix material constituent, an anisotropic constituent attributed to the dispersion of collagen fibers in the tissue and an anisotropic smooth muscle cell constituent. Several research groups have modeled the matrix and fiber constituent through phenomenological [323, 331] or microstructurally-motivated [325, 368] constitutive descriptors. In this study, we chose to model the passive deformational response of the intact esophagus based upon the pioneering work of Gasser et al. in arterial tissue mechanics [89]. The third constituent, related to the smooth muscle cells (and their active contraction), was motivated by Murtada et al.'s model of mechanical smooth muscle cell activation [238]. In their work, the smooth muscle cells (SMCs) were oriented with their longest axes along the contractile direction and evenly distributed along the depth and height of the muscle tissue. Famaey et al. similarly combined Gasser's passive and Murtada's active material model in a cardiovascular setting, studying the stiffness degradation and critical loading regimes during arterial clamping [68].

3.2.1.1 *Invariants*

As discussed in paragraph 2.1.1.1.3, we can describe the tissue's SEF using strain combinations which are invariant under coordinate transformations. We typically use invariants of the right and left Cauchy-Green tensors, denoted $\boldsymbol{C}$ and $\boldsymbol{b}$ respectively, and their isochoric counterparts, denoted $\bar{\boldsymbol{C}}$ and $\bar{\boldsymbol{b}}$ respectively, associated with $\bar{\boldsymbol{F}}$ [329] (see Eq. 1.5). With λ_r, λ_θ and λ_z being the principal distortional stretches in the radial, circumferential and axial direction, the invariants describing the deformation of the isotropic matrix material can be expressed as follows (compare this with Eq. 2.8):

$$\bar{I}_1 = {\lambda_r}^2 + {\lambda_\theta}^2 + {\lambda_z}^2 \tag{3.1a}$$

$$\bar{I}_2 = \frac{1}{2}\left(\bar{I}_1^2 - \left({\lambda_r}^4 + {\lambda_\theta}^4 + {\lambda_z}^4\right)\right) \tag{3.1b}$$

$$\bar{I}_3 = {\lambda_r}^2 {\lambda_\theta}^2 {\lambda_z}^2 \tag{3.1c}$$

while the stretches along the collagen fiber (there are two distinguishable collagen fiber families in the submucosa (section 3.1)) or muscle cell directions are described as follows:

$$\bar{I}_4^{fib} = {\lambda_\theta}^2 \cos^2\alpha^{fib_1} + {\lambda_z}^2 \sin^2\alpha^{fib_1} \tag{3.2a}$$

$$\bar{I}_6^{fib} = {\lambda_\theta}^2 \cos^2\alpha^{fib_2} + {\lambda_z}^2 \sin^2\alpha^{fib_2} \tag{3.2b}$$

$$\bar{I}^{smc} = {\lambda_\theta}^2 \cos^2\alpha^{smc} + {\lambda_z}^2 \sin^2\alpha^{smc} \tag{3.2c}$$

with α^{fib_1}, α^{fib_2}, α^{smc} the angle between the first fiber, the second fiber, the smooth/striated muscle cell respectively and the circumferential direction. To account for the dispersion of collagen fibers along their averaged direction, Gasser et al. [89] proposed the use of the following pseudo-invariants

$$\bar{I}_4^{fib'} = \kappa \bar{I}_1 + (1 - 3\kappa)\, \bar{I}_4^{fib} \tag{3.3a}$$

$$\bar{I}_6^{fib'} = \kappa \bar{I}_1 + (1 - 3\kappa)\, \bar{I}_6^{fib} \tag{3.3b}$$

in which κ is a structure parameter representing the fiber distribution in an integral sense describing its 'degree of anisotropy' (κ = 0 corresponds to an anisotropic non-dispersed fiber state while $\kappa = 1/3$ corresponds to the totally dispersed fiber, and thus isotropic, state). This parameter should be determined from histological data.

3.2.1.2 *Strain energy function*

As the esophageal tissue can be considered nearly incompressible due to the high liquid content of the ground substance [117, 242], we decomposed the SEF Ψ in a volumetric Ψ_{vol} and a deviatoric $\bar{\Psi}$ part:

$$\Psi = \Psi_{vol} + \bar{\Psi} \tag{3.4}$$

The deviatoric part was additively decomposed in the isotropic contribution of the matrix material $\bar{\Psi}_{mat}$, the anisotropic contribution of two families of collagen fibers $\bar{\Psi}_{fib_1}$ and $\bar{\Psi}_{fib_2}$, and the contribution of the smooth/striated muscle cells $\bar{\Psi}_{smc}$.

$$\bar{\Psi} = \bar{\Psi}_{mat} + \bar{\Psi}_{fib_1} + \bar{\Psi}_{fib_2} + \bar{\Psi}_{smc} \tag{3.5}$$

3.2.1.2.1 Volumetric bulk material. As discussed in paragraph 2.1.1.1.4, imposing the nearly incompressible tissue behavior in a finite element analysis (FEA) framework can be done in two ways: using a hybrid/mixed displacement-pressure formulation or by modeling a minimal amount of compressibility. Here, we chose for the second option and decided to characterize the volumetric free energy Ψ_{vol} using the hyperelastic constitutive Arruda-Boyce model, which can be expressed as:

$$\Psi_{vol} = \frac{K}{2}\left(\frac{J^2 - 1}{2} - \ln(J)\right) \tag{3.6}$$

with K being the bulk modulus. To ensure near-incompressibility, the bulk modulus had to be set high enough to ensure the ratio of the bulk modulus to the initial shear modulus K_0/M_0 is large enough. In this study, this ratio was chosen to be equal to 100 [46].

3.2.1.2.2 Non-collagenous ground matrix. The extracellular matrix and randomly organized elastin content is characterized by means of an incompressible neo-Hookean model, i.e.

$$\bar{\Psi}_{mat} = \frac{1}{2} c_{NH} \left(\bar{I}_1 - 3 \right) \tag{3.7}$$

where $\bar{I}_1$ denotes the previously defined first invariant of the isochoric Cauchy-Green tensor, and c_{NH} the Neo-Hookean parameter, which characterizes the matrix's stiffness through its initial shear modulus ($c_{NH} = M_0$). The neo-Hookean material model (Eq. 2.13) is a special case of the polynomial hyperelastic material (also called generalized Rivlin model).

3.2.1.2.3 Collagen fibers. As mentioned in section 1.4.5, soft tissues typically show nonlinear behavior due to the gradual recruitment of (elastin and) collagen fibers (see Figure 1.7). Given that in the esophagus (mostly in the submucosa) these collagen fibers are oriented according to two helical downward winding fiber families, the tissue response is quite anisotropic. This anisotropic behavior is not covered by the elastin matrix constituent in Eq. 3.7 and thus required a seperate anistropic collagen fiber constituent to the microstructurally motivated SEF. The collagen fibers have no strength under compression and can thus only contribute to the SEF when under tension. Due to the high similarity between the submucosal collagen fiber organization in esophageal tissue and arterial tissue (see Figure 3.4), we particularized the collagen's transversely isotropic free-energy contribution for the i_{th} family of collagen fibers following the work of Gasser et al. for arterial tissue [89]:

$$\bar{\Psi}_{fib_i} = \frac{k_1}{2k_2} \exp\left(k_2 \langle \bar{I}_4^{fib'} - 1 \rangle^2 - 1 \right) \tag{3.8}$$

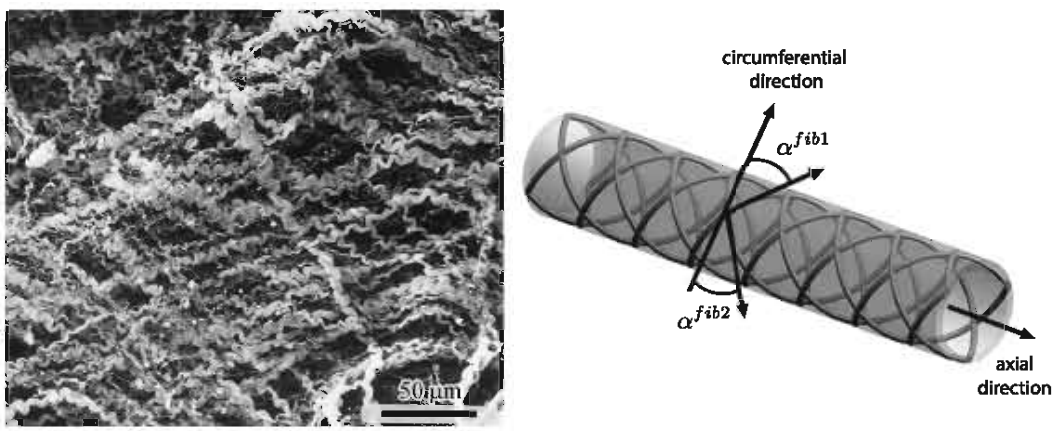

Figure 3.4: Distribution of collagen fibers within the submucosa: (left) scanning election micrograph, (right) schematic representation of fiber arrangement. Image adapted from [242]

in which $k_1 > 0$ is a stress-like parameter and $k_2 > 0$ is a dimensionless parameter to be determined from mechanical tests of the tissue (see section 2.1.2). Here, the Macauley brackets $\langle\rangle$ enforce this constituent to contribute to the SEF only when the collagen fibers are in a stretched state (see also Figure 1.7).

3.2.1.2.4 Smooth and striated muscle cells. The muscle cells form an integral part of the matrix constituent, both in their passive and active state. Smooth and striated muscle cells' contractile units consist of two thin filaments (actin) and one thick filament (myosin) in a side-polar structure with cross-bridges connecting these filaments. These filaments slide relative to each other, causing contraction and relaxation as depicted in Figure 3.5. This relative sliding is accomplished by conformational changes of the cross-bridges, or myosin heads, that connect the myosin to the actin filament.

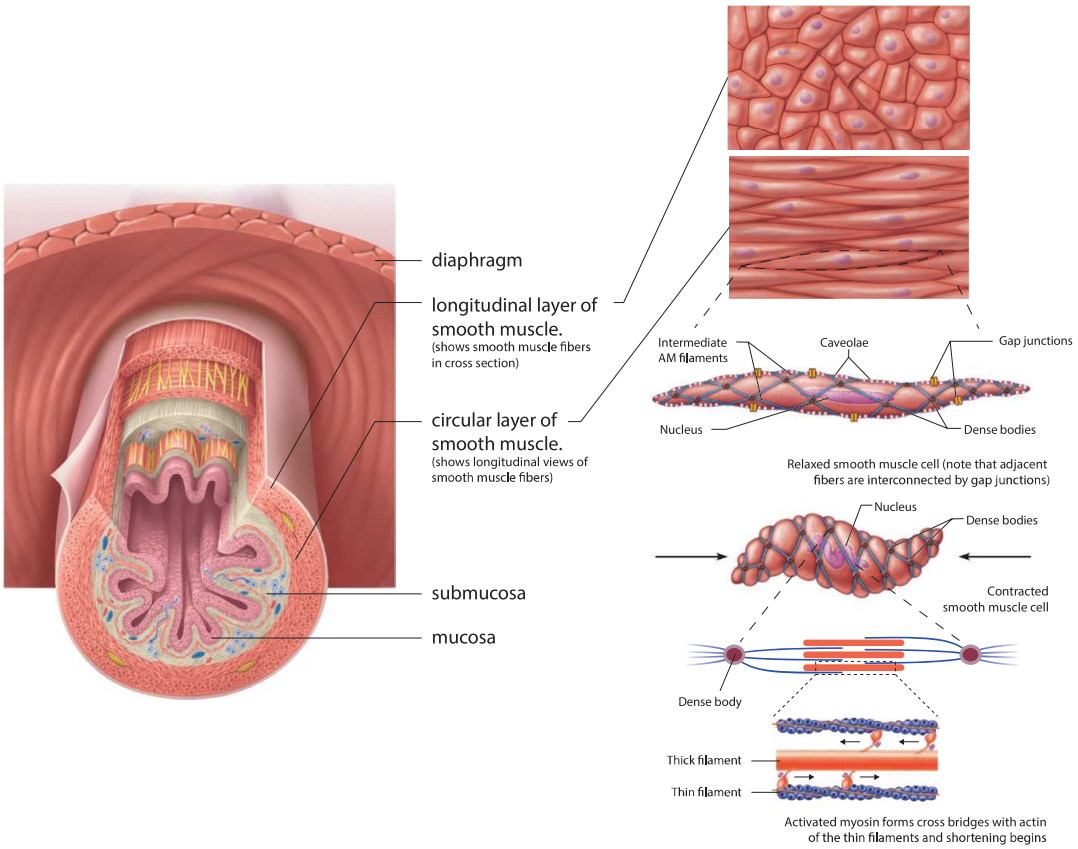

Figure 3.5: Arrangement and microstructure of smooth muscle cells in the esophageal wall. (left) Cross section of the esophagus showing the smooth muscle layers (an inner circular and an outer longitudinal muscle layer) running perpendicularly to each other. (right) Cell-to-filament breakdown of the internal structures in a smooth muscle cell, where intermediate actin-myosin filaments connected to dense bodies harness the smooth muscle fiber's power-stroked pull generated by cycling actin-myosin cross bridges. Images adapted from [220, 305].

These conformational changes are caused by phosphorylation and dephosphorylation of the myosin heads, as a function of the intracellular calcium concentration (see section 2.2) [69, 238]. The muscle cells' contractile units are modeled to be arranged in series, separated by dense bodies forming long contractile fibers inside the muscle tissue (see left panel of Figure 3.8). In addition, they are assumed to contract uniformly and acting as a single unit. Inspired by Murtada et al.'s mechanochemical model [238], the energy of the smooth muscle cells was expressed as follows

$$\bar{\Psi}_{smc} = \frac{1}{2}\mu_{smc}\left(\bar{I}^{smc} + u_{fs} - 1\right)^2 \tag{3.9}$$

where μ_{smc} characterized the stiffness of the actin-myosin filament apparatus and u_{fs} stands for the averaged normalized relative sliding between the actin and myosin filaments. Due to the strong hyperelasticity of the esophageal muscle tissue (ex infra), a quadratic degree did not suffice to constitutively describe the tissue. A quartic degree proved to be more appropriate (ex infra):

$$\bar{\Psi}_{smc} = \frac{1}{2}\mu_{smc}\left(\bar{I}^{smc} + u_{fs} - 1\right)^4 \tag{3.10}$$

3.2.1.2.5 Layer-specific equations. The full three-constituent material model summarized to:

$$\Psi = \Psi_{vol} + \bar{\Psi} = \Psi_{vol} + \bar{\Psi}_{mat} + \bar{\Psi}_{fib_1} + \bar{\Psi}_{fib_2} + \bar{\Psi}_{smc} \tag{3.11}$$

Due to the esophagus's composition, we chose to build up a model consisting of five seperate layers (see Figure 3.8): the mucosa (M), the submucosa (SM), the interfacial layer (IF), the inner and the outer muscularis externae (IME and OME respectively). The stabilizing influence of the adventitial connective tissue was not explicitly modeled but incorporated in the model as described in section 3.2.4.

For the mucosa (M) with its loosely and randomly organized thin collagen fibrils, an isotropic hyperelastic material description suffices. The same assumption was made for the interfacial layer (IF) between the submucosa and the muscle tissue.

$$\Psi_M = \Psi_{vol} + \bar{\Psi}_{mat} \tag{3.12}$$

The submucosa with its thick aligned fibers running helically down the esophagus, was modeled as follows:

$$\Psi_{SM} = \Psi_{vol} + \bar{\Psi}_{mat} + \bar{\Psi}_{fib_1} + \bar{\Psi}_{fib_2} \tag{3.13}$$

Both muscle layers consist mostly out of smooth/striated muscle cells and no cumulative collagen fibers are present, which led to:

$$\Psi_{ME} = \Psi_{vol} + \bar{\Psi}_{mat} + \bar{\Psi}_{smc} \tag{3.14}$$

The outlined constitutive model was implemented in the *Abaqus* user subroutines *UMAT* and *VUMAT*, a family of implicit (*Abaqus/Standard*) and explicit (*Abaqus/Explicit*) subroutines respectively designed to define a material's mechanical behavior, in which the stress state in the local material orientations gets updated at the end of the increment for which it is called. In the implicit subroutine, the material Jacobian matrix $\delta\boldsymbol{\sigma}/\delta\boldsymbol{\varepsilon}$ also needs to be fed back to the FEA solver at the end of each increment. More information on the FEA implementation can be found in section 2.1.1.6.

3.2.1.3 *Evaluation of the constitutive parameters*

The material parameters introduced by the outlined constitutive model need to be calibrated based on specific experimental setups (see section 2.1.2 and section 2.2.2). As we did not have access to any esophageal tissue ourselves, we had to rely on literature to pin-point the values of these parameters. Several studies have characterized the passive material properties of each layer of the esophageal wall [72, 205, 242, 323–325, 331, 367, 368]. Unfortunately, only a fraction of these studies [205, 323, 324, 331] focused on the multiaxial characterization of the passive behavior of esophageal tissue, mostly based on extension-inflation tests. Sommer et al. [325] investigated the heterogeneity of the multi-layered composite esophageal structure by performing (layer-specific) uniaxial tensile, biaxial tensile and extension-inflation tests on ovine esophagi, forming the most complete data set available to date. Based on these data, the constitutive parameters for each layer of our model were calibrated in a non-linear least-squares fitting procedure in which the constitutive biaxial response of the model was compared to the ex vivo results. More specifically, we used *Python* to set up a function that analytically computes the biaxial tensile testing stress response to a certain set of constitutive parameters. Consequently, an error function was set up to compute the square root of

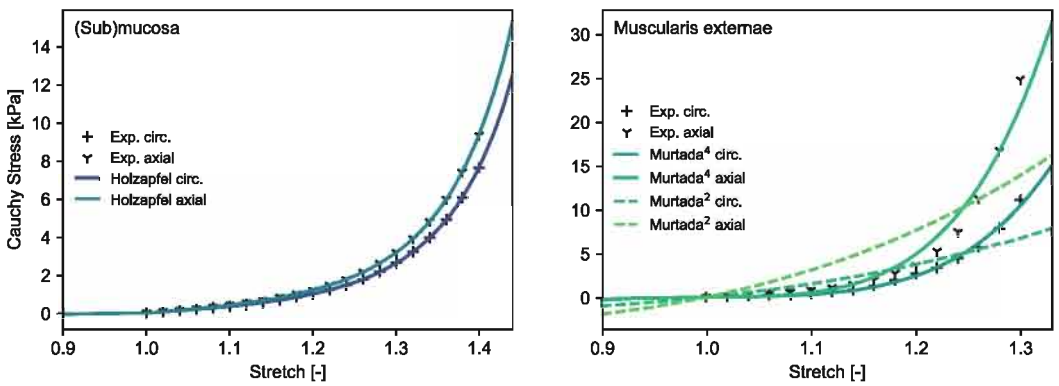

Figure 3.6: Esophageal constitutive material model fit. Comparison of averaged experimental results on ovine tissue samples (extracted from [325]) and the constitutive material model fit.

the sum of the squared differences between the computed stress responses and the experimentally measured stress responses taken from literature. The constitutive parameter set leading to the best fit was found using Python's built-in *SciPy* module to minimize the error function using the Sequential Least SQuares Programming (SLSQP) method [169, 181].

As Sommer et al. studied the combined mucosa-submucosa layer and the full double-layered muscle layer, some assumptions had to be made whilst fitting the constitutive parameters to their averaged experimental results. Focusing on the mucosa and submucosa, the esophageal histology (section 3.1) allowed us to assume a mechanically similar non-collagenous ground matrix for both these layers. All stiffening of the tissue based on the recruitment of the anisotropic distributed embedded wavy collagen fibrils was assumed to be attributed to the submucosa's collagen content. For the loose connective tissue between the submucosa and the muscularis externa, we assumed isotropic hyperelastic behavior one order of magnitude softer than the mucosal layer. Both the circumferential and longitudinal muscle layers were assumed to mechanically behave identically except for their smooth muscle cell orientations. To fit the material parameters to the experimentally measured passive strength of the full (two-layered) muscularis externa slab, we assumed the muscularis externa to behave as a single layer with smooth muscle cells oriented per Sommer et al.'s fitted 'collagen fiber' orientations. Taking into account the different thickness in the IME and OME (see Table 3.2), this led to an angle of 55.3° with respect to the circumferential direction. The fitted constitutive material parameters can be found in Table 3.1 and the fit is depicted in Figure 3.6. As noted before, a

Table 3.1: Fitted constitutive parameters esophageal tissue based on experimental data taken from [325].

	Mucosa (M)	Submucosa (SM)	Interfacial Layer (IF)	Inner Muscularis Externae (IME)	Outer Muscularis Externae (OME)
μ_0 (kPa)	0.09	0.09	0.009	0.17	0.17
α (°)	-	50.4	-	0	90
k_1 (kPa)	-	0.61	-	-	-
k_2	-	1.4	-	-	-
κ	-	0.001	-	-	-
μ_{smc} (kPa)	-	-	-	14.2	14.2
u_{fso}	-	-	-	0.1	0.1
a_0	-	-	-	0.5	0.4
c (mm/s)	-	-	-	80	80
ΔL	-	-	-	40	40
t_0 (s)	-	-	-	0.25	0

second-degree muscle cell invariant dependency of the strain energy function proved inadequate to describe the strong hyperelastic behavior of the muscle cells. The aforementioned quartic muscle cell invariant dependency strain energy potential model resulted in a better fit.

3.2.2 Geometry

The esophagus models present in literature are always represented with simple axisymmetric tubular sections to easily incorporate residual and in vivo stresses in the model [170, 180, 204, 370, 371]. However, the output of such FEA models depends heavily on the assumed geometry. Liao et al showed significant circumferential stress and strain variation due to the irregular esophageal geometry, demonstrating the need to model the esophagus as (at least) a two-layered system based on its real 3D geometry [203].

Hence, a thoracic CT acquisition of a 69-year-old male patient suffering from a malignant esophageal tumor (6cm long circumferential esophageal carcinoma 25cm below the denture line) was collected and segmented using *Mimics* (Materialise – Leuven, Belgium), see Figure 3.7. Based on the histology (see Figure 3.3 and section 3.1) and the proposed constitutive material model (section 3.2.1), the esophagus model consists of the aforementioned five layers. The image resolution did not allow for separate segmentation of each layer, so a cross-sectional layer distribution of clinically measured layer thicknesses (see Table 3.2) was morphed inside the discriminable patient-specific esophageal vessel geometry (in plane CT resolution was 0.717 mm,

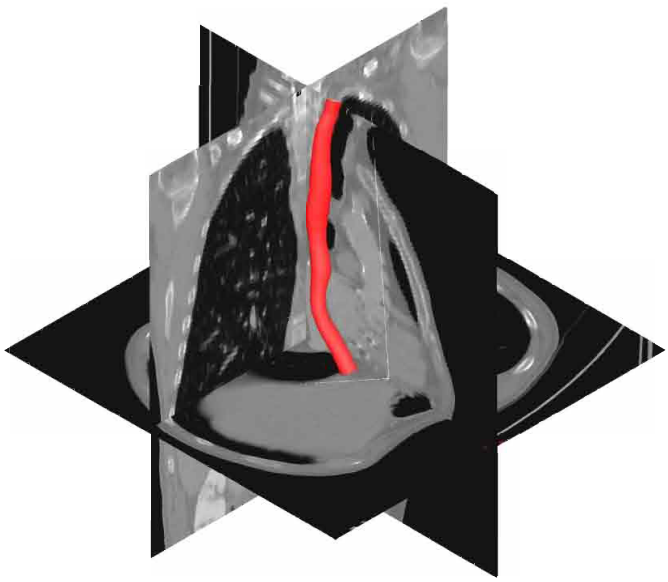

Figure 3.7: Segmentation procedure performed in *Mimics* to delineate the patient-specific esophageal tube geometry of a 69-year old man who has a 6cm long circumferential esophageal carcinoma starting just above the aortic arch.

Table 3.2: Thickness of each esophageal layer: clinical data [278] and data used in our model. (NA: not available)

Thickness (mm)	Mucosa (M)	Submucosa (SM)	Interfacial Layer (IF)	Inner Muscularis Externae (IME)	Outer Muscularis Externae (OME)
Clinical data		1.85	NA	0.55	0.49
Geometrical model	0.1	1.0 ± 0.75	0.1	0.55	0.49

with a 5.0 mm slice thickness). In more detail, the mean layer thicknesses shown in Table 3.2 and the inner lumen radius of around 7.0 mm were scaled such that each geometrical cross-section matches the segmented local esophageal cross-section diameters which were deduced using the Voronoi diagram method of the open-source *Vascular Modeling ToolKit* (VMTK; www.vmtk.org). This image-proportional scaling leads to changing layer thicknesses and varying inner lumen and outer wall diameters throughout the geometrical model. The average outer esophageal wall diameter averaged around 13mm, which leads to an inner lumen radius around 3.5mm. The lumen wall can then stretch to a 20-to-30mm-diameter when passing a food bolus [185]. These geometrical operations and discretizations were performed in *pyFormex*, our in-house developed geometrical modeling and FEA pre- and post-processing toolkit (see section 1.4.6).

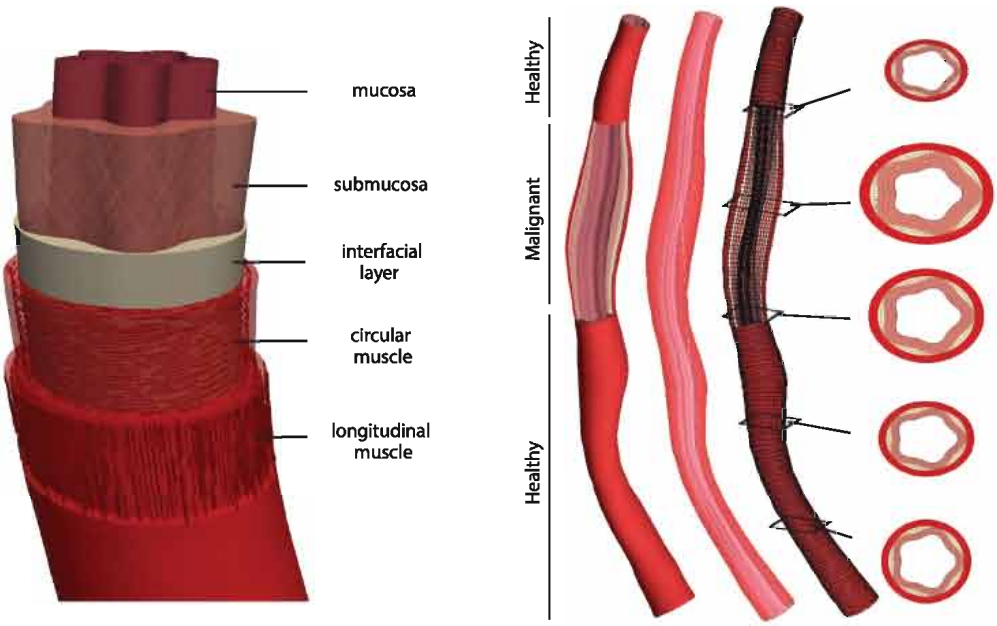

Figure 3.8: Patient-specific esophagus model: (left) detailed histology-based layer buildup and (right) detailed representation of the introduced patient-specific 6cm long pathological circumferential wall thickening, starting just above the aortic arch.

The final geometrical model is depicted in Figure 3.8. Given that these layer thicknesses were measured in the resting state with the esophageal lumen minimally dilated by the intruded catheter, a model based on these dimensions corresponds to an esophagus at rest [278]. The submucosal layer consists of two helically arranged families of collagen fibers with a mean fitted orientation of 50.4° (see Table 3.1). In the inner and outer muscle layer, the smooth muscle cells are oriented in the circumferential and longitudinal direction respectively (see Figure 3.8(left)). Given that the patient was suffering from a malignant esophageal tumor which caused local structural changes in the esophageal tissue, this local tissue remodeling had to be incorporated in the geometrical model. In consultation with the clinician, the submucosal tissue in the malignant zone was modeled 100% thicker than in the healthy zones due to the carcinoma's malignant tissue proliferation [347], as can be seen in Figure 3.8(right). A mesh sensitivity study showed the need for 160,000 hexahedral elements to end up with an accurate, yet computationally efficient *patient-specific esophageal wall model.*

3.2.3 Buckling

Even though the mucosa-submucosa is very stiff in extension, it can hardly sustain any compressive or bending loads [118]. Consequently the (sub)mucosa even buckles at the *bonded* no-load state where no active muscle contraction (only a basal tone) or external pressure acts on the tissue, as can be observed in Figure 3.9. As this buckling will greatly influence the internal stress-strain distribution of both the mucosa-submucosa and the muscle layers, we need to account for its effect by incorporating the buckled

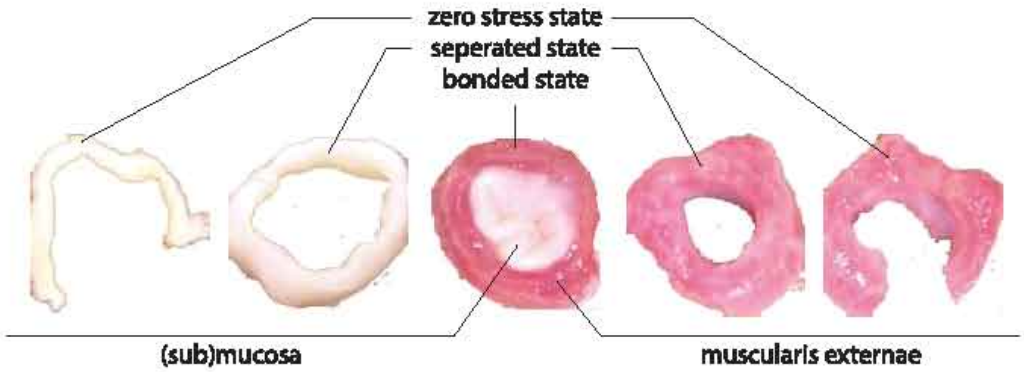

Figure 3.9: Experimental evidence of buckled state (sub)mucosa and the radial mismatch between the (sub)mucosa and the muscularis externae layers in the porcine esophagus. The annotation clarify the difference between the described *bonded* (no-load) state, the *separated* (no-load) state and the full zero-stress state. Images reproduced from [370].

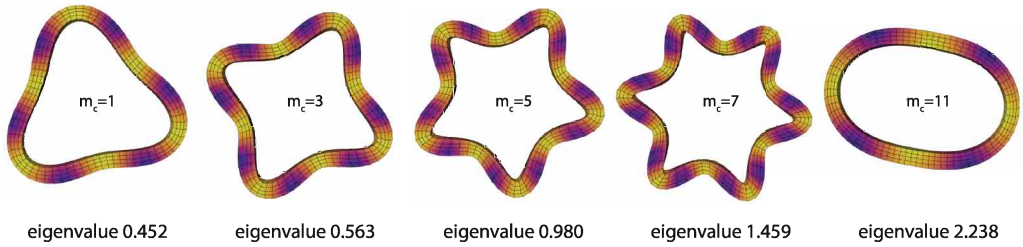

Figure 3.10: Some perturbation 'loads' and corresponding buckling modes of the mucosa-submucosa: selected results of the linear eigenvalue buckling analysis run in correspondence with [371] on a mucosa-submucosa slice following the constitutive behavior described in section 3.2.1 and Table 3.1 and the dimensions defined in Table 3.2 (the color plot represents the relative corresponding displacement from minimal (dark purple) to maximum values (light yellow) for each shown buckling mode.

configuration and the corresponding residual stresses (compressive for the mucosa-submucosa, tensile for the muscle layers, see section 3.2.4).

To incorporate mucosa-submucosa buckling, we followed Yang et al.'s approach in which a linear eigenvalue analysis was run in *Abaqus/Standard* to estimate the critical buckling load and the corresponding buckling modes [371]. Therefore, we developed a circular esophageal (mucosa-submucosa only) slice based on the dimensions in Table 3.2 which we took as the base state. Applying a radial perturbation of 1.0mm (radial mismatch between muscle layer and (sub)mucosa in the *separated* state seen in experimental observations [370]) led to the buckling modes (eigenvectors) and corresponding perturbation 'loads' (eigenvalues) shown in Figure 3.10. Since the actual experimentally measured mismatch between the mucosa and the muscle was around 1.0mm and the same radial perturbation has been set as the reference perturbation 'load', the buckling mode with eigenvalue closest to 1 was chosen: $m_c = 5$. For that reason, the 5-folded buckling mode pattern coupled with this buckling mode was incorporated as a geometrical imperfection in the previously described geometrical patient-specific model (see Figure 3.8).

3.2.4 In vivo stress state

During the in vivo CT acquisition used to set up the patient-specific esophagus model, the esophageal tube functions under in vivo loading conditions. Intrinsically, the model thus presents itself in an *in vivo stressed state*, which can be decomposed into load-induced and residual stresses. First, the esophagus constantly performs under luminal pressures which amount to 7.5mmHg on average [117, 228, 229, 243]. Second, even in a no-load state, residual (both circumferential and axial) stresses are present in the tissue

(see section 2.1.1.5). Circumferentially, the diameter mismatch (ex supra) between the *bonded* no-load state and the *separated* no-load state causes the muscle layer and the mucosa-submucosa layer to be in residual tension and compression respectively, in the *bonded* no-load state [119] (see Figure 3.9). Axially, the esophagus is observed to shrink by about 20% after being excised out of the body [203]. In order to avoid an inaccurate assessment of the mechanical behavior of esophageal tissue in our patient-specific model, we need to incorporate this in vivo stress state into the model.

For simple axisymmetric slice models (e.g. [204, 370, 371]), the inclusion of such a stress state into the model is relatively simple because the model can be build up from its completely stress-free state. By starting from the layer-separated, cut open (radially and axially), no-load geometry, these models incorporate all residual and load-induced stresses by performing geometrical operations to close, reassemble, pull and eventually load the slice. For the in vivo imaging deduced patient-specific 3D models however, nor the unloaded state, nor the cut open, nor the layer-separated geometry of the tissue is known. Therefore, the inclusion of an in vivo stressed state in such models is a lot more challenging, which explains why, to the best of the authors' knowledge, this has not yet been attempted for full organ patient-specific gastro-intestinal (GI) soft tissue models.

In a classical mechanical *forward* problem where the reference configuration is the undeformed stress-free configuration, the equilibrium equations in section 1.4.1 are solved to compute the stress state $\boldsymbol{\sigma}$ corresponding to a certain deformation $\boldsymbol{u}$ caused by loading the solid body. To solve for the in vivo stress state, we however need to solve an *inverse* problem. Here, the stress state in its deformed state needs to be determined given the deformed configuration and the loads causing this deformation. The undeformed stress-free configuration, and thus the corresponding deformation field $\boldsymbol{u}$ are unknown. Multiple methodologies have been proposed to solve this inverse problem over the last decades. These methodologies can be categorized as iterative and direct methodologies (see also chapter 8).

Here, we chose to compute the in vivo stress state based on the Backward Incremental method (BI) proposed by De Putter et al. [54]. In short, the BI method is an *iterative* approach that starts from the load-deformed geometry to find the internal stresses under a given load. Convergence is reached when the resulting stress state in the image-deduced (and thus deformed geometry) is in equilibrium (section 1.4.1) with the applied load, leading to no further displacements.

This methodology was implemented by setting up a *Python*-based wrapper program around *Abaqus* which continuously sets up, runs and

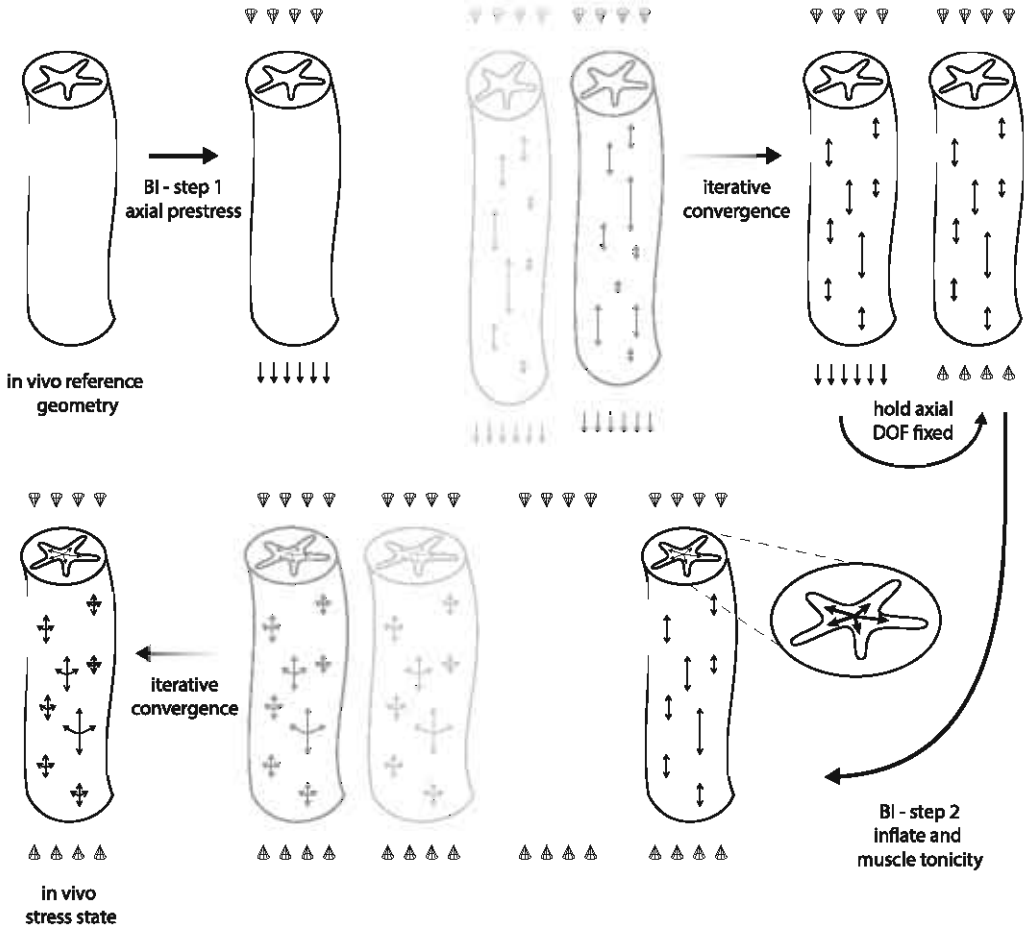

Figure 3.11: Schematic describing the double Backward Incremental (BI) approach to compute the in vivo stress state of the patient-specific esophagus. In the first BI step, we iteratively approached the in vivo stress state induced by the axial prestress only. Holding the axial degrees of freedom of the luminal ends fixed after convergence of this first BI step, we started the second BI step. In this step, we gradually built up the luminal pressure on the esophagus and activated the internal muscle tonicity (not explicitly illustrated in the schematic) to iteratively converge to the complete in vivo stress state.

post-processes iterative computations of forward (implicit) computations to iteratively update the initial stress state until convergence is reached. In more detail, the residual and load-induced stress state was computed in two main steps as shown in Figure 3.11. We first applied an axial prestress (leading to $\lambda_z = 1.25$) to the distal cross sectional boundary of the model while fixing the proximal cross sectional boundary. The axial load was smoothly increased in 10 steps and kept constant afterwards. Next, the load-induced and circumferential residual stress state was incorporated by performing a second BI calculation with altered loads and boundary conditions. At the inner surface of the esophagus, both the pressure and the muscle layer tone were simultaneously increased to 7.5mmHg and $u_{fso} = 0.1$ (see Table 3.1) respectively in 20 steps and kept constant afterwards. This time, only radial

displacement was allowed at both the proximal and distal boundaries. The itertively updating stress field started from the axially prestressed esophagus from the first BI step which cannot relax because no axial displacement was allowed. The second BI-inflate/tone step resulted in the *in vivo* stresses in the geometry under the aforementioned circumferential and axial prestress and an in vivo present luminal pressure load.

3.2.5 External tissue support

The stabilizing influence of external tissue (the adventitia) was modeled by imposing an elastic foundation on the outer muscularis layer surface which models the stiffness effects of a distributed support without actually modeling the details of the support. A foundation stiffness equal to 2% of the tissue stiffness was chosen [46].

3.2.6 Peristalsis

During normal esophageal transport, the precisely synchronized circumferential muscle contraction and longitudinal muscle shortening are well-coordinated [229, 277]. In the current model, the sequential muscle activation is implemented by imposing a sliding between the actin and myosin filaments in the same way it would be neurologically incited. To do so, the normalized relative filament sliding parameter u_{fs} was forced to follow a nonuniform muscle activation profile in which the cylindrical muscle fibers shortened 50% and the longitudinal fibers shortened 40%. In a coordinate system where z denotes the distance traveled along the centerline of the esophageal tube starting at the top end with $z = 0$ and the bottom end located at $z = l$ (with l equal to the total length of the esophagus), the implemented nonuniform muscle activation profile can be described as:

$$u_{fs} = \begin{cases} u_{fs0} & t - t_0 \leq \frac{z}{v} \\ u_{fs0} + a(z,t) & \frac{z}{v} < t - t_0 \leq \frac{z+\Delta L}{v} \\ u_{fs0} & \frac{z+\Delta L}{v} < t - t_0 \end{cases} \tag{3.15}$$

in which u_{fs0} denotes the resting state's averaged normalized relative sliding between the filaments (which was set equal to 0.1 accounting for the *bonded* state tone in the muscle cells, see section 3.2.4 [222]), v is the speed of the activation wave, ΔL is the contracting segment's length in the reference coordinate system and t_0 is the initiation time of activation. The circumferential muscle layer's contraction was modeled having a small delay Δt_0 on the longitudinal muscle activation [229]. $a(z,t)$ is the non-uniform activation function, which is defined as

$$a(z,t) = a_0 \cos^2\left(\frac{\pi}{\Delta L} z(t)\right) \tag{3.16}$$

in which a_0 is the implemented contraction and is set equal to 50% and 40% for the circumferential and longitudinal muscle cells respectively. The specified parameter values for modeling the peristaltic contraction can also be found in Table 3.1. Given that the inner luminal pressure varies significantly during peristaltic contractions, it was, for now, ignored during the modeled peristaltic contractions.

3.3 RESULTS

3.3.1 In vivo stress state

The in *Python-Abaqus* implemented and applied Backward Incremental method (BI) led to the in vivo stress state depicted in Figure 3.12. Overall, a clear difference in stress state between the mucosa-submucosa and the

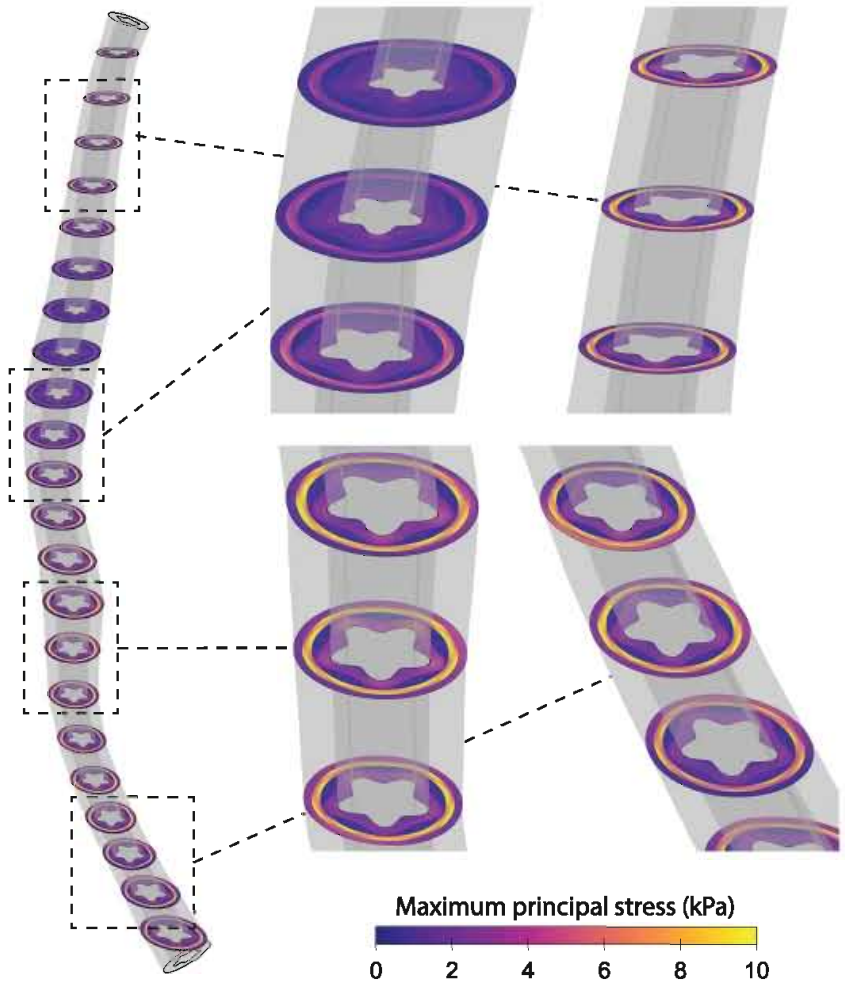

Figure 3.12: In vivo stress state (maximum principal stress) in the patient-specific esophagus, accounting for the luminal pressure load, the *bonded* state configuration of the mucosa-submucosa and the muscle layers and the axial residual stretch experimentally seen upon excising the esophagus.

muscular layers could be noted with the mucosa-submucosa presenting maximum principal stresses ranging between 1.0 and 5.0 kPa and muscle layers presenting maximum principal stresses ranging between 0.5 kPa and 10.0 kPa. The difference in stress magnitudes between the different layers can be explained by the differences in tissue stiffness and the in vivo stress state holding into account the axial prestretch and the *bonded* state configuration of the mucosa-submucosa and the muscle layers. As can be seen in the top right panel of Figure 3.12, the thickening of the mucosal-submucosal tissue in the malignant region clearly has its effect on the local stress measures which are approximately only half as high as the stress levels in the healthy tissue.

3.3.2 Peristalsis

The in Eqs. (3.15) and (3.16) prescribed circumferential muscle contraction and longitudinal muscle shortening led to buckling of the mucosa-submucosa layers and closed off most of the lumen completely. Figure 3.13 depicts this peristaltic motion, together with the local stress and stretch state at multiple points in time. The effect of the small time lag Δt_0 between full longitudinal and circumferential muscle layer activation can be observed in both these plots (e.g. maximum principal stress rises first in the longitudinal muscle layer prior to a rising maximum principal stress in the circumferential muscle layer). In their buckled state, the mucosa-submucosa layers locally present both compressed and stretched regions and the compressive pressures on the mucosal layers led up to 0.860 kPa (maximum of the 95% percentile pressures in the active region at each time step). The smallest and largest circumferential stretches were measured in the submucosa, non-surprising due to its buckling behavior, with circumferential stretches ranging from 0.456 to 1.454 (minimum and maximum of the 5% and 95% percentile circumferential stretch in the active region of the submucosa at each time step). For the circular and longitudinal muscularis externae layers, these stretches ranged from 0.593 to 1.300 and 0.633 to 1.336 respectively. The highest maximum principal stresses were recorded in the circumferential muscle layer with stresses up to 6.030 kPa, followed by the longitudinal muscle layer and the submucosa where stresses up to 3.303 kPa and 0.528 kPa were computed (maximum of the 95% percentile maximum principal stress in each layer's active region at each time step). The effect of the pathologic proliferation of the submucosa in the *malignant region* (see Figure 3.8) was seen in all three aforementioned biomechanical measures. The average maximum buckling contact pressures in the malignant zone, for instance, amounted to 0.159 kPa vs 0.382 kPa in the healthy zone. In like manner, the average maximum principal stress in the circular muscle layer and submucosa totaled 5.418 kPa vs 4.345 kPa and 0.352 kPa vs 0.433 kPa in these layers' malignant vs healthy zones respectively. Moreover, the muscle contraction did not lead to a full 'pinched off' lumen in the malignant zone.

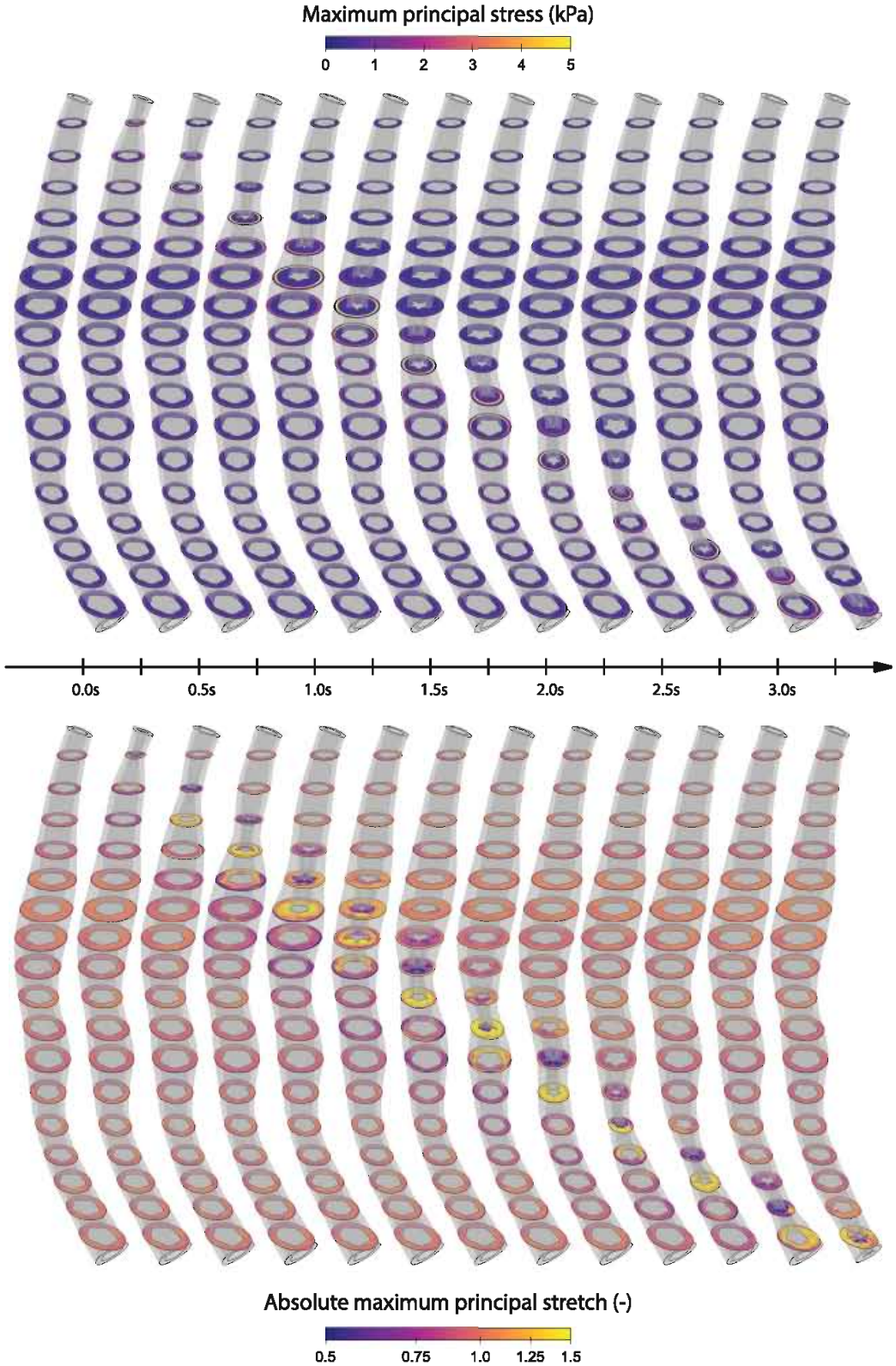

Figure 3.13: Esophageal peristalsis evoked by spatiotemporal activation of the outer longitudinal and circumferential muscle layers at multiple points in time during a regular swallow. The stress state depicts the maximum principal stress in the tissue, whilst the stretch state depicts the absolute maximum principal stretch (log scale).

3.4 Discussion

The esophageal function includes the coordination of food movement, secretion, muscle contraction and circulation. To study this behavior, it is crucial to integrate knowledge at various structural and functional scales and levels [206]. Numerical esophageal models can provide such insights but some shortcomings were still impeding their effective use to better understand the physiological and pathophysiological functioning of the esophagus. This study set forth to overcome these shortcoming and to simultaneously develop a 'virtual esophagus' framework which forms a new and improved standard in gastro-intestinal (GI) structural finite element analysis (FEA).

Studying the current shortcomings in esophageal FEA, we first need to consider the constitutive description of esophageal tissue. Most of our current biomechanical insights in tissue behavior originate from Gregersen et al. who launched the incentive to develop appropriate constitutive equations of gastrointestinal tissue to overcome the limitations faced by simplified analytical models on food transport or mucosal buckling [200]. Over the last 15 years, numerous research groups have focused on experimental testing, calibration and validation of constitutive equations and the tissue-specific material parameters of the esophagus [203, 242, 323–325, 331, 369]. Most recently, Sokolis et al. [324] characterized the passive multiaxial mechanical response of rabbit esophagi using Fung's SEF framework as did Sommer et al. [325] for ovine esophagi using Gasser, Ogden and Holzapfel's well-known three-dimensional microstructurally based SEF [89]. Even though these models seem to accurately capture the tissue's passive behavior, the esophagus is an active organ. Looking at current literature, muscle contraction - when included - has always been implemented by imposing external displacement- or load-based boundary conditions on a passive muscle layer [370, 371]. Passive constitutive material models fail to grasp the esophagus' food transportation function correctly. In fact, Gregersen et al. stated that the effect of the zero-stress state on the physiology of the esophagus may not be obvious until the full Hill model [135], which connects the active and passive tissue elements together, is analyzed [117]. Completing this interaction between passive and contractile elements has been declared as the most important future work.

Second, to the best of our knowledge, the esophagus models present in literature have always been represented with simple axisymmetric tubular sections to easily incorporate residual and in vivo stresses into the model [170, 180, 204, 370, 371]. However, the output of these FEA models depends heavily on the assumed geometry. Liao et al [203] showed significant circumferential stress and stretch variation due to the irregular esophageal

geometry, demonstrating the need to model the esophagus as (at least) a two-layered system based on its real three-dimensional geometry.

Third, it is well known that the esophagus exhibits (sub)mucosal folding to favor its normal function. In vivo surface folds at the luminal surface caused by the compression of the inner (sub)mucosa layer and the passive stretch and tonic contraction of the outer muscle layer greatly reduce the contractile force that the muscularis externa needs to exert to keep the gastrointestinal lumen closed [117]. This behavior has a large effect on the computed stress-stretch behavior of the tissue and should therefore be included in the framework. The buckling pattern can be theoretically computed, and even though it has been included in smaller axisymmetric slice models [370, 371], to date it had not been implemented in a full esophagus model.

To deal with and overcome the aforementioned pitfalls which would lead to erroneous FEA computed stress and stretch distributions, this study proposed and implemented a general constitutive equation which incorporated the active contractile behavior of the striated and/or muscle cell behavior in the esophageal wall. Layer-specific constitutive parameters were calibrated based on experimental passive tensile testing data of ovine esophagi [325]. A non-axisymmetric pathologic 3D patient-specific esophagus model was developed and a linear eigenvalue buckling analysis, proposed by [371], determined the incorporated buckling pattern. The calculated critical buckling mode number which led to the incorporation of 5 folds into the geometrical model matches the 4 to 6 folds range calculated and typically seen in porcine and human samples [289, 370]. The difference in critical buckling mode (6 folds versus 5 folds in this study) with [371] can be explained by the difference in material stiffness and thickness of the inner mucosa-submucosa layer. Finally, using a backward incremental method, we corrected for the in vivo stress-state of the image-deduced esophagus model.

A spatiotemporal activation of the muscle layers, leading to simulated peristaltic contractions, showed the power of the developed framework to numerically model human esophagi, especially whilst comparing local biomechanical phenomena. The acquired quantitative measures of the spatiotemporal variations in compressive mucosal contact pressure and in esophageal intraluminal stress and strain distributions can explain why bolus transport is impaired in patients suffering from certain disorders. More specifically applied to the studied patient, the inclusion of the carcinoma-induced proliferation of submucosal tissue in the patient-specific model (see Figure 3.13) led to decreased contact pressures on the inner lumen surface, higher stresses in the muscle layers and incomplete lumen closure, showing a decreased *downward force* on a potential (not explicitly modeled) food bolus.

Mechanical forces are a major determinant of tissue behaviour and are likely the single most important factor influencing growth and remodelling

of tissue. An understanding of this relationship is important in deciphering how the gastrointestinal tract responds and adapts to changes in the physical environment [116]. Consequently, biomechanical metrics such as the local stretch and stress distribution in the tissue are of key interest for describing the tissue's (patho)physiology and to describe diseases caused by structural remodeling of the esophagus, e.g. achalasia and systemic sclerosis [201]. For example, it was demonstrated that stretch is a potent stimulus for gastrointestinal mechanoreceptors rather than increased transmural pressure [116]. Unfortunately, direct experimental methods for a full three-dimensional assessment of regional stress and stretch states are not available. Nonetheless, numerical soft tissue models provide an interesting means to describe the structure-function relations appropriate to multiple spatial and temporal domains and to associate the tissue behavior at one level to a more detailed description of structure and function on adjacent levels. Such numerical finite element models are only effective when the anatomical site under consideration is correctly described in a morphometric sense, when these models are combined with appropriate loading and boundary conditions, and when the used constitutive models are capable to describe the tissue's mechanical response. As stated by Liao et al., more insight into swallowing disorders in corroboration with physiological and pathological experimental data requires highly sophisticated anatomically and physiologically accurate virtual esophagus models [206]. In that sense, this work comprises an important step forward through overcoming the lack of patient-specific esophagus models, which incorporate active tissue behavior, realistic buckling of the inner mucosa-submucosa layers and the in vivo stress state. As discussed in section 3.5, these models should be further developed to fine-tune the modeled esophageal tissue behavior and to validate the numerical results with 4D in vivo imaging data. Eventually, such models will serve as a basis to assess remodeling processes of esophageal tissue in diseased states and to run computer simulations of surgical interventions and medical device applications (see also chapter 4). Moreover, in combination with pain perception threshold data [222], (regional) critical stress states can even be potentially correlated to specific thresholds being felt through sensory innervation.

3.5 FUTURE WORK

Continual development of increasingly sophisticated esophagus models enriched by both ex vivo and in vivo data provides opportunities to better characterize esophageal disorders. The in this study used dataset [325] for the constitutive material fit comprises, to the authors' knowledge, the most complete multiaxial study on esophageal tissue to date. However, it should

be noted that a high variability in stiffness can be found in different studies focusing on the passive behavior of esophageal tissue [323, 325, 368] which is dependent on the experimental protocol, the tissue origin (e.g. ovine, porcine, rat) and tissue preparation. As this study set forth to develop patient-specific esophagus models, we have to note that Gregersen et al. [121] have recently shown that the human esophageal properties and function deteriorate with age (the wall becomes stiffer and the maximum active esophageal muscle tension deteriorated after the age of 40 years). The proposed constitutive material parameter fit was not tuned and/or scaled to the considered patient's esophageal function or age, but based on the passive multiaxial study of ovine tissue by Sommer et al. [325]. More quantitative data (being it through elaborate in vitro experimental testing on more esophageal tissue samples and/or combining in vitro experimental data with in vivo imaging based compliance data for example) is needed to personalize the material behavior of these tissues. Moreover, esophageal muscle fibers are characteristically aligned along multiple spatial axes. For accurate identification of the 3D spatial distribution of the esophageal fiber network, the microstructure of the esophagus has to be inspected in much greater depth using modern imaging modalities such as confocal microscopy or nuclear magnetic resonance imaging of proton diffusivity [105, 364]. Due to a lack of experimental data, we were also necessitated to assume homogeneous layer-specific constitutive parameters throughout the whole esophageal tube, even though we can expect a stiffer response for the upper third of the esophageal tube where the muscle tissue mostly consists of striated instead of smooth muscle tissue [222]. Further, like most other biological soft tissues, the esophagus is characterized by time-dependent mechanical behavior such as layer specific stress-relaxation [369] and anisotropic stress softening [167, 207] properties. The visco-hyperelastic constitutive models developed and successfully adopted for blood vessel tissue [145, 242] are needed in future constitutive models of the esophagus [206].

Here, we chose to introduce muscular contraction using the *active fiber* approach as discussed in [112]. This approach allowed for a first crude phenomenological tissue-level approximation of the active esophageal tissue behavior during peristaltic contractions. The relative filament sliding parameter u_{fs} allowed us to impose a well-coordinated 'fiber activation' (see Eqs. (3.15) and (3.16)) leading to active force generation. Even though the amount of active tension buildup in Eq. 3.10 is dependent on the amount of stretch in the smooth/striated muscle cell direction, it does not describe the (typically parabolic) muscular length-tension relationship as depicted in Figure 2.10. In order to equip future models with this behavior, more experimental characterization of active esophageal muscle tissue (through ex vivo or in vivo isometric and/or isotonic contraction experiments) should

be applauded [336]. Eventually, such data can even be used to study the full multiscale process controlling active tone and contractility. More specifically, Murtada et al. recently proposed a multiscale (tissue, cellular, filament to myosin motor level) evolution law for the relative filament sliding which is dependent a.o. on the activation of the SMC myosin motors and the accompanying myosin-actin cross-bridge kinetics, the myosin filament structure, the filament lattice spacing which is dependent on the myosin length, the filament overlap, etc. [237] which, once experimentally calibrated for active esophageal tissue, could form an interesting approach to improve our understanding of esophageal motor disorders.

Even though the in vivo stress state of the current models introduced the stresses induced by the luminal pressure load, the *bonded* state configuration of the mucosa-submucosa and the muscle layers and the axial residual stretch experimentally seen upon excising the esophagus, the stress induced due to the circumferential residual stretches seen upon performing a radial cut through the separated layers is not accounted for. As previously mentioned, including these residual stresses is more challenging in patient-specific full organ models compared to simple (axisymmetric) slice models. Therefore, future work should explore the strategies discussed in section 2.1.1.5.

CHAPTER 4

ESOPHAGEAL STENTING

In this chapter, we first describe the stent-related complications that currently prevent esophageal stenting of becoming a recommended treatment strategy for multiple benign esophageal disorders. To develop improved esophageal stents, we need more mechanistic insights in the interaction between a specific stent design and the patient-specific esophagus. Therefore, we developed a numerical model capturing the mechanical behavior of a gradually degrading bioresorbable polymeric braided fiber stent. This model was calibrated and validated in corroboration with an in vitro degradation study where both the complete stent and seperate stent fibers were mechanically tested in radial compression tests and tensile tests respectively at multiple points in time. Subsequently, this virtual stent was virtually implanted in the 'virtual esophagus' developed in chapter 3. This combined framework allowed us to compute the biomechanical interaction between tissue and device and study the esophageal stenting procedure in more detail [*].

4.1 INTRODUCTION

As mentioned in the previous chapter, several gastro-intestinal disorders originate from problems in the esophagus. Dysphagia is a frequently encountered problem and leads to a decreased quality of life due to malnutrition,

[*]This chapter is based on M. Peirlinck, N. Debusschere, F. Iannaccone, P. D. Siersema, B. Verhegghe, P. Segers, and M. De Beule, "An in silico biomechanical analysis of the stent–esophagus interaction", *Biomechanics and Modeling in Mechanobiology*, vol. 17, no. 1, pp. 111–131, 2018

weight loss and aspiration. Most frequently, dysphagia is caused by strictures (see Figure 4.1), achalasia and esophageal leakage. Malignant strictures are generally caused by primary esophageal cancer, but can also be caused by a malignant mediastinal mass or lung cancer leading to extrinsic compression of the esophagus [138]. Benign strictures can be caused by gastroesophageal reflux disease, congenital anomalies, radiotherapy, ablative therapy, external/foreign trauma or corrosive ingestion. Stricture treatment strategies typically involve dilation (stretching) of the esophagus, but quite often patients do not experience any meaningful improvement after endoscopic dilation with bougies or balloons [266]. Achalasia involves incomplete lower esophageal sphincter (LES) relaxation, increased LES tone, and lack of peristalsis of the esophagus. Here, the therapy focuses on the relaxation or mechanical disruption of the esophagus and/or the LES, which can be done in multiple ways (e.g. Heller myotomy involving an endoscopically performed longitudinal cut along the LES, endoscopic botulinum toxic injections to temporarily paralyze the LES muscles, endoscopic balloon dilation to stretch and slightly tear some muscle fibers in the LES). Similar to the clinical management of strictures, most achalasia treatment strategies only have temporary effects and need to be repeated multiple times. Esophageal leakage can be subdivided into three forms, benign esophageal perforations (iatrogenic and spontaneous), anastomotic leakage after reconstructive esophageal surgery, and fistula [346]. Traditionally, gold standard treatment for an acute esophageal perforation has been operative repair, but less invasive alternatives are preferred [259].

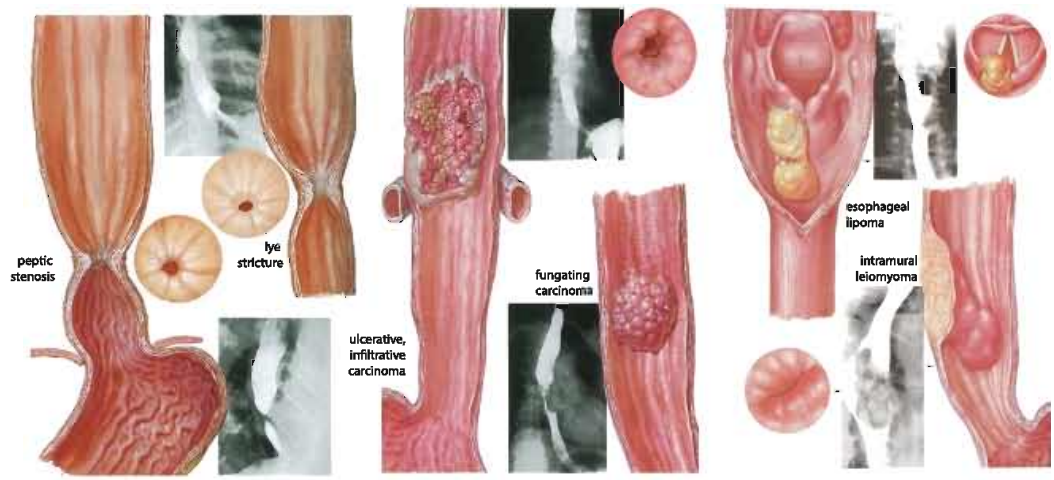

Figure 4.1: Medical illustrations and X-ray examples depicting some common causes for esophageal strictures, from left to right: inflammatory, corrosive, malignant and benign strictures. Images reproduced from [288].

During the last decade, permanent and temporary stent placement has been on the rise as an alternative therapeutic strategy to treat the aforementioned esophageal disorders. Indications for esophageal stenting can be subdivided into two groups. The first group consists of patients suffering from malignant or benign dysphagia (due to strictures or achalasia). These patients require a restoration of the luminal patency of their esophagus. When endoscopic repeated bougie dilation and other endoscopic treatment modalities have failed, an esophageal stent could be considered. The second group consists of patients with leakage from the esophageal lumen into the surrounding tissue. In carefully selected patient groups, a covered esophageal stent may be used to seal the leakage, thereby preventing further contamination of the surrounding tissue [346]. The increasing use of esophageal stents as a treatment strategy was facilitated by continuous technological innovations in esophageal stent design (from rigid, plastic tubes in the early 1980s to partially or fully covered self-expanding metal stents (SEMSs) in the 1990s and self-expanding plastic stents (SEPSs) in the beginning of the 21st century) [266]. All these innovations have led to a multifold of different esophageal stent designs currently available on the market (see Figure 4.2).

Notwithstanding the huge improvements in stent design, esophageal stenting still suffers from migration problems, severe complication rates (e.g. perforations, bleeding, chest pain, nausea, fistula, malpositioning) and

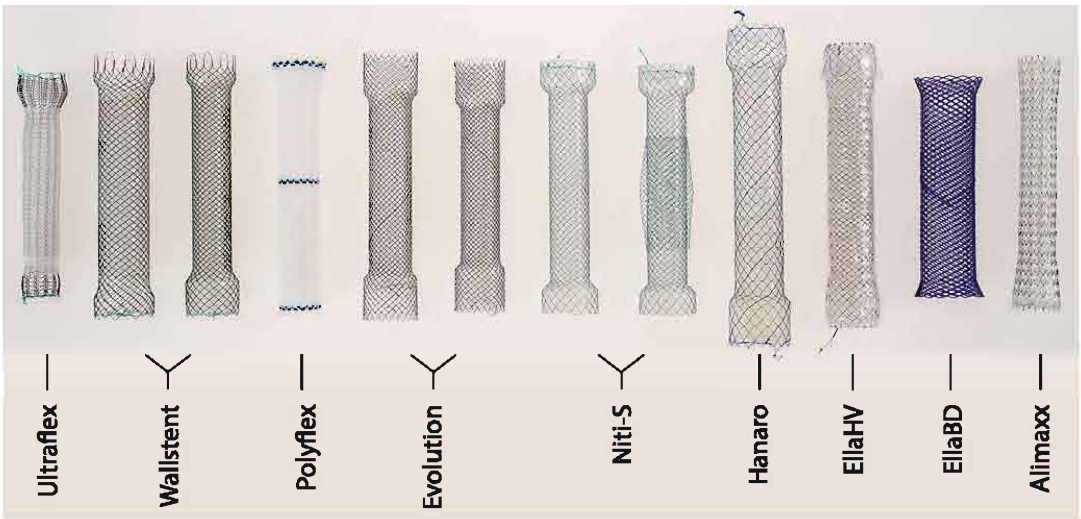

Figure 4.2: An overview of all self-expanding esophageal stents anno 2014. From left to right: the specially knitted *Ultraflex* stent, the small- and large-diameter partially covered *Wallflex* stent; the polyester *Polyflex* stent; the small- and large-diameter braided, partially covered *Evolution* stent; the single- and double-layered *Niti-S* stent; the *Hanaro* stent; the *EllaHV* stent; the braided *EllaBD* stent; and the lasercut *Alimaxx* stent. Image reproduced from [137].

morbidity during stent removal. Consequently, esophageal stenting is still not considered an optimal treatment strategy for benign dysphagia [320]. Apart from the *Polyflex* stent, no other partially or fully covered SEMSs and SEPSs is currently recommended or U.S. Food and Drug Administration (FDA)-approved to treat benign esophageal conditions. The quality of evidence to use esophageal stents in those circumstances is very low and significant improvements in the stent designs have to be made to open up its list of indications. The *Polyflex* SEPS formed the only exception as it is licensed in the United States for use in benign conditions, but given its high risk of stent migration and other adverse events, the production of the Polyflex has been terminated [346].

Bioresorbable esophageal stents form the latest addition to the esophageal stent market. Given that these stents do not require dangerous stent removal procedures, they form a potentially more cost-effective and patient-friendly alternative compared to other permanent stent designs [346]. These stents support or stretch the lumen wall for a certain period of time and gradually degrade afterwards. As the stent does not require prevention of tissue ingrowth, the open-mesh design suffers less from migration issues than the partially or fully covered stent design alternatives. The first bioresorbable esophageal stent, the *EllaBD* stent has recently been introduced in Europe. Since the first study with these bioresorbable stents in 2010 [287], their safety and efficacy has been assessed further [28, 81] which led to the conclusion that these stents are safe to use for benign conditions. However, moderate long-term dysphagia relief scores [28] and low success rates of sequential biodegrable stenting [136] for benign dysphagia relief were also reported. The limited success of these stents can be linked to insufficient radial force and premature degradation. Again, these findings demonstrate the need for improved esophageal stent designs for use in benign conditions.

An optimally designed esophageal stent should be flexible, nontraumatic and have an internal diameter that is large enough to allow normal food passage. Furthermore, placement, repositioning and removal of the stent should be easy, without a risk of stent migration, and without nontumoral and tumoral tissue ingrowth or overgrowth. To get more insight in the association between the stent design and clinical success, Hirdes et al. have performed in vitro evaluations of the radial and axial force of the currently most frequently used commercially available esophageal stents [137]. Their study was the first attempt to postulate the clinical relevance of specific esophageal stent characteristics which proved to be ambiguous based on these ex-vivo measured factors alone.

Most of the available stent designs for esophageal applications are braided wire/fiber stents made of filaments (nitinol wires, stainless steel wires and

(bioresorbable) polymer fibers) interwoven in a crisscross pattern to form a tubular mesh configuration. To assess the mechanical behavior of these stents without extensive in vitro and in vivo experiments for each potential prototype, analytical models have been developed and validated for metallic braided wire stents [49, 165]. Unfortunately, these models are generally restricted to linear elastic materials, simplistic geometries and idealized boundary conditions. Computational models on the other hand allow for more complexity and form an excellent research tool. In contrast to the numerous FEA studies dedicated to the mechanics of balloon- or self-expendable laser cut stents, little attention has been paid to FEA of braided wire/fiber stent designs [48, 175, 376] which is surprising due to their wide clinical application range. Consequently, it was deemed meaningful to extend the 'virtual esophagus' framework developed in chapter 3 with numerical models incorporating the complete mechanical behavior of (bioresorbable) polymeric braided fiber stents (PBFSs). For these stent models it will be important to consider the effect of friction between the thick polymeric stent fibers which has been neglected in existing models (both analytically and numerically) and basically renders them invalid [251].

Combined, the virtual esophagus (chapter 3) and stent model will allow us to virtually deploy a PBFS into a patient-specific esophagus and quantitatively study the interaction between the device and the tissue. Specifically, the complete (stent-esophagus) framework provides insights into the stent's intrinsic mechanical capability to open up the (constricted) lumen (i.e. does the stent have enough radial force to dilate the patient's stricture?), to study the localized stress and distributions prior to (see chapter 3), during and after stent expansion and to compute contact pressures between the device and the esophageal wall, all having their influence on the aforementioned complications for esophageal stenting. Once developed, we anticipate the combined framework to accelerate the quest towards the optimal design of (new) esophageal stents. Given the potential clinical treatment niche that bioresorbable esophageal stents can occupy, this study focused the development of appropriate numerical PBFS models of the aforementioned bioresorbable *EllaBD* stent.

4.2 METHODS

The stent model is based on the bioresorbable esophageal *EllaBD* stent (ELLA-CS, s.r.o., Hradec Kralove, Czech Republic), with the geometry shown in Figure 4.3. Two *EllaBD* stent samples (ref. n° 019-10A-25/20/25-100 and 019-10A-31/25/31-100) with a 20 and 25 mm nominal stent body diameter, 25 and 31 mm nominal stent flare diameter and 100 mm nominal stent length respectively were mechanically tested.

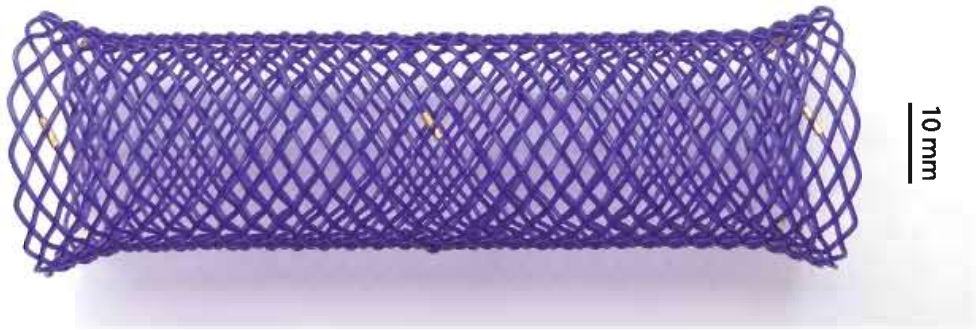

Figure 4.3: The *EllaBD* biodegradable esophageal stent is made of one long single braided fiber made of poly-p-dioxanone, a colorless, crystalline, biodegradable synthetic polymer. Radio-opaque gold markers at each end of the stent and at the mid-point are integrated in the stent design, which allows, according to the manufacturer, an excellent visualization and precise stent positioning (using fluoroscopy). Image courtesy: ELLA-CS, s.r.o., Hradec Kralove, Czech Republic.

4.2.1 In vitro experimental testing stent samples

The *EllaBD* stent is braided from polydioxanone (PDS) monofilaments, the current standard material for biodegradable sutures. This bioresobable polymer does not present itself as a foreign body and thus no adverse immunological responses occur to stents made from this material.

To characterize the stent's mechanical strength, we first performed compression tests measuring the radial force of both stent samples (see Figure 4.4a). The radial force of the stent can be divided into the radial resistance force during compression by the contracting esophageal wall and the chronic outward force the stent exerts during expansion to its original diameter. These forces were measured with an axial force measurement machine (Instron 5940 series) which was equipped with a radial-to-axial stent compression unit from MPT Europe [266]. The stent was placed in the middle of the stent compression unit and with a vertical upward movement of its axial shaft, a unique diaphragm-like crimping head consisting of 8 segments constricted radially without leaving any open gaps. The measured axial forces were correlated to the actual radial forces exerted by the stent by taking the (internal) friction and the virtual work principle into account [266]. The stent was radially compressed to crimp to a diameter of 10mm (compression rate 0.15 mm/s), which translates to a compression ratio of 38% and 31% with respect to the initial outer stent flare diameter (taking the measured fiber thickness of 600 µm into account). This set-up meets the current standards for radial testing methodology [137, 162] and provides much more realistic results to the in vivo situation than any other compression test (e.g. compression between parallel plates or between two semi-cylindrical grooves [251]). Due to the friction between the fibers, the foreshortening

did not completely recover to its initial nominal length. Consequently, the foreshortening recovery ratio (FRR) was measured, depicting the relative difference in nominal stent length before and after each radial compression test (see Figure 4.4b).

Second, the stiffness of the individual *EllaBD* stent fibers was determined in separate tensile tests (Instron 5940 Series) on cut fiber specimens from the 31/25/31-100 stent sample after the radial compression tests of day 0 (see Figure 4.4c). Three specimens (each with length 6.0 cm) were clamped, pre-loaded to 1.5N and consequently pulled until failure. Based on the obtained stress-strain curve data, the Young's modulus of the fibers E (see Eq. 2.1) was determined by averaging the three resulting linear slope gradients. As PBFSs are designed to be used in an elastic regime, measurement of the Young's Modulus E was assumed to suffice to characterize the material strength at a certain time point during the degradation of the stent.

Finally, to study the degradation mechanism and its effect on the mechanical properties, in vitro degradation studies were performed. The *EllaBD* 25/20/25-100 stent and cut *EllaBD* 31/25/31-100 stent fiber specimens were placed in a phosphate buffered solution (pH=7.2) at 37°C (thermostatic batch Julabo, model SW22) during 10 weeks. Every week, radial compression tests and tensile tests as described were conducted on the full stent and stent fiber specimens, respectively. After the first week, we decided to compress the *EllaBD* 25/20/25-100 to a diameter of 9mm, corresponding to 34% of the outer flare diameter, to be more conform with the testing protocol in [137].

Figure 4.4: In vitro experimental testing *EllaBD* stent samples: (a) radial compression tests, (b) measurement of the foreshortening recovery ratio (FRR) and (c) tensile fiber specimen tests at day 48.

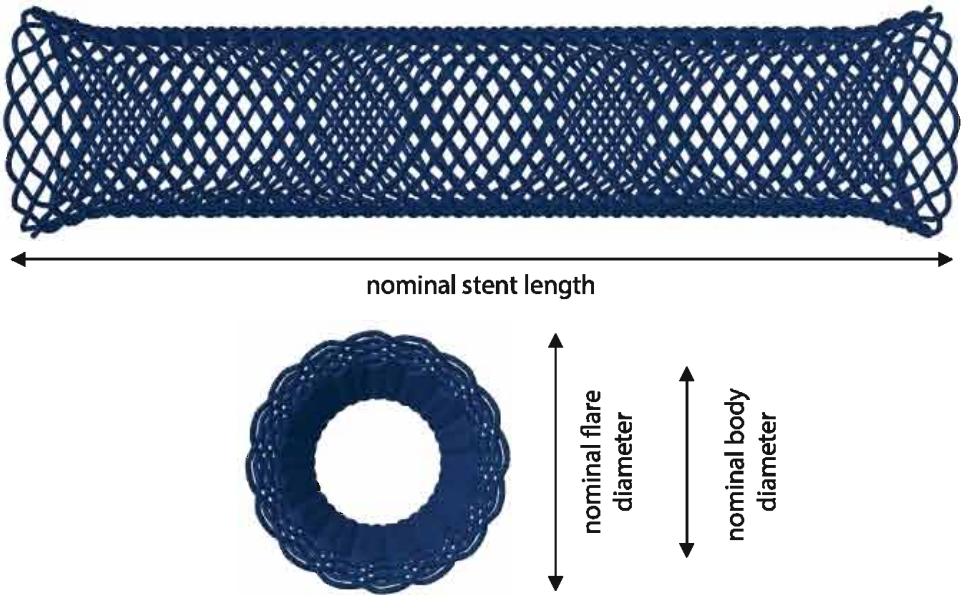

Figure 4.5: Parametrically defined geometrical model reflecting every length, thickness, angle and orientation of the PDS fibers in the actual *EllaBD* stents.

4.2.2 Finite element PBFS model

As depicted in Figure 4.5, a parametric braided fiber stent model of the *EllaBD* stent, geometrically reflecting every length, thickness, angle and orientation of the PDS fibers in the actual *EllaBD* stents [266] was developed using *pyFormex* (Ghent University, Belgium; http://pyformex.org), an in-house developed geometrical and finite element pre- and post-processor (see section 1.4.6). This model was then transformed into a finite element method (FEM) to be processed in *Abaqus-Explicit*. Hall and Kasper [131] compared various methodologies to analyze typical biomedical stent devices within a finite element setting. Based on their analysis, we chose to use B31 elements, being linear 2-node Timoshenko beam elements [46]. These are the most suited elements to end up with a computationally efficient model considering problem size, time and memory requirements without losing accuracy in computed stress and strain distributions. The measured elastic moduli of the fiber samples (ex supra) were used to set the mechanical behavior of the linear elastic stent fibers. By incorporating the changing Young's modulus through time, the model accounted for the stent's degrading mechanical behavior. Following a mesh sensitivity study [266], the stent was modeled using 4 beam elements per fiber crossing. To incorporate the effect of friction between the PDS fibers, the Coulomb friction model was incorporated and different modeling strategies were implemented and studied (incorporating 'Join', 'Hinge', 'Planar' or no connectors, self-contact, etc.). The conditions of the performed in vitro experiments (e.g. boundary conditions, displacement controlled radial loading) were simulated as realistic as possible (ex supra).

Given that the friction between the fibers of a PBFS is nearly impossible to measure experimentally, three possible friction coefficients (FCs) were compared based on literature [175]: FC = 0.1/0.2/0.3.

Both the experimental elongation and radial force measurements during compression and expansion were compared to the numerical results of in vitro bench tests mimicking the performed in vitro tests on the finite element stent model to assess the appropriate amount of friction between the fibers.

4.2.3 Modeling the implantation procedure

The validated PBFS FEM was used to perform a virtual implantation procedure in the patient-specific anatomy taken from chapter 3. The stent implantation was simulated in *Abaqus-Explicit* using a specific user subroutine which prescribes the displacement of a deformable surface. This deforming surface represents the stent's delivery system and the different steps taken to implant the stent device in the patient's esophagus. The PBFS is crimped onto a catheter through contact and bended as if it were endoscopically inserted in the constricted esophagus. Subsequently, the stent is gradually released by pulling back the sheath (the deformable surface) holding the crimped catheter [51]. This virtual procedure is consistent with the Instructions For Use of the *EllaBD* stent. Due to the braided fiber stent design, these stents shorten considerably upon release and the physician is advised to take this into account by releasing the distal end of the stent at least 2 cm beyond the lower margin of the stenosis. An appropriate virtual landing zone has been found iteratively.

4.3 RESULTS

4.3.1 Degradation through time

The in vitro degradation study revealed two different degradation stages of the stent fibers. Figure 4.6 (left) shows the radial resistance and chronic outward force of the stent sample measured at different time points during the degradation process. Figure 4.6 (right) depicts the weekly evolution of the elastic modulus E of the fibers. Each week, E was determined from tensile testing experiments on three different fiber samples as can be seen in the resulting stress-strain curve depicting the strength and the linear elastic stiffness fit at day 14 (Figure 4.6 (right subplot)). The first 5 weeks of the in vitro degradation studies, the radial force of the stent samples remained relatively stable (for clarity, only the average radial force during the first 5 weeks is shown in the left figure), while from week 6-7, the radial resistance and chronic outward force started to decline. By week 8 to 9, the stent fibers became more and more fragile and disintegrated, which can be seen by the

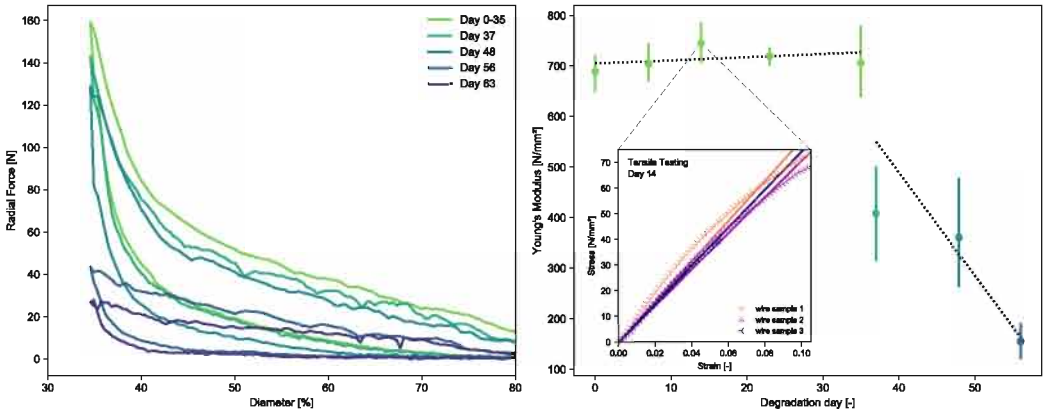

Figure 4.6: In vitro degradation study *EllaBD* stent and stent fibers. (left) Radial force measurements *EllaBD* 25/20/25-100 stent during degradation study. (right) Young's Modulus of the degrading *EllaBD* stent fiber samples. Trend lines show the trend for the two degradation phases of the polydioxanone fibers. (right subplot) Detailed experimental stress-strain curves depicting the strength of three different fiber samples taken out of the thermostatic phosphate buffer solution bath at Day 14. The solid lines represent the elastic linear Young's Modulus fit that was used to calculate the average stiffness at that point in time.

significant drop in radial resistance and chronic outward force (to 29.9% and 18.6% of the initial radial resistance at week 8 and 9 respectively). The same degradation stages can be seen in the weekly evolution of fiber stiffness. Week 5 of the in vitro degradation study can be considered as a tipping point between two degradation phases.

4.3.2 Friction calibration and stent model validation

The developed stent FEM was used to pinpoint the most realistic strategy to incorporate friction into the model. The mechanical behavior of models with 'Join', 'Hinge', 'Planar' or no connector elements, with and without self-contact were compared to the collected experimental results.

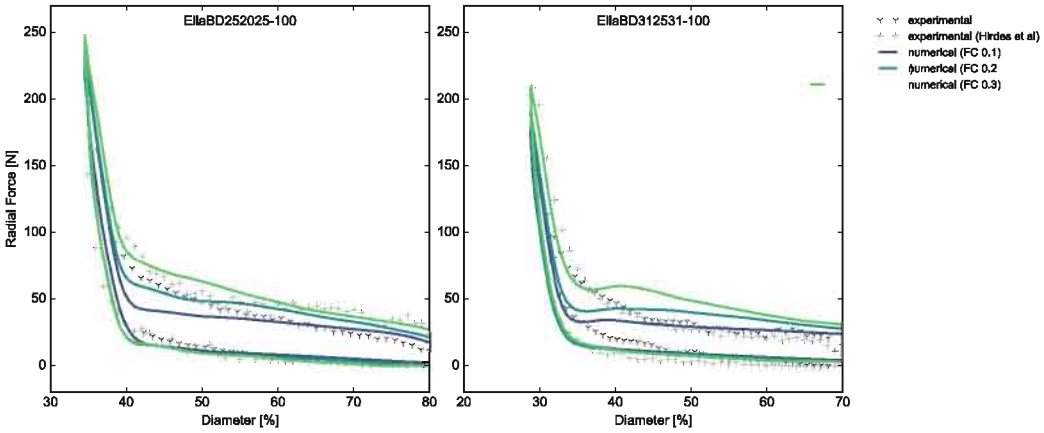

Figure 4.7: Calibration friction coefficient by comparison between experimental and simulation results of the radial force of the *EllaBD* stent samples at day 0.

Table 4.1: Calibration of the friction coefficient by comparison of measured and simulated foreshortening recovery ratios (FRRs) of the *EllaBD*252025-100 stent ($\Delta FRR_{sim/exp}$ reflects the relative difference in elastic recovery between simulation and experiment)

Day	FRR_{exp}	FRR_{sim} - $\Delta FRR_{sim/exp}$ (%)					
		FC = 0.1		FC = 0.2		FC = 0.3	
0	1.258	1.058	84.10%	1.225	97.40%	1.667	132.50%
7	1.277	1.101	86.20%	1.195	93.60%	1.677	131.30%
14	1.272	1.117	87.80%	1.189	93.50%	1.68	132.00%
23	1.226	1.095	89.30%	1.186	96.80%	1.681	137.20%
35	1.205	1.012	83.90%	1.188	98.60%	1.68	139.40%
37	1.188	1.104	92.90%	1.211	101.90%	1.676	141.10%
48	1.176	1.046	89.00%	1.199	102.00%	1.674	142.30%

In the in silico bench tests, 'Join' and 'Hinge' connector elements overconstricted the fiber-crossings degrees of freedom leading to computational models that overestimate the stent's radial strength. In contrast, including no connector elements in the stent's computational model, solely incorporating pure self-contact between the fibers, underestimated the stent's radial strength. Eventually, a combination of 'Planar' connector elements and self-contact captured the mechanical behavior of the PBFS most appropriately.

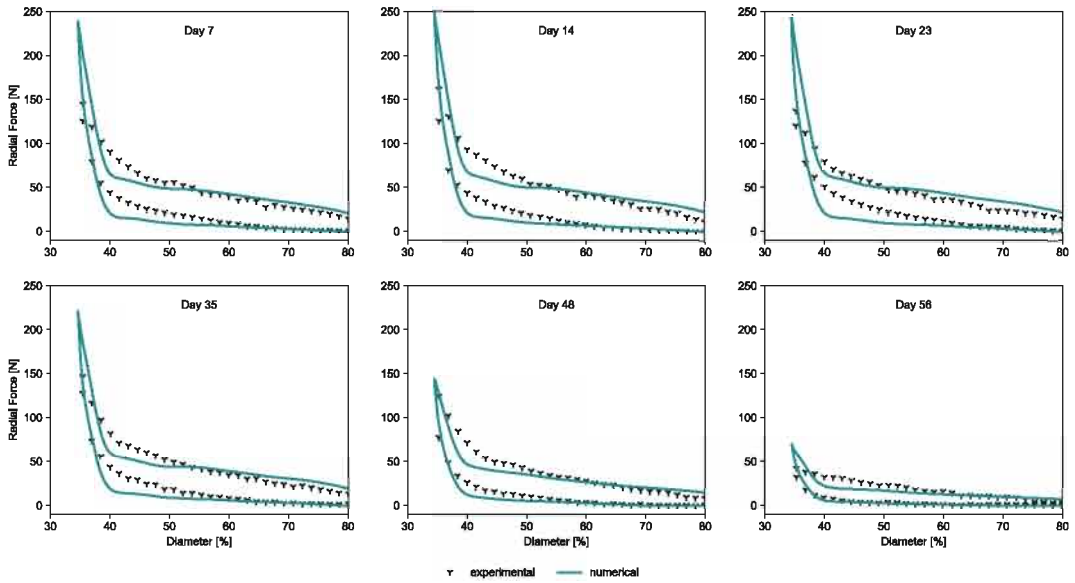

Figure 4.8: Qualitative validation of the numerical stent model by comparison of the experimentally measured and computationally predicted radial force throughout the degradation process.

The amount of friction was calibrated based on the comparison of the experimental and computational results of both the radial force and the elastic recovery of the actual device and the virtual device model. Figure 4.7 and Table 4.1 depict these results and show that a friction coefficient FC= 0.2 led to the best fit. The developed framework was validated by a qualitative week-to-week comparison between the experimental in vitro degradation study results and the simulation results as depicted in Figure 4.8.

4.3.3 Virtual stent implantation

In consultation with the clinician and based on the 69 year old male's patient-specific esophageal anatomy, an *EllaBD* stent with nominal length of 80mm, body diameter 18mm and flare diameter 23mm (reference number 019-10A-23/18/23-080) was chosen as the most appropriately sized treatment device. As shown in Figure 4.9, the *EllaBD* stent was, following the instructions for use, virtually crimped into a 28.0 Fr (9.4mm) sheath and bended to be released in the in vivo stressed esophagus (accounting for residual circumferential strain with the *bonded* state tonicity in the muscular layers, for the residual axial strain and for internal pressure-induced stress state computed with the Backward Incremental method (BI), see section 3.2.4). The virtual implantation procedure took 64 hours of walltime to be computed on a CentOS Linux 7 cluster with one compute node containing two Intel Xeon Gold 6140 (Skylake) processors each of which contains 18 cores (2.30 GHz processor base frequency, 96 GB of memory/node, equipped with 10GBE network). This procedure was run in parallel with different initial release

Figure 4.9: The virtual stent implantation procedure. The *EllaBD* stent is virtually crimped and subsequently bended to be eventually released in the esophageal lumen following the stent's instructions for use.

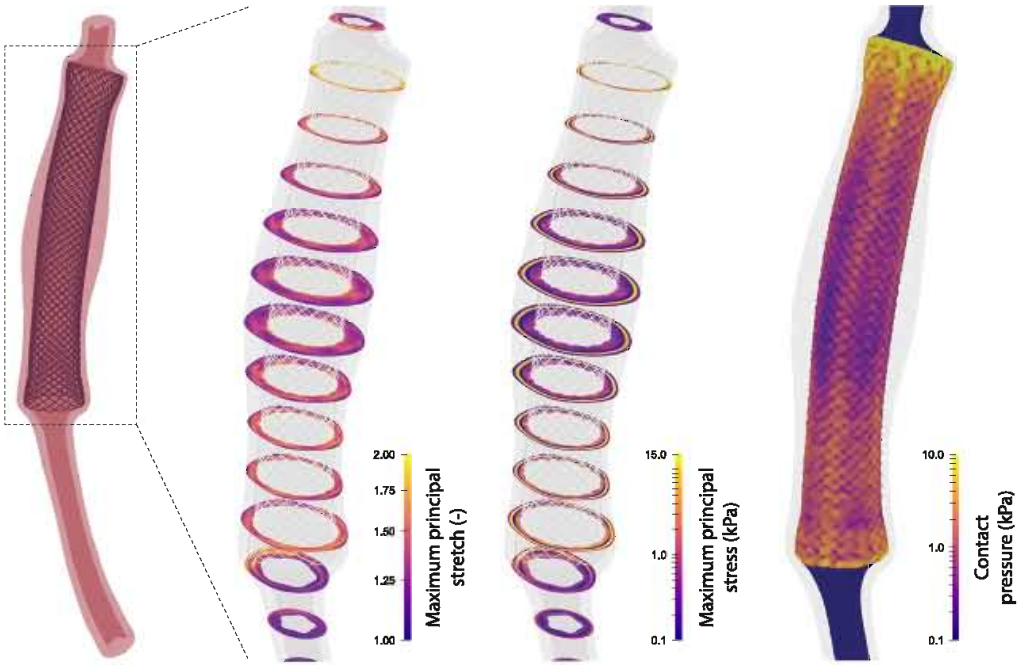

Figure 4.10: The in-silico esophagus-stent interaction. The virtually implanted *EllaBD* stent stretched the patient-specific esophageal wall up to the depicted maximum principal stretches and maximum principal Cauchy stresses in the 5 distinct layers. The corresponding stent-induced contact pressure on the inner lumen wall is depicted in the right panel.

positions to establish a satisfactory landing zone. In more detail, each of the stent ends (flares) had to extend beyond the stricture, within healthy tissue. Figure 4.10 shows that the stent's intrinsic chronic outward force, captured in the PBFS FEM, proved strong enough to restore the patient's esophageal lumen patency. The wall got stretched elastically to maximum principal Cauchy stresses up to 26.13 kPa and 10.44 kPa in the circumferential and longitudinal muscle layers respectively. The computed Cauchy stresses in the collagen-rich submucosal layers amounted up to 15.66 kPa. The maximum principal stretch ranged from up to 1.49 in the stent body region to a maximum stretch of 1.92 in the stent's flare region. The risk for device migration can be assessed by the amount of contact pressure exerted on the inner esophageal wall. In this case, contact pressures up to 1.190 kPa in the stent body region and 9.67 kPa in the stent flare region were recorded.

4.4 Discussion

4.4.1 Mechanical behavior of the (biodegradable) PBFS

When studying the effect of different design parameters on a stent's mechanical behavior, different research and development (R&D) strategies can be followed: prototyping and in vitro bench testing, analytical modeling or finite element modeling [48]. Physical test methods are often expensive and difficult (or even impossible) to implement. On the other hand, analytical models are restricted to linear elastic materials, idealized geometries and boundary conditions. As it has been demonstrated that these analytical models cannot capture the mechanics of (bioresorbable) polymeric braided fiber stents [251], only a more general computational framework can bring solace to the design challenge [78]. Even though the finite element method has shown its effectiveness in evaluating the performance of laser-cut stents during their deployment [4, 9, 10, 35, 50, 55, 59, 122, 158, 163], braided wire/fiber stent FEA models are generally scarce in literature. This may be due to the intrinsic complexity of fiber interactions in these stents. Kim et al. [175] used FEA modeling to study the effect that fiber frequency and braiding angles have on the radial strength of nitinol stents. De Beule et al. [11, 48] developed a parametric finite element model to investigate and optimize the mechanical performance of metallic braided wire stents bringing forward intrinsic competing stent characteristics that could be associated to specific geometrical design parameters. More recently, Zhao et al. [376] compared the performance of braided and welded nitinol wire stents in a moderately stenosed artery. In thin-wired metallic stents, the effect of friction could be ignored [251], which is not the case for thick-fiber polymeric stents such as the *EllaBD* stent. Moreover, the biodegradable nature of the stent material causes its behavior to change over time.

For that reason, we first assessed this stent design's mechanical behavior in vitro. The measured radial forces of the *EllaBD* stents at day 0 are in good correspondence with the results of Hirdes et al. [137] as can be seen in Figure 4.7. Our measurements revealed that the radial force in compression is up to 3 times as high as the radial force during expansion, which depicts the amount of elastic energy consumed by friction between the fibers. This energy loss also became clear studying the lack of foreshortening recovery during the experimental tests, as was depicted in Table 4.1. The experimentally showcased *elastic hysteresis* demonstrates the need for new strategies that incorporate the friction between the fibers into numerical models capturing the mechanical behavior of thick polymeric fiber braided stents. The in vitro degradation study revealed two different stages of degradation of the polydioxanone (PDS) stent fibers, which is in correspondence with other studies performed on PDS [199, 266]. During the first stage, the PDS fibers keep their mechanical strength (or even appear to get slightly stronger). During this phase, random chain scission of the ester groups in the material bulk takes place via hydrolysis in which the amorphous regions are affected first because water molecules can infiltrate these regions more easily. The local ester bonds get more exposed and cleaved more rapidly. However, these cleaved chains can rearrange within the polymer structure, leading to an improved packing. This maintains or even increases the level of crystallinity and explains the initial strength-increase. During the second phase, all remaining molecular chains are attacked over their total length generating increasingly smaller chains. These small molecular pieces can eventually diffuse out of the polymer structure leading to the in Figure 4.6 observed strength decrease [266]. Long-term effects, such as the inclusion of a viscoelastic and a constitutive degradation material model [58, 59] were not considered needed for the calibration of the stent model because the performed and simulated radial force measurements cannot be considered as long-term testing regimes. The development of a correct numerical model was thus independent of these effects.

Building up a numerical model incorporating friction between the fibers, it was shown that a pure fiber-to-fiber self-contact approach (no connectors) underestimated the stent's radial strength. Conversely, a self-contact approach proved appropriate for the (thin-wired) braided wire stent model proposed by Kim et al. [175]. On the other hand, the incorporation of 'Join' and 'Hinge' connector elements overconstricted the crossing fibers' degrees of freedom as slippage between the fibers was blocked. This caused the FEM of the stent to be too stiff. *Abaqus* 'Planar' connector elements allow fibers to slide parallel to each other and rotate about the normal direction to the parallel plane. Imposing a Coulomb friction model in these connector elements proved successful in modeling the frictional hysteresis

effect measured in the radial compression tests as seen in Figure 4.7. A qualitative comparison of the experimental and numerical radial compression test and elastic foreshortening led to a calibrated Coulomb friction coefficient of 0.2. Imposing the degradation-induced softening of the PDS fibers (Figure 4.6) demonstrated the mechanical predictive power of the model to simulate the stent's changing mechanical behavior throughout time. The experimental and computational methodology described in this chapter was partially described in the first author's master dissertation [266] and has very recently been reproduced by [319] in which the effect of the polydioxanone's viscoelastic behavior was complementarily included. The 'Hinge' connector elements which we initially proposed in [266] were adopted in [319] and, agreeing with our results, showed to overestimate the virtual stent model's radial strength. Since no visible advantage was seen in using a viscoelastic material model, the assumptions we made regarding the viscoelastic effects of the PDS material on the complete stent model's mechanical behavior were rendered valid. Moreover, given that Shanahan et al. [319] completely replicated our experimental and computational methodology and also came to a good fit in the elastic regime, the predictive robustness of our work in [266] and in the current study was reconfirmed.

The developed model allows us to study the stent's mechanical behavior in additional loading conditions (e.g. cyclic loading or danger of kinking in bending). Moreover, the parametric nature of the stent's geometrical description in *pyFormex* allows us to easily open up our numerical stent model library to all available *EllaBD* stent sizes or new alternative PBFS designs. As prototyping and in vitro testing is expensive and time-consuming, these virtual bench test simulations can help device manufacturer to significantly reduce R&D costs and speed up the process to bring improved stent designs to the market [48].

4.4.2 Stent-esophagus interaction

Hirdes et al. hypothesized that the ideal (esophageal) stent should have a relatively high radial force and lower axial force. The luminal patency should be maintained and proper fixation in the esophageal wall must be guaranteed while good flexibility is needed to minimize trauma. Axial and radial force data from experimental testing alone are nonetheless inadequate to predict the clinical performance of a stent [137]. Such data is insufficient to assess the device's potential to restore lumen patency, to study the degree of foreshortening, to predict the contact pressure between device and lumen wall or to compute the risk for ruptures caused by an overstretched esophageal wall. By bringing both the computational polymeric braided fiber stent model and virtual esophagus model from chapter 3 together in a virtual implantation procedure, we completed the framework to study the association between

stent design and patient anatomy on the one hand with the clinical outcome of esophageal stenting on the other hand. As current esophageal stent designs suffer from complications such as migration, perforations, bleeding, chest pain, nausea, fistula, mal-positioning, etc., we believe our framework could offer tools to assess the risk for these complications with a certain stent design prior to the intervention. The migration risk of stents can be assessed based on the computed contact pressure between the tissue and the scaffolding stent as seen in computational cardiovascular studies [230]. The impact of an explicitly modeled food bolus was not considered here but could be added to the framework to determine more accurate drag forces impacting the stent device during peristaltic contractions. The esophageal transmural stress distribution upon stent implantation and in more detail, the peak wall stresses, could be used to estimate the perforation risk by comparing the peak stresses close to the stent's proximal flare end (see Figure 4.10) to ultimate tensile strengths of (sub)mucosal and muscle tissue, as seen in abdominal aortic aneurysm rupture risk assessment [88]. Given that these ultimate strength values seem to be quite species-dependent and no human data is currently available [325, 368], we refrained from making such an explicit risk assessment for this patient case. In general, the developed framework integrates physical and biomechanical properties of both the host and the device in the recipient patient-specific esophageal anatomy which can help the clinician to select the appropriate device size, design and landing zone that should lead to the best results for the individual as is currently well-established for transcatheter aortic valve replacement procedures [312].

The stresses and contact pressures induced by the *EllaBD* stent in the esophageal tissue are in the order of kPa's and the maximum stretch varies between 1.5 and 1.9. Comparing this to other literature, we could only find related work by Kajzer et al. [170] where no details were given on the used material model and how it was calibrated. We can only assume their material is substantially stiffer than ours as they record stent-induced esophageal wall stresses in the order of MPa's and stretches up to 1.3.

4.5 LIMITATIONS AND FUTURE WORK

All results based on in vitro experimental results and numerical models should be interpreted carefully as they inherently contain a number of assumptions and approximations. In the experimental radial compression tests, the internal friction in the stent compression unit is difficult to estimate and was assumed constant based on an initial unloaded radial compression test. The internal friction might however increase as the contact area in between the diaphragm-like closing segments increases with an ever-decreasing compression ratio. This might account for the small discrepancies

between the experimental and numerical results at lower compression ratios seen in Figure 4.8. During the degradation study, the stents were submersed in a phosphate-buffered saline, which does not fully reflect the speed of the in vivo degradation process. The sensitivity of the polydioxanone degradation to potential pH fluctuations (e.g. acid reflux) or to tissue ingrowth might explain why stent integrity and radial force only maintained for 5 weeks in our degradation studies, in contrast with the 6 to 8 weeks acclaimed by the manufacturer [190].

Future work should focus on setting up validation procedures in which pre- and post-implantation computed tomography (CT)/magnetic resonance (MR) imaging acquisitions could be used to study the esophagus' response to stent implantation in parallel with the developed numerical framework. Local layer-specific comparisons between reality and the developed numerical framework might not be possible due to image resolution limitations but comparing the full wall response and deformation should be obtainable. If post-implantation 4D MR imaging data would be available, we could extend the framework to model peristaltic contractions after stent implantation and compare the results to reality, but this was considered outside the scope of the current study. As this study set forth to tackle the current shortcomings in numerical esophageal tissue (chapter 3) and polymeric stent modeling (chapter 4), only one patient case was considered. Nevertheless, both stent model and esophagus model creation were automated in *pyFormex* and allow for an easy set-up of different cases and stent dimensions.

The developed framework could definitely offer great advantages over pure (swallowing) fluoroscopy, CT and/or MRI and in vitro stent studies for both the patient, the gastroenterologist and the engineer. Inaccessible information such as local deformation, strain and stress distribution in the esophageal wall can be consulted allowing the gastroenterologist to assess the patient-specific (patho)physiological state of the esophagus. In addition, each stent design aspect can be considered while assessing the risk of adverse events. The diameter of the stent, the flares, the used material(s), the fiber thickness and stiffness, the braiding angle, the strut coverage ... all have their influence on the flexibility, the radial force, the foreshortening, the amount of friction with the esophageal wall, etc. If run in parallel with a randomized controlled trial, the association between mechanical wall metrics such as contact pressure, stress and strain and observed complications could lead to new insights in the esophagus's (patho)physiological response to stent implantation. Except for some randomized controlled trials, no strong evidence is currently available proving the superiority of one esophageal stent design over another [138, 341]. In patients with benign esophageal strictures, only prospective, single-arm studies have been performed to evaluate the

safety and efficacy of new stent designs. When high complication rates are reported in a series, it is no straightforward task to determine if stent-related factors (e.g. design, flexibility, radial forces, degradation speed) can be considered (partially) responsible for these clinical complications. The comparison of stent design efficiency is complicated due to randomization difficulties, the large number of possible variables (such as tumor size, tumor location and patient health) or even discrimination between different possible outcomes, apart from survival (especially in the malignant cases). For the engineer, the developed tools also lend themselves to perform virtual bench tests and parametric optimization procedures as mentioned before, but this time based on clinically weighed costs such as lumen gain, migration risk, overstretching, dysphagia risk, ... A generic optimized stent for a whole population probably does not exist, but the developed tools allow comparison of different stent designs (other stent models can be developed following the same procedure) in the exact same clinical situation (e.g. tumor size, stricture location, stiffer wall etc.) or compare the complication risk of one specific stent design in a multitude of clinical (modeled) esophageal pathologies.

II

Cardiac Biomechanics

Chapters

Clinical rationale 109

5 The 'virtual heart' 113

6 Kinematic BCs in ventricular modeling 145

7 Heart failure modeling validity across the scales 171

Clinical rationale

Cardiovascular diseases (CVDs) are a major cause of mortality worldwide, responsible for nearly a third of all deaths (more than 17 million lives worldwide every year) [106, 337]. In the European Union (EU), CVD even accounts for 52% of female deaths and 42% of male deaths every year [356]. CVD is also a leading cause of morbidity, which has a huge social and economical impact on society. On a social level, patients suffering from CVD often require lengthy rehabilitation periods and continuous informal care. Often, this does not only lead to a loss of income for the patient (who might no longer be able to work), but also for their relatives who become caregivers (mostly in developing countries). Due to significant health care costs, productivity losses and the need for informal care for those impacted with cardiovascular disease, The economic impact comes both in direct costs to the health care system and indirectly in losses to the economy through work loss both to those with disease and their family members who become de facto caregivers or who suffer loss of income because the breadwinner is not in the workforce [90]. In 2017, the overall cost of CVD to the EU economy was estimated at € 210 billion a year, but this cost keeps increasing. Despite the recent advancements of pharmaceutical, surgical, device and tissue engineered therapy strategies, CVD remains one of the most costly, common and deadly medical conditions. Moreover, projections up to 2060 show no significant changes in predicted mortality, keeping cardiovascular disease the global leading cause of death for the foreseeable future [360]. Combining this with the epidemiologic transition towards CVD that we are currently seeing in all developing countries in the world [90], it is clear that a global cardiovascular disease epidemic is rapidly evolving.

If we want to address this growing burden to society, we need to significantly improve the current clinical treatment strategies for cardiovascular disease. Therefore, an improved comprehensive understanding of the structural and mechanical behavior of the heart is vital. Computational modeling offers a platform which integrates detailed geometrical, functional and microstructural information in a consistent and objective manner. Similar to the other soft tissue biomechanics applications in this dissertation, this finite

element analysis (FEA) platform uses the basic laws of physics to produce important, otherwise unobtainable, metrics (e.g. local straining coupled to stress generation in the tissue) allowing us to study the underlying multiscale soft tissue mechanisms in more detail. In contrast to the gastro-intestinal biomechanics field discussed and studied in part I, cardiac computational models have evolved significantly more over the past decades, up to the point where model-based interpretations of clinical imaging data have already improved our current understanding of cardiac structure and function considerably [353]. Moreover, such models have already been shown useful to help clinicians diagnose, to evaluate drug effects, to gain better insights on risk-benefit ratio of certain interventions and to explore or predict the outcome of certain treatment strategies (e.g. [2, 13, 30, 163, 179, 193, 195, 292, 298, 301]).

The advent of recent advancements in image processing combined with improved numerical methods and the proliferation of inexpensive high performance computing power has aided integrative cardiac computational models to provide, with appropriate data collection, calibration and tuning, a more and more *patient-specific* window into acute and chronic heart functioning. Such patient-specific biophysical heart models show huge potential to actually assist the detection, diagnosis and treatment of cardiac diseases in the clinical practice in the near future. More specifically, these models allow for the identification of individual patient characteristics that could be clinically relevant [129]. Furthermore, they enable personalized in silico tests of potential treatments or surgical procedures, assisting tailored and ultimately effective therapy strategies. Even though the wealth of clinical data available for each individual patient keeps increasing, there is still a huge gap between what is theoretically possible and what is practically possible in the hospital for each and every patient. To produce and validate highly realistic subject-specific heart models, multiple sources of in vivo and ex vivo data are required [299], which are not always available in the clinical practice. On a quest to bring cardiac computational modeling derived technologies closer to the patient, this part of the dissertation developed a guideline to produce personalized computational cardiac models with the limited imaging data available in the clinical practice. Given that the accurate mathematical representation of a highly complex organ such as the human heart intrinsically entails a number of modeling assumptions, chapter 5 first discusses the model-based interpretation of cardiac structure and function, and how this interpretation leads to the current state-of-the-art in cardiac computational modeling allowing personalized modeling of heart mechanics. Due to the absence of some relevant data in the clinical practice, important modeling attributes such as the myocardial fiber distribution, the boundary conditions or the reference geometry need to be approximated.

To improve model fidelity, the impact of any of these assumptions needs to be carefully studied. Whilst the impact of myocardial fiber orientation is studied more extensively in e.g. [66, 263, 300], the impact of different kinematic boundary conditions to account for the non-explicitly modeled surrounding tissue on in silico ventricular models remained insufficiently studied. Therefore, the assumptions made to realistically account for the absent surrounding structures tethering and constraining the movement of the computational cardiac model were studied in more detail in chapter 6. The influence of the cardiac reference geometry is studied in more detail in chapter 8. Additional modeling aspects (including the chosen constitutive law, the tuning of patient-specific constitutive parameters, the degree of compressibility, etc.) are carefully selected and discussed in chapter 5.

Instead of primarily treating the symptoms of cardiovascular disease, which still remains the standard treatment strategy nowadays, it has been hypothesized that mechanism-targeted treatment strategies will be more effective [104]. To develop such strategies, an increased understanding on cardiac disease mechanisms is imperative. Using the modeling guideline disclosed in chapter 5, subject-specific multiscale cardiac growth models can enable us to examine disease mechanisms in more detail using animal studies. Such models hold huge promise for simulating the patient-specific timeline of heart failure and for optimizing surgical or pharmacological treatment strategies. While scientists are increasingly recognizing the predictive potential of cardiac growth models, the clinical community is rather skeptical, mainly because the predictive power of these models remains unknown. To overcome the current stagnation in clinical heart failure (HF) management, validation efforts on prognostic cardiac growth models need to be made. Given that growth model validity can only be assessed in close correlation with experimental data which shows large multiscale (both spatial and temporal) variability in disease progression among different animals, this is a challenging endeavor. To integrate experimental, computational and clinical data from different scales and times in an effort to quantify the predictive power of cardiac growth models and their underlying disease mechanism hypotheses, we designed a new approach where we combine multiscale experiments and simulations using tools of machine learning in chapter 7. This approach is anticipated to allow us to design, calibrate, and validate a new generation of multiscale cardiac growth models to explore the interplay of various subcellular, cellular and organ level contributors to HF to provide a more holistic picture of the failing heart and point towards new and effective mechanism-targeted treatment strategies.

CHAPTER 5

THE 'VIRTUAL HEART'

This chapter provides a short summary on heart anatomy and function and a short guideline on how we integrate knowledge on multiple processes at different temporal and spatial scales into computational cardiac subject-specific models representing the (electro)mechanical behavior of the heart. Concurrently, this guideline reveals some aspects* that hinder successful adoption of these models in the clinical practice, which are further addressed in chapters 6 and 7.

5.1 CARDIAC STRUCTURE AND FUNCTION

The heart is the cardiovascular system's vital transport pump, which continually propels blood, containing oxygen, nutrients, wastes and many other substances, through the hollow blood vessels to service all cells in the body. This blood flow results from the combined action of the cardiac valves and rythmic contractions of the heart's four chambers. These contractions are generated by the high density of contractile cells within the chamber walls. These muscle cells are in turn packed with dense arrays of contractile structures known as sarcomeres [245].

*i.e. appropriate kinematic boundary condition definition to accomodate for non-explicitly modeled difficult-to-segment surrounding tissue structures in clinically available image data and appropriateness of certain mechanistic stimuli driving hypertrophic responses to changing hemodynamic loading conditions of the heart

5.1.1 Anatomy and cardiac cycle

As can be seen in Figure 5.1, the heart is located within the thoracic cavity, medially between the lungs in the space known as the mediastinum. Within the mediastinum, this specialized muscle is separated from the other mediastinal structures by a membrane known as the *pericardium*, or pericardial sac, and sits in its own space called the pericardial cavity. The large veins, the superior and inferior venae cavae, and the large arteries, the aorta and pulmonary trunk, are attached to the superior surface of the heart, called the *base*. The inferior tip of the heart, the *apex*, lies just to the left of the sternum between the junction of the fourth and fifth ribs.

The heart has the dual role of circulating both oxygenated and deoxygenated blood through the systemic and pulmonary circulation respectively. Consequently, the heart is divided in two functional halves, each containing an atrium and a ventricle. Following the blood through the body (see Figure 5.2), the right atrium (RA) collects deoxygenated blood coming from the superior vena cava (SVC) and inferior vena cava (IVC) and propels this blood to the right ventricle (RV) through the tricuspid valve. Subsequently, the blood is pumped to the pulmonary arteries and lungs through the pulmonary valve, where the blood gets oxygenated in the pulmonary capillaries. This blood returns to the heart entering the left atrium (LA) through the

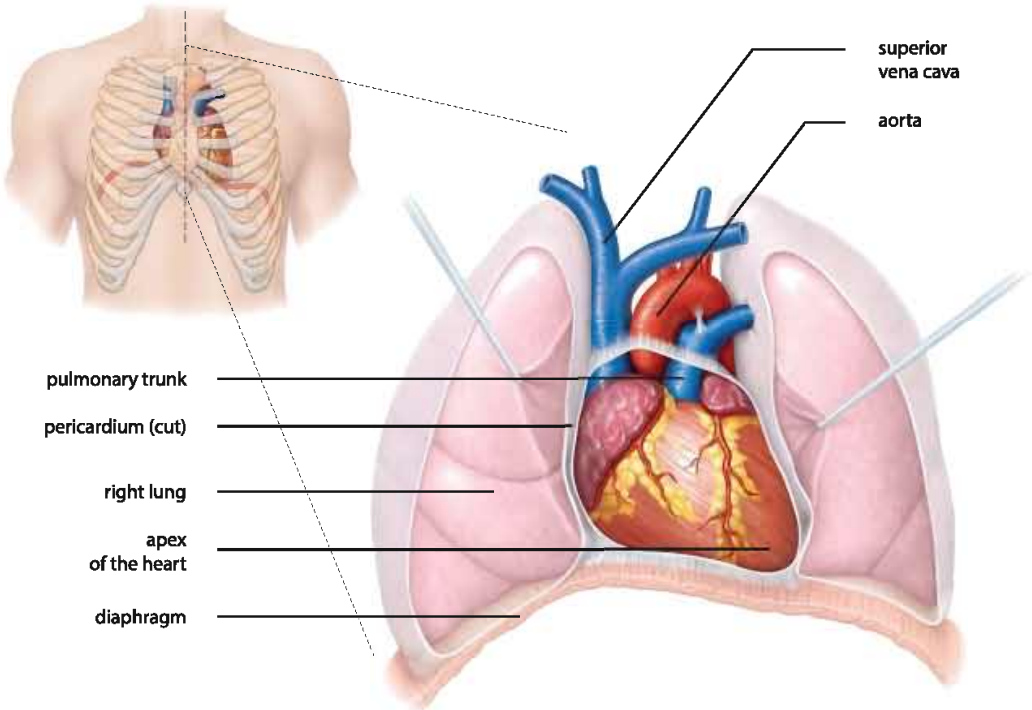

Figure 5.1: Location of the heart in the mediastinum and the heart's relationship with the great vessels and the lungs. Image adapted from [220].

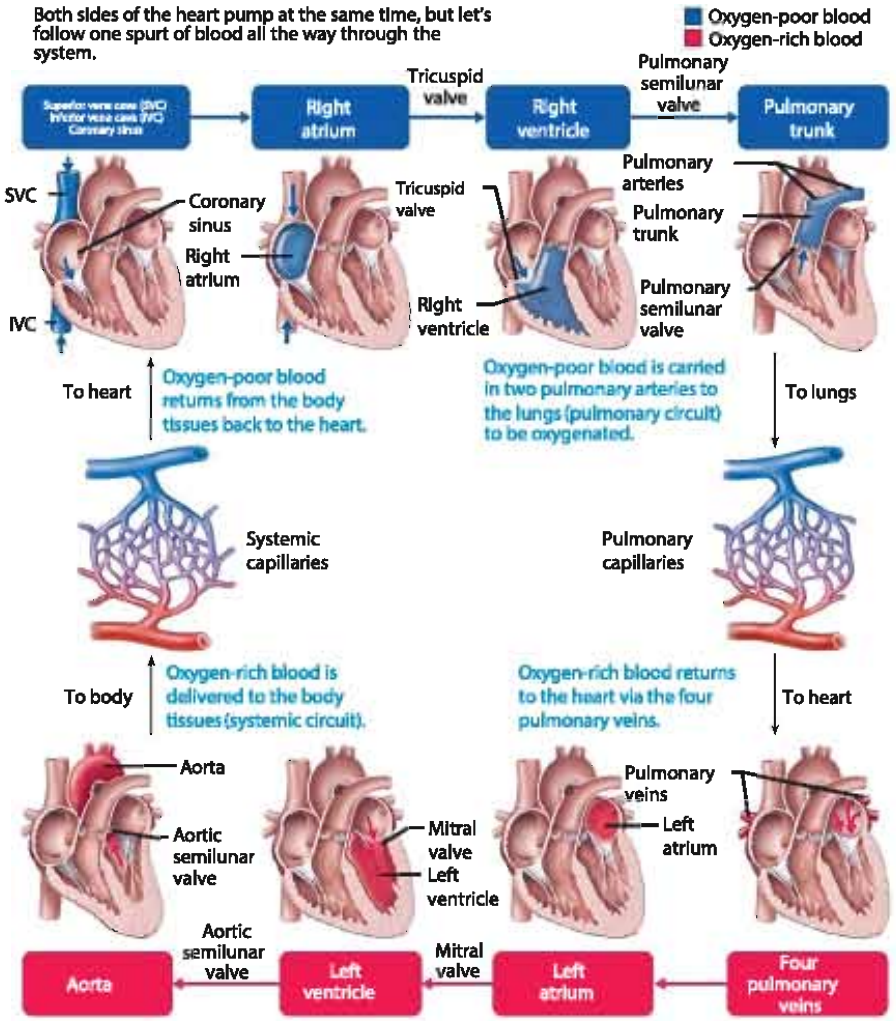

Figure 5.2: Schematic diagram of the blood pathway depicting the double-pump function of the heart, each side supplying its own circuit. Image reproduced from [220].

pulmonary veins. Pumped to the left ventricle (LV) via the mitral valve, the contracting LV redirects the blood to the aorta through the aortic valve. Finally, the aorta and all its downstream branches distribute all the oxygen-rich blood to all the systemic organs and tissues (including the heart itself through the coronary circulation).

Given that the atria only need to propel blood received from the venous system to the ventricular chambers, and that the ventricles pump the blood further through the arterial system to the rest of the body, both chambers show a significantly different structure. The atria are thin-walled reservoirs whereas the ventricles are thick-walled pumps. Functionally, the left side of the heart drives the systemic circulation, whereas the right side of the heart sustains the pulmonary circulation. Given that the systemic circuit is a long and high-pressure pathway and the pulmonary circuit is a short low-pressure

circulation, the left ventricular wall is approximately three times as thick as the RV wall, rendering the LV a far more powerful pump than the RV. Anatomically, the thicker LV has a cylindrical ellipsoidal shape, whereas the RV is crescent shaped and wraps around the LV (see Figure 5.3). During the cardiac cycle, alternating muscle contraction (*systole*) and relaxation (*diastole*) drive the pressure changes that control the blood flow in and out of the heart. More specifically, the cardiac cycle can be split into four phases. During *diastolic filling*, blood moves from the atrium to the ventricle, passively stretching the ventricle. until the valve closes. During *isochoric/isovolumic contraction*, the ventricle starts to contract and active tension builds up within the wall. The mitral/tricuspid valve closes and thus the ventricular pressure rises with no change in volume. During *ventricular ejection*, the aortic/pulmonary valve opens allowing blood to leave the ventricle but active contraction is still occuring in the muscle. Finally, upon *isochoric/isovolumic relaxation*, the aortic/pulmonary valve closes again and the wall tension decreases. Since all valves are closed during this phase, the corresponding pressure decrease occurs at constant volumetric conditions.

5.1.2 Cardiac wall structure

Exploring the structure of the cardiac wall in more detail, different membranes and layers can be discriminated as can be seen in Figure 5.4. As

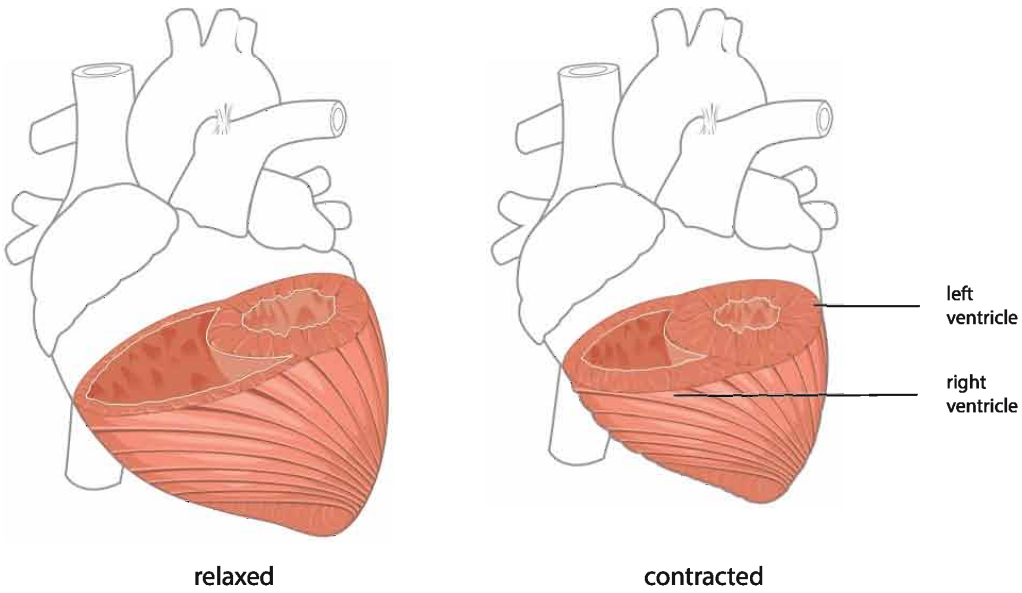

Figure 5.3: Ventricular muscle thickness. The left ventricular myocardium is significantly thicker than that of the right ventricle. Both ventricles pump the same amount of blood, but the left ventricle must generate a much greater pressure to overcome greater resistance in the systemic circuit. The ventricles are shown in both relaxed and contracting states. Note the relative differences in ventricular lumen volumes. Image reproduced from [220].

mentioned before, the heart is snugly encapsulated by the *pericardium* which consists of two distinct submembranes: the *fibrous pericardium* and the *serous pericardium*. The fibrous pericardial membrane consists of though, dense connective tissue to protect the heart, maintain its position in the thorax and prevent overfilling of the heart. The more delicate serous pericardium is a thin, two-layered membrane built up from a *parietal layer* lining the internal surface of the parietal pericardium and an inner *visceral pericardial layer*, also called the *epicardium*, which is fused to the heart and part of the heart wall. The *pericardial cavity* lies between the epicardium and pericardium and is filled with lubricating serous fluid, the *pericardial fluid*, which reduces friction as the heart contracts and the lungs and diaphragm move around.

Focusing on the layers of the heart wall itself, three layers of unequal thickness can be distinguished in Figure 5.4: the *epicardium*, the *myocardium* and the *endocardium*. The first layer, the epicardium, is both the outermost layer of the heart wall and the innermost layer of the pericardium as discussed before. The middle layer, the myocardium, is the middle and thickest layer of the heart wall and largely made up of cardiac muscle cells. These muscle cells are anchored in a connective tissue framework, mainly built up from collagen and elastin fibers. This so-called *fibrous skeleton* of the heart reinforces the myocardium internally, anchors the cardiac muscle fibers and limits the direct spread of action potentials throughout the heart wall. The innermost layer of the heart wall, the endocardium, lines the inner myocardial surface with a thin layer of connective tissue consisting of simple squamous epithelium. This *endothelium* is continuous with the endothelial lining of the blood vessels. To pump more efficiently, the ventricular surfaces are marked with irregular muscular columns projecting outwards, called the *papillary muscles* and *trabeculae carneae* for the left and right ventricle respectively. Through their connection with the chordae tendinae, some of these muscular ridges also avoid inversion of the atrioventricular valves during contraction.

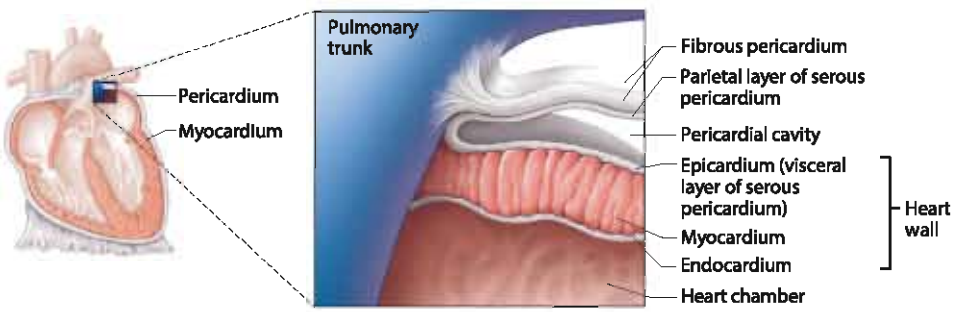

Figure 5.4: Cardiac wall structure depicting the pericardial membranes and the different layers of the heart wall. Image reproduced from [220].

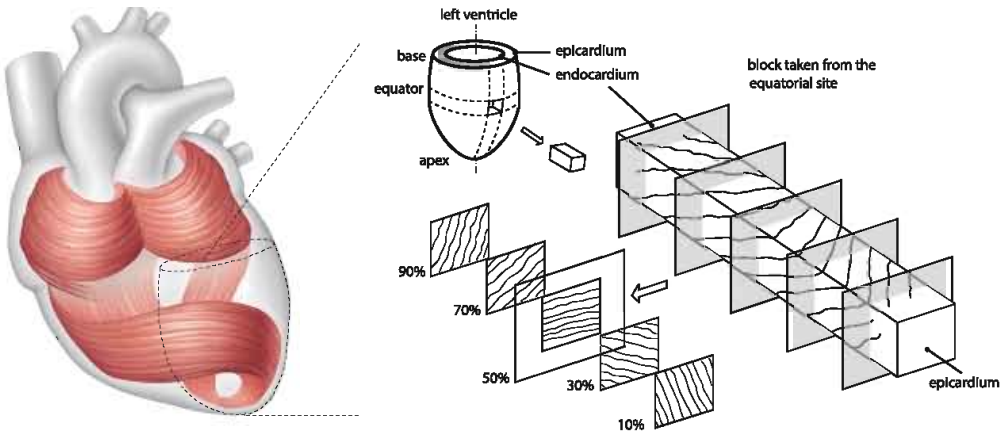

Figure 5.5: Heart Musculature. (left) The swirling circular and spiral arrangement of cardiac muscle bundle fibers contributes significantly to the heart's ability to pump blood effectively through the body. (right) Schematic diagram of the left ventricle of the heart where the structure through the thickness with the corresponding local cardiac muscle fiber orientations is shown on a block taken from the left ventricular equator. Image adapted from [147, 220].

5.1.3 Structure of the myocardium

The myocardium forms the bulk of the heart (e.g. the left ventricular myocardium is approximately 0.6 cm to 1.1 cm thick at end diastole) and it is this layer's contraction that pumps blood through the heart and into the major arteries. Contrarily, the endocardium and epicardium are of the order of 100 μm and have little functional influence for mechanical considerations [297]. Consequently, studying the heart's contractile function or dysfunction mostly focuses on the myocardial tissue behavior (see section 5.3). The cardiac muscle cell fibers that built up the myocardial layer are organized in an elegant and complex pattern as depicted in Figure 5.5. The muscle cells (see section 5.1.4) swirl and spiral around the chambers of the heart, forming a figure 8 pattern around the atria and bases of the great vessels. A similar pattern can be found deeper into the ventricular muscle layer, swirling around each ventricular cavity. More superficial ventricular muscle layers wrap around both ventricles. Focusing on the ventricles, it has been shown that the predominant cardiac muscle fiber orientation rotates from -50° to -70° in the sub-epicardial region to nearly 0° in the mid-wall region to +50° to +70° in the sub-endocardial region with respect to the circumferential direction of the ventricle [147, 210]. However, away from the sub-endocardial and sub-epicardial layers, most muscle fibers are generally not oriented parallel to the ventricular walls, where transverse angle components ranging between +9° and +34° can be found for the left ventricle on average [210]. Given that these transverse angles are relatively small compared to the aforementioned rotating helix angle

component, it is often assumed that the cardiac muscle fibers remain relatively parallel to the ventricular walls throughout the thickness (see section 5.4.2).

5.1.4 Cardiac muscle fibers

As explained in section 5.1.2, the myocardium is mainly composed of cardiac muscle cells, forming cardiac muscle fibers that are organized following the aforementioned complex transmural myoarchitecture. Cardiac muscle cells, like skeletal muscle cells, are striated and contract by the sliding filament theory (see also section 2.2). However, in contrast to the long, cylindrical, multinucleate skeletal muscle fibers, cardiac muscle cells are short, fat, branched, mostly uninucleate and interconnected through intercalated discs. As depicted in Figure 5.6, the intercalated discs form the junctions between different cardiac muscle cells, anchoring them together. Such an intercalated disc is built up from desmosomes, cell structures that anchor the ends of cardiac muscle fibers to allow contraction to occur, and gap junctions, allowing ions to pass from one cell to another, electrically coupling them to each other (see also section 5.2). Similar to skeletal muscle cells, each cardiac muscle cell (also called *cardiomyocyte* or *cardiac myocyte*) contains *myofibrils*, which are specialized organelles consisting of long chains of *sarcomeres*, the fundamental contractile units of muscle cells.

The in Figure 5.7 depicted sliding filament model of contraction, further disclosed in section 2.2, describes how muscle cells produce internal displacements and shape modifications leading to active tension through relative sliding of the actin-myosin filaments. Focusing on a sarcomere, the smallest

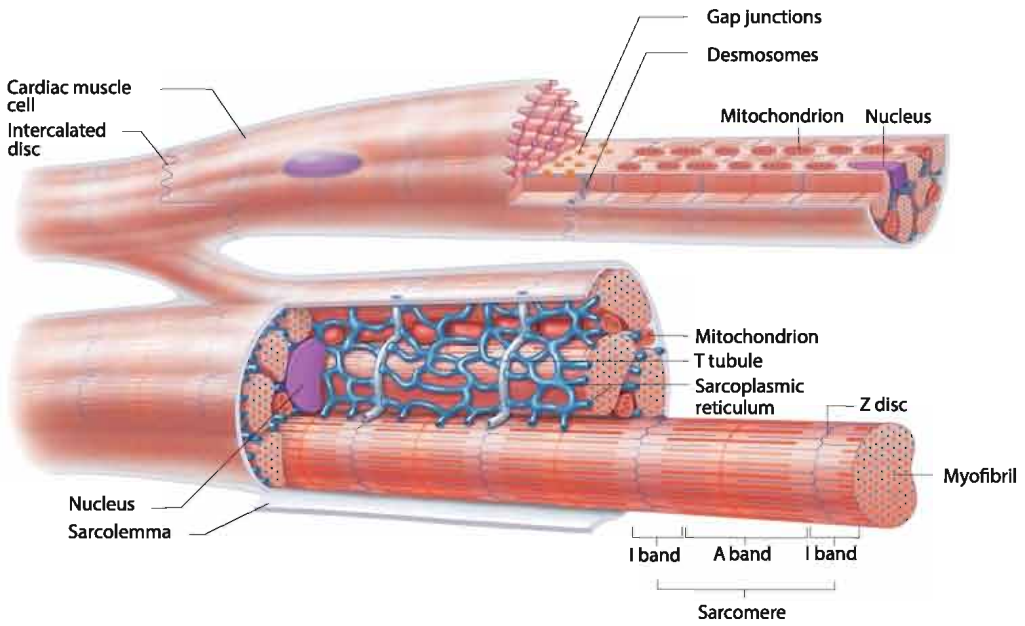

Figure 5.6: Microscopic anatomy of cardiac muscle. Image adapted from [220].

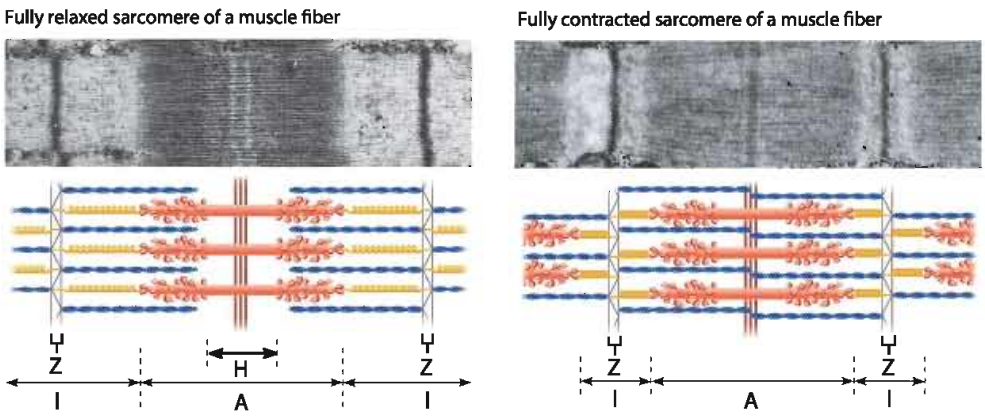

Figure 5.7: Sliding filament model of contraction; (left) a fully relaxed and (right) a fully contracted sarcomere. At full contraction, the thin and thick filaments overlap each other completely. Images adapted from [220].

functional unit of contraction, the interdigitated thin actin and thick myosin filament structure can interact through myosin motors attaching to binding sites on the thin actin filaments. Formation of such an attachment (also called crossbridge) causes myosin to undergo an adenosine triphosphate (ATP)-driven molecular rearrangement called a powerstroke, which distorts the crossbridge and creates a pulling force that tends to slide the thin and thick filaments past each other [245]. As sufficient numbers of myosin heads cyclically attach, pull and detach, the sarcomere contracts.

As a pulsatile pump, the activation and deactivation of contractile powerstrokes in the sarcomeres needs to be well-coordinated. Governed by the intrinsic cardiac conduction system (see section 5.2), a traveling action potential propagates down a cardiac muscle cell's T tubulus, releasing the Ca^{2+} from the sarcoplasmic reticulum that regulates the contraction of sarcomeres. Subsequently, the Ca^{2+} transient recovers as Ca^{2+} is removed

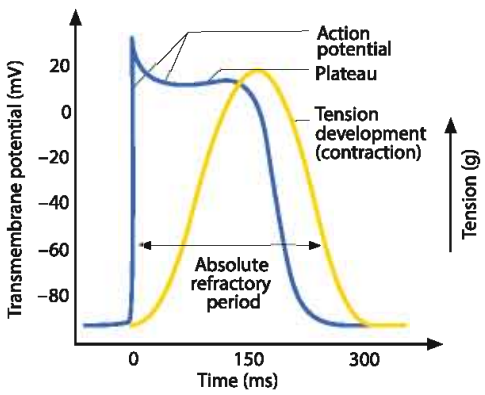

Figure 5.8: Excitation-contraction coupling in cardiac muscle cells.

from the cytosol by the sarcoplasmic reticulum and the membrane ion channel exchangers [245]. Ca^{2+} controls whether or not the sarcomere's interdigitated thin and thick filament structure can slide past one another. More specifically, under conditions of low Ca^{2+}, (tropomyosin) proteins block myosin binding sites on the thin actin filaments preventing crossbridge formation. Consequently, the sarcomere is in its so-called relaxed state. When Ca^{2+} is present, conformational changes in the tropomyosin proteins are triggered, exposing the myosin binding sites and initiating contraction. As can be seen in Figure 5.8, Ca^{2+} recovery starts prior to peak tension.

5.2 CARDIAC ELECTROPHYSIOLOGY

A heart beat is the result of an electrical signal that passes through the myocardium, triggering within each cell a transient increase in Ca^{2+}. Even though this dissertation will not focus on cardiac electrophysiology (EP), it is important to have a basic understanding of the electrical activity and conduction in the heart, given that the cell's action potential drives the individual cardiac muscle cells to contract mechanically.

Cardiac electrophysiology is a multiscale process where individual cardiomyocytes (heart cells) maintain an internal ionic state while also triggering activation across the tissue by exchanging ions through gap junctions [276]. The ability of the heart to depolarize (and consequently contract) is intrinsic, which means that the heart does not depend on the nervous system to beat. Autonomic nerve fibers can however alter the basic rythm of heart activity. The heart's independent, but coordinated, activity is a function of the presence of gap junctions, and the activity of the heart's intrinsic cardiac conduction system [220]. At the cellular level, the exchange of ions (primarily potassium, sodium and calcium) through voltage-gated membranes in the cell membrane causes a rapid change in the membrane potential, also known as the *action potential.* This action potential is characterized by 5 different stages: the resting potential, the depolarization, the notch, the plateau and the repolarization, as depicted in Figure 5.8. The sequence of electrical excitation of the heart is further controlled by non-contractile cardiac cells specialized to initiate and distribute impulses throughout the heart. Figure 5.9 shows this intrinsic cardiac conduction system, where autorhytmic cardiac cells in the sinoatrial (SA) node, the atrioventricular (AV) node, the AV bundle, the right and left bundle branches and the Purkinje fibers coordinate and synchronize heart activity. More specifically, electrical activity is initiated at the SA node allowing for depolarization propagation through the atria. Once the wave of activation reaches the AV node, there is a small delay in conduction. This is to allow the atria to finish contraction before activating the ventricles. Once

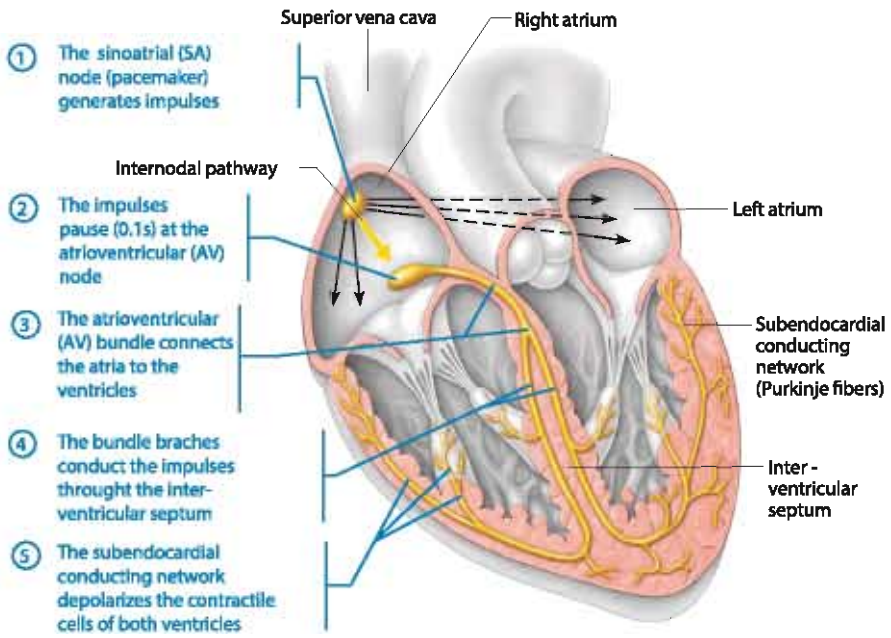

Figure 5.9: Anatomy of the intrinsic cardiac conduction system showing the sequence of electrical excitation. Image adapted from [220].

the AV node is activated, depolarization propagates through the His-Purkinje system and through ventricular tissue.

Defects in the intrinsic cardiac conduction system can cause irregular heart rythms, or *arrhythmias*, uncoordinated atrial and ventricular contractions and even *fibrillation*, a condition of rapid and irregular out-of-phase contractions in which control of heart rythm is taken away from the SA node by rapid activity in other heart regions [220]. Given that fibrillating ventricles no longer manage to pump blood around, defibrillation needs to happen quickly in order to avoid a ceased circulation and (brain) death.

Modeling cardiac tissue EP requires the combination of two underlying physics: cell-level ion channel-mediated currents and cell-to-cell diffusion via gap junctions. The cell-level ion channel-mediated currents are typically characterized by a set of ordinary differential equations (ODEs) based on parameters with physiological meaning, e.g. permeability of the membrane or changing uptake strength of a certain ion. Multiple sets of ODEs, each having their own complexity, have been proposed and are used to model the action potential of individual human cardiomyocytes (e.g. the Ten Tusscher-Panfilov, Priebe-Beuckelmann, Iyer-Mazhari-Winslow, Bueno-Orovio-Cherry-Fenton, Grandi-Pasqualini-Bers, O'Hara-Virág-Varró-Rudy models, see [38]). Combining these action potential cell models with reaction-diffusion partial differential equations describing the cell-to-cell transmission of the impulse via gap junctions between the cardiac muscle cells, allows us to study electrophysiological defects in the heart's intrinsic conduction

system and the multi-scale mechanisms by which arrhythmias develop in more detail, e.g. [302].

5.3 CARDIAC MECHANICS

5.3.1 Passive myocardial mechanics

The myocardium exhibits, similar to most other biological soft tissues (see chapter 2), a large deformability, together with non-linear, pseudo-elastic, anisotropic and nearly-incompressible material behavior due to its complex 3D architecture and high liquid content. To characterize the myocardium's mechanical behavior, a functional relationship between stress and stretch is needed. As described in paragraph 2.1.1.1.3, anisotropic hyperelastic material properties can be adequately represented constitutively by means of a strain energy function (SEF) [83].

As mentioned in section 5.1.2, the myocardium consists largely of cardiac muscle cells encapsulated in a fibrous elastin and collagen skeleton network anchoring these cells together. More specifically, the layered organization of parallel cardiomyocytes occupies about 70% of the myocardial volume, where the remaining 30% consists of various interstitial components [147]. Only 2-5% of this interstitial volume is occupied by collagen fibers arranged in a spatial network forming lateral connections between adjacent muscle fibers [196], as schematically depicted in Figure 5.10. Here, it has to be noted that we can differentiate between endomysial and perimysial collagen fibers. The *endomysial* collagen fibers surround the myocytes within one myocyte layer and form lateral connections between adjacent myocytes. The *perimysial* fibers span cleavage planes between adjacent muscle layers, connecting them to each other. These perimysial collagen fibers can be considered the major structural elements of the extracellular matrix [147]. The discovery of this laminar-sheet based microstructure in myocardial tissue and the experimental myocardial shear testing data in [62] motivated a shift from transversely isotropic myocardial constitutive models (e.g. [127]) towards orthotropic constitutive material models to account for the sliding between adjacent sheets, e.g. [40, 147, 240, 311]. In this dissertation, we decided to impose the orthotropic material model proposed by Holzapfel and Ogden [147] given that it takes into account the morphological structure of the myocardium (see Figure 5.10) and that the model is consistent with standard inequalities required from convexity, strong ellipticity and material stability considerations. Moreover, the constitutive material parameters are partly based on the underlying histology. Being geometry independent and only requiring knowledge of the local preferred material directions, this constitutive material model is based on four invariants (see also

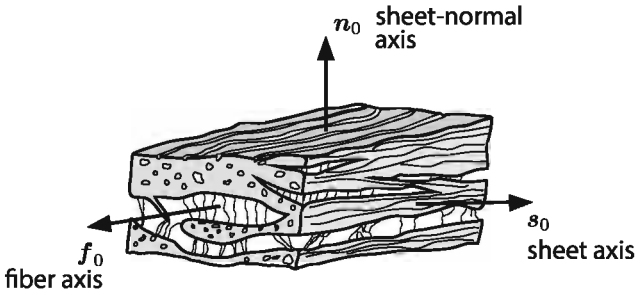

Figure 5.10: Laminar-sheet based microstructure in myocardial tissue. Schematic illustration showing the layered organization of myocytes and collagen fibers between the sheets referred to a right-handed orthonormal coordinate system with fiber axis $\boldsymbol{f}_0$, sheet axis $\boldsymbol{s}_0$ and sheet-normal axis $\boldsymbol{n}_0$. Image adapted from [147].

paragraph 2.1.1.1.3) comprising an isotropic component (representing the underlying non-collagenous and non-muscular matrix) and transversely isotropic components (describing mechanical responses associated with the collagenous structures aligned with the myocardial fiber $\boldsymbol{f}_0$ and cross-fiber $\boldsymbol{s}_0$ directions) [353]. For a more in-depth review of other existing constitutive material models for passive myocardial tissue, we refer the interested reader to [147].

5.3.1.1 *Invariants*

Following the kinematic deformation framework described in sections 1.1 and 2.1.1, we can define the principal isotropic invariants of the right Cauchy-Green stretch tensor $\boldsymbol{C}$ (or the left Cauchy-Green stretch tensor $\boldsymbol{b}$, see also Eq. 2.8) as follows

$$\bar{I}_1 = \operatorname{tr} \bar{\boldsymbol{C}} \tag{5.1a}$$

$$\bar{I}_2 = \frac{1}{2}\left(\left(\operatorname{tr} \bar{\boldsymbol{C}}\right)^2 - \operatorname{tr} \bar{\boldsymbol{C}}^2\right) \tag{5.1b}$$

$$\bar{I}_3 = \det \bar{\boldsymbol{C}} = J^2 \tag{5.1c}$$

The additional (transversely isotropic) invariants describing the deformation in the preferred direction $\boldsymbol{N}_i$ (and $\boldsymbol{N}_j$) are defined by

$$\bar{I}_{4ij} = \boldsymbol{N}_i \bar{\boldsymbol{C}} \boldsymbol{N}_j \tag{5.2a}$$

$$\bar{I}_{5ij} = \boldsymbol{N}_i \bar{\boldsymbol{C}}^2 \boldsymbol{N}_j \tag{5.2b}$$

For the Holzapfel-Ogden SEF (see the following section), we will need the isotropic invariant $\bar{I}_1$ in accordance with Eq. 5.1 and the anisotropic invariants

$\bar{I}_{4ff}$, $\bar{I}_{4ss}$ and $\bar{I}_{4fs}$ in accordance with Eq. 5.2 in the fiber and sheet directions $\boldsymbol{f}_0$ and $\boldsymbol{s}_0$:

$$\bar{I}_{4ff} = \boldsymbol{f}_0 \bar{\boldsymbol{C}} \boldsymbol{f}_0 \tag{5.3a}$$

$$\bar{I}_{4ss} = \boldsymbol{s}_0 \bar{\boldsymbol{C}} \boldsymbol{s}_0 \tag{5.3b}$$

$$\bar{I}_{4fs} = \boldsymbol{f}_0 \bar{\boldsymbol{C}} \boldsymbol{s}_0 \tag{5.3c}$$

5.3.1.2 *Strain energy function*

To structurally describe the mechanical response of passive myocardium, it was shown sufficient to introduce an isotropic contribution to the SEF associated with the underlying non-collagenous and non-muscular matrix coupled with anisotropy along the muscle fiber direction and the sheet structure direction [147]. The relevant constituents in this SEF are depicted in an unloaded state, in tension and under compression in Figure 5.11.

5.3.1.2.1 Non-collagenous and non-muscular ground matrix. The contribution of the non-collagenous and non-muscular ground matrix in Figure 5.11 to the tissue's strain energy could be modeled as a neo-Hookean material (as done in paragraph 3.2.1.2.2 and section 8.3 for the esophageal and arterial

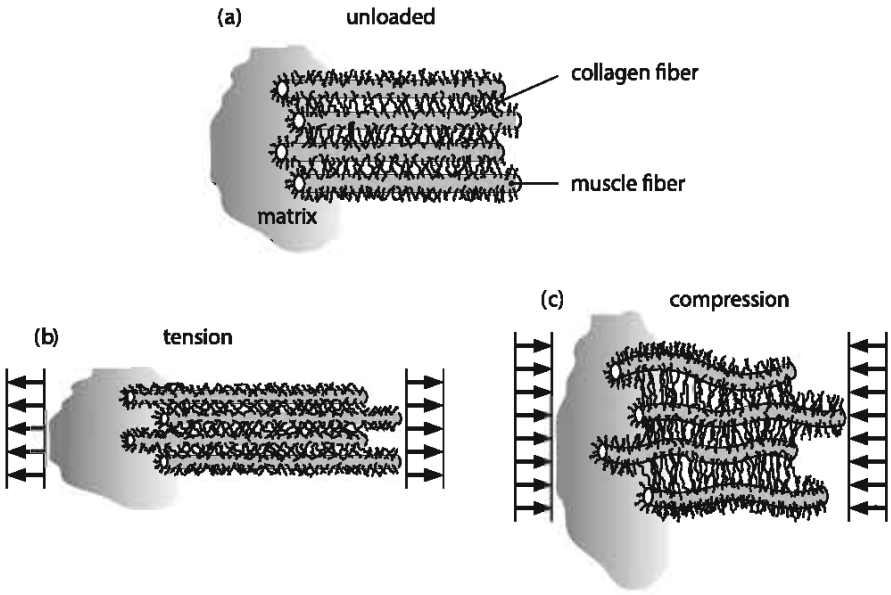

Figure 5.11: Schematic of the arrangement of muscle and collagen fibers and the surrounding matrix: (a) unloaded structure, (b) structure under tensile load in the muscle fiber direction, showing decreased inter-fiber separation so that the collagen network bears load primarily in the muscle fiber direction, (c) structure under compressive load in the muscle fiber direction, showing the muscle fibers buckled and lateral extension of the collagen network. Image reproduced from [147].

ground matrix respectively). However, for myocardial tissue, Holzapfel and Ogden decided to characterize the ground matrix's hyperelastic behavior using the following exponential dependency on $\bar{I}_1$:

$$\bar{\Psi}_{mat} = \frac{a}{2b} \exp\left[b\left(\bar{I}_1 - 3\right)\right] \tag{5.4}$$

where a and b are positive constitutive material constants. The parameter a has a dimension of stress and b is dimensionless.

5.3.1.2.2 Collagen-muscle fiber structure. As depicted in Figure 5.11 (b), tensile loading of the collagen-muscle fiber skeleton in the muscle fiber direction leads to extension of the muscle fibers and decreasing inter-myofiber distances. Concurrently the collagenous network offers little resistance laterally but contributes to the exponentially increasing stress in the muscle fiber direction. Tensile loading of the collagen-muscle network lateral to the muscle fiber direction also leads to exponential stress stiffening, which can be related to the gradual recruitment of the collagen network. Next to the network's behavior in tensile loading conditions, Figure 5.11 (c) depicts the tendency of muscle fibers to buckle when subjected to compressive loads in the muscle fiber direction. Similarly to lateral tensile loading, compression leads to stretched collagen cross-fibers, which can explain the relatively high compressive stiffness of the myocardium.

Following Holzapfel and Ogden, the aforementioned stiffening behavior in the muscle fiber direction $\boldsymbol{f}_0$ and sheet direction $\boldsymbol{s}_0$ is constitutively modeled using two exponential functions of the invariant $\bar{I}_{4ff}$ and $\bar{I}_{4ss}$ respectively. In tension, these fibers contribute significantly to the stored strain energy. Under compression, however, their contribution is minimal because the fibers do not support compression. Therefore, these terms are only included to contribute to the SEF if $\bar{I}_{4ff} > 1$ and $\bar{I}_{4ss} > 1$. This assumption is similar to the SEF contributions from the collagen fiber family invariants in esophageal tissue (see Eq. 3.8) and in arterial tissue (see Eq. 2.19). Given that $\bar{I}_{4nn}$ depends on $\bar{I}_1$, $\bar{I}_{4ff}$ and $\bar{I}_{4ss}$, this constituent is not included seperately and the tensile and compressive behavior in the normal direction is accommodated by the term $\bar{I}_1$ [147]. The detailed myocardial shear behavior characterized in the shear data experiments by Dokos et al.[62] does however require to include one more invariant $\bar{I}_{4fs}$, which finally leads to

$$\bar{\Psi}_{aniso} = \sum_{\alpha=f,s} \frac{a_\alpha}{2b_\alpha}\left(\exp\left[b_\alpha\left(\bar{I}_{4\alpha\alpha} - 1\right)^2\right] - 1\right) + \frac{a_{fs}}{2b_{fs}}\left(\exp\left[b_{fs}\bar{I}_{4fs}^2\right] - 1\right) \tag{5.5}$$

where, similar to the previous paragraph, a_f, a_s and a_{fs} are stress-like and b_f, b_s and b_{fs} are dimensionless constitutive material parameters.

5.3.1.2.3 Volumetric bulk material. As discussed in paragraph 2.1.1.1.4, imposing the nearly incompressible tissue behavior in a finite element analysis (FEA) framework can be done in two ways: using a hybrid/mixed displacement-pressure formulation or by modeling a minimal amount of compressibility. Here, we chose for the second option and decided to characterize the volumetric free energy Ψ_{vol} using the hyperelastic constitutive Arruda-Boyce model, which can be expressed as:

$$\Psi_{vol} = \frac{K}{2}\left(\frac{J^2-1}{2} - \ln(J)\right) \tag{5.6}$$

with K being the bulk modulus. To ensure near-incompressibility, the bulk modulus had to be set high enough to ensure the ratio of the bulk modulus to the initial shear modulus is large enough. In the following studies, this ratio was chosen to be equal to or larger than 100 [46].

5.3.1.2.4 Passive myocardium. Combined, this leads to the following SEF to describe the hyperelastic behavior of the passive myocardium:

$$\begin{aligned}\Psi = &\frac{a}{2b}\exp\left[b\left(\bar{I}_1 - 3\right)\right] + \sum_{\alpha=f,s}\frac{a_\alpha}{2b_\alpha}\left(\exp\left[b_\alpha\left(\bar{I}_{4\alpha\alpha}-1\right)^2\right]-1\right)\\ &+\frac{a_{fs}}{2b_{fs}}\left(\exp\left[b_{fs}\bar{I}_{4fs}^2\right]-1\right) + \frac{K}{2}\left(\frac{J^2-1}{2} - \ln(J)\right)\end{aligned} \tag{5.7}$$

5.3.1.3 Evaluation of the passive constitutive parameters

The constitutive material parameters introduced by the outlined constitutive model need to be calibrated based on specific experimental setups. In collaboration with Sack et al. [299], the material parameters a, a_f, a_s, a_{fs}, b, b_f, b_s and b_{fs} were determined from the calibration of normal myocardium specimen samples to experimental tri-axial shear data of human myocardial tissue (from 18 human subjects) [326]. More specifically, in silico cubes of myocardium with edge lengths of 4mm (i.e. the dimensions matching the myocardial test cubes in [326]) were meshed into a uniform 27 linear hex-element mesh. Using *Abaqus* as the forward solver, these in silico myocardial cubes were subjected to shear deformation in the mean fiber, sheet and sheet-normal directions. To evaluate the corresponding constitutive material parameters, a nonlinear least-square optimization routine with the trust-region-reflective algorithm option [169] was used to minimize the following objective function which compared the computed stresses $\boldsymbol{\sigma}_{\text{FEA}}$ to the experimentally measured stress values $\boldsymbol{\sigma}_{\text{exp}}$

$$\min \phi_1(\boldsymbol{v}_1) = \sum_i \sum_j \left(\sigma^i_{\text{FEA},j} - \sigma^i_{\text{exp},j}\right)^2 \tag{5.8}$$

where $i = fs, fn, sf, sn, nf, ns$ are the six shear mode combinations, $\boldsymbol{v}_1$ is the to be optimized vector of constitutive material parameters given by $[a, b, a_f, b_f, a_s, b_s, a_{fs}, b_{fs}]$ and index j spans the data points in the shear vector for shear test i [299]. This procedure resulted in the constitutive material parameter fit depicted in Figure 5.12 and summarized in Table 5.1. It should be noted that the experimental triaxial shear test data taken from Sommer et al. represents the mean elastic shear behavior (i.e. the mean curve of the loading and unloading curve) of all specimens at shear level 0.5 (n=18) [326]. The very same calibration procedure based on similar experimental data for porcine myocardial tissue (from 6 porcine subjects) [62] resulted in the second constitutive parameter set reported in Table 5.1. Comparing both these sets, the experimental characterization of the human myocardium showed significantly softer behavior than the experimental porcine test data. As discussed in [299], this difference in tissue compliance can be explained by the different methodologies used to approximate in vivo tissue conditions during experimental testing.

Even though the in Table 5.1 reported human constitutive parameter set is calibrated based on myocardial tissue which was perfused using a cardioplegic solution in vivo before extraction and subsequently kept in a cardioplegic solution with an additional nucleophile agent after excision, the

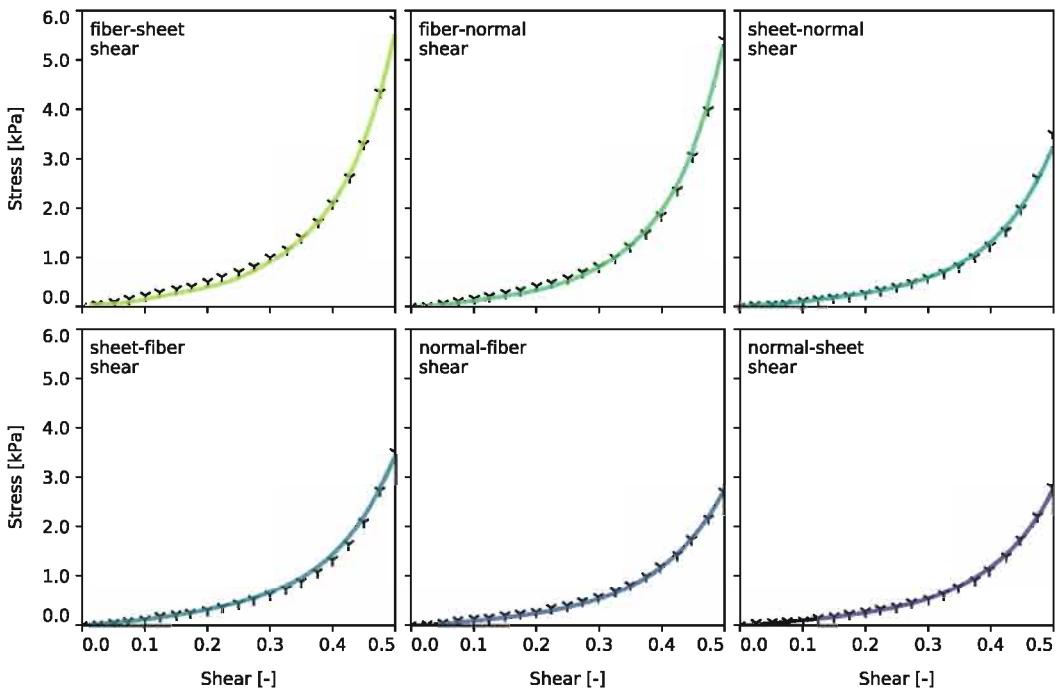

Figure 5.12: First-stage passive myocardial tissue response calibration: 'tri' markers depict the mean experimental triaxial shear data of healthy human tissue (from 18 subjects) [326] and solid lines depict the fitted passive material response of an idealized tissue cube to all 6 shear modes [299].

Table 5.1: Calibrated Holzapfel-Ogden myocardial constitutive parameters using human (18 subjects) and porcine (6 subjects) triaxial shear test data from [326] and [62] respectively.

tissue	a (kPa)	b (-)	a_f (kPa)	b_f (-)	a_s (kPa)	b_s (-)	a_{fs} (kPa)	b_{fs} (-)
human	1.051	7.542	3.465	14.472	0.481	12.548	0.283	3.088
porcine	0.261	10.767	19.539	13.615	3.406	5.6523	0.313	14.068

resulting constitutive parameter is still an ex vivo approximation of in vivo tissue behavior. To correct this calibrated constitutive parameter set for a potential mismatch between ex vivo and in vivo material behavior in subject-specific models, we adopted, in collaboration with Sack et al. [299], a second stage fitting procedure where the in Table 5.1 fitted human material behavior is scaled to match subject-specific in vivo pressure-volume measurements. More specifically, the linear (a, a_f, a_s and a_{fs}) and exponential (b, b_f, b_s, b_{fs}) terms were subjected to uniform scaling by parameters α and β, a scalar and an exponential multiplier, respectively. These multipliers were found by minimizing the error between the in silico diastolic pressure-volume (PV) relation and the analytical subject-specific Klotz curve [177], which is capable to describe the diastolic PV relation of the normal and diseased ventricle. Using *Abaqus* as the forward solver, we started the passive diastolic inflation simulations from the unloaded LV volume until the end-diastolic volume (EDV) was reached at the specified end-diastolic pressure (EDP). Combining these simulations with a *Python* script containing the same sequential least squares programming optimization algorithm as before [169], we calibrated the subject-specific in vivo constitutive material parameter set by minimizing the following objective function [299]:

$$\min \phi_2(\boldsymbol{\nu}_2) = \sum_j^N \left(P_{\text{FEA},j} - P_{\text{in vivo},j}\right)^2 + \left(EDV_{\text{FEA},j} - EDV_{\text{in vivo},j}\right)^2 \quad (5.9)$$

where the vector of material parameters is given by $\boldsymbol{\nu}_2 = [\alpha, \beta]$ and N equals the total number of data points along the PV curve. Given that this second stage calibration relies on subject-specific ventricular FEA models, the results of this second calibration step will be discussed ex infra (sections 6.3.4.2 and 7.3.3): see Figures 6.7 and 7.5.

5.3.1.4 *Viscoelasticity*

Soft tissue, such as the myocardium, typically shows viscoelastic behavior. The viscous effects in the myocardium can be related to the extracellular fluid matrix in which the fibrous elastin and collagen skeleton network anchoring myocardial fibers together is embedded. Without explicitly

modeling such biphasic systems [366], we can incorporate viscosity into the passive constitutive models using Voigt, Maxwell and 3 parameter models as discussed in section 2.1.1.2 (e.g. for myocardial tissue: [146, 157, 315]). Most recently, new orthotropic viscoelasticity models have been proposed which can be tuned to distinctly model the relaxation mechanism along each of the material axes [29, 128]. Even though testing facilities and procedures have evolved in such a way that it is now possible to characterize this anisotropic nature of myocardial viscoelasticity experimentally, experiments involving stress relaxation or creep, or both, remain challenging to perform [353]. Consequently, the cardiac modeling community typically assumes negligible viscous effects in their models. Similarly, inclusion of viscoelastic effects in our models was considered beyond this research work's scope. For preliminary investigations into the effect that (constitutive) viscoelasticity has on the passive behavior of the myocardium, we refer the interested reader to the recent works by Cansız et al. [29] and Gültekin et al. [128].

5.3.2 Active myocardial mechanics

As discussed in section 2.2, this dissertation focuses on the active (cell and tissue scale) force generation caused by the subcellular sliding actin and myosin filaments. Consequently, we refrain from explicitly modeling the subcellular mechanochemical and/or biochemical processes that govern the cyclically attaching, pulling and detaching myosin head processes themselves. We refer the interested reader to [245] for a detailed overview on the current state-of-the-art and remaining unknowns in cardiac-specific biochemical modeling of selected protein-protein interactions governing the excitation-contraction coupling between the sliding filaments.

Following section 2.2.1, we rather define a constitutive law describing the active stress generation's (upon following an active stress approach, see Eq. 2.21) or active deformation gradient's (upon following an active strain approach, see Eq. 2.24) dependence on the overall deformation $\boldsymbol{F}$ and non-mechanical factors β. To set up such a constitutive law, numerous groups have studied the cardiac muscle cell's contractility as a function of time, Ca^{2+} concentration, sarcomere length (see length-tension relationship discussed in section 2.2), rate of sarcomere length change (i.e. velocity) and load [125]. These experiments led to different active stress models (e.g. [126, 209, 241, 342]) and active strain models (e.g. [3, 34, 239, 274]), both having their intrinsic advantages and disadvantages. In active stress models, the active tension T_{act} is typically defined as a function of the aforementioned cell electrophysiology parameters, where the underlying microstructural changes are indirectly linked to the observed macroscale deformations. In the active strain models, the deformation in the contractile element is directly imposed as a function of these electrophysiology parameters. Where such a framework

allows for direct manipulation of the fiber deformation, there is only one elastic element controlling the stiffness of the myocardium during the cardiac cycle, while it has been shown that the myocardial stiffness is different during the passive (diastolic) and active (systolic) phases [275].

Following Göktepe and Kuhl [110], we decided to follow the active stress approach and assumed that the active stress distribution is entirely anisotropic. The active stress dependency on the aforementioned factors was accounted for by incorporating the time-varying elastance model initially proposed by Guccione and McCulloch [126]. In this model, the active tension is given by

$$T_{act} = \frac{T_{max}}{2} \frac{[Ca^{2+}]_0^{\,2}}{[Ca^{2+}]_0^{\,2} + E[Ca^{2+}]_{50}^{\,2}(\lambda_f)} \left(1 - \cos\left(\omega\left(\mathrm{mod}(t), \lambda_f\right)\right)\right) \tag{5.10}$$

$$\text{with} \quad \omega\left(\mathrm{mod}(t), \lambda_f\right) = \begin{cases} \pi \frac{\mathrm{mod}(t)}{t_0} & \mathrm{mod}(t) \le t_0 \\ \pi \frac{\mathrm{mod}(t) - t_0 + t_r}{t_r} & t_0 < \mathrm{mod}(t) \le t_0 + t_r \\ 0 & \mathrm{mod}(t) > t_0 + t_r \end{cases}$$

$$t_r = ml + b$$

$$l = \lambda_f l_r$$

where T_{max} is the maximum isometric tension achieved at the longest sarcomere length and maximum peak intracellular calcium concentration $[Ca^{2+}]_{max}$, $[Ca^{2+}]_0$ is the peak intracellular calcium concentration, $\mathrm{mod}(t)$ enforces the time variable to wrap around after each cardiac cycle (i.e. $0 \le \mathrm{mod}(t) \le HR/60$), λ_f is the stretch in the fiber direction, t_0 is the time to reach peak tension, t_r is the duration of relaxation, l_r is the stress-free sarcomere length, l_0 is the sarcomere length at which no active tension develops and m and b are coefficients that govern the shape of the linear relaxation duration and sarcomere length l relaxation.

The length-dependent calcium sensitivity is given by

$$E[Ca^{2+}]_{50}(\lambda_f) = \frac{[Ca^{2+}]_{max}}{\sqrt{\exp\left[B(l - l_0)\right] - 1}} \tag{5.11}$$

where B is a constant governing the shape of peak isometric tension-sarcomere length relation and l_0 is the sarcomere length at which no active tension develops. Based on experimental data, the general constitutive parameters for this time-varying elastance model were determined in [125] and are summarized in Table 5.2.

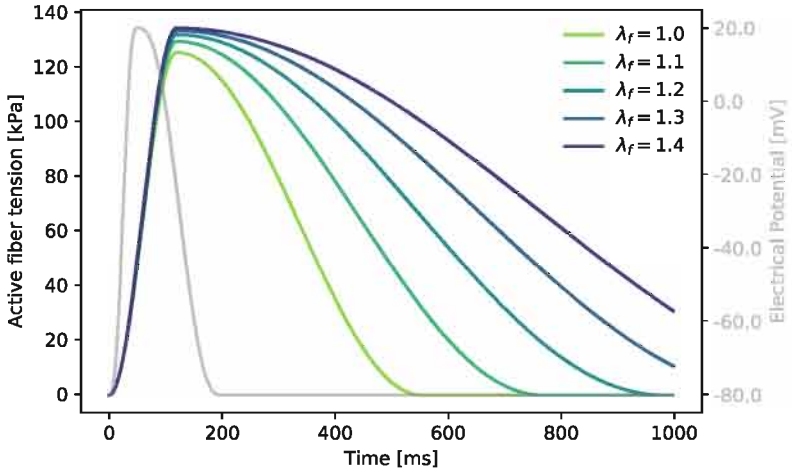

Figure 5.13: Electrically induced active fiber tension development at different myocardial fiber stretches depicting the Frank-Starling mechanism.

Table 5.2: Active myocardial constitutive parameters based on [125].

active constitutive parameter			description
T_{max}	135.7	kPa	isometric tension under maximal activation
$[Ca^{2+}]_0$	4.35	μM	peak intracellular calcium concentration
$[Ca^{2+}]_{max}$	4.35	μM	maximum peak intracellular calcium concentration
t_0	0.1	s	time to peak tension
l_0	1.58	μm	sarcomere length at which no active tension develops
l_r	2.035	μm	sarcomere length in the unloaded configuration
m	1.0489	s/μm	slope of linear relaxation duration sarcomere length relation
b	-1.429	s	time-intercept of linear relaxation duration-sarcomere length relation
B	4.75	μm	peak isometric tension-sarcomere-length relation shape constant
HR	60	bpm	heart rate

This elastance model accounts for the *Frank-Starling* effect (i.e., the intrinsic property of myocardium by which the strength of the heart's systolic contraction is directly proportional to its diastolic expansion [234]) by an imposed active stress response's dependence on regional sarcomere lengths (see also the length-tension relationship for muscle tissue in section 2.2). As can be seen in Figure 5.13, an increased fiber stretch leads to an increased and prolonged duration of myocardial active tension. Consequently, the heart contracts more and longer when it is stretched further, which will lead to increased stroke volumes in response to an increased diastolic stretching of the tissue.

Adding the active tension to the passive stress controlled by the subject-specifically in vivo tuned Holzapfel-Ogden passive material behavior in section 5.3.2, we get the following stress state in the fiber direction:

$$\sigma_{ff} = \sigma_{pass,ff} + T_{act} \tag{5.12}$$

Given that biaxial investigations on actively contracting rabbit myocardium revealed significant cross-fiber stress development that could not be completely attributed to fiber dispersion or deformation effects [208], a proportion (scaled by n_s, a scalar value less than 1.0, which describes the interaction between the adjacent muscle fibers) of the active stress developed in the fiber direction is transferred onto the stress in sheet direction:

$$\sigma_{ss} = \sigma_{pass,ss} + n_s T_{act} \tag{5.13}$$

This interaction has an influence on both the total contractility of the chambers and the amount of twist developed in the chamber during the cardiac cycle.

Similar to the experimentally deduced passive tissue parameters in section 5.3.1.3, there is still a mismatch between the ex vivo and actual subject-specific in vivo active tension generation. Therefore, we adopted, in collaboration with Sack et al. [299], a subject-specific active tension fitting procedure where the maximum allowable active tension T_{max} and the fiber-sheet active coupling scalar $n_s \in [0, 1[$ are optimized to ensure that the correct stroke volume (SV) (SV = EDV – ESV) and left ventricular long axis shortening (LVLS) for each subject was achieved. The LVLS target was given a lower weighted contribution to the overall objective function than the stroke volume (SV) target, but was needed to avoid optimization convergence producing ventricular enlongation and/or wall thinning [299]. This led to the following subject-specific active tissue optimization objective function:

$$\min \phi_3(\boldsymbol{v}_3) = \left(\mathrm{SV}_{\mathrm{FEA}} - \mathrm{SV}_{\mathrm{subject}}\right)^2 + 0.2\left(\mathrm{LVLS}_{\mathrm{FEA}} - \mathrm{LVLS}_{\mathrm{subject}}\right)^2 \tag{5.14}$$

which optimized $\boldsymbol{v}_3 = [T_{max}, n_s]$ with the same non-linear least-squares optimization procedure used for the passive material behavior before, see Figure 6.7.

Here, we chose to incorporate the active myocardial contraction using Guccione's time-varying elastance model which takes into account the sarcomere length, the myocardial fiber stretch, the Ca^{2+} concentration and the heart rate. Even though it was shown that this elastance model is suitable to model the mechanics of myocardial contraction, a more complete model should include the deactivating effects of shortening velocity and history dependence in cardiac muscle. For a detailed overview of other myocardial contraction models, we refer the interested reader to [353].

5.4 HEART MODELING

5.4.1 Subject-specific geometry

Due to the advancement of in vivo imaging modalities, it has become increasingly feasible to construct subject-specific geometrical heart models

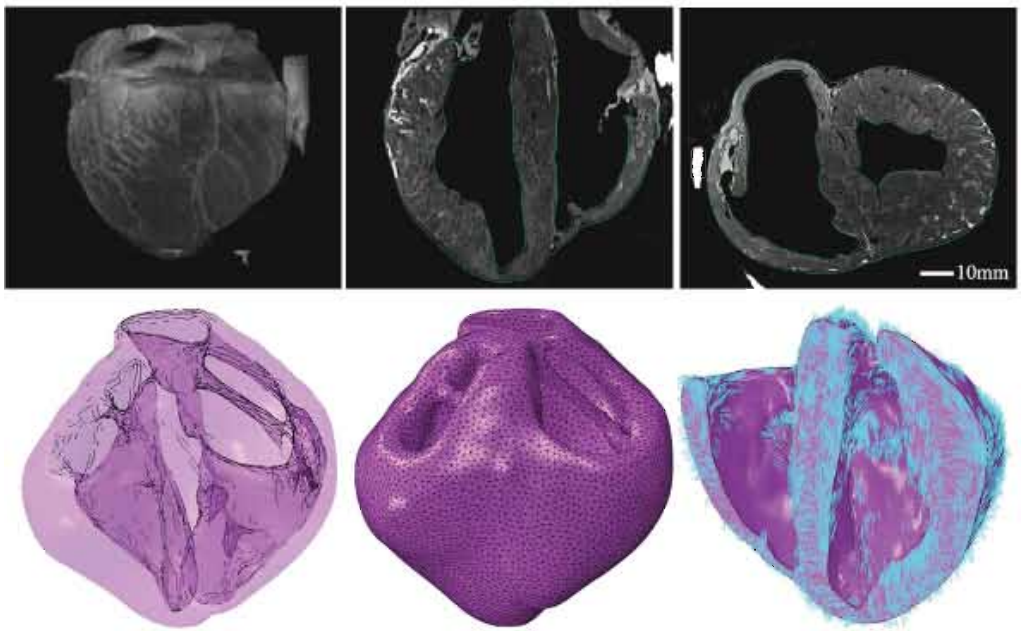

Figure 5.14: Sack et al.'s subject-specific porcine biventricular geometry created from high-resolution (0.3 x 0.3 x 0.8mm) diffusion tensor magnetic resonance imaging (DT-MRI) data [299]. To create these models, healthy and failing pig hearts were arrested in diastole, excised, fixated, and filled prior to performing anatomical magnetic resonance imaging (MRI) and DT-MRI. These MRI data sets (top panels) were imported and processed in *Simpleware ScanIP* (Synopsys Inc. - Mountain View, CA, USA) to end up with the geometry and quadratic tetrahedral mesh depicted in the bottom left and mid panels. Diffusion tensors representing the local myofiber orientations were reconstructed from the diffusion-weighted images using linear regression and custom Matlab routines as can be seen in the bottom right panel. Images taken from [299].

as depicted in Figures 5.14 and 5.15. Developing realistic subject-specific computational heart models is a challenging endeavor. Apart from the aforementioned subject-specific in vivo material response (both passive and active), one must account for the complex geometry of the heart and the myocardial fiber structure. To further complicate modeling efforts, the circulatory system and the interaction of the heart with the surrounding (not explicitly modeled) tissue needs to be numerically reproduced as the heart does not function in isolation [299]. In this section, we will summarize the different additional steps that need to be taken to set up an appropriate 'virtual heart' model.

To construct a 3D mesh geometry which incorporates the subject-specific geometrical heterogeneity of the heart, different types of imaging data can be used: echocardiography, cardiac computed tomography (CT) and cardiac magnetic resonance (MR) imaging. Using commercial software packages (e.g. *Mimics* (Materialise - Leuven, Belgium), *Simpleware ScanIP* (Synopsys Inc. -

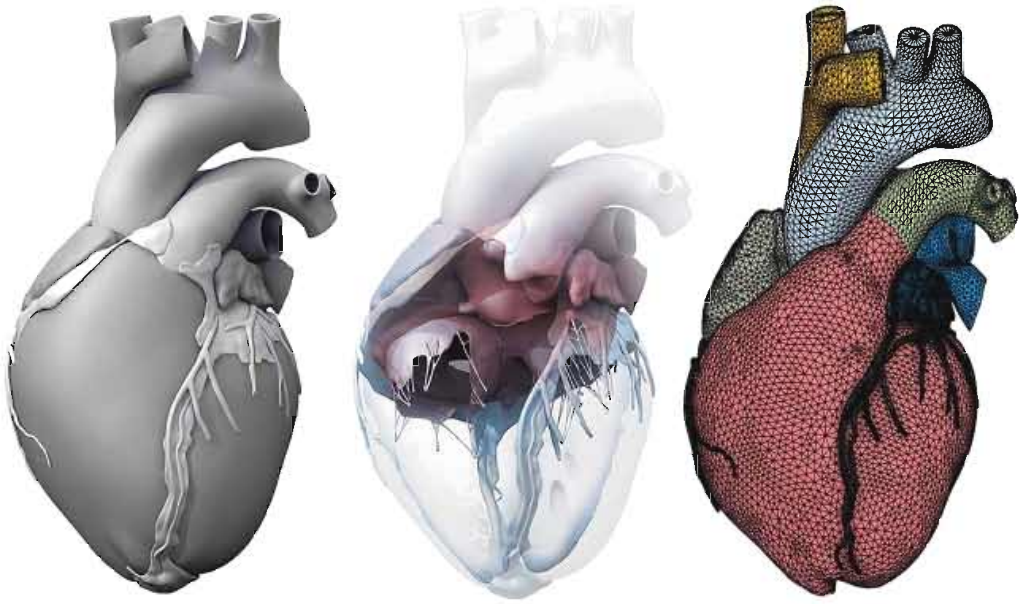

Figure 5.15: Baillargeon et al.'s Living Heart Human Model (LHHM) geometry created from magnetic resonance images of a healthy, 21-year old, 50th percentile U.S. male (Zygote Media Group, Inc.- American Fork, Utah, USA). Images were reconstructed from 0.75 mm thick slices using a medium soft-tissue kernel with retrospective electrocardiogram gating [380]. Data acquisition and reconstruction were performed during 70% diastole. The resulting anatomically accurate model includes all four chambers, the left and right atria and ventricles, connected by the four valves. The tricuspid and mitral valves connect the right and left atria to the right and left ventricles; the pulmonary and aortic valves connect the right and left ventricles to the pulmonary and systemic circulation. The major vessels including the aorta, the pulmonary arteries and the superior vena cava are included, together with the coronary arteries and some cardiac fat tissue. To create the finite element model, *Abaqus/CAE* was used to discretize this geometrical model into 598,862 linear tetrahedral elements and 140,160 nodes [14].

Mountain View, CA, USA)) or script-based in-house customized *Python*- or *Matlab*-based scripts, the in vivo imaging data can be segmented and post-processed to set up tetrahedral or hexahedral geometrical discretizations of the subject-specific macro-scale heart geometry.

Each imaging modality has its advantages and disadvantages. Echocardiography provides a cheap, easy and real time low-resolution view of the internal structure and is strongly integrated in the clinical preliminary diagnosis process. Cardiac CT uses harmful ionizing radiation and potentially risky contrast agents to capture images with a high spatial resolution. Cardiac MRI allows characterization of cardiac anatomy, functions and diseased muscle without any harmful radiation and with a good temporal resolution. Therefore, subject-specific heart models are typically constructed based on electrocardiogram (ECG)-gated cardiac MRI data. To incorporate all all key

anatomical structures of the heart (e.g. atria, valvular planes, papillary muscles) in subject-specific models we do however require very high-resolution imaging data. For example, the in Figures 5.14 and 5.15 depicted geometries required the collection of very high resolution in vivo and/or ex vivo imaging data from different modalities to come to such a high level of anatomic detail. Even though modeling the heart as a whole is considered superior to studying the diseased subsystems in complete isolation [338], the available imaging data resolution in the clinical practice is often insufficient to accurately segment the atrial wall, which is typically an order of magnitude thinner than the ventricular wall. However, it is increasingly feasible to construct patient-specific biventricular (BV) models from clinical data, where the computational domain is truncated at the base and thus limited to the left and right ventricle (LV and RV). Despite the absence of surrounding tissue (e.g. atria, valves, proximal arteries), such biventricular models are of clinical relevance and the influence of the absent surrounding structures on the modeled ventricles is accounted for by imposing kinematic boundary conditions (see section 5.4.3.2 and chapter 6)

5.4.2 Myocardial muscle fiber orientation

As mentioned before, cardiac myocardial tissue has a highly anisotropic micro-structure governed by the complex hierarchial architecture of biological fibrous components. The principal component, the grouped arrangement of myocytes (often referred to as myofibers), has a complex arrangement throughout the heart that is considered critical for the successful transduction of the one-dimensional description of individual cardiac cell behavior, both electrically and mechanically, to the overall pumping function of the heart [40, 110, 149, 362]. Many cardiac disorders or events, e.g. cardiac infarction and myocardial fibrosis, lead to myofiber misalignments, which eventually evolve to further disorganization and subsequent impairment of proper heart function [217, 261]. Today, two methods are commonly used to describe the myofiber orientations in patient-specific heart models: DT-MRI and rule-based reconstructions. Diffusion tensor magnetic resonance imaging (DT-MRI) is a specific MR imaging technique that applies diffusion sensitizing gradients to the scanned tissue specimen to measure diffusion in 6 or more non-collinear directions. As tissue components, such as cell walls and collagen, act as natural barriers to diffusion, the DT-MRI measured diffusion forms a direct assessment of the scanned tissue's underlying micro-structure [223]. Consequently, DT-MRI approaches are considered ideal to describe patient-specific myofiber architecture (see Figure 5.14). However, its use in *in vivo* studies is limited due to technical challenges that deteriorate spatial resolution and measurement quality [133]. Rule-based algorithms, on the other hand, construct dense fiber orientation fields based on interpolation

functions, which have recently been cast into boundary value problems [16, 156, 358]. In these boundary value problems, a fiber orientation field, based on observations from histology and DT-MRI [6, 39, 74, 93, 210], is prescribed on the endocardial and epicardial surfaces after which the local fiber orientation distribution is solved throughout the structure.

5.4.3 Boundary conditions

5.4.3.1 Hemodynamic loading during cardiac cycle

Blood pressure loading on the endocardial boundaries of the heart chambers has a substantial effect on ventricular deformations [353]. Theoretically, these absolute pressures can be measured in vivo using pressure transducers. However, such measurements require interventional technologies and only provide an acute snapshot of the hemodynamic loading caused by the cardiovascular circulation. Therefore, inclusion of hemodynamic loading condition in cardiac mechanics is typically done using a lumped parameter network (LPN) that models (a part of) the hemodynamic circulation using an electrical circuit analog including resistances, capacitors, inductors, source terms, etc. Such models offer a benefit over directly imposing in vivo pressure measurements given that they simulate the cardiovascular system in various and changing physiological conditions.

The required complexity of an appropriate hemodynamic LPN model depends on the considered application. For example, if we are only concerned with a good estimation of the cardiac afterload (aortic pressure) experienced by the left ventricle during a single contraction, the arterial system's afterload can simply be modeled using a 3-element Windkessel model as depicted in Figure 5.16. Here, R_1 and R_2 represent the characteristic impedance and peripheral resistance respectively and C represents the arterial system's compliance. More complete multi-beat biventricular or full heart models typically require more elaborate closed-loop LPN models modeling the full body circulatory system, such as the CircAdapt model [7] which is schematically depicted in Figure 5.17.

The parameters of such open- and closed-loop LPN models can subsequently be tuned to the considered patient specifically based on cuff measurements or other noninvasive techniques using ultrasound (US) or MR imaging. For more information on these noninvasive pressure measurement techniques, we refer the interested reader to [353].

5.4.3.2 Surrounding tissue

For mechanical heart models that do not explicitly incorporate all of the key anatomical structures of the heart (e.g. atria, valves, proximal arteries), kinematic constraints can be used to account for their roles in regulating

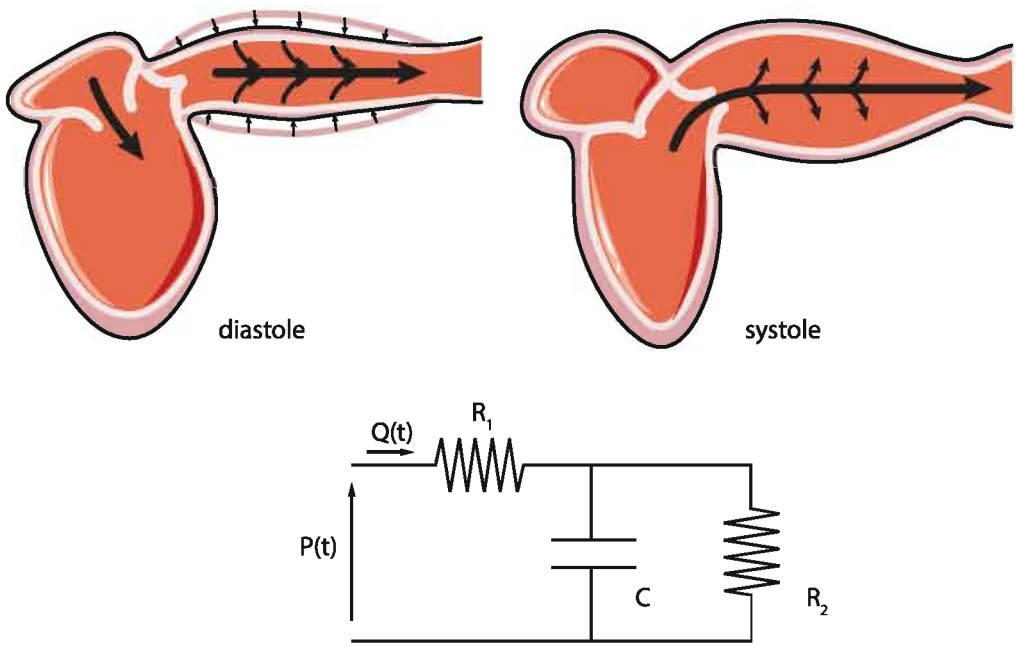

Figure 5.16: An open-loop RCR-LPN model imposing the arterial buffer function of the elastic arteries. This Windkessel circuit mathematically describes the pressure-flow interaction between the stroke volume and the compliance of the aorta and large elastic arteries (Windkessel vessels) and the resistance of the smaller arteries and arterioles. Images adapted from [317].

myocardial deformations [353]. Whereas flow and pressure boundary conditions (BCs) associated with truncations in the fluid domain have already been studied extensively using the aforementioned hemodynamic flow models, boundary conditions in the solid domain remain relatively uninvestigated. Consequently, a wide variety of strategies to mechanically anchor these ventricular models exists in the literature. Even though Niederer et al. [246] showed that the use of different anchoring strategies on a failing heart model has an influence on the predicted behavior, the appropriateness of such generic BCs remains insufficiently studied. Therefore, chapter 6 reviews the current diversity in kinematic boundary conditions found in literature and consequently develops a patient-specific biventricular (BV) model based on 4D tagged magnetic resonance imaging (TMRI) data, which will be used to systematically investigate the role of a subset of current boundary conditions on the modeled ventricular behavior at a global and local scale.

5.5 HEART FAILURE

Heart failure is a clinical syndrome caused by structural and functional defects in the myocardium resulting in impairment of ventricular filling or the ejection of blood [160]. This condition can be acute or chronic. Chronic

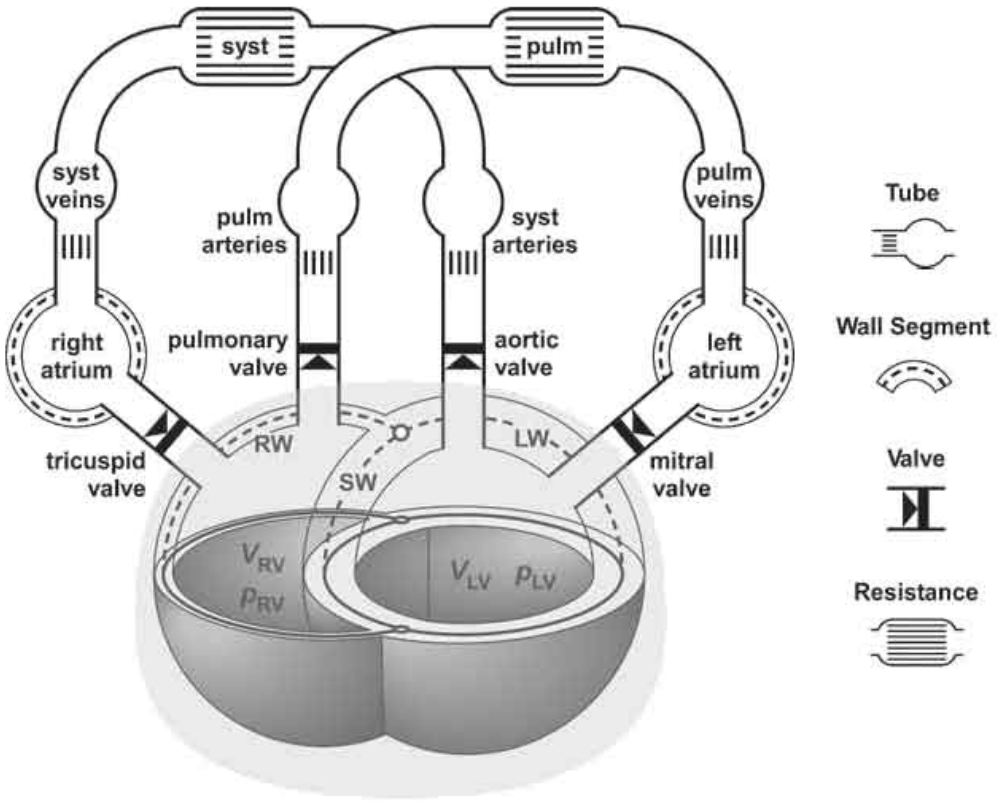

Figure 5.17: Schematic illustration of the closed-loop CircAdapt model which models cardiac hemodynamics by coupling the ventricles in a systemic circulation including atria, valves, arteries, organs and veins, each represented by their own conduit. Image adapted from [7, 213]

heart failure (HF) affects about 2% of the adult population worldwide. The prevalence of heart failure is age-dependent, ranging from less than 2% of people younger than 60 years to more than 10% of those older than 75 years [226]. Patients with heart failure have a poor prognosis, with high rates of hospital admission and a 5-year mortality rate of 50%. Despite current worldwide efforts and recent advancements of pharmaceutical, surgical, device and tissue engineering therapies, projections show that chronic HF will remain a leading cause of morbidity and mortality worldwide in the foreseeable future [360].

The pathophysiology of chronic heart failure is that of a progressive condition. Apart from abnormal heart rythms (see section 5.2) and coronary artery disease (leading to ischemia), common risk factors for HF involve high blood pressure (hypertension), malfunctioning heart valves and congenital heart defects. Overall, these etiologies all force the heart to work harder to effectively pump blood around. To accommodate excessive cardiac energy expenditure and workload, neurohormonal, chemical and mechanical cues induce adaptive or maladaptive processes in the myocardium that are

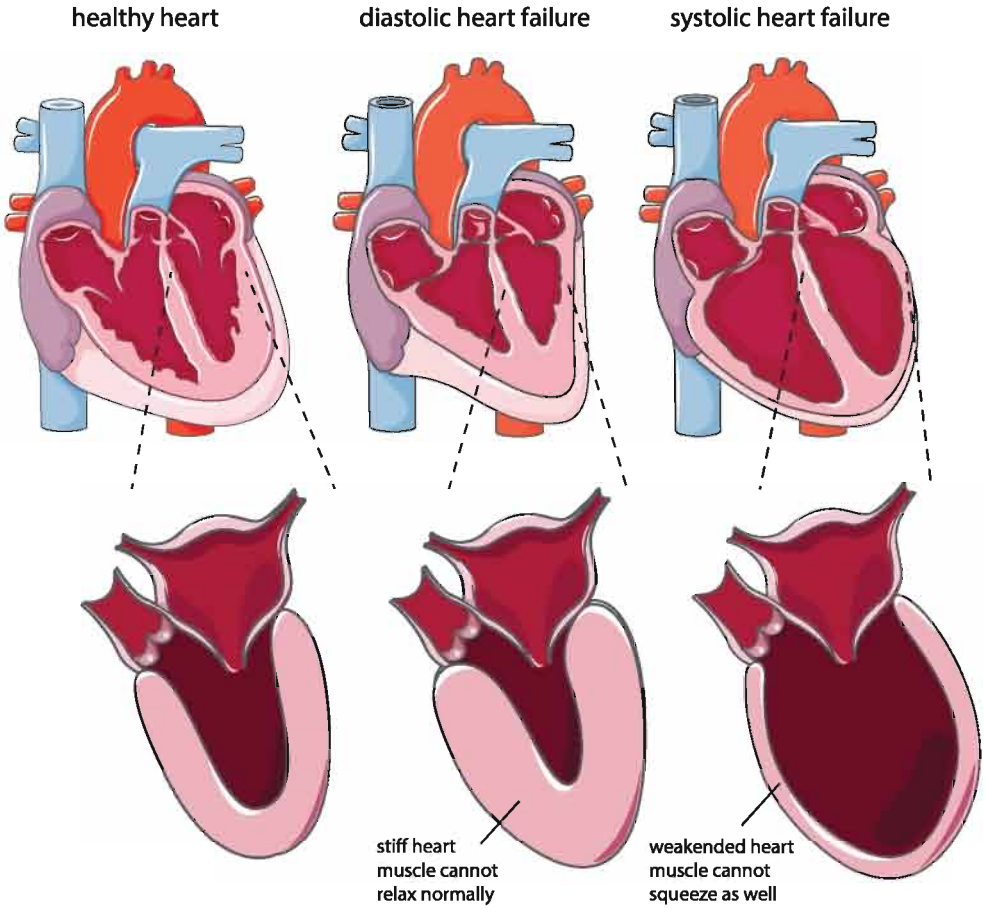

Figure 5.18: The two major patterns of chronic heart failure. In diastolic heart failure, concentric hypertrophy and wall stiffening result in inadequate ventricular filling during diastole and a subsequent decrease in stroke volume (SV) and cardiac output (CO). In systolic heart failure, eccentric hypertrophy leads to stretched and dilated ventricular tissue, making it weaker. Consequently, the myocardial contractile function is impaired, resulting in a decreased SV and CO. Image adapted from [317]

commonly referred to as *cardiac growth and remodeling* [262]. Although HF is a heterogeneous condition with many different causes, all etiologies eventually activate a final common pathway with similar mechanisms that become, at least partially, independent from the initial cause [226]. Based on the worsening progressive anatomical changes that the myocardium undergoes during progressive HF, we can discriminate between diastolic and systolic heart failure, as depicted in Figure 5.18. Diastolic HF is typically associated with a chronic pressure overload where the cardiac muscle has to contract while experiencing an excessive *afterload*. This afterload can be caused by hypertension, stenosis (being it arterial or pulmonary) or a coarctation of the aorta. Structurally, chronic pressure overload leads to *concentric hypertrophy*, which causes the myocardial wall to gradually become stiffer and thicker leading to inadequate ventricular filling during diastole. On the cell scale, concentric hypertrophy is associated with parallel

sarcomere additions increasing the wall thickness and an increase in cardiac fibroblasts with consequent fibrosis increasing ventricular stiffness [349]. Systolic heart failure on the other hand, is mostly associated with volume overload where one of the heart chambers is filled with too large a blood volume for it to function efficiently (related to the aforementioned Frank-Starling mechanism (section 5.3.2) and more general to the strength-tension relationship of muscle cells in section 2.2). Consequently, ventricular volume overload is approximately equivalent to an excessive *preload*. An excessive left-ventricular preload can be caused by aortic and/or mitral regurgitation, congenital heart defects including a patent ductus arteriosus or a ventricular septal defect, and arteriovenous malformations or fistula. For the right ventricle, tricuspid and/or pulmonary regurgitation and atrial septal defects can cause increased preloads. Structurally, this excessive preload induces *eccentric hypertrophy* causing the myocardial wall to dilate and impair systolic contractility. On the cell scale, eccentric hypertrophy is associated with cell elongation due to a serial deposition of additional sarcomeres [349].

Initially, these hypertrophic responses can be considered effective adaptive mechanisms to volume or pressure overload stimuli, and might even be well-tolerated for many years [174]. However, at a certain point in time, all salutary adaptive mechanisms get surpassed and overdilated ventricles comprise insufficient cardiac contractility (systolic heart failure) whereas a thick ventricular wall undermines the diastolic filling of the heart (diastolic heart failure). Next to its effect on the mechanical functioning of the heart (reduced cardiac output), these pathoanatomical changes also distort the heart's electrical activation and conductivity [173]. Consequently, the patient experiences an increasingly higher risk for ischemia, arrhythmia and sudden death. Therefore, the most pertinent clinical questions surrounding disorders leading to hypertrophy tend to be prognostic: even simply anticipating the rate of progression can be essential when planning treatment [357]. Even though the underlying genetic, molecular and neurohumoral mechanisms responsible for hypertrophy remain elusive [79, 194, 248, 262, 349], increasing evidence points to mechanical factors as mediating stimuli, both at the tissue and cellular levels. Consequently, mechanistic growth models have the potential to provide insight into the development of hypertrophy and guide clinical decision making, in addition to aiding in the design of device-based therapies to slow or reverse remodeling [357].

In section 2.3, we discussed the two main theoretical frameworks that exist to take into account growth and remodeling in the continuum mechanics problems we solve using the finite element method. Compared to the kinematic-based growth theory, the constrained mixture model is relatively more complex to work with, due to the need to computationally track

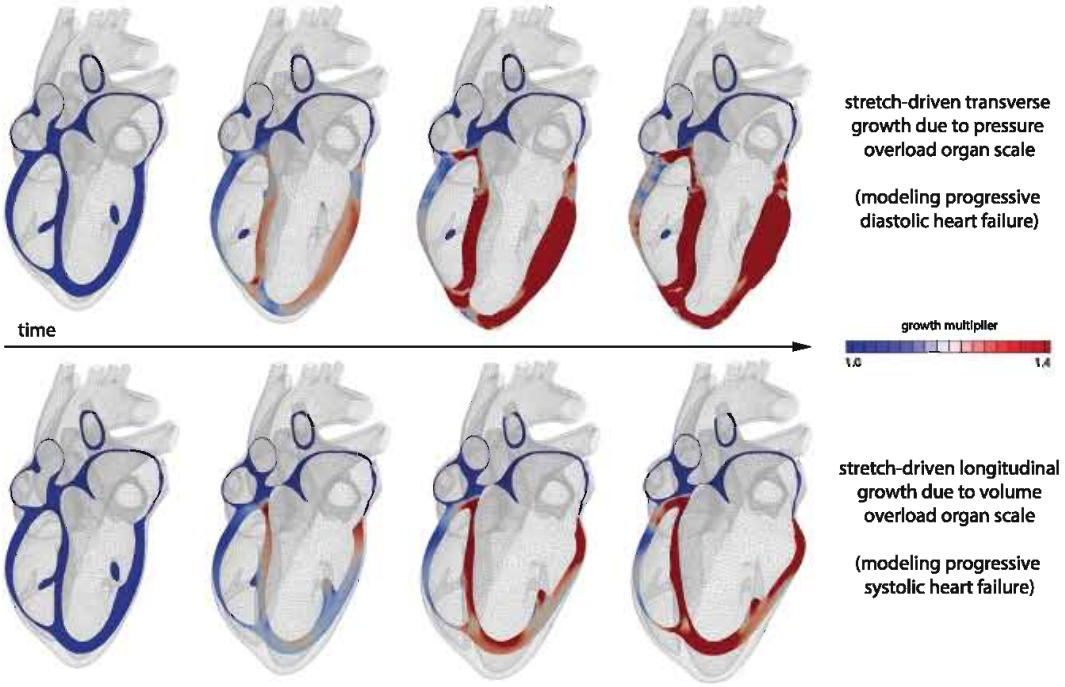

Figure 5.19: Kinematics-based multiscale cardiac growth modeling pathologies of diastolic and systolic heart failure on a full 4-chamber human heart model. Whole organ scale changes in hemodynamic pressure (top panels) and volume (bottom panels) overload respectively lead to transverse and longitudinal growth respectively using a stretch-driven growth law. The resulting predicted structural response of the myocardium did predict not only predict the primary effects of heart failure including ventricular wall thickening or dilation, but also the characteristic secondary effects including papillary muscle dislocation, mitral annular dilation, tricuspid annular dilation, regurgitant flow, and outflow obstruction. Showcased computational results taken from [96].

the evolving natural configurations of the constituents during growth and remodeling (G&R) and the lack of experimental data for cardiac constituent evolution in single well controlled experiments. Consequently, most cardiac G&R studies conducted over the last decade applied the kinematics-based growth theory. As shown by Genet et al. [96] in Figure 5.19, combining the computational cardiac modeling approach disclosed in this section with the kinematics-based growth theory provides a powerful tool to reveal how local changes in cytoskeletal architecture and cellular morphology translate into global alterations of whole organ form and function and vice versa. Assuming stretch-driven growth kinetics on a full four-chamber human heart model (LHHM, see Figure 5.15), multiscale kinematics-based cardiac growth modeling allowed them to naturally connect molecular events of parallel and serial sarcomere deposition with cellular phenomena of myofibrillogenesis and sarcomerogenesis to whole organ function prediction impacting wall thickness, chamber size and cardiac geometry that agrees favorably with the clinical observations.

Even though a stretch-driven kinematics-based multiscale growth model showed excellent qualitative agreement with the clinically observed progressive evolution of diastolic and systolic heart failure, there is still considerable debate around the underlying mechanistic stimuli that trigger cardiac growth. In eccentric hypertrophy for example, initial studies suggested that the end-diastolic wall stress would trigger cardiac dilation [124], while later studies opposed this hypothesis and suggested the end-diastolic wall stretch as a stimulus for cardiac growth [257]. To identify the best basis for formulating growth models, it is critical to quantify the predictive power of a model in tight correlation with experimental data. However, such an assessment is challenging for multiple reasons: First, the highly patient-specific time course and extent of disease progression associated with hypertrophy calls for subject-specific data collection and modeling; second, the multiscale nature of cardiac growth requires the characterization at multiple spatial scales ranging from the subcellular via the cellular to the whole organ level; third, the intrinsic uncertainty associated with sparse experimental data has a strong influence on the predicted outcome. Therefore, chapter 7 proposes a novel approach to quantify the predictive power of cardiac growth modeling using a unique chronic volume overload study, multiscale subject-specific kinematics-based growth modeling and machine learning techniques to quantify and propagate uncertainty on experimentally sparse data through the models.

CHAPTER 6

ACCOUNTING FOR SURROUNDING TISSUE IN VENTRICULAR MODELING

This chapter* reviews the current diversity in kinematic boundary conditions found in literature and consequently develops a patient-specific biventricular (BV) model based on 4D tagged magnetic resonance imaging (TMRI) data, which will be used to systematically investigate the role of a subset of current boundary conditions on the modeled ventricular behavior at a global and local scale. In vivo measured strains are used as a reference to quantify and determine the more appropriate boundary conditions (BCs) to be used for ventricular modeling.

6.1 INTRODUCTION

Cardiac computational models are gaining interest in the clinical community as a tool to better understand cardiac function and to investigate new therapies. Patient-specific biophysical models of cardiac behavior have proven competent in elucidating the fundamentals of cardiac (patho)physiology.

*This chapter is based on M. Peirlinck, K. L. Sack, P. De Backer, P. Morais, P. Segers, T. Franz, and M. De Beule, "Kinematic boundary conditions substantially impact in silico ventricular function", *International Journal for Numerical Methods in Biomedical Engineering*, vol. 35, no. 1, e3151, 2019

Recently, computational models have been used to help clinicians diagnose, to evaluate drug effects, to gain better insight on risk-benefit ratios and to predict the outcome of different treatment strategies [13, 21, 163, 171, 179, 186, 193, 292, 298, 312, 338, 339]. Even though full four-chamber heart models [14] are the most comprehensive, the application of such models in the clinical environment is challenging because the available imaging data resolution is often insufficient to accurately segment the atrial wall, which is typically an order of magnitude thinner than the ventricular wall. Moreover, the development and calibration of these models also demands more, typically unavailable, sources of clinical data (i.e. pressure catheter measurements, strain imaging, MRI diffusion tensor imaging, etc.). However, it is increasingly feasible to construct patient-specific BV models from clinical data, where the computational domain is truncated at the base and thus limited to the left ventricle (LV) and right ventricle (RV). Despite the absence of surrounding tissue (e.g. atria, valves, proximal arteries), these models are of clinical relevance and the influence of the absent surrounding structures on the modeled ventricles is accounted for by imposing kinematic BCs. In order to incorporate the influence of external tissues and organs tethering and constraining the movement of these ventricles, one could directly prescribe displacements inferred from the image sequence as time-dependent Dirichlet BCs [8], but this approach would have a limited predictive character. Therefore, the choice to use more generic BCs is often pursued. Whereas flow and pressure BCs associated with truncations in the fluid domain have already been studied extensively (see section 5.4.3.1), boundary conditions in the solid domain remain relatively uninvestigated. Consequently, a wide variety of strategies to mechanically anchor these ventricular models exists in the literature. Even though Niederer et al. [244]showed that the use of different anchoring strategies on a failing heart model has an influence on the predicted behavior, the appropriateness of such generic BCs remains insufficiently studied.

6.2 CURRENTLY USED KINEMATIC CONSTRAINTS

Despite the wide range of (bi)ventricular modeling studies found in literature, no consistent approach in incorporating the effect of external tissue support into these models could be found (we considered a non-exhaustive subset of (bi)ventricular modeling studies (published over the last decade) where generic kinematic BCs were used, see Table 6.1). Overall, most studies adopted the practice to apply Neumann BCs (see Eq. 1.19b) on the endocardial surface and to constrain basal out-of-plane motion by constraining the basal nodes not to move along the basal surface's normal direction (be it using an exact or penalty-method based Dirichlet BC (see Eq. 1.19a). The former practice accounts for the hemodynamic pressures within the ventricles during

the cardiac cycle whereas the latter practice is often justified by the anatomical presence of relatively rigid fibrous tissue in which the atrioventricular valves are embedded.

When considering the basal surface some studies completely constrain all degrees of freedom (DOFs) of all basal nodes [18, 64, 97, 166], of all nodes on the inner and outer basal endo- and epicardial rings [355], or the basal epicardial ring only [128, 244]. Others constrained nodes in the basal plane's circumferential direction, being it all basal nodes [86, 182] or just the nodes on the basal epicardial ring [1, 333, 351]. Another strategy to restrict free body rotation of the model relied on fixing two different nodes A and B on the basal surface in one and two in-plane directions, respectively [187, 250]. Weaker alternative boundary conditions entailed constraining the average translation and rotation of the basal nodes [273] or incorporating linear springs that attached the basal endocardial nodes (the so called 'valve vertices') to their reference position [43, 218, 316]. Tuning the stiffness values of these springs allowed for a small movement of the (absent) valves. Other studies [1, 66, 350] incorporated a Robin-type boundary condition (see Eq. 1.20), which translates to applying traction to penalize excessive displacements (elastic constraint) and excessive displacement rates (viscoelastic constraint). The few studies that account for the pericardium, the conical sac of fibrous tissue surrounding the heart, introduced additional kinematic BCs on the ventricular epicardial surface. These epicardial BCs range from constraining the epicardium not to move along the surface normal [359] or in the circumferential direction [263] to elastic constraints [76, 363], viscoelastic constraints [359] or both elastic and viscoelastic constraints (Robin-type BCs) [140]. A few studies also constrained the movement of the apex, in all directions [1, 244, 264] or only in the lateral directions [20]. Table 6.1 gives an overview of the variety in BCs we found in the studies considered. In this study, we selected 5 different kinematic BC cases to compare, which are discussed in more detail in section 6.3.2.

6.3 METHODS

In vivo imaging data was used to segment a subject-specific biventricular geometry and also to quantify the in vivo strains, which were quantitatively compared against the in silico strains of multiple BC cases.

First, we discuss the in vivo imaging data analysis performed to evaluate the in vivo strains and to segment the patient-specific ventricular geometry for the finite element models to be computed in the *Abaqus* finite element analysis (FEA) solver. Next, the studied kinematic boundary condition cases are discussed, followed by the hemodynamic pressure loading conditions

Table 6.1: Overview of kinematic boundary conditions of in silico ventricular studies published over the last decade. All these models entailed a Dirichlet zero boundary condition on longitudinal motion of the base, except for the * cases where axial basal translation was incorporated to ensure a still apex. The ‡ case only constrained the longitudinal displacement on the epicardial ring of the base. (R, θ and Z denote radial, circumferential and longitudinal direction respectively; RF reaction force; k and c are tunable parameters; LV left ventricular model; BV biventricular model).

Type	Description	Study and geometry		
Basal surface ∂V_{base}	$u_Z = 0$ for all			
Fully constrained	$u_R = u_\theta = 0$	Genet et al. (2014) [97]	LV	
		Dorri et al. (2006) [64]	LV	
		Berberoglu et al. (2014) [18]	LV	
		Land et al. (2015) [188]	LV	
		Jiang et al. (2015) [166]	BV	
Rotationally constrained	$u_\theta = 0$	Gao et al. (2014) [86]	LV	
		Krishnamurthy et al. (2013) [182]	BV	
Two-node-fix in basal plane	$u_{R,\text{nodeA}} = u_{\theta,\text{nodeA}} = 0$	Nordbo et al. (2014) [250]	LV	
	$u_{R,\text{nodeB}} = 0$	Lamata et al. (2011) [187]	BV	
Fully constrained epi-ring	$u_{R,\text{epi}} = u_{\theta,\text{epi}} = 0$	Gültekin et al. (2016) [128]	LV	
		Niederer et al. (2009) [244]	LV	
Rotationally constrained epi-ring	$u_{\theta,\text{epi}} = 0$	Wang et al. (2013) [351]	LV	
		Sun et al. (2009) [333]	LV	
		Walker et al. (2005) [350]	LV	
		Eriksson et al. (2013) [66]	LV	‡
		Aguado-Sierra et al. (2011) [1]	BV	
Fully constrained endo- and epi-ring	$u_{R,\text{epi}} = u_{\theta,\text{epi}} = 0$	Wenk et al. (2013) [355]	BV	
	$u_{R,\text{endo}} = u_{\theta,\text{endo}} = 0$			
Constrained mean translation and rotation	$\bar{u}_R = \bar{u}_\theta = 0$	Pezzuto and Ambrosi (2014) [273]	BV	
Elastic constraint	RF = $k\Delta u_{\text{endo}}$	Sermesant et al. (2008) [316]	BV	
		Marchesseau et al. (2013) [218]	BV	
		Cutrì et al. (2016) [43]	BV	
Robin-type BC	RF = $k\Delta u + c\dot{u}$	Gerbi et al. (2017) [101]	LV	
		Sainte-Marie et al. (2006) [304]	BV	*
		Hirschvogel et al. (2017) [140]	BV	
		Landajuela et al. (2018) [189]	BV	
Epicardial surface ∂V_{epi}				
Constrained outward movement	$u_\perp = 0$	Wong et al. (2010) [359]	BV	
Circumferentially constrained	$u_\theta = 0$	Palit et al. (2015) [263]	BV	
Elastic constraint	RF = $k\Delta u$	Ponnaluri et al. (2017) [275]	LV	
		Xi et al. (2016) [363]	BV	
		Finsberg et al. (2018) [76]	BV	
Viscoelastic constraint	RF = $c\dot{u}$	Wong et al. (2010) [359]	BV	
Robin-type BC	RF = $k\Delta u + c\dot{u}$	Gerbi et al. (2017) [101]	LV	
		Hirschvogel et al. (2017) [140]	BV	
Apex ∂V_{apex}				
Fully constrained	$u = 0$	Niederer et al. (2009) [244]	LV	
		Aguado-Sierra et al. (2011) [1]	BV	
		Palit et al. (2017) [264]	BV	*
Lateral apex constraint	$u_R = u_\theta = 0$	Bettendorff-Bakman et al. (2008) [20]	BV	

that incorporated the changing blood volume loads endured by the ventricles during the cardiac cycle. The fourth section focuses on the incorporation of realistic cardiac tissue behavior by implementing an intricate myofiber architecture in combination with passive and active tissue behavior using constitutive models with parameters tuned to the considered patient. The final methods section discusses the metrics used to compare the in-silico results of the different cases reciprocally and with the in vivo measured myocardial strain distributions.

6.3.1 In vivo imaging analysis

The images were acquired from a healthy 39-year-old male (weight: 81.65 kg, height: 1.8 5m, heart rate upon acquisition 71 bpm) who underwent magnetic resonance imaging (MRI) with Spatial Modulation of Magnetization. Twenty short axis and six long axis images at 22 discrete time points during one heart cycle were collected. This 4D TMRI data was provided under a Creative Commons ANC Use Agreement on the *SimTK* platform [97]. The short-axis MRI slices had an in-plane resolution of 1.1 x 1.1 mm with a 5 mm slice thickness and two series of tags, forming an orthogonal grid caused by the modulation of the magnetization gradient at the onset of systolic contraction. The long-axis MRI slices had a resolution of 1.1 x 1.1 mm and were oriented circumferentially at an interval of 30° around the LV. They contained one series of tags orthogonal to the ventricular long axis. The imposed grid's tag spacing was 6 mm in both short- and long-axis images.

6.3.1.1 Quantification of myocardial strain

The systolic regional strains in the LV wall of each subject were computed from the tagged magnetic resonance (MR) images using the *Segment* software (Medviso - Lund, Sweden). We started by manually segmenting the endo- and epicardial walls of the LV myocardium and defining the segmental model as described in [31]. Then, each contour (with a total of 5 concentric contours through the wall thickness) is automatically propagated throughout the entire sequence through a non-rigid image registration approach. In detail, the image registration algorithm uses an iterative strategy to estimate dense inter-frame displacement maps modeled through a B-spline tensor product transform, posteriorly applying these dense maps to estimate the specific displacement value of each contour position. In order to increase the tracking method's robustness to image artifacts or noise, the spatial and temporal information of the entire cardiac sequence are taken into account at once [232]. Finally, the spatial differences between contours in each frame are used to compute the strain values as described in [231]. Short-axis and long-axis sequences were processed independently. This procedure can subsequently also be used to compute the top basal diastolic

Figure 6.1: Interpolation of TMRI registered diastolic tissue displacement from the LV top basal short axis image slice to top surface nodal displacements of the finite element mesh.

tissue displacement to quantitatively inform realistic boundary conditions as depicted in Figure 6.1.

6.3.1.2 Subject-specific ventricular geometry

The subject-specific biventricular geometry depicted in Figure 6.2 was manually segmented in both the short- and long-axis TMRI images that correspond to the beginning of diastole, which was assumed to correspond to the relaxed (i.e. unloaded) configuration (see also chapter 8). This segmentation was done using the *Mimics* software suite (Materialise - Leuven, Belgium). The ventricular geometry was truncated right underneath the mitral valve, at the first proximal short axis slice where the papillary muscles showed up. The resulting endo- and epicardial surfaces were imported into *Simpleware*'s FE module to create a finite element mesh consisting of 30,891 quadratic tetrahedral elements. The mesh density was chosen such that the myocardial walls consisted of multiple element layers through its depth (minimally 3 quadratic elements). Multiple elements throughout the wall thickness are needed to allow for a smooth transitioning of the fiber orientation field (see section 6.3.4.1) and to get detailed information on the transmural differences in tissue loading. To allow for regional comparisons between different model simulations, the LV was partitioned into the 17 AHA

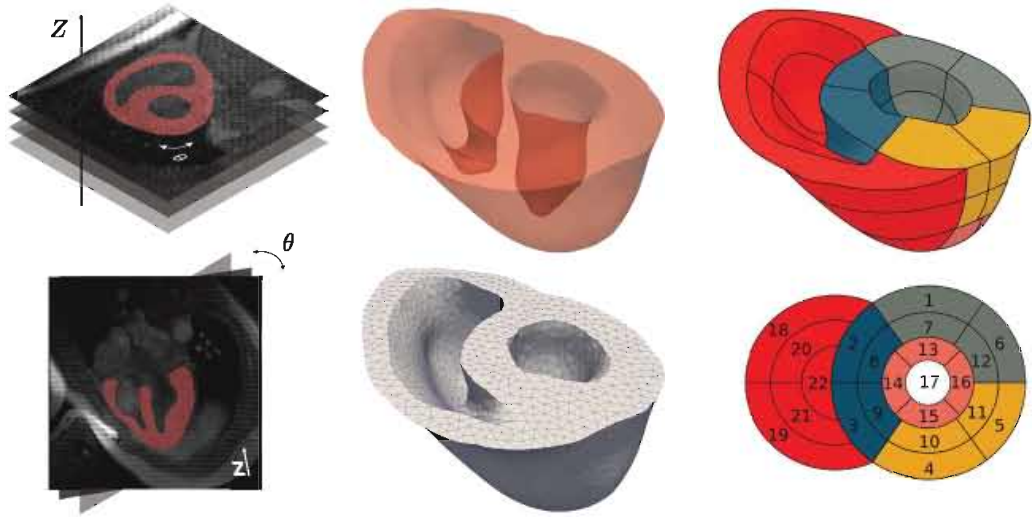

Figure 6.2: From image data to patient-specific computational biventricular mesh. Twenty short-axis slices (top left) and six rotational long-axis slices (bottom left) were segmented to come to the smoothed transparent geometry shown mid top. This geometry was transformed into the quadratic tetrahedral mesh shown mid bottom. This BV geometry was subsequently partitioned into 17 regions for the LV and five regions for the RV. The top right image portrays the segmentation in 3D, and the bottom image provides a corresponding 2D representation with American Heart Association (AHA) region numbers.

regions [31]. This partitioning system was extended to the RV free wall, where we used the same longitudinal and circumferential divisions to introduce 5 regional partitions to the RV free wall, as illustrated in Figure 6.2 (right).

6.3.2 Kinematic boundary conditions

Figure 6.3 depicts the 5 different boundary conditions cases that were investigated, for which we used two different kinds of constraints in the *Abaqus* FEA framework: exactly imposed Dirichlet BCs (see Eq. 1.19a) and continuum distributed coupling constraints. The latter couple the translation of a reference node to the average translation of a set of coupling nodes [46]. In the cases where we used continuum distributed coupling constraints, we added a reference node to the model located at the center of mass of the group of to-be-constrained nodes. This reference node was then fixed in all directions, which results in a zero-average translation and rotation of all coupled nodes, without constraining each of these nodes to translate or rotate individually.

As can be seen from Table 6.2 which summarized the five studied BC cases, each case constrained any longitudinal movement of the basal nodes. In case 1, we fixed all basal top surface nodes in the other two directions as well, similar to [18, 64, 97, 166]. In case 2, all DOFs of the nodes lying

Table 6.2: Studied boundary condition cases. Each row defines complementary conditions to the conditions defined in the rows above. u_R, u_θ, and u_Z denote (constrained) degrees of freedom in the radial, circumferential, and longitudinal direction, respectively. $\bar{u}_R$ and $\bar{u}_\theta$ denote a continuum distributed coupling of the overall (constrained) motion of these nodes in the radial and circumferential direction, respectively.

	Case 1	Case 2	Case 3	Case 4	Case 5
Basal top	$u_R = u_\theta = u_Z = 0$	$u_Z = 0$	$u_Z = 0$	$u_Z = 0$	$u_Z = 0$
Epicardial ring		$u_R = u_\theta = 0$	$\bar{u}_R = \bar{u}_\theta = 0$		
Endocardial ring				$u_R = u_\theta = 0$	$\bar{u}_R = \bar{u}_\theta = 0$

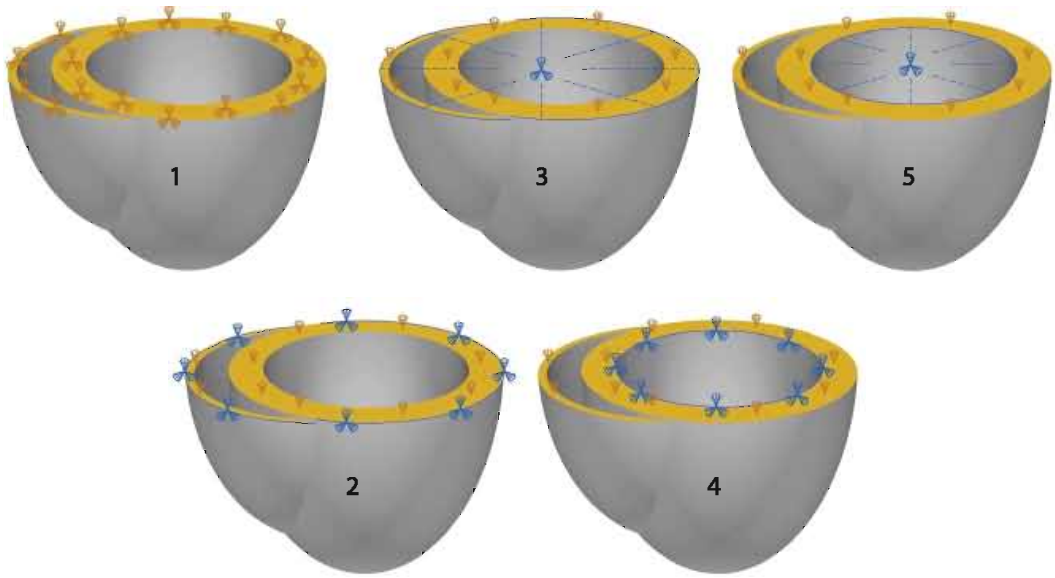

Figure 6.3: Schematic illustration of the studied boundary condition cases.

on the biventricular epicardial ring were fixed, in correspondence with [128, 244, 263, 355]. Instead of fixing all basal-epicardial nodes' DOFs, case 3 constrained the motion of these nodes to the translation and rotation of a fixed node located at the basal-epicardial edge's center of mass using the aforementioned continuum distributed coupling approach. This strategy indirectly constrained the epicardial base ring so it remained free to move in the top basal surface given that its averaged displacement with respect to the central reference node remained zero. Thus, relative displacements between the constrained nodes individually were allowed. Case 2 and 3 embodied the influence of the pericardial stiffness on the base. In case 4, we constrained all nodes that sit on the basal LV endocardial ring in all directions, which is different from [355] where both the basal endo- and epicardial ring were fixed in all directions. In case 5, the surrounding tissue constraining the ventricles was approximated by defining a continuum distributed coupling constraint of all basal LV endocardial nodes to a fixed node located at the center of mass

of the basal LV endocardial ring, similar to case 3 for the basal epicardial ring. Case 4 and 5 encompassed two different methods to incorporate the effect of the fibrous structure around the valves into the ventricular behavior.

Different from elastic constraints using a soft penalty-based method to impose displacement boundary conditions [359] or spring-like elements [76, 140, 218, 316, 363], the continuum distributed coupling constraint used in this study does not call for the tuning of a soft penalty or spring stiffness value. The continuum distributed coupling constraint relates more to the BCs imposed to the ventricular model in [273], but instead of constraining all the basal nodes, case 3 and 5 only constrained the average translation and rotation of the epi- and endo-cardial ring respectively. Consequently, both case 3, 4 and 5 can be considered newly proposed kinematic BCs.

6.3.3 Hemodynamic pressure loading conditions

As discussed in section 5.4.3.1, tuned hemodynamic lumped parameter network (LPN) models are the most convenient method to incorporate the load experienced by the heart to pump blood through the systemic or pulmonary arterial systems. Therefore, we equipped our subject-specific computational BV model with the open looped lumped parameter circulatory model depicted in Figure 6.4. Using this LPN, we mathematically described both arterial system's afterloads using 3-element Windkessel models, in which R_{Ao} and R_{PA} represent the characteristic impedance of the proximal aorta and pulmonary artery, R_{art} and R_{pulm} defines the peripheral systemic and pulmonary arterial resistance and C_{art} and C_{pulm} represent the systemic and

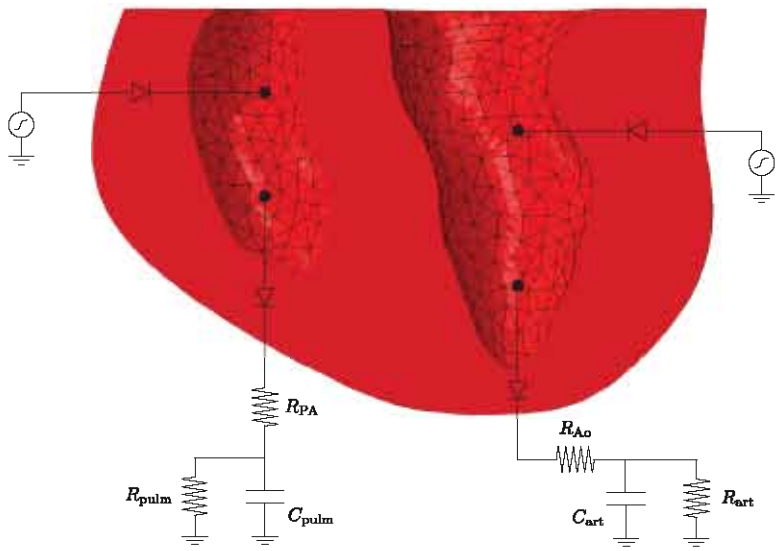

Figure 6.4: Open loop lumped parameter circulatory model which implements hemodynamically realistic pressure loading conditions on the left and right ventricle cavity of the patient-specific biventricular mechanical model.

pulmonary arterial circulation compliances. These afterload Windkessel models were coupled to the LV and RV cavities of our patient-specific biventricular mechanical model and provide realistic hemodynamic loading conditions so that both ventricles experience a dynamic afterload during ejection.

To implement this LPN in *Abaqus*, we set up two additional fluid cavities defined as cubic volumes representing the (proximal) systemic and pulmonary circulation systems. Each of these cavities is allowed to expand/shrink through one single free wall connected with a grounded spring. The stiffness of this spring is tuned to provide the appropriate pressure-volume response (i.e. compliance C_{art} or C_{pulm}) for that specific cavity. Blood flow between the ventricular cavities and the systemic/pulmonary fluid cavities, and between the systemic/pulmonary fluid cavities and the environment (i.e. the rest of the body) is modeled using *Abaqus*'s fluid exchange capabilities. More specifically, the fluid exchange's mass flow rate $\dot{m}$ and pressure difference Δp are controlled by

$$\Delta pA = C_V \dot{m} + C_H \dot{m}|\dot{m}| \tag{6.1}$$

where A is the effective exchange area, C_V is the viscous resistance coefficient, and C_H is the hydrodynamic resistance coefficient [46]. Setting $C_H = 0$ and knowing that $\dot{m} = \rho \dot{V} A$ with ρ the mass density and $\dot{V}$ the volumetric flow rate, we can define the inter-cavity fluid exchange resistance as

$$\frac{\Delta p}{\dot{V}} = \frac{C_V \rho}{A} = R \tag{6.2}$$

As such, R_{Ao} and R_{PA} are defined using the viscous resistance coefficient and effective area defining the fluid exchange properties between the left ventricular fluid cavity and the systemic compliance fluid cavity and between the right ventricular fluid cavity and the pulmonary compliance fluid cavity respectively. Similarly, the set fluid exchange properties the systemic compliance fluid cavity and the environment and between the pulmonary compliance fluid cavity and the environment impose the LPN's R_{art} and R_{pulm} respectively.

Each ventricular cavity was connected to its own pressure source circuit component, which enforced the diastolic filling of both fluid cavities. We chose to fill the left and the right ventricle to a uniform pressure of 12 and 3 mmHg respectively, falling within the average healthy ranges of 4-12 mmHg and 1-8 mmHg for left and right ventricular end-diastolic pressure (EDP) [217]. 12 mmHg can be seen as an upper limit to healthy LV EDP ranges, but was chosen due to the discrepancy reported in other literature studies which record LV EDP in excess of 20mmHg [1, 263]. These pressure source components were implemented in *Abaqus* using smooth step amplitudes and cavity pressure boundary conditions.

6.3.4 Cardiac tissue behavior

The heart's structural architecture defines its function, so to study its mechanical behavior computational models need to numerically portray the internal architecture appropriately. In addition to determining boundary conditions (focus of this chapter), establishing an appropriate model requires the description of the geometry (ex supra), the underlying fiber arrangement of the myocardium and an anisotropic material description (including active and passive components). The material description requires calibration in order to capture the patient-specific functional performance (i.e. end-diastolic volume (EDV), stroke volume (SV), ejection fraction (EF), etc.). Here we detail each of these steps applied to the considered subject-specific BV model.

6.3.4.1 *Myocardial muscle architecture*

As discussed in section 5.4.2, diffusion tensor magnetic resonance imaging (DT-MRI) approaches are considered ideal to describe the patient-specific myofiber architecture. However, the typical unavailability of DT-MRI data in standard clinical practice requires us to use rule-based algorithms to define a realistic myocardial fiber distribution throughout the cardiac wall based on DT-MRI atlases, e.g. [210]. Here, we chose to implement Bayer et al.'s Laplace-Dirichlet Rule-Based (LDRB) algorithm [16, 156] in which the myofibers's helical angle varies transmurally from -41° in the sub-epicardium, the outer wall, to +66° in the sub-endocardium, the inner wall [210]. In summary, this algorithm implied solving a series of Laplace problems ϕ on the biventricular mesh where different Dirichlet boundary conditions were prescribed to the different regions of the biventricular boundary, see

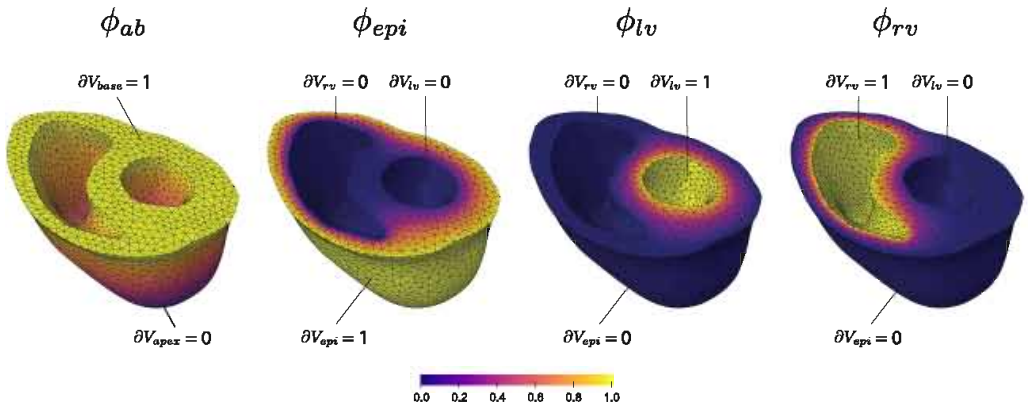

Figure 6.5: Solutions to Laplace's equation with different Dirichlet boundary condition sets. The gradients of the ϕ_{ab} and the combined ϕ_{epi}, ϕ_{lv} and ϕ_{rv} Laplace-Dirichlet scalar fields intrinsically provide an apicobasal and transmural vector for each mesh node respectively.

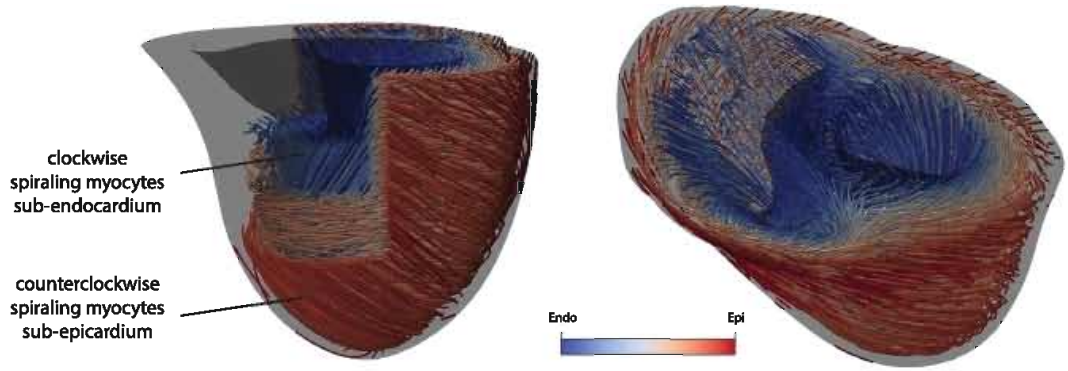

Figure 6.6: Laplace-Dirichlet Rule-Based (LDRB)-derived myofiber directions in the patient-specific BV model. The figure on the left side shows a peeled representation to visualize the internal (helical angle +66°) versus the external (helical angle -41°) myofiber orientation. The color scale depicts the gradient through the wall thickness.

Figure 6.5. By taking the gradient of these Laplace solutions, $\nabla\phi_{ab}$ is used to define the apicobasal direction, and $\nabla\phi_{epi}$, $\nabla\phi_{lv}$ and $\nabla\phi_{rv}$ are used to find the transmural directions. Next, we performed some vector operations and a sequential bidirectional quaternion spherical linear interpolation to describe smooth continuous fiber orientation between the RV and the LV and between the endocardium and epicardium respectively. This allowed us to recover a continuous fiber, sheet and sheet-normal orientation map at all nodes of the biventricular mesh. Finally, these local coordinate systems are interpolated to the elements' integration points, as showcased in Figure 6.6.

In a similar way, we established a local cylindrical coordinate system in each element, necessary to compute local strains in the radial, circumferential and longitudinal directions respectively.

6.3.4.2 *Passive and active constitutive modeling*

In section 5.3, we described the highly anisotropic microstructure of the myocardium and how different constitutive material models were proposed to inherently account for this structure's mechanical behavior. In section 5.3.2, we splitted the tissue's total stress response into a passive and an active contribution, $\boldsymbol{\sigma}_{\text{pass}}$ and $\boldsymbol{\sigma}_{\text{act}}$ respectively [110].

In this study (and dissertation), we describe the passive cardiac tissue behavior using Holzapfel and Ogden's invariant-based constitutive model [147] which currently serves as the standard passive material law for cardiac mechanics for the reasons discussed in section 5.3.2. Combined with an Arruda-Boyce material model to incorporate quasi-incompressibility

(paragraph 5.3.1.2.3), this leads to the following strain energy function (SEF)

$$\Psi = \frac{a}{2b}\exp\left[b\left(\bar{I}_1 - 3\right)\right] + \sum_{\alpha=f,s}\frac{a_\alpha}{2b_\alpha}\left(\exp\left[b_\alpha\left(\bar{I}_{4\alpha\alpha} - 1\right)^2\right] - 1\right) + \frac{a_{fs}}{2b_{fs}}\left(\exp\left[b_{fs}\bar{I}_{4fs}^2\right] - 1\right) + \frac{K}{2}\left(\frac{J^2-1}{2} - \ln(J)\right) \tag{6.3}$$

which is equivalent to Eq. 5.7.

In this study (and dissertation), we describe the active cardiac tissue behavior using the time-varying elastance model described in section 5.3.2. This elastance model accounts for the Frank-Starling effect (i.e., the intrinsic property of myocardium by which the strength of the heart's systolic contraction is directly proportional to its diastolic expansion [234]) by an imposed active stress response's dependence on regional sarcomere lengths. The choice for the given time-varying elastance model ensured a smooth yet steep transition from zero to peak active tension at time t_0 followed by a smooth decline back to zero for the specified relaxation time t_r [298]. Given that the tissue's active response is dependent on the cardiac cell's action potential (dependence on $[Ca^{2+}]_0$), we assumed a homogeneous action potential pulse throughout the whole biventricular model which varies from -80 mV to 20 mV to -80mV over 200ms as depicted in Figure 5.13. The active stress distribution is assumed to be entirely anisotropic, and combining Eqs. (5.12) and (5.13), we get

$$\boldsymbol{\sigma}_{act} = T_{act}\,\boldsymbol{f}_0 \otimes \boldsymbol{f}_0 + n_s T_{act}\,\boldsymbol{s}_0 \otimes \boldsymbol{s}_0 \tag{6.4}$$

where T_{max} is the maximum isometric tension achieved at the longest sarcomere length and maximum peak intracellular calcium concentration $[Ca^{2+}]_{max}$ and n_s is a scalar describing the fiber-sheet $\boldsymbol{f}_0$-$\boldsymbol{s}_0$ interaction (see section 5.3.2 for a more detailed description of the active material model).

Both the passive $(a, b, a_f, b_f, a_s, b_s, a_{fs}, b_{fs})$ and the active (T_{max}, n_s) constitutive material properties were found using optimization techniques minimizing the objective functions defined in Eqs. (5.8), (5.9) and (5.14). Summarizing these techniques, which are described in detail in sections 5.3.1.3 and 5.3.2: initial passive constitutive parameter values were taken from Table 5.1, whereby we identified material parameters that replicated the experimental triaxial shear data of normal human myocardium [326]. To adapt these material parameters to our patient-specific case, and to minimize any potentially unrealistic stiffening effects resulting from ex vivo tissue preparation, 'scaling' was needed. Here, linear (a, a_f, a_s, a_{fs}) and exponential (b, b_f, b_s, b_{fs}) terms were subject to uniform scaling by parameters α and β, a scalar and an exponential multiplier, respectively. These were found by

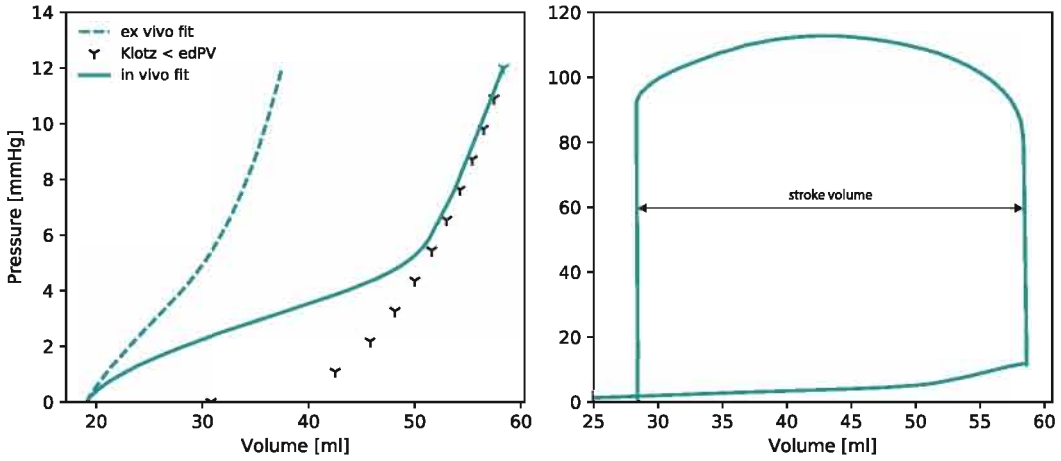

Figure 6.7: Second-stage passive and active myocardial tissue response calibration. Passive calibration (left): dashed lines represent the diastolic filling pressure-volume relation using the first-stage passive myocardial tissue response calibration from Figure 5.12 and Table 5.1 [326], 'tri' markers depict the theoretical diastolic pressure volume relation deduced from the experimentally measured subject-specific end diastolic pressure volume data [177] and solid lines depict the passive material response fitted to represent the subject-specific passive in vivo response. Active calibration (right): solid lines depict the active material response fitted to represent the in vivo contractility based on the stroke volume.

minimizing the error between the in silico diastolic pressure-volume (PV) relation and the analytical Klotz curve [177], which is capable to describe the end-diastolic PV relation of the normal and diseased ventricle. Material parameters were calibrated using *Abaqus* as the forward solver and an in-house *Python* script containing the sequential least squares programming optimization algorithm [169]. This resulted in passive parameters that enable the LV to be loaded from the initial LV volume V_0 until the EDV was reached at the specified EDP (a = 0.0943 kPa, b = 5.874, a_f = 0.311 kPa, b_f = 11.271, a_s = 0.0431 kPa, b_s = 9.772, a_{fs} = 0.0254 kPa and b_{fs} = 2.405). Once passive parameters were found, the active parameter T_{max} was identified (T_{max} = 71.08 kPa) by minimizing the error between predicted and specified stroke volume and assuming that 25% of active tension was transferred in the sheet direction (i.e. n_s = 0.25). To minimize the error between the in silico diastolic PV relation and the analytical Klotz curve, a choice for one specific kinematic boundary condition case had to be made prior to the actual comparison of the different boundary condition cases. Based on the registered diastolic tissue displacement from the LV top basal short axis 4D TMRI image slice (ex infra: Figure 6.1), it was seen that the full septal wall deforms freely which qualitatively encourages a choice for boundary condition case 3 or 5. Here, we chose to use BC case 5 to tune the constitutive parameters because this BC case follows the classic reasoning of a stiffer

annular tissue around the aortic valve more and it is a boundary condition that can also be applied to LV models. The result of this in vivo tuning for both the passive and active constitutive parameters is depicted in Figure 6.7.

6.3.5 Experimental design

The aforementioned boundary condition cases led to five ventricular cardiac cycle simulations run in *Abaqus*, where all conditions (e.g. geometry, myofiber orientation field, hemodynamic loading conditions, constitutive parameters) were kept constant except for the kinematic boundary conditions themselves. The corresponding FEA results were subsequently post-processed so we could rigorously compare regional systolic strain distributions with the processed in vivo TMRI results for validation purposes. Apart from a qualitative regional comparison of systolic strain distributions, we quantitatively compared in silico versus in vivo results in terms of Cohen's d size effect, which expresses the standardized difference between each case's systolic strains and the TMRI results as follows:

$$d_{i,j} = \frac{\bar{\varepsilon}^{G}_{\mathrm{FEA}_{i,j}} - \bar{\varepsilon}^{G}_{\mathrm{TMRI}_i}}{\varsigma^{*}_{i,j}} \tag{6.5}$$

where ε^G is the Green-Lagrangian strain (Eq. 1.6), i stands for the considered AHA region (given that the TMRI tissue-tracking algorithm only gave us access to the LV systolic strains we could only compare AHA regions 1 to 16 shown in Figure 6.2), j is the considered boundary condition case and ς^* stands for the pooled standard deviation

$$\varsigma^{*}_{i,j} = \sqrt{\frac{\left(n_{\mathrm{FEA}_{i,j}} - 1\right)\left(\varsigma_{\varepsilon^{G}_{\mathrm{FEA}_{i,j}}}\right)^{2} + \left(n_{\mathrm{TMRI}_i} - 1\right)\left(\varsigma_{\varepsilon^{G}_{\mathrm{TMRI}_i}}\right)^{2}}{n_{\mathrm{FEA}_{i,j}} + n_{\mathrm{TMRI}_i} - 2}} \tag{6.6}$$

where n is the amount of systolic strain measurements and ς the standard deviation. These in silico and in vivo Green-Lagrangian strains were compared in the circumferential direction given that the TMRI data had the highest intrinsic tag density resolution in the circumferential direction.

Subsequently, we compared the effects that different mechanical boundary conditions had on global cavity metrics (such as pressure-volume loops, stroke volumes and ejection fractions) and both the global and regional stress and strain distributions. We performed one-way analysis of variance (ANOVA) on the regional strain distributions to determine whether there are any statistically significant differences between the means of the different cases. Given that Green-Lagrangian strain is a 3D-tensor, we conducted these one-way ANOVA tests on a strain invariant, the maximum principal strain, in each region. Next, we performed post hoc paired t-tests to localize statistically significant strain differences between the different cases specifically.

6.4 RESULTS

6.4.1 In vivo strain analysis

Regional systolic strains (radial and circumferential) derived from the in vivo imaging analysis are depicted in Figure 6.8. The TMRI systolic longitudinal strains were excluded given that white noise and lower resolution in the long axis slices led to suboptimal results. The systolic circumferential Green strains in the LV were -0.095 ± 0.050 in the basal region, -0.115 ± 0.044 in the mid region and -0.110 ± 0.029 in the apical region. The systolic radial Green strains were 0.084 ± 0.151, 0.112 ± 0.185 and 0.024 ± 0.062 respectively in the aforementioned regions. Overall, we see smaller variances in the circumferential strains compared to the radial strains. The most important result can be seen in the basal surface experiencing non-zero strain. Figure 6.1 depicts the interpolated radial and circumferential displacement to the base nodal surface (from the finite element (FE) model) extracted from the TMRI tissue-tracking algorithm. Both the endo- and epicardial LV basal ring experience circumferential and radial strains that appear qualitatively similar to the surrounding tissue.

6.4.2 Model validation

The systolic strains in the myofiber directions are depicted in Figure 6.9 for all 5 cases. Although the inter-case strain differences might seem minimal, they are quite substantial in the basal zones. Note for example the smaller contractile strains in case 1 and 4 compared to case 2, 3 and 5 in the basal

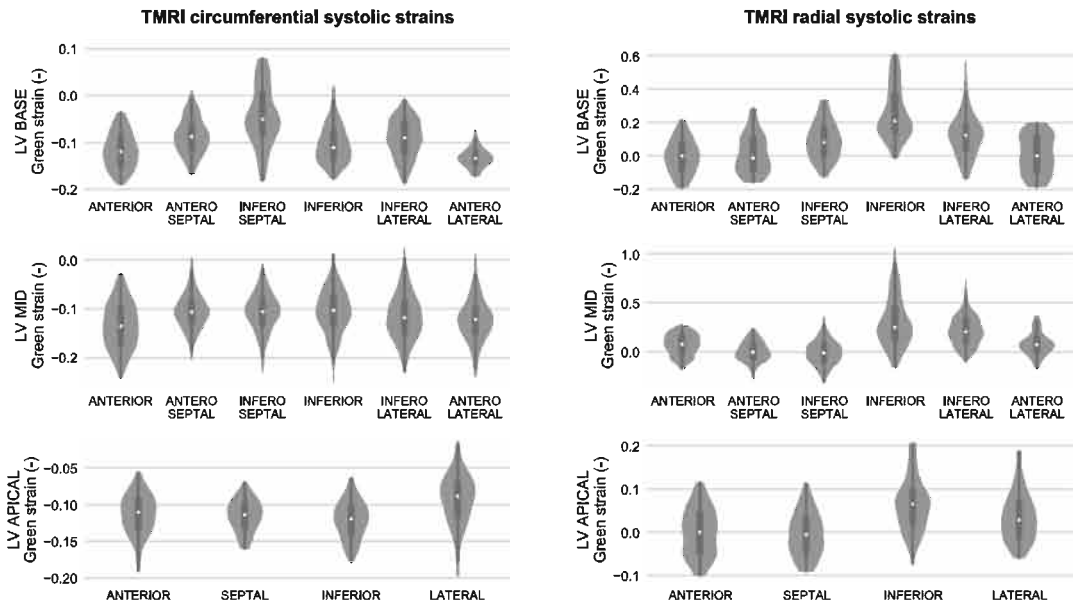

Figure 6.8: Tagged MRI results: systolic circumferential (left) and radial (right) strains.

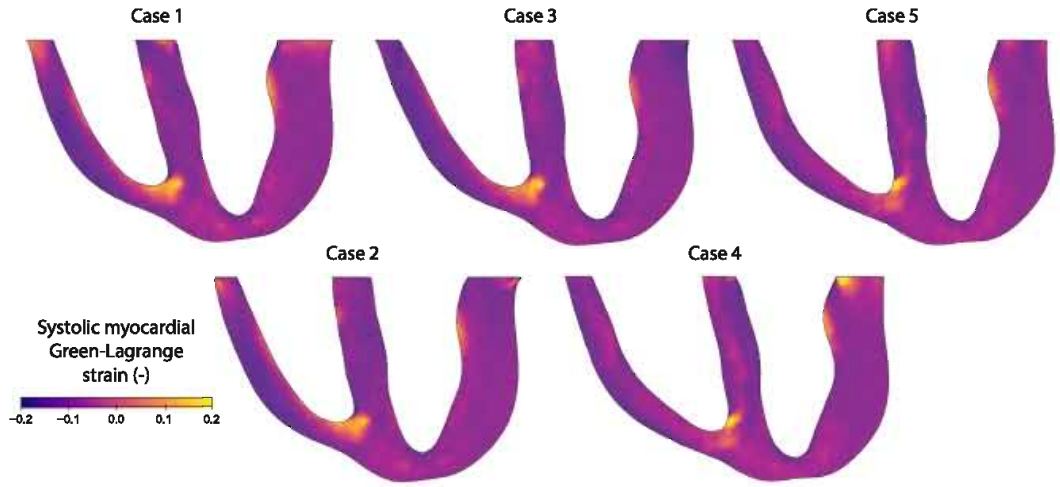

Figure 6.9: Finite element analysis (FEA) computed systolic Green-Lagrange strains in the direction of the myocardial cells.

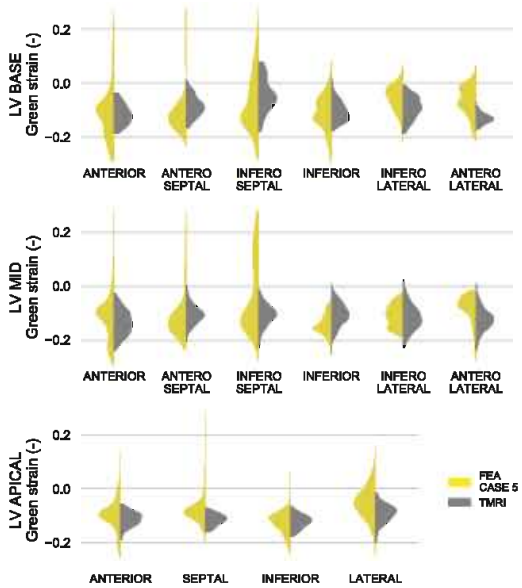

Figure 6.10: Systolic circumferential strains predicted by the FE model for boundary condition case 5, compared to the measured TMRI strains.

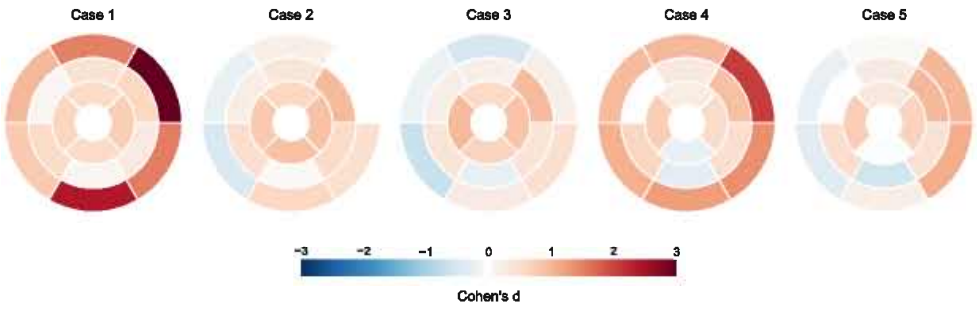

Figure 6.11: Regional standardized difference in systolic circumferential strains between the measured in vivo strains and each boundary condition case respectively.

region or the RV wall strain differences across all cases. Given the superior intrinsic tag density and the most confined strain variance (see Figure 6.8) in the circumferential direction, the in silico results were validated by comparing the systolic circumferential FEA and TMRI strains. Overall, these computed regional systolic strains agreed well with the in vivo TMRI strains (as shown in Figure 6.10 for case 5). The standardized difference between the cases is expressed in Figure 6.11. Cases 2, 3 and 5 resulted in the best match with the in vivo measured strains, with an average absolute mean difference of approximately 0.55 times the pooled standard deviation. These cases all have smaller differences between numerical and in vivo results in the basal regions. When we discard the basal results, the differences do not significantly favor one case over another.

6.4.3 Comparison of BC cases

The effect of the boundary conditions was also quantified by examining the differences in global cavity metrics (pressure-volume loops, stroke volume and ejection fractions) and regional strain variations.

Figure 6.12 depicts the LV cavity metrics across the different BC cases. During diastolic filling, case 1 and case 4 led to higher end diastolic volumes (EDVs 63.2 ml and 63.1 ml respectively) compared to case 2, case 3 and case 5 (60.2 ml, 58.7 ml and 59.3 ml respectively). The end-systolic volume (ESV) amounted to 26.0 ml, 28.5 ml, 28.5 ml, 28.7 ml and 28.1 ml for case 1 to case 5 respectively. These differences in EDV and ESV caused a differing SV and EF across cases. The EFs varied between 51.5% and 58.8% (SVs between 30.2 ml and 37.2 ml) for the different boundary condition cases. For the right

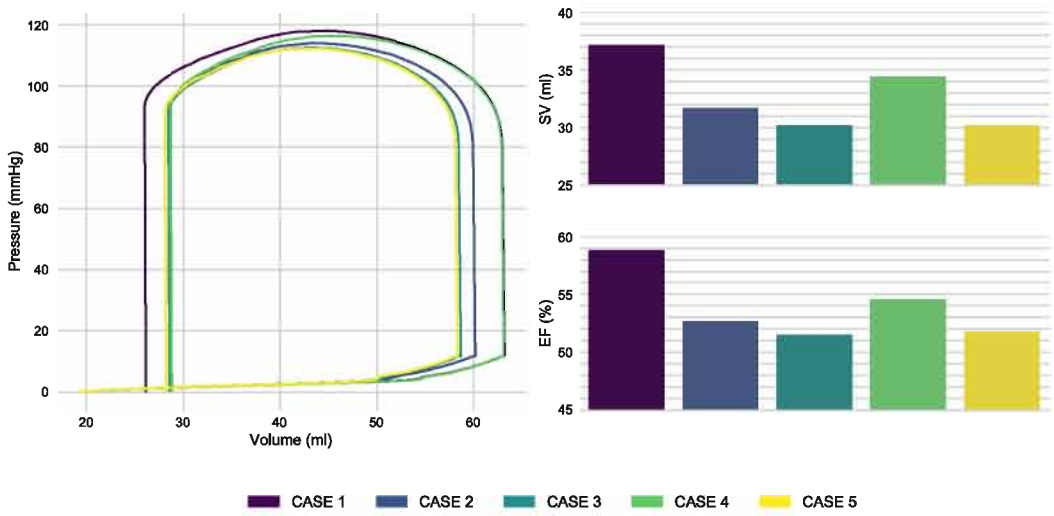

Figure 6.12: Numerical pressure-volume loops, stroke volumes and ejection fractions for the LV, comparing the effect of changing boundary conditions (case 1 to 5) on these clinically important cavity metrics.

ventricle, similar differences were seen across the different BC cases, e.g. the RV EFs amounted to 36.4%, 34.7%, 33.2%, 32.7% and 32.1% for case 1 to case 5 respectively.

The case-to-case variance in end-diastolic maximum principal strain is shown in Figure 6.13. Regional case-to-case diastolic strain variances in both the circumferential and radial direction are shown in Figure 6.14. The overall diastolic circumferential and radial strains are positive and negative respectively. The most obvious discrepancies in diastolic strains across the different BC strategies were noticed in both the left and right ventricular basal zones. In the mid and apical zones, i.e. further away from the different BCs on the FE model's basal top surface, the discrepancies between the different cases diminishes. Based on the ANOVA tests on the inter-case differences between the maximal principal strains, statistically significant ($p < 0.01$) strain differences were found in most AHA regions except for AHA region 3, 11, 12, 13, 16, 17, 21 and 22 (see Figure 6.13). Along the LV longitudinal axis, 7 out of 8 basal regions, 5 out of 8 mid regions and 3 out of 8 apical regions showed significant regional strain differences between cases. Subsequent post hoc paired t-tests localized statistically significant regional strain differences in case-by-case comparisons (see Figure 6.15). In the LV basal anteroseptal region, for example, all cases disclose statistically significant strain differences except for case 3 compared to case 5. Conversely, the RV mid anterior AHA

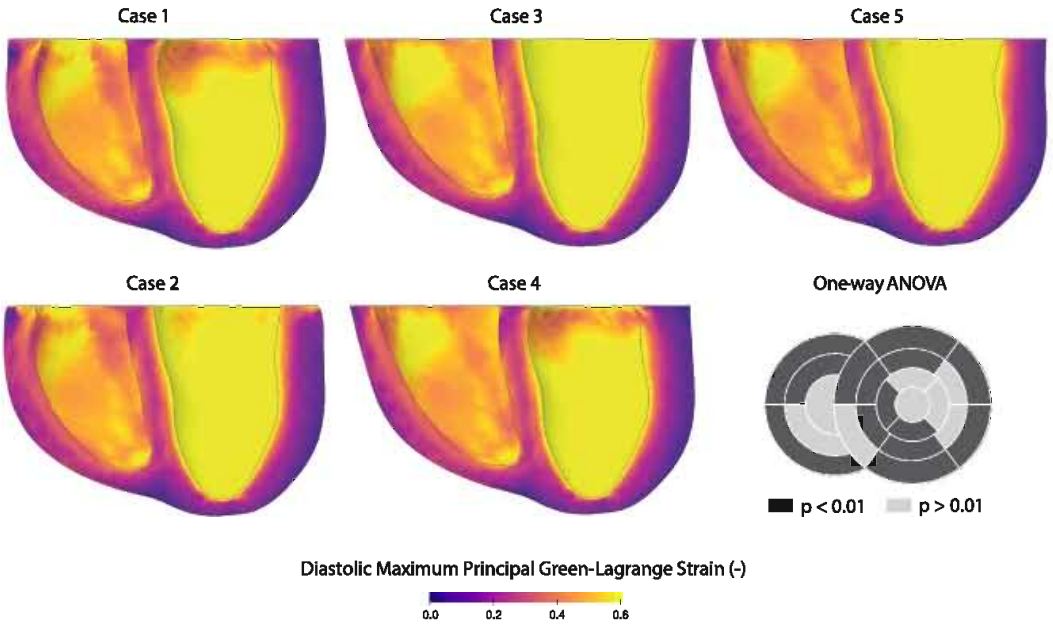

Figure 6.13: Finite element analysis case-to-case variance of diastolic maximal principal strains, including the regional one-way analysis of variance results depicting the regions where statistically significant differences ($p < 0.01$) between cases were found (dark grey: $p < 0.01$, light grey: $p > 0.01$).

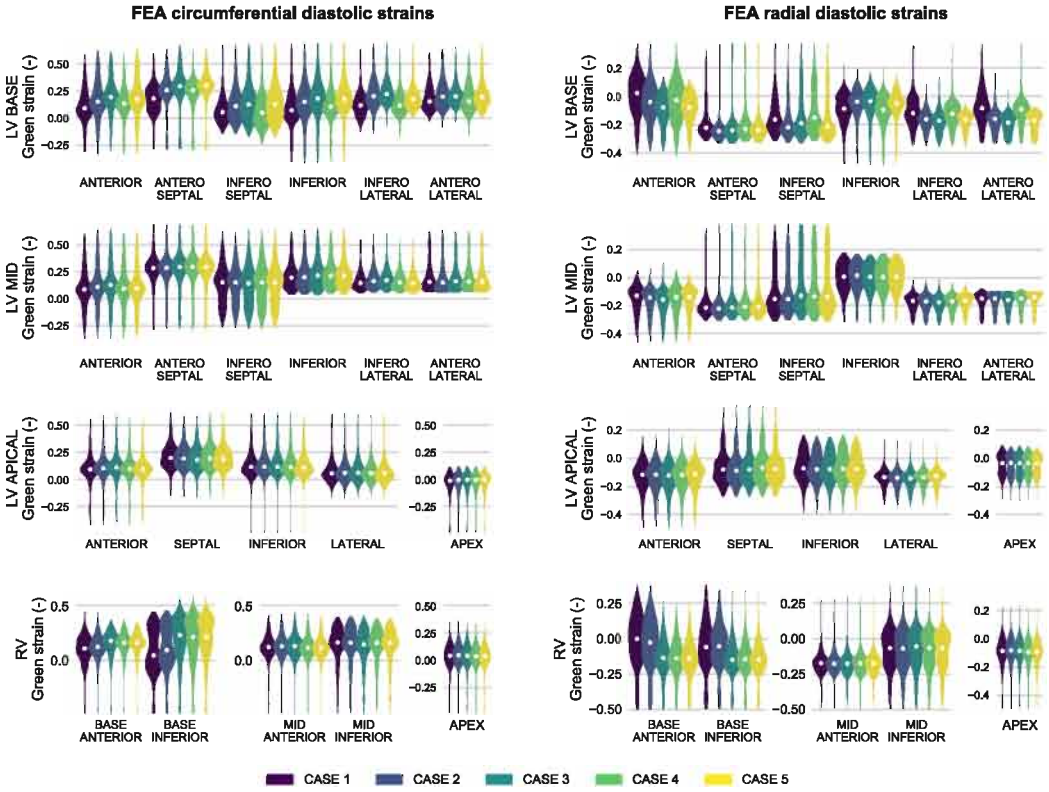

Figure 6.14: Finite element analysis case-to-case variance of diastolic strains – regional quantitative comparison of the circumferential (left) and radial (right) strains.

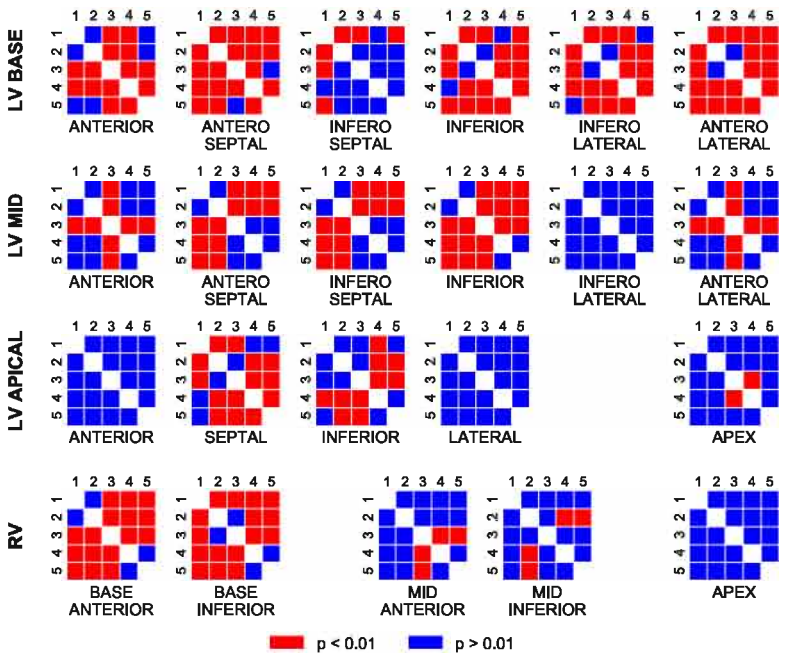

Figure 6.15: Regional case-to-case strain variance: reciprocal paired t-tests to determine statistically significant differences in maximal principal strains in between cases (the partially transparent regions were already determined to include no statistically significant differences in maximal principal strains in between cases in the initial one-way ANOVA test).

segment only features statistically significant differences between case 3-4 and case 4-5. Overall, both the LV and RV basal zones show more statistical case-to-case differences in strain magnitude than the mid and apical zones.

6.5 DISCUSSION

This study depicts a workflow that is adequate and clinically manageable with the current technology to deliver a predictive patient-specific in silico ventricular model, that compares relatively well with literature and in vivo recorded strains. These methods establish a baseline that can easily be extended to enable research on pathophysiology, optimization of cardiac procedures and/or devices, for diagnostic evaluation and even to investigate the fundamentals of healthy cardiac physiology. Given the known influence of RV deformation on the LV [80, 263], both ventricles should be considered.

Functionally, all cases led to ejection fractions in the lower normal range for healthy humans [97, 172]. However, the traditional method of validating myocardial models only by comparing the LV end-diastolic volumes has been proven to be insufficient [264]. Therefore, the in vivo reference biventricular behavior was conjointly studied by measuring the in vivo systolic regional strains using the *Segment* software suite, which led to the 3,540 circumferential and 2,880 radial strains in the LV depicted in Figure 6.8 (plus 1,975 longitudinal strain measurements of inferior quality). These strains gave expected results (systolic mid, base and apical radial Green-Lagrange strains were 0.084 ± 0.151, 0.112 ± 0.185 and 0.024 ± 0.062 respectively whereas the systolic circumferential Green-Lagrange strains were -0.095 ± 0.050, -0.115 ± 0.044 and -0.110 ± 0.029 in the corresponding basal, mid and apical regions respectively) and correlated well with published data. More specifically, Del-Canto et al. [60] reported systolic radial Green-Lagrange strains of 0.138 ± 0.041, -0.094 ± 0.041, -0.127 ± 0.041 in the basal, mid and apical zone respectively. Venkatesh et al. [345] reported systolic circumferential Green-Lagrange strains of -0.139 ± 0.032, -0.164 ± 0.022, -0.163 ± 0.025 in the basal, mid and apical zone respectively. These are slightly higher than the results we reported in this study, which may be related to the large patient variability in strain distributions. Additionally, our strategy computed circumferential strains along 5 concentric rings through the LV wall tissue instead of purely computing the midwall strain, which might affect the comparison with other literature data as well. Rigorous comparison of the computed systolic circumferential strains to in vivo measured regions showed reasonable agreement (Figure 6.10 and Figure 6.11) with a total mean strain difference of 0.038 (strain means of AHA region vs corresponding TMRI region averaged over all regions over all cases). The agreement was particularly good for regions distal from the basal anchoring zone (total

mean strain difference of 0.029). While in vivo imaging techniques often suffer from tag fading and low spatial resolution to measure reproducible strains in the RV [310], our FE models produce these strains easily. This level of systematic strain analysis (i.e. regional for both ventricles) at both end diastole and end systole (whereas Palit et al. [264] only studied diastolic distributions) is state-of-the-art and plays an important role for clinical decision making [164, 322]. The depicted regional strains in Figure 6.8, Figure 6.9, Figure 6.10, Figure 6.13 and Figure 6.14 and the depicted regional strain differences in Figure 6.11 clearly show that averaging strain data over the whole ventricle would lead to an immense loss of information on local biomechanical behavior. The global systolic circumferential Green strain difference between TMRI (-0.111 ± 0.042) and FEA (case 5; -0.077 ± 0.087) amounted to 0.034 ± 0.097 which corresponds very well with values reported in Genet et al. [97] and outperforms those reported in [98]. Discrepancies between FE model results and in vivo measurements, while small, may be attributable to registration errors in the in vivo data acquisition and/or model simplifications in the numerical model (see section 6.5.1).

The different boundary conditions which can be used in absence of image-derived motion proved to have substantial influence on the in silico functioning of the biventricular heart model, which was seen in both the global and regional parameters of cardiac function. Globally, the different BCs induced variance in the ventricular cavity metrics (see Figure 6.12), which are often used in clinical practice to describe their morphology and function. Functionally, we noticed inter-case ejection fraction differences up to 7%. In more detail, for the LV, constraining the circumferential and radial displacement of the basal layer (especially cases 1, 4 and to a lesser extent 2) leads to an increased EDV (63.2 ml, 63.1 ml and 60.2 ml for case 1, 4 and 2 respectively vs. 58.7 ml and 58.7 ml for cases 3 and case 5 respectively). Moreover, this led to increased stroke volumes and ejection fractions (58.8%, 54.5% and 52.7% ejection fractions for cases 1, 4 and 2 respectively vs 51.5% and 51.8% for cases 3 and 5 respectively). Given that the same set of constitutive parameters resulted in different EDVs and ESVs showed that overconstraining the basal cut plane influences the stiffness of the ventricular relaxation/contraction, a finding also noted by Quarteroni et al. [279]. For the RV, the boundary conditions affect the SV and EF less than for the LV. We, however, observe an opposite phenomenon for the RV compared to the LV; decreased limitations of basal motion (for the RV, this corresponds to cases 3, 4 and 5) resulted in higher, instead of lower, end diastolic volumes (EDVs of 113.0 ml and 118.0 ml were recorded for cases 1 and 2 respectively compared to EDVs for cases 3, 4 and 5 of 129.8 ml, 129.0 ml and 127.4 ml respectively). On a local scale, specific regional strain distributions

were also found to be dependent on the chosen kinematic BCs. A case-to-case mechanical comparison of end diastolic strains produced a consistent measurement (based on the same reference geometry for all cases). Again, the most statistically significant differences between cases were recorded in the basal zone. Except for the inferoseptal zone, any other basal zone of both the left and right ventricle proved to deform in at least one case statistically significantly different from another case (7 out of 8 regions). Comparing this to the mid, apical and apex zones (5 out of 8, 2 out of 4 and 0 out of 2 zones respectively statistically significantly different), we can conclude that the most profound effect of the BC on localized strain distributions can be found at the base with diminishing influence towards the apex where no significant differences were found. Post-hoc t-tests (Figure 6.15) allowed pair-wise regional comparisons between the different cases but did not reveal significant similarities between any two specific cases.

Regional standardized differences in systolic circumferential strains between the measured in vivo strains and each boundary condition case respectively (see Figure 6.11) suggested case 2, case 3 and case 5 to correspond better to in vivo measurements than case 1 and 4. In global strain measures, case 3 and case 5 seem to equally correspond best to in vivo measurements (global systolic circumferential discrepancy between TMRI and case 3 and 5 amounted to 0.034 ± 0.093 and 0.034 ± 0.097 respectively whereas for case 2, 4 and 1 this amounted to 0.040 ± 0.092, 0.044 ± 0.102 and 0.045 ± 0.092 respectively. In a like manner, the interpolated movement of the epicardial ring seen in the top basal slice of the TMRI short axis data (see Figure 6.1) showed relative motion in the basal plane. These results suggest that case 1, 2 and 4 are too strict and lead to non-physiological stresses, strains and pressure in the tissue. Given the differences seen in global and local metrics describing the mechanics of the heart, the relevance of using appropriate mechanical boundary conditions is clearly brought forward.

The fundamental utility of cardiac modeling lies in its prognostic power to assess the patient-specific outcome for a specific therapy. Acute, image-derived BCs inherently do not accommodate for changes in mechanical environment upon performing (virtual) surgeries or (virtually) implanting a device. To meet the goal of tailored or patient-specific treatment planning, generic kinematic BCs should be proposed that are adaptive and independent from the availability of detailed imaging data, which is not a given in a clinical setting. This study shows that different approaches to incorporate the effect of surrounding tissue through different kinematic BCs affect the reliability of the numerical results. As interest in using numerical simulations to assist in the approval of new therapies grows [332], the need to properly validate numerical models is critical. Proper validation of methods and subsequent

models will require interdisciplinary efforts and high quality experimental data, which may be difficult to obtain. It is therefore important that these efforts are coupled with studies that quantify model assumptions and their effects. By comparing the results to in vivo imaging data, we showed that artificially constraining all degrees of freedom of all (or a subset) of basal nodes is unrealistic and should be substituted by constraining these nodes' average motion.

6.5.1 Limitations

First, suboptimal long-axis TMRI data and the lower tag density in the radial direction led to a relatively larger variation in measured systolic strains in both longitudinal and radial directions (also seen in previous studies [61, 333]) due to which only the in vivo circumferential strains could be used for validation purposes. Second, the used acquisition and estimation motion and deformation tracking method does not account for out-of-plane motion which could lead to discrepancies with the FEA computed systolic strains, similar to [85, 333]. To study the effect of out-of-plane motion on the strain results, which is considered beyond the scope of this study, synthetic MRI sequences should be built from the finite element electromechanical ground-truth model (e.g. [377]) and subsequently processed with the used motion tracking algorithm to study its performance. Future work should focus on collecting higher quality image data and inclusion of appropriate tracking algorithms so we could assess right ventricular deformation as well. Higher quality image data would also allow us to use image-derived boundary conditions upon calibrating the material properties, which would not favor the pressure-volume loop of any specific boundary condition to match the reference data better than another (which explains why we did not compare the in silico and in vivo pressure-volume relationship or any other PV-derived cavity metrics to deem any boundary condition case more appropriate than another in this study). Nevertheless, the TMRI analysis resulted in realistic strain results in all directions. The lumped circulatory model used in this study relies on a simplified, outflow-only representation. Even though it would not influence the comparison of different BCs in this study, further studies could include more complex representations to model more realistic flow conditions and multiple cardiac cycles (see section 5.4.3.1). Apart from the top basal boundary conditions, our modeling strategy did not include any other constraints on the ventricular motion. Even though it is common practice in cardiac patient-specific studies to assume that the pericardial boundary energy is negligible [130], some studies (e.g. [218, 264]) introduced additional boundary conditions to mimic the heart's enclosure in the pericardial sac. While additional BC cases, such as Robin-type BCs, would have been interesting to explore, they present a much larger subsection of

BCs that require additional parameter identifications (elastic and viscoelastic stiffness tuning). The variety in Robin-type BC stiffness parameters in [43, 76, 101, 140, 189, 218, 363] shows the difficulty to set up a single Robin-type BC case to compare to the other BC cases. Therefore, these (visco)elastic BCs were excluded from the comparison and the study remained focused on pure kinematic BCs only. Future work would benefit from exploring Robin-type BCs further as an alternative formulation. These pericardial constraints limit the global radial body motion of the ventricle but do not impact the global volume or pressure evolution, thus have no effect on the diastolic filling and systolic contraction behavior shown in Figure 6.12. The local case-to-case strain discrepancies, extensively compared in this study, are not affected by discarding this constraint either. Similarly, the use of a rule-based myofiber aggregate structure instead of the (clinically typically unavailable) DT-MRI-derived patient-specific myofiber architecture description [263, 300] and the assumption that the heart is in an initial stress-free state at end diastole [99, 267, 352] is expected to induce a consistent global mismatch in stress and strain throughout all cases. However, it will not influence the individual discrepancies across cases and therefore not alter the conclusions drawn from the study.

6.6 CONCLUSION

The ongoing advancements in cardiac modeling provide the clinician and researcher with otherwise immeasurable measures on cardiac function such as local strains and stresses, tissue stiffness and contractility. Given that these additional insights are to be used for diagnosis, prognosis and treatment planning, any inconsistency between model and reality should be minimized. This study reported statistically significant differences in global functioning and local strain distributions between different strategies to impose the influence of surrounding tissue. These differences show the importance of selecting appropriate boundary conditions for biventricular models to be used in clinical practice. Based on this study's results, future ventricular models set up to obtain improved understanding of the physiology of human hearts should avoid an over-constrained basal boundary condition and allow for circumferential and radial tissue motion in the basal plane.

CHAPTER 7

HEART FAILURE MODELING VALIDITY ACROSS THE SCALES

Heart failure is a progressive chronic condition in which the heart undergoes detrimental changes in structure and function across multiple scales in time and space. Multiscale models of cardiac growth can provide a patient-specific window into the progression of heart failure and guide personalized treatment planning. Yet, the predictive potential of cardiac growth models remains poorly understood. Therefore, this chapter* quantifies the predictive power of a stretch-driven growth model using a chronic porcine heart failure model, subject-specific multiscale growth simulations, and machine learning techniques.

7.1 INTRODUCTION

Cardiovascular disease is the single leading cause of death worldwide with an estimated 17.3 million deaths in 2016, representing 31.5% of all global deaths [337]. With a 5-year mortality rate of 50%, heart failure remains, and will remain in the foreseeable future, one of the most common, costly, disabling, and deadly medical conditions. In a traditional biomechanics

*This chapter is based on M. Peirlinck, F. Sahli Costabal, K. L. Sack, J. S. Choy, G. S. Kassab, J. M. Guccione, M. De Beule, P. Segers, and E. Kuhl, "Using machine learning to characterize heart failure across the scales", *Biomechanics and Modeling in Mechanobiology*, 2019, in press

sense, cardiac growth and remodeling, can be considered a protective and reparative homeostatic mechanism [123]. However, when combined with chronic alterations in the heart's loading conditions, these mechanisms lead to pathoanatomical changes that compromise the heart's electrical and mechanical function. As shown in Figure 5.18, the underlying structural alternations can be categorized in two major patterns: eccentric hypertrophy associated with myocyte lengthening caused by a chronic overload in volume and concentric hypertrophy associated with myocyte thickening caused by a chronic overload in pressure [108]. Eccentric hypertrophy results in enlarged, dilated ventricles at a relatively constant wall thickness while concentric hypertrophy results in thickened ventricular walls at a relatively constant cardiac size [109]. In addition to a compromised mechanical function, these pathoanatomical changes distort the heart's electrical activation and conductivity resulting in an increasingly higher risk for ischemia, arrhythmia, and sudden death [173].

One of the most pertinent clinical questions in treatment planning is to anticipate and predict the rate of disease progression [357]. Consequently, the mechanobiological factors that regulate cardiac hypertrophy have been the subject of extensive research throughout the past decades [262]. Cardiac growth models have the potential to provide mechanistic insight in disease onset and progression [286] and can aid clinical decision-making or the design of emerging therapies [32]. Yet, a considerable debate remains around the underlying stimuli that trigger cardiac growth. Increasing evidence points to mechanical factors as mediating stimuli, both at the tissue and cellular levels. In eccentric hypertrophy, initial studies suggested that the end-diastolic stress would trigger cardiac dilation [124], while later studies opposed this hypothesis and suggested the end-diastolic stretch as a stimulus for cardiac growth [257]. Here we explore this hypothesis and characterize to which extent a mechanistic stretch-driven growth model can explain cardiac dilation in a unique chronic animal study where we induce and characterize eccentric hypertrophy across multiple length scales.

7.2 METHODS

To correlate whole organ, tissue, cellular, and subcellular levels, we used a multiscale continuum growth model. We characterized end-diastolic volumes and myocyte dimensions in a longitudinal study of volume overload using cardiac echocardiography and tissue histology. To account for uncertainties in both sets of measurements, we combined Bayesian inference, uncertainty quantification, and Gaussian process regression. To quantify the predictive potential of our multiscale growth model, we characterized the agreement between the computationally simulated and experimentally measured myocyte lengths for six animals throughout a period of eight weeks.

7.2.1 Animal model

As previously described in [36, 301], our study[†] included six Yorkshire domestic pigs of either sex with a body weight of 46.3 ± 8.0 kg. At the day of surgery, the animals were sedated with telazol-ketamine-xylazine and anesthesia was maintained with isoflurane. To monitor the pressure and provide access to the left ventricle for mitral valve chordae disruption, we percutaneously inserted sheaths into the jugular vein to administer fluids and drugs into the right femoral artery. Using transesophageal echocardiography guidance, moderate to severe mitral regurgitation was created by disrupting one or more chordae. The degree of regurgitation was confirmed using echocardiography. At the day of surgery and then bi-weekly for a period of eight weeks, transthoracic and transesophageal echocardiograms were recorded and endomyocardial biopsy samples were collected. For the organ level characterization, we recorded echocardiographic images, two- and three-dimensional in short and long axis views, with the animal in the supine and left lateral decubitus positions. From these images, dynamic surface models of the left ventricle were automatically constructed to extract end-diastolic volumes, end-systolic volumes, stroke volumes, ejection fractions, and wall thicknesses. For the cell level characterization, four to six endomyocardial biopsy samples were collected from the apex and the left ventricular free wall. The samples were incubated in cardioplegic solution at 37°C, prepared in 7-μm-thick slices, mounted on glass slides, and incubated with Wheat Germ Agglutinin to characterize myocyte widths and lengths and with Anti-Sarcomeric Alpha Actinin to characterize sarcomere numbers and lengths. Under fluorescence microscopy, the images were merged using *ImageJ* to identify the sarcomere numbers within each myocyte. At eight-weeks post surgery, the measurement protocol was terminated. At that time the animal was deeply anesthetized and the heart was arrested in diastole with potassium chloride to be subsequently excised. Finally, transmural punch biopsies were collected from the apex and free wall.

7.2.2 Multiscale model of cardiac growth

To correlate the changes in end-diastolic volume to changes in myocyte length and width, we adopted the kinematics-based finite growth theory disclosed in section 2.3.1. In this theory, the deformation gradient $\boldsymbol{F}$, which is the derivative of the non-linear deformation map $\boldsymbol{\varphi}$ (see Eq. 1.1),

[†] All animal experiments were performed at the California Medical Innovations Institute animal care facilities following an approved IACUC protocol according to U.S. national and local ethical guidelines, including the Guide for the Care and Use of Laboratory Animals, the Public Health Service Policy on Humane Care and Use of Laboratory Animals, and the Animal Welfare Act.

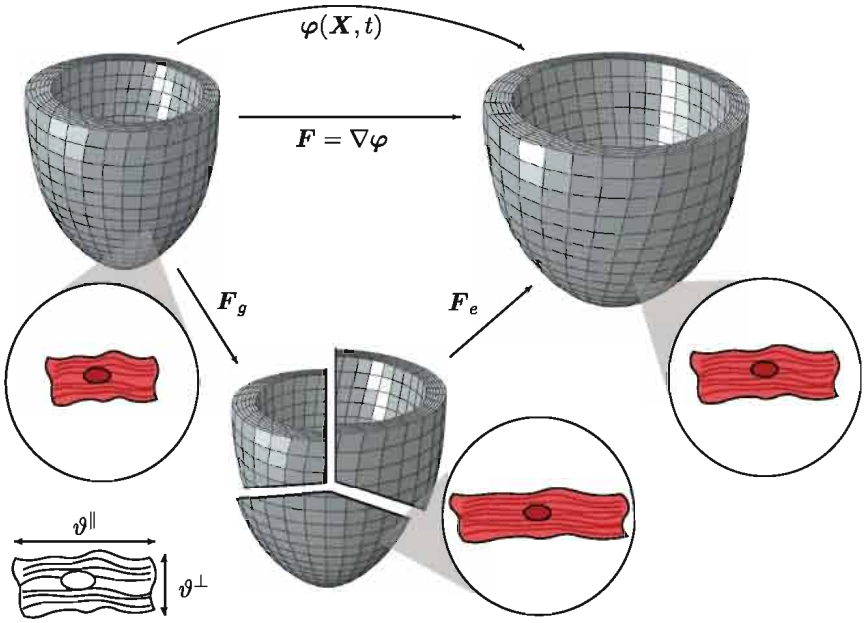

Figure 7.1: Multiscale model of cardiac growth. Multiplicative decomposition of the deformation gradient $\boldsymbol{F} = \nabla\boldsymbol{\varphi} = \boldsymbol{F}_e \cdot \boldsymbol{F}_g$ into an elastic tensor $\boldsymbol{F}_e$ and a growth tensor $\boldsymbol{F}_g$; the growth tensor $\boldsymbol{F}_g = \vartheta^{\parallel} \boldsymbol{f}_0 \otimes \boldsymbol{f}_0 + \vartheta^{\perp}[\boldsymbol{I} - \boldsymbol{f}_0 \otimes \boldsymbol{f}_0]$ introduces the longitudinal and transverse growth $\vartheta^{\parallel}$ and $\vartheta^{\perp}$, which are directly correlated to changes in myocyte length and width.

is multiplicatively decomposed into a growth tensor $\boldsymbol{F}_g$ (which maps the original reference state to an intermediary unstressed (and typically incompatible) grown state) and an elastic tensor $\boldsymbol{F}_e$ (which maps the intermediary state into a compatible, intact, and loaded state):

$$\boldsymbol{F} = \nabla\boldsymbol{\varphi} = \boldsymbol{F}_e \cdot \boldsymbol{F}_g \tag{7.1}$$

As discussed in section 2.3.1, experimental observations have confirmed the existence of a preferred mechanical homeostatic state $\boldsymbol{G}_h$ in soft living tissues, at which no net growth occurs. Disturbing the tissue away from this homeostatic state through a certain mechanical growth and remodeling (G&R) stimulus $\Delta\boldsymbol{G}$ initiates growth changing the volume and stress-free state of the tissue. As generally disclosed in Eq. 2.30, this stimulus then drives a certain evolution equation $\dot{\boldsymbol{F}}_g$, typically decomposed in different direction tensors. For cardiac tissue specifically, we assumed that growth is transversely isotropic with respect to the fiber direction $\boldsymbol{f}_0$ [224, 379]:

$$\boldsymbol{F}_g = \vartheta^{\parallel} \boldsymbol{f}_0 \otimes \boldsymbol{f}_0 + \vartheta^{\perp}[\boldsymbol{I} - \boldsymbol{f}_0 \otimes \boldsymbol{f}_0], \tag{7.2}$$

where growth is a direct result of the relative changes in myocyte length $\vartheta^{\parallel}$ and myocyte width $\vartheta^{\perp}$ (see Figure 7.1). Consequently, for cardiac tissue the

evolution law for the time dependent directional growth multipliers β^j in Eq. 2.30 translates to two evolution laws for the longitudinal $\vartheta^{\parallel}$ and transverse $\vartheta^{\perp}$ growth multipliers respectively.

7.2.2.1 *Growth law*

In this study, we set forth to test the validity of the assumption that the end-diastolic stretch state is the leading mechanical stimulus defining the growth response during volume overload [257]. Consequently, we adopted an established stretch-driven growth model in the longitudinal direction and assumed that there is no growth in the thickness direction [96, 108, 109, 283, 357],

$$\dot{\vartheta}^{\parallel} = \frac{1}{\tau}\langle \lambda^e - \lambda^{crit} \rangle \quad \text{and} \quad \dot{\vartheta}^{\perp} = 0\,. \tag{7.3}$$

Here, the Macauley brackets $\langle\rangle$ enforce longitudinal growth activation only if the elastic fiber stretch, $\lambda^e = [\, \boldsymbol{f}_0 \cdot \boldsymbol{F}_e{}^T \cdot \boldsymbol{F}_e \cdot \boldsymbol{f}_0 \,]^{1/2}$, exceeded the homeostatic baseline fiber stretch, λ^{crit}. If $\lambda^e \leq \lambda^{crit}$, there was no growth. If $\lambda^e > \lambda^{crit}$, the growth parameter τ controls the speed of growth. Importantly, the parameter λ^{crit} is not a free parameter but follows from the regionally varying baseline stretch at end diastole, prior to inducing volume overload.

7.2.2.2 *Myocardial tissue response*

For the baseline elastic material response, we adopted the classical cardiac Holzapfel-Ogden strain energy function (SEF) as discussed in section 5.3.2:

$$\begin{aligned} \bar{\Psi} = {} & \frac{a}{2b}\exp\left[b\left(\bar{I}_1 - 3\right)\right] + \sum_{\alpha=f,s}\frac{a_\alpha}{2b_\alpha}\left(\exp\left[b_\alpha\left(\bar{I}_{4\alpha\alpha} - 1\right)^2\right] - 1\right) \\ & + \frac{a_{fs}}{2b_{fs}}\left(\exp\left[b_{fs}\bar{I}_{4fs}^2\right] - 1\right) \end{aligned} \tag{7.4}$$

where $\bar{I}_1$, $\bar{I}_{4ff}$, $\bar{I}_{4ss}$, and $\bar{I}_{4fs}$ are the invariants that characterize the trace of the right elastic Cauchy-Green deformation tensor, the elastic fiber stretch, sheet stretch, and coupled fiber-sheet stretch in terms of the elastic tensor $\boldsymbol{F}_e$ and a, b, a_f, b_f, a_s, b_s, a_{fs}, and b_{fs} are the eight Holzapfel-Ogden material parameters [107, 147].

7.2.2.3 *Computational model*

We simulated volume-overload induced growth using the finite element analysis (FEA) software package *Abaqus*. For each animal, we created a FEA model of the left ventricle (LV) using the subject-specific echocardiography images at the minimum cavity volume of the cardiac cycle and assume that this is the stress free state. Figure 7.1 shows a typical left ventricular model discretized with 3,456 linear hexahedral elements, 4,152 nodes, and 12,456

degrees of freedom. Similar to section 6.3.4.1, a discrete fiber orientation $\boldsymbol{f}_0$ was assigned for each element using the Laplace-Dirichlet Rule-Based (LDRB) algorithm proposed by Bayer et al. [16, 156]. Here, we assumed the myofibers's helical angle to vary transmurally from -60° in the sub-epicardium, the outer wall, to +60° in the sub-endocardium, the inner wall [358]. Following chapter 6, we accounted for surrounding tissue by constraining the longitudinal motion of the top basal surface and constraining the in-plane motion through a distributed continuum coupling between the endocardial ring nodes and a central fully constrained valvular plane node (see 'case 5' in Figure 6.3).

We loaded the heart in two steps, *homeostatic loading* and *pathologic overloading*. For homeostatic loading, the ventricle was loaded to the experimentally recorded end-diastolic volume (EDV). At the end of this step, the maximum stretch at each integration point was recorded and stored as the critical stretch λ^{crit} beyond which growth is activated. During pathologic overloading, the EDV was gradually increased following the recorded EDV evolution through time. This resulted in an increase in the elastic fiber stretch λ^e, which activated growth and triggered an increase in myocyte length $\vartheta^{\parallel}$.

7.2.2.4 Identification of elastic parameters

To calibrate the eight Holzapfel-Ogden material parameters for each animal at baseline, we followed the two-stage passive calibration approach disclosed in section 5.3.1.3. In summary, an initial set of Holzapfel-Ogden parameters was first characterized which reproduced ex vivo triaxial shear test behavior of human myocardial tissue (see Eq. 5.8 and Table 5.1). Next, this set of ex vivo parameters was mapped onto our subject-specific in vivo stiffness parameters a, a_f, a_s, and a_{fs} and our subject-specific in vivo exponential parameters b, b_f, b_s, and b_{fs} via two scaling coefficients α and β respectively [299]. To calibrate these scaling coefficients, we minimized the error between the analytical Klotz curve of the experimentally recorded end-diastolic pressure-volume (PV) relation at baseline [177] and the computationally simulated diastolic PV relation using *Abaqus* and a sequential least squares programming optimization algorithm [169], see Eq. 5.9. For the resulting set of in vivo Holzapfel-Ogden material parameters, the recorded end-diastolic pressure (EDP) inflated the subject-specific LV from the recorded minimal volume to the recorded EDV.

7.2.3 Sensitivity analysis of growth speed

To explore the effects of the kinetics of growth, the effect that the only free parameter in Eq. 7.3, the growth parameter τ, has on the growth response needed to be systematically studied. Therefore, we examined a wide range of growth parameters, $\tau = [\,0.03, 0.10, 0.33, 1.00, 3.33, 10.00\,]$ week, and

highlighted their effect on the longitudinal growth $\vartheta^{\parallel}$, the longitudinal growth rate $\dot{\vartheta}^{\parallel}$, and the elastic stretch in the fiber direction λ^{e}. From this sensitivity analysis, we rationalized a growth parameter of $\tau = 0.1$ week, which was used for all further studies. This value ensured a rapid growth response to hemodynamic alterations which matches the quasi-constant growth rates observed in other experimental studies [372]. Contrary to τ, λ^{crit} in Eq. 7.3 was not a free parameter, but rather the regionally varying baseline stretch at end diastole, prior to inducing volume overload (see section 7.2.2.3). Importantly, throughout the entire process, no cellular information from tissue histology was introduced to prescribe growth as was done in a previous study [301]. Rather, we used this cellular information to objectively assess the predictive power of the growth law.

7.2.4 Uncertainty quantification using Bayesian inference

To characterize volume-overload-induced changes in the measured organ and cell level variables, we employed Bayesian inference [301]. For all recorded samples, it was postulated that the measurements were drawn from distributions that evolve in time. Since end diastolic volume, myocyte length, and myocyte width cannot take negative values, we assumed these measurements to be log-normally distributed around their mean μ at any point in time. We further postulated that the myocyte length and width are correlated through a bivariate log-normal likelihood,

$$\begin{bmatrix} \log\left(y_{ml}^{i,j}\right) \\ \log\left(y_{mw}^{i,j}\right) \end{bmatrix} \sim \mathcal{N}\left(\begin{bmatrix} \mu_{ml}^{i}\left(t_j\right) \\ \mu_{mw}^{i}\left(t_j\right) \end{bmatrix}, \boldsymbol{\Sigma}\right), \tag{7.5}$$

where $y_{ml}^{i,j}$ and $y_{mw}^{i,j}$ are the myocyte length and width measurements j of subject i, $\mu_{ml}^{i}(t_j)$ and $\mu_{mw}^{i}(t_j)$ are the means of their distributions at the time of measurement j, and $\boldsymbol{\Sigma}$ is the covariance matrix between these quantities. For the end-diastolic volume, we assumed a simple log-normal likelihood,

$$\log\left(y_{edv}^{i,j}\right) \sim \mathcal{N}\left(\mu_{edv}^{i}\left(t_j\right), \varsigma_{edv}\right), \tag{7.6}$$

where $y_{edv}^{i,j}$ is the j^{th} end-diastolic volume measurement for subject i, $\mu_{edv}^{i}(t_j)$ is the mean of its distribution at the time of measurement j, and ς_{edv} is the standard deviation. We propose a linear relationship between the mean and time,

$$\mu_{k}^{i}(t) = a_{k}^{i} + b_{k}^{i} t \quad \text{with} \quad k = \{edv, ml, mw\}, \tag{7.7}$$

where a_{k}^{i} and b_{k}^{i} represent the intercept and slope of the line $\mu_{k}(t)$ for subject i and k represents the end-diastolic volume (edv), the myocyte length (ml) and the myocyte width (mw) respectively. To take into account

the variability between subjects and, at the same time, take advantage of the entire acquired dataset, a hierarchical model was postulated [95]. Specifically, we assumed that the different parameters of the model in Eq. 7.7 for each subject i are drawn from normal distributions, $a_k^i \sim \mathcal{N}(\mu_k^a, \varsigma_k^a)$ and $b_k^i \sim \mathcal{N}(\mu_k^b, \varsigma_k^b)$. Altogether, this approach introduced four hyper-parameters, μ_k^a, μ_k^b, ς_k^a and ς_k^b, which control the variability between the intercept a_k^i and slope b_k^i for each subject i. This allowed us to estimate the individual response of each subject by considering the totality of the cohort. To complete our statistical model in a Bayesian setting, weakly informative priors were selected through hyper parameters $\mu_k^a, \mu_k^b \sim \mathcal{N}(0, 100^2)$ and $\varsigma_k^a, \varsigma_k^b \sim$ Half-Cauchy($\gamma = 10$) [94], and through the remaining parameters $\varsigma_{edv} \sim$ Half-Cauchy($\gamma = 100$) and $\mathbf{\Sigma} \sim$ LKJ($\eta = 2$), where LKJ denotes the Lewandowski-Kurowicka-Joe distribution [198]. This distribution is particularly suitable for multi-variate normal co-variance matrices [306]. Finally, we computed posterior distributions for the parameters using Bayes' theorem where statistical inference was performed using a Hamiltonian Monte Carlo method implemented in PyMC3 [306]. We then computed new samples of our quantities of interest y_k from a predictive posterior distribution at different time points and illustrated the discrete measurement points, their medians, their 95% confidence intervals, and their inferred probability density functions throughout our entire study interval of eight weeks.

7.2.5 Uncertainty propagation using Gaussian process regression

To account for the uncertainty on the organ level, for each subject, we propagate the volume overload uncertainty to the predicted longitudinal growth. The uncertainty on imposed volume overload, i.e. the normalized end diastolic volume $\hat{ed}$ was characterized through hierarchical modeling and Bayesian modeling for each subject (ex supra), which resulted in the a_{ed}^i and b_{ed}^i parameters; $ed = \exp\left(a_{ed}^i\right) \exp\left(b_{ed}^i t\right)$. Normalized by its value at $t = 0$, the volume overload reads $\hat{ed} = \exp\left(b_{ed}^i t\right)$ and its uncertainty is characterized by the last 500 samples of b_{ed} from the Hamiltonian Monte Carlo chain. However, instead of performing a single forward growth simulation for each of these 500 samples, we train a Gaussian process regression [281, 282] to predict the median longitudinal growth $\tilde{\vartheta}^{\parallel}$ (output) based on the time and the normalized end diastolic volume (inputs),

$$\tilde{\vartheta}^{\parallel} = f\left(t, \hat{ed}\right) \tag{7.8}$$

For each subject, in the expected range of uncertainty, we perform n = 20 simulations for training and an additional n = 10 simulations for validation [271]. Since the intermediate steps towards the final solution are also valid

data points, this represents a total of 621 points for training and 311 points for validation for each subject. After training the Gaussian process regression on the training set, the root mean squared error in median growth on the validation set was less than 0.27% for all animals. Once validated, the Gaussian process regressor f is used to propagate the 500 b_{ed} samples describing the volume overload uncertainty through the multiscale growth model, which results in the evaluation of the median longitudinal growth at 31 time points between weeks 0 and 8. As such, a total of 15,500 values of $\tilde{\vartheta}^{\parallel}$ were generated for each subject. To account for the uncertainty in our cellular measurements, we correlate the longitudinal growth, $\vartheta^{\parallel} = \exp(b_{ml}\, t)$, to the parameter b_{ml} from the experimentally measured histology in Eq. 7.7. Similar to the volume overload, this correlation arises naturally from normalizing the myocyte length, $ml(t) = \exp(a_{ml})\exp(b_{ml}t)$, from Eq. 7.5 by its initial value at time $t = 0$, $\exp(a_{ml})$ [301]. To quantify the agreement between the simulated and experimental longitudinal growth $\vartheta^{\parallel}$, we compute the probability density functions of both distributions at week 8 and determine the overlap as the percentage agreement between both probability density functions.

7.3 Results

7.3.1 End-diastolic volumes increase with volume overload

Table 7.1 summarizes our echocardiography measurements at baseline and throughout a bi-weekly follow up period of eight weeks of volume overload. Altogether, we collected n = 28 measurements of end-diastolic and end-systolic volumes. The mean end-diastolic and end-systolic volumes increased from 67.9 ± 20.6 ml and 30.2 ± 9.5 ml at baseline to 100.2 ± 17.9 ml and 51.3 ± 9.0 ml at week eight. This defines a decrease in ejection fraction from $55.6 \pm 4.9\%$ to $47.7 \pm 9.5\%$. Figure 7.2 shows the end-diastolic volumes in all six animals in response to eight weeks of ventricular volume overload. The gray cross markers represent the n = 28 individual measurements, the solid gray

Table 7.1: Changes in end-diastolic volume *edv*, end-systolic volume *esv*, myocyte length *ml*, myocyte width *mw*, sarcomere number *sn*, and sarcomere length *sl* in response to left ventricular volume overload. Results are summarized as mean ± standard deviation.

	w0	w2	w4	w6	w8	Δ/week
edv [ml]	67.9 ± 20.6	71.3 ± 11.0	77.7 ± 9.5	86.8 ± 13.4	100.2 ± 17.9	+5.95%
esv [ml]	30.2 ± 9.5	34.4 ± 7.2	40.1 ± 7.8	44.6 ± 5.7	51.3 ± 9.0	+8.73%
ml [μm]	85.45 ± 22.30	84.77 ± 17.17	86.85 ± 18.45	84.38 ± 18.93	107.75 ± 26.57	+3.26%
mw [μm]	13.67 ± 3.73	13.04 ± 3.20	14.19 ± 2.96	13.85 ± 2.92	12.98 ± 3.01	-0.63%
sn [-]	47.5 ± 11.67	49.91 ± 9.96	50.36 ± 10.76	49.97 ± 11.62	62.07 ± 16.35	+3.83%
sl [μm]	1.75 ± 0.15	1.78 ± 0.13	1.75 ± 0.10	1.76 ± 0.10	1.77 ± 0.11	+0.14%

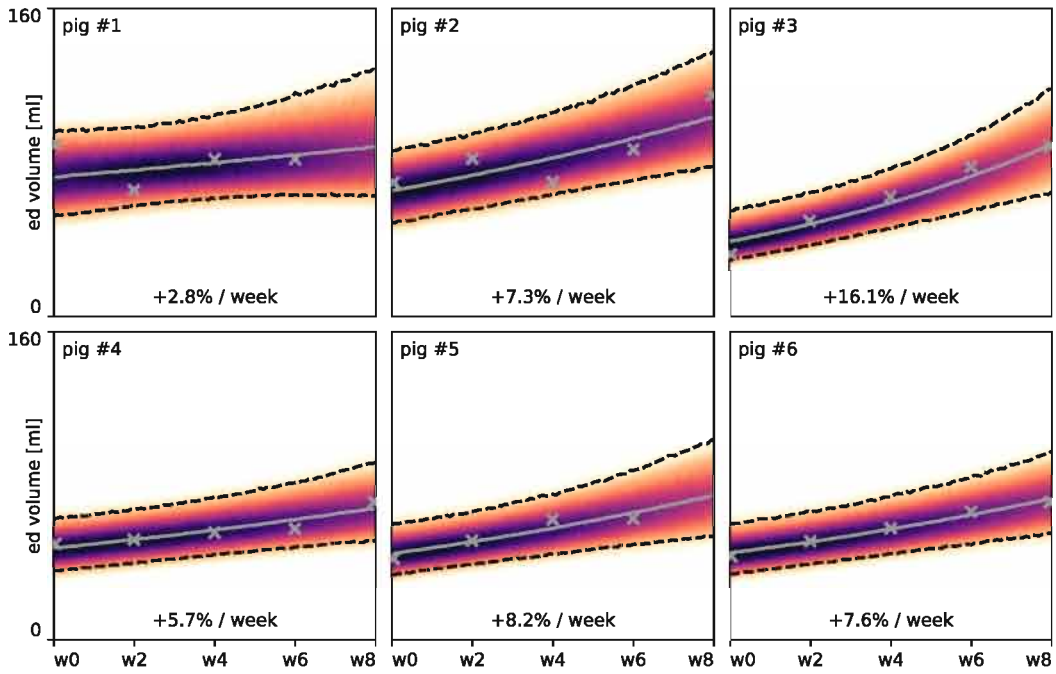

Figure 7.2: Evolution of end-diastolic volumes in response to left ventricular volume overload. Gray cross markers represent n = 28 individual measurements of end-diastolic volume, solid gray lines represent their medians, and dashed black lines their 95% confidence intervals. Color contours from dark to light highlight the probability density from high to low.

lines represent their medians, and dashed black lines their 95% confidence intervals. The mean end-diastolic volume increased by +5.95%/week, with a rapid increase between weeks 6 and 8. The direct comparison between the six animals illustrates the inter-animal variation: Pig #3 displayed the largest increase in end-diastolic volume with +12.4%/week, pig #1 the smallest with +2.5%/week. Since the end-systolic volume increased by +8.73%/week, more rapidly than the end-diastolic volume, the overall ejection fraction decreased, by −1.78%/week. As the hearts dilated, the left ventricular mass increased by 9.88%/week.

7.3.2 Myocyte lengths increase with volume overload

Next to the echocardiography measurements, Table 7.1 also summarizes the histological measurements at baseline and throughout a bi-weekly follow up period of eight weeks of volume overload. Altogether, n = 460 measurements of myocyte length and width were collected. The mean myocyte length increased, from 85.45 ± 22.30 µm to 107.75 ± 26.57 µm, with a relatively constant myocyte length throughout the first six weeks and a steep increase between weeks 6 and 8. At the same time, the mean myocyte width remained virtually constant at 13.55 µm, varying marginally between minimum values of 12.98 ± 3.01 µm and maximum values of 14.19 ± 2.92 µm.

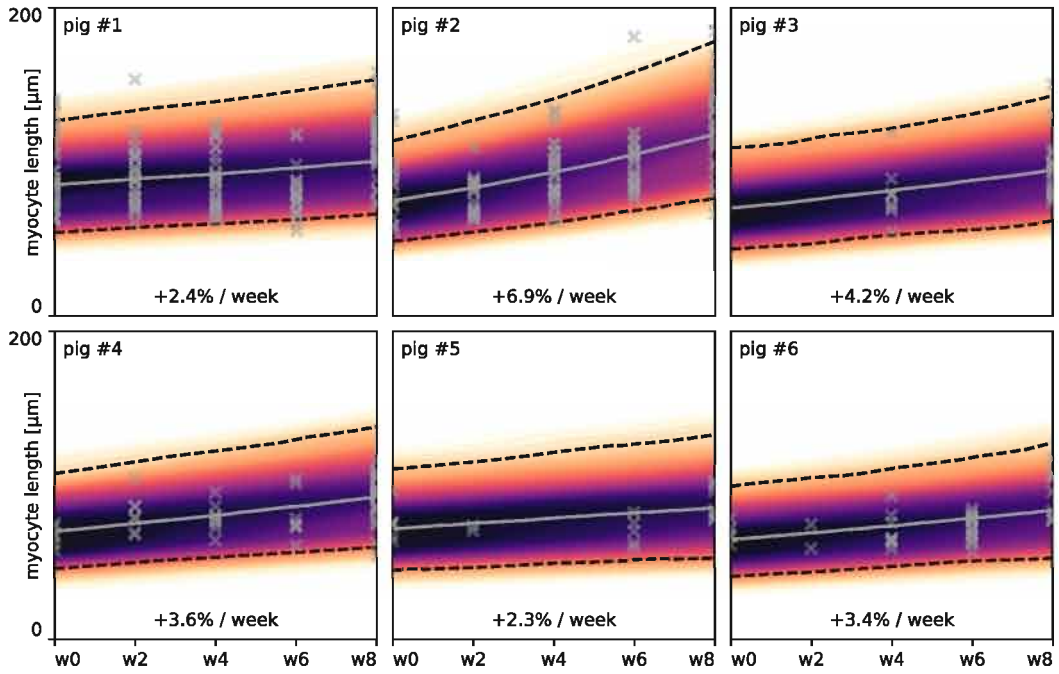

Figure 7.3: Evolution of myocyte lengths in response to left ventricular volume overload. Gray cross markers represent n = 460 individual measurements of myocyte lengths, solid gray lines represent their medians, and dashed black lines their 95% confidence intervals. Color contours from dark to light highlight the probability density from high to low.

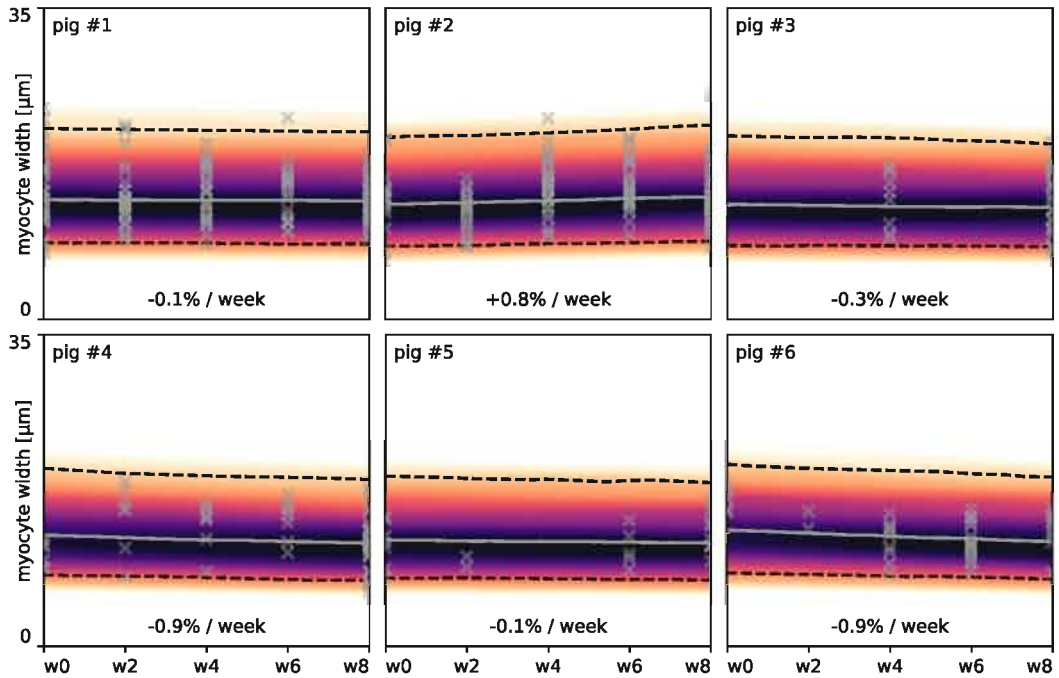

Figure 7.4: Evolution of myocyte widths in response to left ventricular volume overload. Gray cross markers represent n = 460 individual measurements of myocyte widths, solid black lines represent their medians, and dashed black lines their 95% confidence intervals. Color contours from dark to light highlight the probability density from high to low.

Figure 7.3 illustrates the myocyte length in all six animals in response to eight weeks of ventricular volume overload. The gray cross markers represent the n = 460 individual measurements, the solid gray lines represent their medians, and dashed black lines their 95% confidence intervals. The mean myocyte length in Figure 7.3 increased markedly, by +3.26%/week, with a rapid increase between weeks 6 and 8. The direct comparison between the six animals illustrates the inter-animal variation; pig #2 displayed the largest increase in myocyte length with +6.9%/week, pig #5 the smallest with +2.2%/week.

Figure 7.4 illustrates the myocyte widths in all six animals in response to eight weeks of ventricular volume overload. The gray cross markers represent the n = 460 individual measurements, the solid gray lines represent their medians, and dashed black lines their 95% confidence intervals. The mean myocyte width in Figure 7.4 varied only marginally, by −0.63%/week. Pig #2 displayed the largest increase in myocyte width with +0.7%/week, whereas pig #6 showed the largest decrease with −0.9%/week. This marginal change in myocyte width justifies the assumption of a constant myocyte width $\vartheta^{\perp} = 1.0$ and $\dot{\vartheta}^{\perp} = 0.0$ in Eq. 7.3 of our growth model.

7.3.3 Elastic behavior in vivo is softer than ex vivo

Figure 7.5 depicts the fitted diastolic filling response for each pig following the subject-specific two-stage passive myocardial tissue response calibration.Table 7.2 summarizes the computed in vivo Holzapfel-Ogden material parameters for each animal in comparison to ex vivo human Holzapfel-Ogden material parameters in Table 5.1. We consistently identified stiffness parameters of the same order of magnitude, with a mean isotropic stiffness of of $a = 153.3 \pm 41.5$ Pa, and mean fiber and sheet stiffnesses of $a_f = 505.4 \pm 136.9$ Pa,

Table 7.2: In vivo Holzapfel-Ogden parameters identified individually for each animal at baseline compared to ex vivo Holzapfel-Ogden parameters in humans. Results are summarized as mean ± standard deviation; α and β are the animal-specific scaling factors of the stiffnesses a_i and exponential parameters b_i from ex vivo human (Table 5.1) to in vivo pig.

	α [%]	β [%]	a [Pa]	b [-]	a_f [Pa]	b_f [-]	a_s [Pa]	b_s [-]	a_{fs} [Pa]	b_{fs} [-]
pig #1	11.30	57.66	118.6	4.35	391.1	8.34	54.3	7.23	31.9	1.78
pig #2	15.62	68.64	164.0	5.18	540.6	9.93	75.1	8.61	44.1	2.12
pig #3	20.74	76.64	217.7	5.78	717.7	11.09	99.7	9.61	58.6	2.37
pig #4	10.01	57.36	105.1	4.32	346.5	8.30	48.1	7.20	28.3	1.77
pig #5	16.88	76.93	177.2	5.80	584.2	11.13	81.1	9.65	47.7	2.38
pig #6	13.07	58.37	137.2	4.40	452.2	8.45	62.8	7.32	36.9	1.80
mean	14.60	65.93	153.3	4.97	505.4	9.54	70.2	8.27	41.2	2.04
std	±3.95	±9.40	±41.5	±0.71	±136.9	±1.36	±19.0	±1.18	±11.2	±0.29

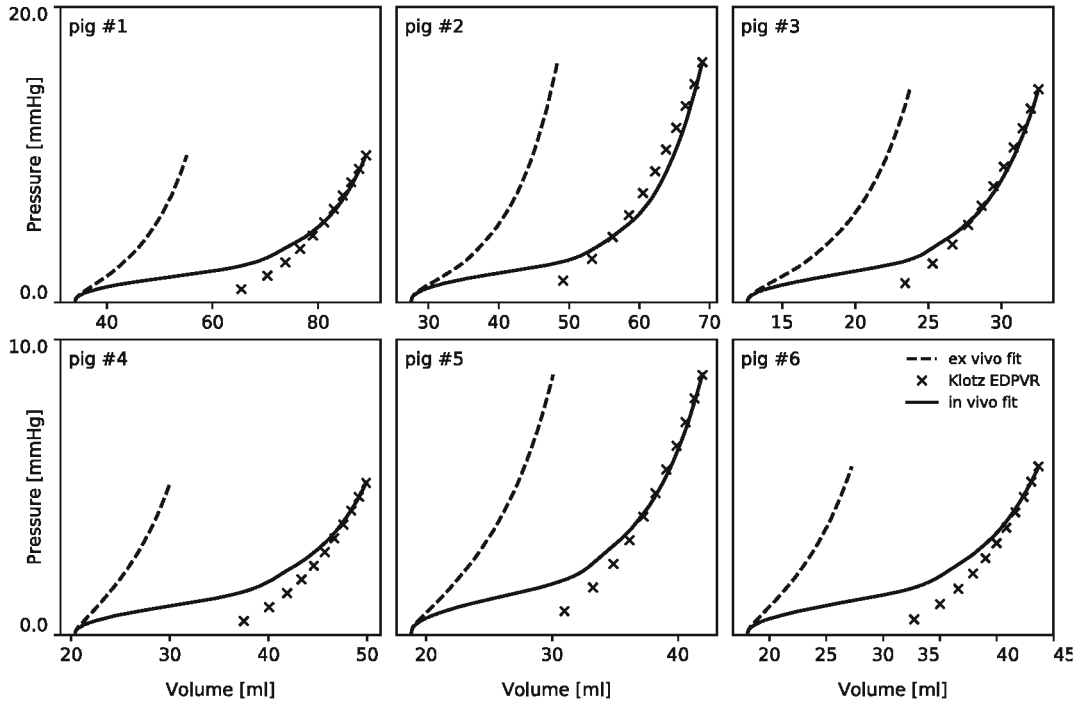

Figure 7.5: Second-stage passive myocardial tissue response calibration: dashed lines represent the diastolic filling pressure-volume relation using the first-stage passive myocardial tissue response calibration from Figure 5.12 and Table 5.1 [326], 'tri' markers depict the theoretical diastolic pressure volume relation deduced from the experimentally measured subject-specific end diastolic pressure volume data [177] and solid lines depict the passive material response fitted to represent the subject-specific passive in vivo response.

a_s = 70.2±19.0 Pa, and a_{fs} = 41.2±11.2 Pa. The exponential parameters varied from b = 4.97 ± 0.71 for the isotropic term to b_f = 9.54 ± 1.36, b_s = 8.27 ± 1.18, and b_{fs} = 2.04 ± 0.29 for the fiber and sheet terms. Notably, the stiffness parameters $a_i = \alpha\,\bar{a}_i$ took values on the order of α = 14.60 ± 3.95% of their ex vivo human counterparts $\bar{a}$. The exponential parameters $b_i = \beta\,\bar{b}_i$ were also smaller than their ex vivo human counterparts $\bar{b}$, but only by β = 65.93 ± 9.40%. The standard deviations in the two scaling parameters were small, 27.05% and 14.26 % of their means, suggesting that our inversely identified in vivo stiffness parameters are consistently smaller than their ex vivo counterparts recorded [326] and identified [299] in the literature.

7.3.4 Growth displays temporal and regional variations

Figure 7.6 illustrates the results of our sensitivity analysis with respect to the growth speed parameter τ. The three graphs show the longitudinal growth $\vartheta^{\parallel}$, the longitudinal growth rate $\dot{\vartheta}^{\parallel}$, and elastic stretch in the fiber direction λ^e for varying growth speeds evaluated for pig #4. The solid lines represent the medians and shaded regions their 95% confidence intervals. According to

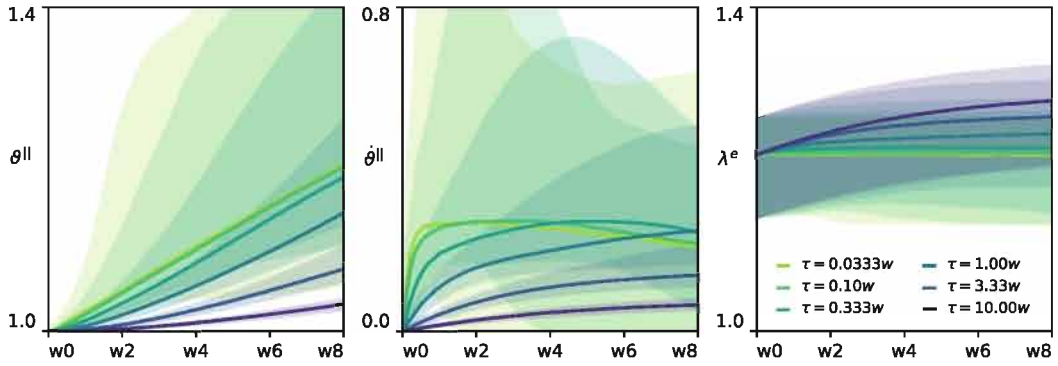

Figure 7.6: Sensitivity analysis of growth with respect to the growth speed τ. Longitudinal growth $\vartheta^{\parallel}$, longitudinal growth rate $\dot{\vartheta}^{\parallel}$, and elastic stretch in the fiber direction λ^e averaged over the ventricle for varying growth speeds τ, here illustrated for pig #4. Solid lines represent the medians and shaded regions their 95% confidence intervals across the ventricle.

Eq. 7.3, the parameter τ is inversely proportional to the longitudinal growth rate, $\dot{\vartheta}^{\parallel} \sim 1/\tau$, as long as the elastic stretch λ^e exceeds the homeostatic baseline stretch λ^{crit}. In the limit of $\tau \to 0$, growth would take place instantaneously and the elastic stretch would immediately relax to the homeostatic baseline stretch, $\lambda^e = \lambda^{crit}$. In the limit of $\tau \to \infty$, there would be no growth and the elastic stretch would always remain equal to the total stretch $\lambda^e = \lambda$. Figure 7.6 shows that for $\tau = 0.03$ week and $\tau = 0.10$ week, the response is close to the first limit case, with a linear longitudinal growth and a continuous relaxation of the elastic stretch to the homeostatic baseline stretch, $\lambda^e = \lambda^{crit}$. In other words, for $\tau = 0.10$ week, the growth model responds fast enough to always accommodate the echocardiographically measured increase in end diastolic volume. For values larger than $\tau = 0.10$ week, the growth model responds slower than the measured increase in volume, and elastic stretches $\lambda^e > \lambda^{crit}$ built up in the heart. Given that $\tau = 0.10$ week results in a fairly constant growth rate $\dot{\vartheta}^{\parallel}$, which is in correspondence with other experimental volumetric overload studies [372], we selected $\tau = 0.10$ week for all future simulations. As such, growth compensates the macroscopically observed changes in cardiac dimensions within a proper time frame, without building up a 'growth lag'. As this study set out to objectively assess the predictive power of an established growth law, we did not tune the growth speed parameter τ to the experimental data specifically.

Figure 7.7 highlights the regional, transmural, temporal, and inter-animal variations of growth throughout our study. The volume overload of 12.4%/week for pig # 3, see Figure 7.2, triggered the largest longitudinal myocyte growth of up to 88%; the volume overload of 2.5%/week for pig # 1, see Figure 7.2, triggered the smallest growth of up to 31%. Within each

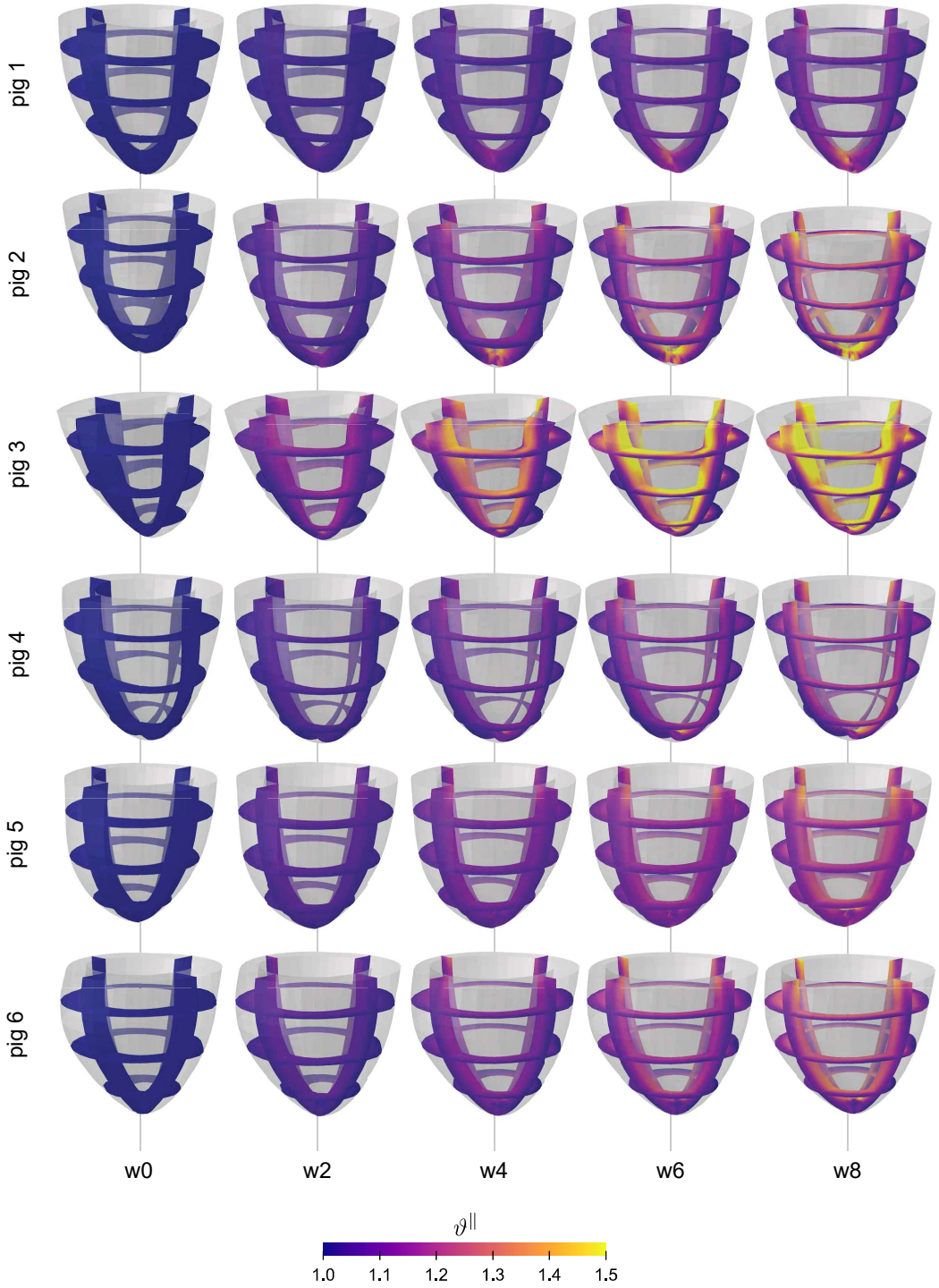

Figure 7.7: Regional, transmural, temporal, and inter-animal variations of growth in response to left ventricular overload. Longitudinal growth $\vartheta^{\parallel}$ displays notable transmural variations with larger values in the endocardium, the inner wall, and smaller values in the epicardium, the outer wall. Growth is largest in pig #3 and smallest in pig #1.

heart, growth displays notable transmural variations with larger values in the endocardium, the inner wall, and smaller values in the epicardium, the outer wall.

7.3.5 Growth model correctly predicts myocyte lengthening

For each animal, we successfully propagated the uncertainties of n = 500 end diastolic volumes from our echocardiography through the Gaussian process regression and obtained simulated myocyte morphologies, which we compared against our experimentally measured myocyte morphologies from our histology.

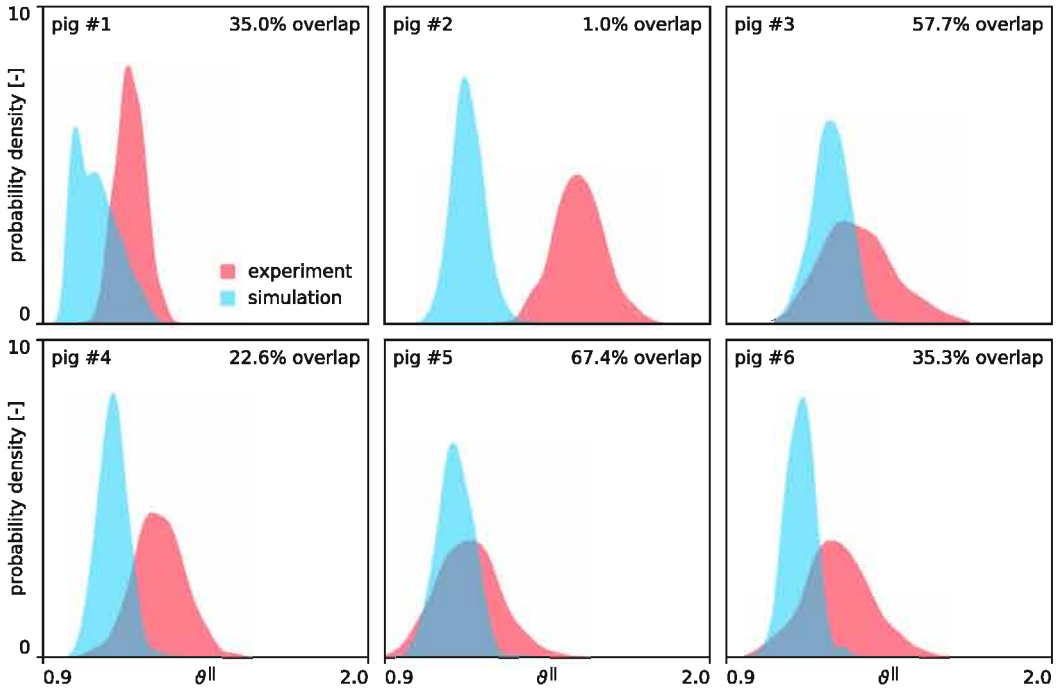

Figure 7.8: Simulation and experiment of chronic myocyte lengthening across the entire ventricular wall. Blue and red probability density functions represent computationally simulated and experimentally measured myocyte lengths throughout the entire left ventricular wall at week 8, both with uncertainty; percentage agreement refers to the region shared between both graphs. The average agreement between simulation and experiment is 36.5%.

Figure 7.8 compares the computationally simulated myocyte lengths across the entire left ventricular wall from the Gaussian process regression to the experimentally measured myocyte lengths. The blue and red probability density functions represent simulation and experiment. The probability density functions are a qualitative and quantitative illustration of the intersubject variability of cardiac growth. The overlap between the blue and red graphs is a quantitative measure of the agreement between the model prediction and the experiment [161]. The average agreement between

simulation and experiment was 36.5%, ranging from a good agreement of 67.4% for pig #5 to a poor agreement of 1.0% for pig #2. For all six animals, the blue graphs are located to the left of the red graphs, which implies that the simulation underestimates the degree of myocyte lengthening. Since our histological samples originated exclusively from endocardial biopsies sampled at the inner wall, we performed the same analysis a second time, but this time by only using simulated myocyte lengths from the endocardial wall to more closely represent our experimental setting.

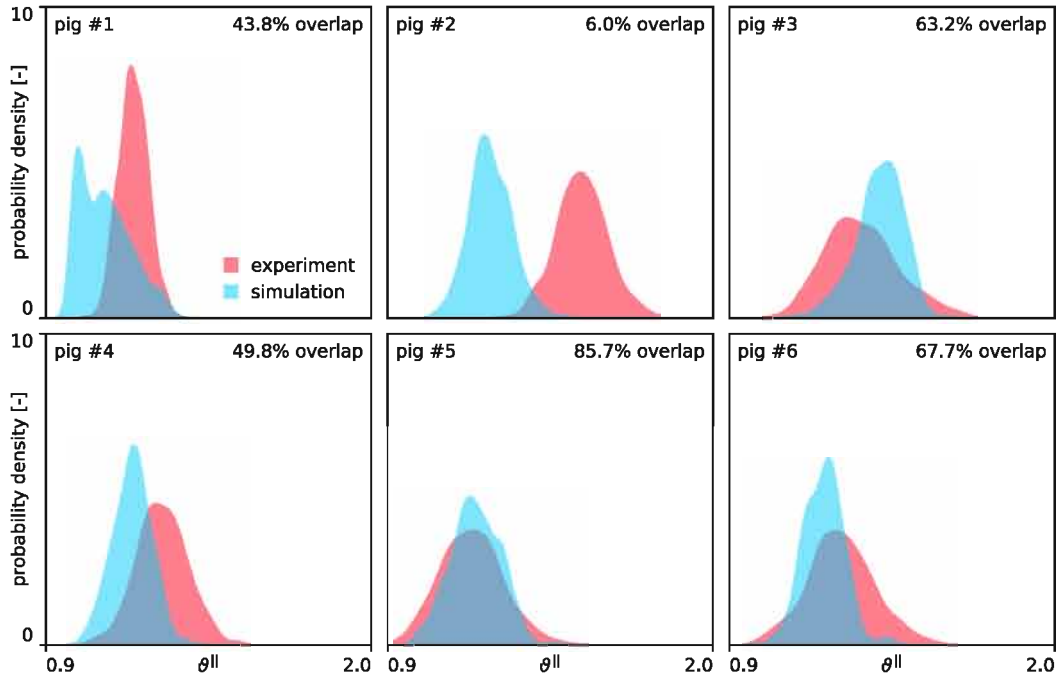

Figure 7.9: Simulation and experiment of chronic myocyte lengthening across the endocardial wall. Blue and red probability density functions represent computationally simulated and experimentally measured myocyte lengths throughout the endocardial left ventricular wall at week 8, both with uncertainty; percentage agreement refers to the region shared between both graphs. The average agreement between simulation and experiment is 52.7%.

Figure 7.9 compares our simulation of myocyte lengths across the endocardial wall from the Gaussian process regression to our experiment of histologically measured myocyte lengths. The experimental data are the same as in Figure 7.9, but now, the simulation only used the myocyte lengths in the endocardial wall (inner 10% of the ventricular wall thickness). Similar to Figure 7.8, the overlap between the blue and red graphs is a quantitative measure of the agreement between the model prediction and the experiment. The average agreement between simulation and experiment was 52.7%, ranging from an excellent agreement of 85.7% for pig #5 to a poor agreement of 6.0% for pig #2. For all six animals, the blue graphs moved

towards the right and were closer to the red graphs than in Figure 7.8. This is in agreement with the regional variation of growth in Figure 7.7, which suggests that myocyte lengthening is larger in the endocardium, where the samples were taken, than in the epicardium. If we excluded pig #2, the largest pig of our study, from our analysis, the agreement for the remaining five pigs was 62.0%. In other words, for pigs #1, #3, #4, #5, and #6, the stretch-driven growth model alone explained changes in myocyte length by 62.0%. Taken together, Figure 7.9 suggests that elevated fiber stretches induced by an increase in diastolic volume are the major stimulus of chronic myocyte lengthening.

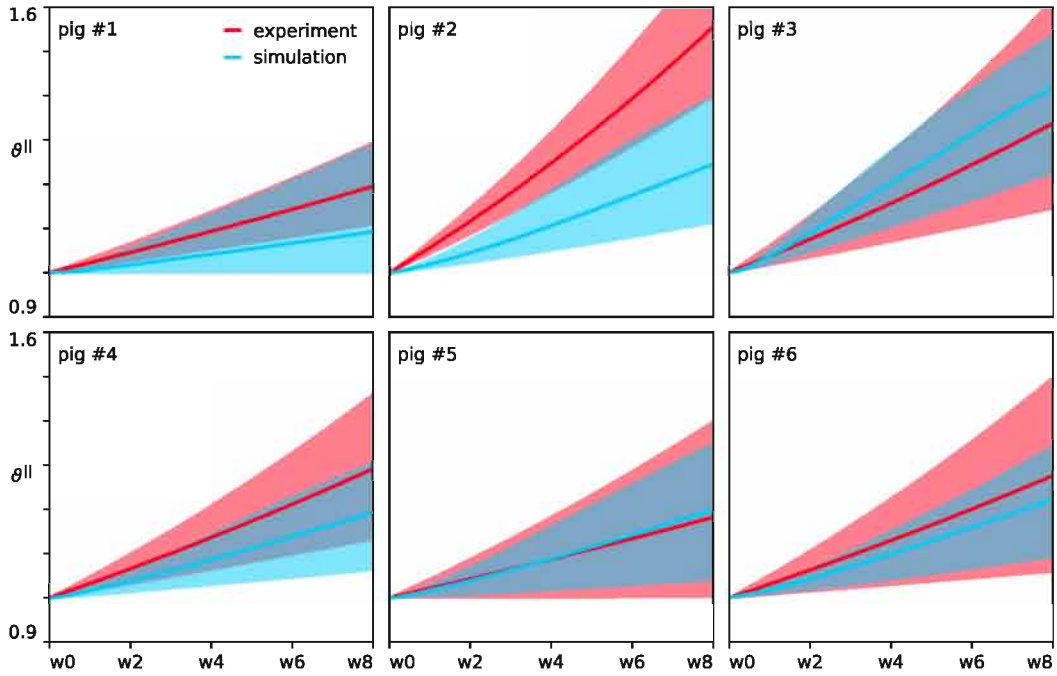

Figure 7.10: Simulation and experiment of chronic myocyte lengthening across the endocardial wall. Blue lines represent medians and shaded regions 95% confidence intervals of computationally simulated myocyte lengthening in the endocardial wall; red lines represent medians and shaded regions 95% confidence intervals of experimentally measured myocyte lengthening from endomyocardial biopsies, both with uncertainties.

Table 7.3 and Figure 7.10 compare the temporal evolution of the computationally simulated and experimentally measured changes in myocyte length. The simulated mean myocyte length increased by 2.84% per week, compared to the measured increase of 3.82% per week. This resulted in a simulated volume increase of 22.7% throughout the period of eight weeks compared to the experimentally measured increase of 30.6%. Pig #5 displayed the best agreement with a simulated and measured weekly increase of 2.47% and 2.27% respectively and an almost perfect overlap in Figure 7.10; pig #2

Table 7.3: Simulation and experiment of chronic myocyte lengthening across the endocardial wall. Computationally simulated myocyte lengths are recorded across the endocardial wall, experimentally measured myocyte lengths are determined from endomyocardial biopsies.

	Δml	W0	W2	W4	W6	W8	$\Delta/week$
pig #1	sim	1	1.02	1.04	1.07	1.09	+1.15%
	exp	1	1.05	1.09	1.14	1.19	+2.43%
pig #2	sim	1	1.04	1.11	1.17	1.24	+3.05%
	exp	1	1.12	1.25	1.39	1.55	+6.92%
pig #3	sim	1	1.09	1.2	1.31	1.42	+5.20%
	exp	1	1.08	1.16	1.24	1.34	+4.20%
pig #4	sim	1	1.04	1.09	1.14	1.19	+2.40%
	exp	1	1.07	1.14	1.21	1.29	+3.63%
pig #5	sim	1	1.04	1.09	1.14	1.2	+2.47%
	exp	1	1.04	1.09	1.13	1.18	+2.27%
pig #6	sim	1	1.04	1.1	1.16	1.22	+2.78%
	exp	1	1.06	1.13	1.2	1.28	+3.44%
overall	sim	1	1.05	1.1	1.17	1.23	+2.84%
	exp	1	1.07	1.14	1.22	1.31	+3.82%

displayed the least agreement with 3.05% and 6.92% and virtually no overlap in Figure 7.10.

7.4 Discussion

Cardiac growth is a complex process that affects the heart across multiple time and length scales. Accurate prediction of this process in response to exercise, disease, devices, or drugs could form an important clinical tool in designing new therapies for a range of pathological conditions. Recent reviews have begun to acknowledge the importance of multiscale computational modeling in providing additional insights into the pathological alterations of heart failure across the scales [32, 109, 285, 309]. Following the very first theoretical mathematical approach of biological growth in the mid 90s [295], various groups have proposed different growth models for the heart throughout the past decade [7, 109, 141, 173, 183, 283, 357]. Motivated by numerous clinical [102, 103, 123, 262, 307, 309] and experimental [192, 308, 340, 372] studies that point to the importance of mechanical forces as modulators of cardiac growth, most of these growth models postulate mechanical measures as drivers for cardiac growth. It is clear from the wide variety of proposed growth models that there still is considerable debate about the specific driving

forces for growth [357]. Naturally, to identify the best basis for formulating growth models, it is critical to quantify the predictive power of a model in tight correlation with experimental data. However, such an assessment is challenging for multiple reasons: First, the highly patient-specific time course and extent of disease progression associated with hypertrophy calls for subject-specific data collection and modeling; second, the multiscale nature of cardiac growth requires the characterization at multiple spatial scales ranging from the subcellular via the cellular to the whole organ level; third, the intrinsic uncertainty associated with sparse experimental data has a strong influence on the predicted outcome.

Here we proposed a novel approach to quantify the predictive power of cardiac growth modeling using tools from machine learning. We designed a unique chronic volume overload study and monitored growth longitudinally, bi-weekly, across multiple spatial scales. We created subject-specific computational models, exposed them to subject-specific loading conditions, calibrated their subject-specific elastic material parameters under physiological conditions, and quantified the predictive power of a multiscale stretch-driven growth model under pathological conditions. Specifically, we performed a systematic sensitivity analysis to explore the role of the growth speed parameter, quantified uncertainty in experimental measurements using Bayesian inference, and propagated the uncertainty through our subject-specific models using Gaussian process regression. In a previous purely *kinematic* study [301], we have used our experimental data to prescribe changes in cardiomyocyte dimensions and characterize resulting alterations in cardiac size. Now, we performed a dynamic study in which changes in cardiomyocyte dimensions *evolve* naturally as a consequence of our stretch-driven growth model. As such, this study truly probes the predictive potential of a multiscale growth model that correlates macroscopic changes in hemodynamic conditions to microscopic changes in myocardial architecture and myocyte ultrastructure. Importantly, nor the growth law, nor any growth parameter was tuned to lead to the best fit between simulated and experimental results. As such, we obtained an objective assessment of the growth law's predictive power in correlation with the experimental data.

7.4.1 Discrepancy between in vivo and ex vivo elastic tissue behavior

Our study characterized the individual subject-specific elastic response of myocardial tissue in the living heart using the Holzapfel-Ogden model [107, 147]. Most existing cardiac growth models are not based on study- and subject-specific experimental data collected for such a purpose. Instead, they adopt elastic model parameters from previous studies designed for a different purpose [194]. The mismatch from using experimental data of other species or other studies, combined with the inter-animal variability in elastic tissue

behavior and left ventricular geometry, highlights the importance of subject-specific modeling to accurately compute the regional stretch and stress distributions as potential drivers for cardiac growth. Specifically, here we adopted a new two-stage method (see section 5.3.1.3), which established ratios of material parameters using published ex vivo triaxial shear experiments [326] and mapped the ex vivo parameters onto their subject-specific in vivo counterparts via two scaling coefficients using our own pressure-volume data [301] as showcased in Figure 7.5. The underlying assumption to reduce the set of unknowns is that the ratios between the four stiffness parameters a, a_f, a_s, and a_{fs} and the four exponential model parameters b, b_f, b_s, and b_{fs} remain unchanged in vivo and ex vivo, but their absolute values change linearly via the scaling coefficients α and β. Here, we identified the means of these coefficients to α = 7.64% and β = 62.74%. Table 7.2 revealed that the subject-specific scaling coefficients α and β displayed a relatively low standard deviation of 17.41% and 13.09 % amongst the six animals, while their means were significantly smaller than their ex vivo counterparts, here 92.36% and 37.26%. This observation is significant since it suggests that the ex vivo identified Holzapfel Ogden stiffness parameters [147] overestimate the myocardial stiffness by more than one order of magnitude. The drastic increase in myocardial stiffness from in vivo to ex vivo is a collective result of ultrastructural and architectural changes within the myocardial tissue post mortem and upon explantation. This trend is consistent with prior studies of α = 16.0% and β = 73.0% for porcine [299] and α = 8.98% and β = 77.9% for human (see chapter 6)[269] myocardial tissue in vivo. In summary, we suggest using Holzapfel-Ogden stiffnesses of a = 80.2 Pa, a_f = 264.5 Pa, a_s = 36.7 Pa, and a_{fs} = 21.5 Pa, and b = 4.73, b_f = 9.08, b_s = 7.87, and b_{fs} = 1.94 when simulating porcine myocardial tissue in vivo.

7.4.2 Growth displays temporal and regional variations

To illustrate the temporal evolution of growth, we performed a systematic sensitivity analysis of the growth parameter τ in Figure 7.6. Our myocyte morphologies in Table 7.1 revealed that our mean myocyte lengthening of +3.26%/week resulted in a total myocyte lengthening of 26.08% throughout the period of eight weeks, while the mean myocyte width remained virtually constant with a small reduction of -0.63%/week. This agrees well with a human cardiomyopathy study in which myocyte lengths from freshly isolated cardiac tissue were on average 40% longer in the cardiomyopathy group than in the healthy control group, while the myocyte widths displayed no statistically significant differences between both groups [102]. Our histological measurements explained chronic myocyte lengthening through an increase in the mean serial sarcomere number of +3.83%/week resulting in a total increase in the serial sarcomere number of 30.64% within eight

weeks, while the mean sarcomere length remained unchanged with a small increase of +0.02%/week. A previous chronic volume overload study in rabbits has shown that myocytes compensate for chronic overstretch by adding sarcomeres in series, initially at a constant rate of approximately one sarcomere per day [372]. Our mean myocyte lengths also increased linearly in time, from 85.45 to 107.75, by adding sarcomeres in series, from 47.50 to 62.07, at a constant rate of one sarcomere per four days [301]. This agrees well with our sensitivity analysis in Figure 7.6, from which we have rationalized a growth parameter of $\tau = 0.10$ weeks associated with a linear increase in myocyte length $\vartheta^{\parallel}$ at a constant rate $\dot{\vartheta}^{\parallel}$. Our four-fold slower sarcomere addition in pigs compared to rabbits [372] translates into a four-fold difference in the parameter τ, and could be a natural consequence of the four-fold difference in metabolic rate between pigs and rabbits [176].

To illustrate the regional, transmural, and intra-animal variations of growth, the myocyte lengthening $\vartheta^{\parallel}$ across the entire volume overloaded left ventricle was plotted in Figure 7.7. Our model revealed a pronounced heterogeneity in the cellular response to volume overload with myocytes in the endocardium, the inner wall, growing more than myocytes in the epicardium, the outer wall. These regional variations agree well with previous volume overload simulations in an idealized bi-ventricular model [108] and in a personalized human heart model [96], and with chronic volume overload experiments in sheep [340], where myocyte lengthening was more pronounced in the endocardial than in the epicardial wall. The observed regional, transmural, and inter-animal heterogeneity of growth elucidates the importance of subject-specific modeling of growth to avoid erroneous results and conclusions.

7.4.3 Bayesian inference reveals chronic dilation and myocyte lengthening

Our study characterized volume overload induced growth at a uniquely high spatial and temporal resolution; however, it was still constrained by the natural limitations of a chronic large animal study associated with sparse and unevenly distributed data for each individual animal [301]. Using the concepts of hierarchical modeling and Bayesian inference proved crucial to interpret our experimental measurements in view of the total cohort of animals. For example, pig #3 only had n = 5 myocyte morphology recordings at week 4 and n = 11 at week 8. Nonetheless, when interpreted within the total cohort of all six subjects, we could observe clear trends of pronounced myocyte lengthening at +4.3% per week in Figure 7.3 and of marginal myocyte thinning of -0.3% per week in Figure 7.4. Using tools from machine learning to interpret our data also allowed us to quantify the uncertainty of our experimental measurements and provided confidence in the finding that

volume overload triggers chronic dilation and myocyte lengthening. On the whole organ level, our results in Table 7.1 and Figure 7.2 confirmed the common understanding that a chronic volume overload induces an increase in end diastolic volume. This resulted in a decrease in ejection fraction, from 55.6% to 47.7%, which agrees qualitatively with clinical observations [184], but is quantitatively less pronounced than in end-stage heart failure patients [102]. A mean weekly increase in end diastolic volume of +5.95% resulted in a total increase of 47.6% after only eight weeks. These values are in good agreement with a clinical study where 88 hypertensive patients were compared to 29 healthy controls [293]. On the cellular level, Figure 7.3 revealed significant changes in myocyte length of +3.83% per week, whereas Figure 7.4 suggested negligible changes in the myocyte width of −0.63% per week. The myocyte lengthening and fairly constant myocyte width resulted in a myocyte length-to-width ratio of 6.3 at baseline and of 8.3 after eight weeks of volume overload. These results are in good agreement with the reported myocyte length-to-width ratios ranging from 7.0 in the healthy left ventricle [23] to 11.5 in the failing left ventricle [102]. Additionally, the approximately constant width of the confidence intervals in Figures 7.2 to 7.4 confirms that the linear evolution assumption on the log-normal mean of the end diastolic volume, the myocyte length, and the myocyte width in Eq. 7.7 is appropriate to describe the temporal evolution of the collected experimental data.

In summary, using tools from machine learning, hierarchical modeling, Bayesian inference, and uncertainty quantification, proved critical to interpret our unevenly distributed data and to quantify the intrinsic uncertainties in our experimental measurements. Using these methods in real time – in parallel to an ongoing study – could guide strategies of adaptive sampling, for example by purposely selecting non-equidistant, unevenly distributed time points to efficiently explore the parameter space and maximize the information content of each measurement [303].

7.4.4 Uncertainty propagation provides quantitative insight into the quality of our model

To date, there is no established method to bridge subcellular, cellular, tissue, and organ levels and to characterize how heart failure alters cardiac form and function across the scales. In a previous study, we have used a purely *kinematic* approach to connect the sarcomere, myocyte, myocardial, and whole heart levels [301]. Here we used a *dynamic* approach and connected the scales via a multiscale cardiac growth model to predict how myocyte morphologies evolve dynamically as a result of ventricular volume overload. Most importantly, we have designed an experimental study that collects data across the scales to precisely quantify the *predictive* features of our model. Specifically, our mechanistic multiscale growth model is sensitive

to volumetric overload, which initially drives individual myocytes away from their homeostatic equilibrium state until they have deposited enough sarcomeres in series to regain homeostatic equilibrium. We quantified the uncertainties in our volume overload recordings that drive myocyte lengthening and propagated this uncertainty through our growth model [281, 282] to the predicted changes in myocyte morphology. However, rather than performing a computationally expensive growth simulation for each realization, we created a computationally efficient surrogate model from Gaussian process regression and propagated the uncertainties through this surrogate model [271]. Figure 7.8 provided a side-by-side comparison of the experimentally measured and the computationally predicted myocyte lengths after eight weeks, both with uncertainties. The mean overlap between both graphs defined the agreement of model and experiment of 36.5%. Since the biweekly biopsy samples for our experimentally measured myocyte morphologies were collected on the endocardial surface of the left ventricle, we re-did the analysis, but now by only sampling our computationally simulated myocyte morphologies across the endocardial wall. Figure 7.9 shows the quantitative comparison between experimentally measured and computationally predicted myocyte lengths. The agreement ranges from excellent with 85.7% for pig #5 to poor with 6.0% for pig #2. On average, our growth model displayed a predictive power of 52.7% to predict myocyte lengths from ventricular volume overload. If we exclude pig #2, the largest pig of our study, from this analysis, the predictive power increased to 62.0%. The average agreement of 36.5% and 52.7% in Figures 7.8 and 7.9 is slightly lower than the average agreement of 54.0% in our previous, purely kinematic analysis [301]. This observation is not unexpected, since our predictive growth model of the *dynamic* evolution of myocyte lengths allows for more freedom than our previous, purely kinematic enforcement of the correlation between the scales.

7.4.5 Limitations

This study proposed a new strategy to develop, calibrate, and validate a multiscale growth model that tightly integrates experiment and simulation using tools from machine learning. While this allowed us, for the first time, to quantify the predictive power of a stretch-based growth model, our study has a few limitations: First, in view of the relatively large inter-animal variability, our initial number of six subjects seems rather low. With our proposed methods, we can easily integrate new subjects into our study and explore the predictive power of our stretch-driven growth model for a larger group. This could also help us to better explain the discrepancies for pig #2 and to assess the uncertainty on the growth rate parameter τ. Second, our subjects were all monitored bi-weekly, throughout a limited time period of eight weeks.

In retrospect, it would have been interesting to continue the study for a few more weeks to more closely approach end stage heart failure. If we had known upfront that we would use Bayesian inference to analyze our data, we could have designed the study more interactively and used adaptive sampling to more efficiently sample the parameter space. Third, we have selected a relatively simple growth model with only one free parameter, the parameter τ. While we have rationalized this parameter from a systematic sensitivity analysis and other experimental studies, a follow-up study could try to 'learn' this parameter from the experimental data specifically. However, a longer study interval would be needed to truly identify the growth parameter τ and compare our simple stretch-driven model to more complex stretch- or stress-driven models for growth. For the considered stretch-driven growth law, a mere tuning of τ to the temporally changing histology data is not expected to improve the overlap. More specifically, the $\tau = 0.10$ week rationalization renders nearly-maximal longitudinal growth for the considered growth law and still underestimates the myocyte lengthening at week 8 for pig #1, #2 and #4. Fourth, we have induced left ventricular volume overload in pigs through controlled regurgitation to ultimately gain insight into the progression of heart failure in humans. While ventricular volumes and myocyte dimensions are relatively comparable between pigs and humans, it remains to be shown to which extent the timeline of cellular and ventricular adaptation to volume overloaded pigs translates into the timeline of heart failure in humans. Finally, in setting up these subject-specific ventricle models at baseline, multiple modeling aspects (i.e. the constitutive material parameters, the ventricular geometry, the myofiber architecture, the boundary conditions, etc.) can have a potential effect on the predicted ventricular mechanics, but quantifying the effect of each of these modeling aspects, as done in e.g. [27, 66, 269, 294] was considered beyond the scope of this study. Here, we followed the current best practices to set up deterministic subject-specific ventricular models for each pig at baseline [299].

7.5 Conclusion

Multiscale cardiac growth models hold huge promise for simulating the patient-specific timeline of heart failure and for optimizing surgical or pharmacological treatment strategies. While scientists are increasingly recognizing the predictive potential of cardiac growth models, the clinical community is rather skeptical, mainly because the predictive power of these models remains unknown. Here we designed a new approach to quantify the predictive power of cardiac growth models by combining multiscale experiments and simulations using tools of machine learning. We adopted techniques of hierarchical modeling, Bayesian inference, and

Gaussian process regression to quantify the uncertainty of our experimental measurements and propagated this uncertainty through a surrogate model for cardiac growth to predict changes in myocyte morphology. Our results suggest that stretch-driven growth is the major contributor to alterations in myocyte morphology. Our simple growth model alone can explain 52.7% of the observed changes in myocyte length. Using machine learning in heart failure research allowed us to seamlessly integrate experimental, computational, and clinical data from different scales and times and to design efficient experimental and clinical studies that adaptively sample the parameter space at varying points in space and time. Machine learning tools naturally provide high-resolution quantitative insight into the quality of the experiments and the predictive potential of the models. Ultimately, our approach has the potential to combine information from different sources, subjects, and scales to provide a more holistic picture of the failing heart and point towards new treatment strategies.

III

Inverse elastostatics

Chapters

8 Pressure-induced in vivo stress state **199**

Conclusion **219**

CHAPTER 8

PRESSURE-INDUCED IN VIVO STRESS STATE

Patient-specific biomechanical modeling of the gastro-intestinal and cardiovascular system is complicated by the constant presence of a physiological pressure load due to which the imaged tissue is in a pre-stressed and -strained state. Neglect of this prestressed state into solid soft tissue mechanics models leads to erroneous metrics (e.g. wall deformation, peak stress, wall shear stress) which in their turn are used for device design choices, risk assessment (e.g. procedure, rupture) and surgery planning. It is thus of utmost importance to incorporate this deformed and loaded tissue state into the computational models, which implies solving an inverse problem (calculating an undeformed geometry given the load and the deformed geometry). In this chapter* we describe the different methodologies to compute the zero-pressure geometry and/or in vivo stress state, each having their own inherent advantages and disadvantages. Next, we propose and implement a novel, modular inverse elastostatics (IE) approach and implemented this methodology in a commercial finite element analysis (FEA) solver with minor user subroutine interventions. Next, the accuracy was demonstrated in an arterial tube and porcine biventricular myocardium model. Finally, the computational power and efficiency of the methodology was demonstrated for two

*This chapter is mostly based on M. Peirlinck, M. De Beule, P. Segers, and N. Rebelo, "A modular inverse elastostatics approach to resolve the pressure-induced stress state for in vivo imaging based cardiovascular modeling", *Journal of the Mechanical Behavior of Biomedical Materials*, vol. 85, pp. 124–133, 2018.

models containing multiple interacting incompressible, anisotropic (fiber-embedded) and hyperelastic material behaviors: a patient-specific abdominal aortic aneurysm and a full 4-chamber human heart model.

8.1 MOTIVATION

Thanks to great progress in modeling approaches in biomechanics, numerical models built from patient-specific image data sets can provide medical researchers with tools to gain insight into biomechanical phenomena and the pathophysiology of gastro-intestinal and cardiovascular diseases [42, 96, 268]. In addition, numerical models offer a computational environment in which both new and existing medical procedures and devices can be virtually tested and optimized, which is both cost-effective and patient-friendly [13, 163, 268, 298]. The esophagus, the aorta and the heart naturally function under permanent physiological loading conditions. Consequently, most of these systems never experience a stress-free state in their 'service life', thus a stress and strain field is present in any in vivo obtained patient-specific gastro-intestinal or cardiovascular geometry. Whilst big strides have been taken in developing these patient-specific models, the presence of in vivo pressure loads and strains is often still ignored which leads to in an inaccurate rating of the stresses and deformations. Several studies have indicated that ignoring the zero-stress state leads to errors in the computed stress, strain, resistance to bolus flow, growth, etc. in the esophagus [117], that the constitutive response of mitral valves is highly sensitive to the level of prestrain [284], that omitting an initial zero-stress state in patient-specific aortic abdominal aneurysm models leads to different effects in wall stress and radius [354], and that failure to recover the zero-pressure configuration of vascular structures used in FSI simulation leads to significant differences in the computed wall deformation, wall shear stress and pressure distribution, as well as in the velocity field, and vorticity patterns [344]. A correct physiological stress state can thus be considered crucial in assessing the tissue's mechanosensory function and behavior, evaluating the mechanical response to interventions and device implantation and estimating possible growth or remodeling of these tissues [96]. To define the in vivo stress state of soft tissue, an inverse problem needs to be solved. Contrary to the classical (direct) problem in non-linear elasticity, the undeformed shape of a body or its stress state in its deformed state needs to be determined given the deformed configuration and the loads causing this deformation. Multiple methodologies have been proposed to solve this inverse problem over the last decades which can be categorized as iterative and direct methodologies. The iterative solution frameworks lack computational efficiency, accuracy and robustness, especially for anisotropic materials (e.g. quasi-incompressible fibrous hyperelastic materials). Direct

methodologies, typically inverse elastostatics (IE) approaches could resolve these issues but are typically problem specific because the formulation is dependent on the material behavior, and require access to the finite element code, which is not trivial for commercial products. This work addresses these issues by implementing a modified, modular and computationally efficient IE approach focused on an easy implementation in existing commercial FEA software.

8.2 PROBLEM DESCRIPTION

As explained in chapter 1, to solve a the standard problem of elastostatics, we typically set up a basic continuum mechanical framework in which the stress-free reference configuration $\mathcal{B}_0$ of the continuous body of interest $\mathscr{B}$ gets transformed to the deformed configuration, denoted $\mathcal{B}$, through $\varphi : \mathcal{B}_0 \subset \mathbb{R}^3 \to \mathcal{B} \subset \mathbb{R}^3$ (see Eq. 1.1). Any particle with position $\boldsymbol{X}$ in the stress-free reference configuration $\mathcal{B}_0$ maps to position $\boldsymbol{x} = \varphi(\boldsymbol{X})$ in the deformed configuration $\mathcal{B}$

$$\boldsymbol{x} = \boldsymbol{X} + \boldsymbol{u} \tag{8.1}$$

where $\boldsymbol{X}$ is known and $\boldsymbol{u}$, the displacement, is being computed, such that the following equilibrium equations (see also section 1.4.1) are satisfied for given boundary conditions

$$\nabla\boldsymbol{\sigma} + \rho\boldsymbol{f} = \mathbf{o} \quad \text{in} \quad \mathcal{B} \tag{8.2a}$$

$$\boldsymbol{u} = \boldsymbol{u}_d \quad \text{on} \quad \partial\mathcal{B}_d \tag{8.2b}$$

$$\boldsymbol{n}\boldsymbol{\sigma} = \boldsymbol{t}_n \quad \text{on} \quad \partial\mathcal{B}_n \tag{8.2c}$$

in which $\boldsymbol{f}$ is a given body force per unit reference volume, $\partial\mathcal{B}_n$ and $\partial\mathcal{B}_d$ are disjoint partitions of boundary where surface traction and displacement are applied, and $\boldsymbol{n}$ is the normal to the surface boundary. To describe this forward local material deformation with respect to the reference configuration, we introduced the forward deformation gradient $\boldsymbol{F}$ (see Eq. 1.2) which is defined as

$$\boldsymbol{F} := \partial_{\boldsymbol{X}}\varphi(\boldsymbol{X}) = \frac{\partial \boldsymbol{x}}{\partial \boldsymbol{X}} \tag{8.3}$$

In the inverse problem, however, we know the deformed configuration $\boldsymbol{x}$ and want to solve for the undeformed configuration $\boldsymbol{X}$.

8.3 A MODIFIED MODULAR INVERSE ELASTOSTATICS METHOD

As has been shown by Govindjee and Mihalic, this inverse class of problems can be solved using an inverse elastostatics (IE) method in which the inverse motion is sought. A simple re-parametrization of the standard equilibrium

equations provides an efficient and straightforward technique to implement these problems in a finite element analysis (FEA) framework [114]. For that reason, we simply defined the inverse deformation gradient as follows

$$\boldsymbol{F}^{-1} := \partial_{\boldsymbol{x}} \boldsymbol{\varphi}^{-1}(\boldsymbol{x}) = \frac{\partial \boldsymbol{X}}{\partial \boldsymbol{x}} = \boldsymbol{I} - \frac{\partial \boldsymbol{u}}{\partial \boldsymbol{x}} \tag{8.4}$$

Operating at an integration point of an element, this inverse deformation gradient translates to

$$\boldsymbol{F}^{-1} = \boldsymbol{I} - \boldsymbol{\beta}^T \boldsymbol{u}^N \tag{8.5}$$

where $\boldsymbol{u}^N$ and $\boldsymbol{\beta}$ denote the vector of nodal displacements and the interpolation function gradients respectively. By algebraically inverting $\boldsymbol{F}^{-1}$, we got the deformation gradient $\boldsymbol{F}$ which maps the unknown initial configuration $\boldsymbol{X}$ to the known deformed configuration $\boldsymbol{x}$. Following Eq. 2.7, we filtered out the volumetric behavior in the deformation gradient $\boldsymbol{F}$ [254], so we got the isochoric deformation gradient $\bar{\boldsymbol{F}} = (\det \boldsymbol{F})^{1/3} \boldsymbol{F}$. As explained in paragraph 2.1.1.1.3, invariance under superposed rigid body motions requires us to bring $\bar{\boldsymbol{F}}$ into the deviatoric part $\bar{\Psi}$ of the strain energy potential function through the deviatoric right Cauchy-Green deformation tensor. Following Spencer, the strain energy function representing the constitutive behavior of hyperelastic fiber embedded anisotropic material could be generated by the following strain invariants [329]:

$$J = \det \boldsymbol{F} \tag{8.6a}$$

$$\bar{I}_1 = \operatorname{tr} \bar{\boldsymbol{C}} \tag{8.6b}$$

$$\bar{I}_2 = \frac{1}{2}\left(\left(\operatorname{tr} \bar{\boldsymbol{C}} \right)^2 - \operatorname{tr} \bar{\boldsymbol{C}}^2 \right) \tag{8.6c}$$

$$\bar{I}_{4ij} = \boldsymbol{N}_i \bar{\boldsymbol{C}} \boldsymbol{N}_j \tag{8.6d}$$

$$\bar{I}_{5ij} = \boldsymbol{N}_i \bar{\boldsymbol{C}}^2 \boldsymbol{N}_j \tag{8.6e}$$

where $\boldsymbol{N}_i$ represents the i^{th} family of fiber orientations in the undeformed configuration. However, in this inverse problem, we only knew the fiber orientations $\boldsymbol{n}_i$ in the deformed configuration:

$$\boldsymbol{n}_i = \boldsymbol{R} \boldsymbol{N}_i \tag{8.7}$$

in which $\boldsymbol{R}$ represents the rotation tensor, typically computed from the polar decomposition of the deformation gradient into $\boldsymbol{R}$ and the symmetric positive-definite right-stretch tensor $\boldsymbol{U}$ (see Eq. 1.4). And thus

$$\boldsymbol{N}_i = \boldsymbol{R}^{-1} \boldsymbol{n}_i = \boldsymbol{R}^T \boldsymbol{n}_i \tag{8.8}$$

Solving the inverse problem, we can implement different material models dependent on the chosen application.

As discussed in section 2.1.1.4, arterial tissue can be considered as an orthotropic incompressible hyperelastic material with two to four families of collagen fibers [12, 89, 148, 151]. Constitutively, the microstructure-based isochoric strain energy function $\bar{\Psi}$ for these models can be generally described as:

$$\bar{\Psi} = C\left(\bar{I}_1 - 3\right) + \sum_{i=1}^{n_{fib}} \frac{k_{1,i}}{2k_{2,i}} \exp\left[k_{2,i}\left(\bar{\lambda}_i^2 - 1\right)^2\right] - 1 \tag{8.9}$$

where the superscript i denotes the the i^{th} fiber family (n_{fib} being the total number of fiber families), C, $k_{1,i}$, $k_{2,i}$ are constitutive material parameters, $\bar{I}_1$ is the isochoric first invariant of the right Cauchy-Green tensor and $\bar{\lambda}_i$ is the isochoric stretch of the i^{th} fiber family. Here, we implemented Gasser et al.'s material model for arterial layers which presumes two distributed collagen fiber orientations (with a certain pitch angle and amount of dispersion) (see also Eq. 2.19)[89]:

$$\bar{\Psi} = \frac{c}{2}\left(\bar{I}_1 - 3\right) + \frac{k_1}{2k_2} \sum_{i=4,6} \exp\left[k_2\langle \bar{I}_i' - 1\rangle^2\right] - 1 \tag{8.10}$$

with $\bar{I}_i' = \kappa \bar{I}_1 + (1 - 3\kappa)\,\bar{I}_i$ and $\bar{I}_i = \bar{\lambda}_\theta^2 \cos^2\alpha_i + \bar{\lambda}_z^2 \sin^2\alpha_i$. Here, $C = c/2$, $n_{fib} = 2$, $k_{1,1} = k_{1,2} = k_1$, $k_{2,1} = k_{2,2} = k_2$ are the corresponding constitutive material parameters, κ denotes the amount of dispersion in collagen fiber direction α_i (the angle between the i^{th} fiber and the circumferential direction) and $\langle\rangle$ stands for the Macauley brackets making sure the collagen fibers only contribute to the strain energy potential when they are stretched (no strength in compression).

As discussed in section 5.3.2, myocardial tissue is a composite of sheets of parallel myocytes (predominant muscle cells), anchored in a connective tissue network, containing mainly collagen and elastin fibers. Solving the inverse problem for this tissue, we implemented Holzapfel and Ogden's passive myocardial constitutive model [147], with the following structure-based isochoric strain energy function:

$$\begin{aligned}\bar{\Psi} = {} & \frac{a}{2b}\exp\left[b\left(\bar{I}_1 - 3\right)\right] + \sum_{\alpha=f,s} \frac{a_\alpha}{2b_\alpha}\left(\exp\left[b_\alpha\left(\bar{I}_{4\alpha\alpha} - 1\right)^2\right] - 1\right) \\ & + \frac{a_{fs}}{2b_{fs}}\left(\exp\left[b_{fs}\bar{I}_{4fs}^2\right] - 1\right)\end{aligned} \tag{8.11}$$

in terms of the fiber axis N_f, and the sheet (cross-fiber) axis N_s. Here, a, a_f, a_s, a_{fs} are stress-like and b, b_f, b_s, b_{fs} are dimensionless constitutive material parameters.

The total strain energy potential Ψ follows from adding the volumetric contributions dependent on the total volume ratio J (see also paragraph 2.1.1.1.4):

$$\Psi = \bar{\Psi} + \frac{1}{D}\left(\frac{J^2-1}{2} - \ln J\right) \tag{8.12}$$

Using the principle of virtual work [47], we can compute the Second Piola-Kirchoff stress tensor $\boldsymbol{S}$ from this strain energy potential as follows (see also Eq. 2.4):

$$\boldsymbol{S} = 2\frac{\partial \Psi}{\partial \boldsymbol{C}} \tag{8.13}$$

which is a measure of the force acting on an element of area in the undeformed configuration, whilst we wished to express equilibrium in the deformed configuration (Eq. 8.2). For that reason, we pushed-forward to the (true) Cauchy stress $\boldsymbol{\sigma}$, being a measure of the force acting on an element of area in the deformed configuration

$$\boldsymbol{\sigma} = J^{-1}\boldsymbol{F}\boldsymbol{S}\boldsymbol{F}^T \tag{8.14}$$

This leads to the internal nodal forces (see section 1.4):

$$\boldsymbol{f}^N_{int} = \int_{V^N} \boldsymbol{\beta}^T \boldsymbol{\sigma} dV \tag{8.15}$$

Instead of writing our own FEA code to solve this 'inverted forward' problem, we chose to implement the described methodology in an *Abaqus UEL* user element subroutine, which turned out to be very straightforward. For compatibility with the existing analyses, a linear tetrahedral topology was chosen. The user element's main contribution to the model during general analysis steps was to provide residuals $\boldsymbol{R}^N$ at the nodes, which depend on the displacements $\boldsymbol{u}^N$ at the nodes

$$\boldsymbol{R}^N = \boldsymbol{t}^N_{ext} - \boldsymbol{f}^N_{int} \tag{8.16}$$

with $\boldsymbol{t}^N_{ext}$ being the external forces (due to applied distributed loads on the known deformed configuration) and $\boldsymbol{f}^N_{int}$ being the internal forces (due to e.g. the stresses $\boldsymbol{\sigma}$) at node N. The rotations of possible initial load terms (which are zero for the unloaded configuration) must be taken into account for computing $\boldsymbol{t}^N_{ext}$. The required tangent stiffness matrix was obtained through numerical differentiation of the nodal forces. Based on our intended application, we introduced pressure loading boundary conditions to the *UEL*. Next, the *Abaqus* FEA architecture minimizes these residuals $\boldsymbol{R}^N$ solving for the displacement $\boldsymbol{u}^N$ from the unknown unpressurized

geometry to the known in vivo deformed geometry, using the Newton-Raphson iterative method (see Figure 1.6). This user element was plugged into an *Abaqus/Standard* simulation in which we disabled the geometrical nonlinearity flag (NLGEOM) to make sure the equilibrium is only evaluated in the reference, in this case deformed, configuration. More specifically, when there is considerable deformation, the probability of the solution being within the convergence radius of the Newton-Raphson method is quite low. In the classic forward problem, an incremental approach is then used to reach the desired result. In contrast, our inverse methodology computes a sequence of total inverse solutions corresponding to progressively larger loads. The total solutions for the displacements $\boldsymbol{u}^N$ of a lower load problem are used as the initial guess for the iterative process of the subsequent solution. Although this methodology appears to be incremental, the sequence of solutions thus obtained has no physical meaning in the traditional sense; it does not represent the deformation path to go from the undeformed configuration to the deformed configuration but rather a sequence of total solutions corresponding to increasing loads, see Figure 8.1.

Given the nearly-incompressible behavior of cardiovascular tissue [249] and our wish to use the same material formulation in both the *Implicit* and *Explicit* *Abaqus* finite element framework, the constant D involved in the volumetric contribution to the total strain energy function (SEF) was chosen in such a way that the material would be almost incompressible, without causing numerical difficulties during the solution of the system of equations, and without later causing an undue small time increment in an *Explicit* analysis. For the constitutive material properties used (summarized in Table 8.1), the equivalent initial Poisson ratio ν was higher than 0.495.

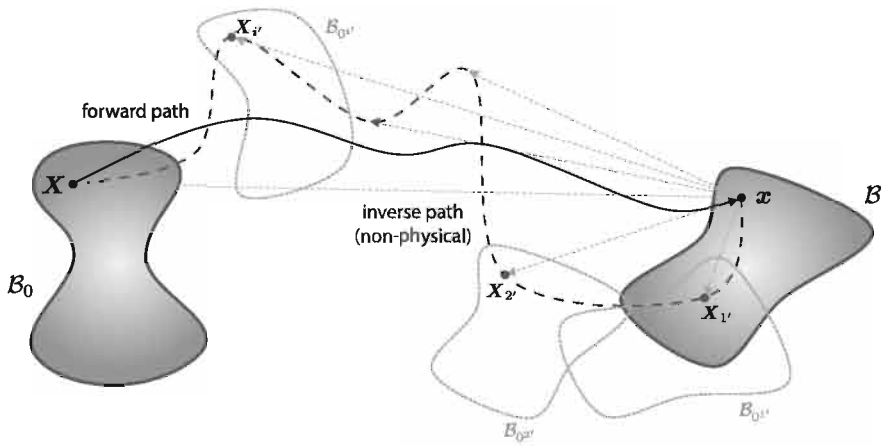

Figure 8.1: Modified inverse elastostatics methodology schematic.

Table 8.1: Constitutive homogeneous parameters used in this study; the anisotropic arterial constitutive parameters for the abdominal aorta and iliac artery were taken from [89, 296], the isotropic neo-Hookean calcified and thrombus tissue was modeled based on the constitutive parameters found in [215], the porcine myocardial tissue and human myocardial tissue parameters were taken from [85, 107] respectively.

			Arterial tissue					
	c (kPa)	k_1 (kPa)	k_2	κ	α (°)			
Abdominal aorta	0.24	244.9	1576.2	0.14	5			
Iliac artery	15.28	996.6	524.6	0.226	49.98			
Calcifications	8929.0							
Thrombus	36.0							
			Myocardial tissue					
	a (kPa)	b	a_f (kPa)	b_f	a_s (kPa)	b_s	a_{fs} (kPa)	b_{fs}
Porcine	0.496	7.209	15.193	20.417	3.283	11.176	0.662	9.466
Human	0.1348	3.243	3.1762	4.7435	0.5426	1.5998	0.2344	3.39

8.4 ACCURACY

8.4.1 Arterial tube

As a first test case, we determined the in vivo stress state of a curved tube as a simple geometrical model for the abdominal aorta. We assumed the arterial tissue to behave as quasi-incompressible, anisotropic and hyperelastic material [296] (see Table 8.1). The arterial tissue encompassed two families of distributed collagen fibers which make an angle of respectively 5.0° and -5.0° with the circumferential direction. These collagen fibers are visualized in the in vivo reference geometry depicted in Figure 8.2 (left). The aortic tube was mechanically constrained by fixing the tube endings' degrees of freedom in the longitudinal direction whilst allowing radial and circumferential displacements. The in silico aorta was modeled in a pressurized state, assumed to be 93.3mmHg (mean arterial blood pressure). We applied the above described inverse elastostatics approach in the *Abaqus* FEA framework and calculated the in vivo stress state depicted in Figure 8.2 (top – right), together with the corresponding zero-pressure geometry shown in transparent gray. The inverse solution took 4 minutes of walltime to be computed on a CentOS Linux 7 cluster with one compute node containing two Intel Xeon E5-2680 processors each of which contains 8 cores (2.60 GHz processor base frequency, 64 GB of memory/node, equipped with FDR InfiniBand).
In order to assess the accuracy of the described inverse approach within the *Abaqus* FEA framework, the calculated zero-pressure geometry (with its corresponding rotated collagen fiber distribution) was pressurized to 93.3mmHg in a forward – ground truth – analysis. The resulting pressurized

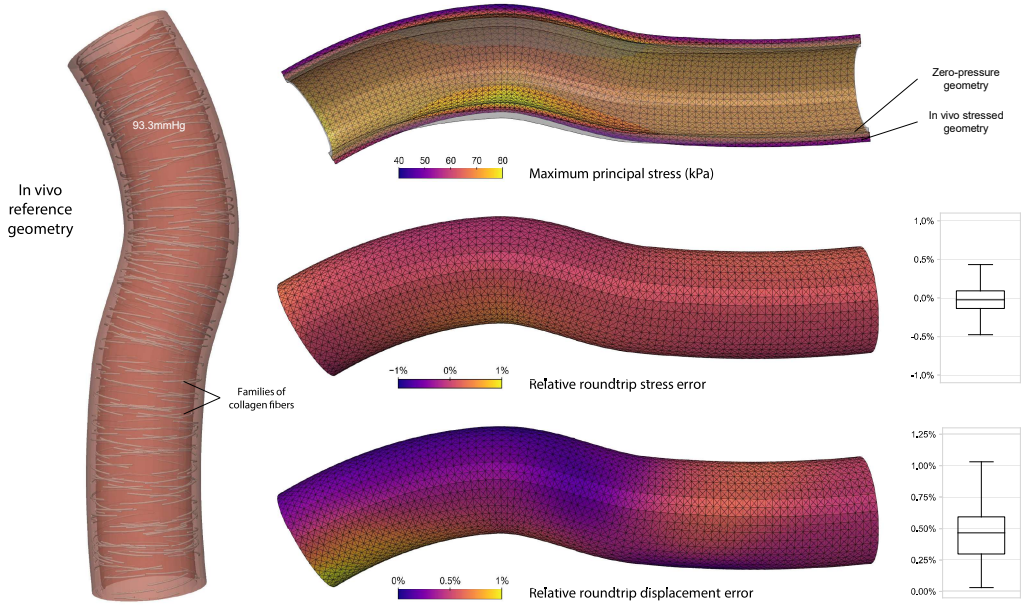

Figure 8.2: Inverse methodology accuracy assessment on a curved arterial tube. (left): An iliac tube with two families of intertwining collagen fibers incorporated in the tissue. (right top): A sliced visualization of the computed in vivo stress state (maximum principal stress) for the arterial tube model. The calculated zero-pressure arterial geometry is depicted in transparent gray. (right mid and bottom): Relative roundtrip stress and displacement error, showing the maximum error between the computed stress state and the roundtrip stress state, and the initial in vivo reference geometry and the roundtrip geometry respectively, coming from the forward inflation of the computed zero-pressure geometry.

geometry, which we will call the 'roundtrip geometry', was compared to the initial in vivo reference geometry, as was the corresponding in vivo stress state. For the relative roundtrip stress error, we compared the element-wise difference in maximum principal stress from the inverse methodology with the forward analysis. This difference was normalized with the maximum principal stress state calculated in the forward analysis. Equivalently, the relative roundtrip displacement error quantifies the nodal coordinate difference between the in vivo reference geometry and roundtrip geometry normalized with the forward nodal displacement values. As shown in the relative roundtrip stress and displacement distribution, as well as in the corresponding box plots (Figure 8.2 right – mid and bottom), the modified inverse elastostatics approach calculated the in vivo stress state with a mean accuracy of 99.86% (minimum 99.59%) and led to a mean roundtrip displacement accuracy of 99.53% (minimum 98.96%). Given that some patients suffer from hypo- or hypertension, we also determined the zero-pressure geometry and in vivo stress state assuming mean arterial pressures of 80mmHg and 120 mmHg respectively. Figure 8.3 shows the accuracy of the proposed methodology for an aortic tube of a subject with a mean aortic blood pressure of 80, 93.3 and 120 mmHg, respectively.

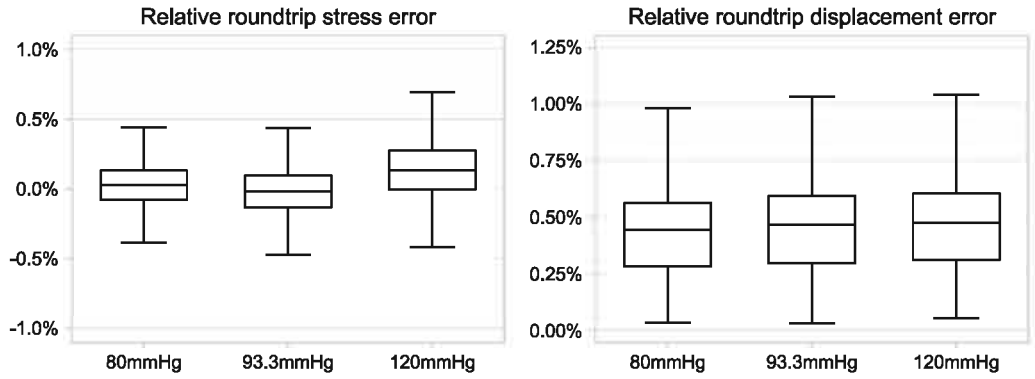

Figure 8.3: Accuracy of the proposed methodology for an aortic tube under assumed mean blood pressure of 80mmHg, 93.3 mmHg and 120 mmHg respectively expressed in relative roundtrip stress (left) and displacement (right) error.

8.4.2 Porcine biventricular model

Figure 8.4 illustrates an anatomically accurate porcine biventricular model deduced from a larger porcine heart model [299], providing an intrinsically more complex validation model for the inverse methodology. Images were reconstructed from T1/T2 MRI scans with a 0.33x0.33x0.66mm resolution and segmented using *Simpleware ScanIP* (Simpleware Ltd., Exeter, United Kingdom). Fiber orientations were deduced from Diffusion Tensor MRI scans with a 1.0x1.0x1.18mm resolution and exhibit a rotating positive to negative helix angle in the left ventricle. We assumed the myocardial tissue to behave as nearly-incompressible, anisotropic and hyperelastic material (see Table 8.1). To fix the ventricles in space, we constrained the top surface from moving perpendicularly and applied a homogeneously distributed Dirichlet boundary condition at the geometric center of the top cut surface constraining the remaining degrees of freedom (see also chapter 6). We considered the left and the right ventricle to be subjected to 8.0 and 4.0 mmHg in vivo pressures respectively (corresponding to 70% diastole). The inverse computation took 15 seconds on the aforementioned computational infrastructure. As done for the arterial tube model, an inverse analysis was set up to determine a zero-pressure geometry of these ventricles and subsequently the calculated zero-pressure geometry (with corresponding updated fiber orientation field) was repressurized in a forward *Abaqus/Standard* analysis leading to the 'roundtrip geometry'. The comparison between the initial in vivo deformed geometry and the inverse-forward analysis (round-trip) can be seen in Figure 8.4. If we compare the inverse calculated in vivo stress state, with the round-trip stress state, the minimum and mean relative accuracy with respect to the forward stress magnitude amounted to be up to 98.2% and 99.9% respectively. Comparing the initial deformed geometry with the round-trip deformed geometry, we obtained a maximum error at the constrained nodes where

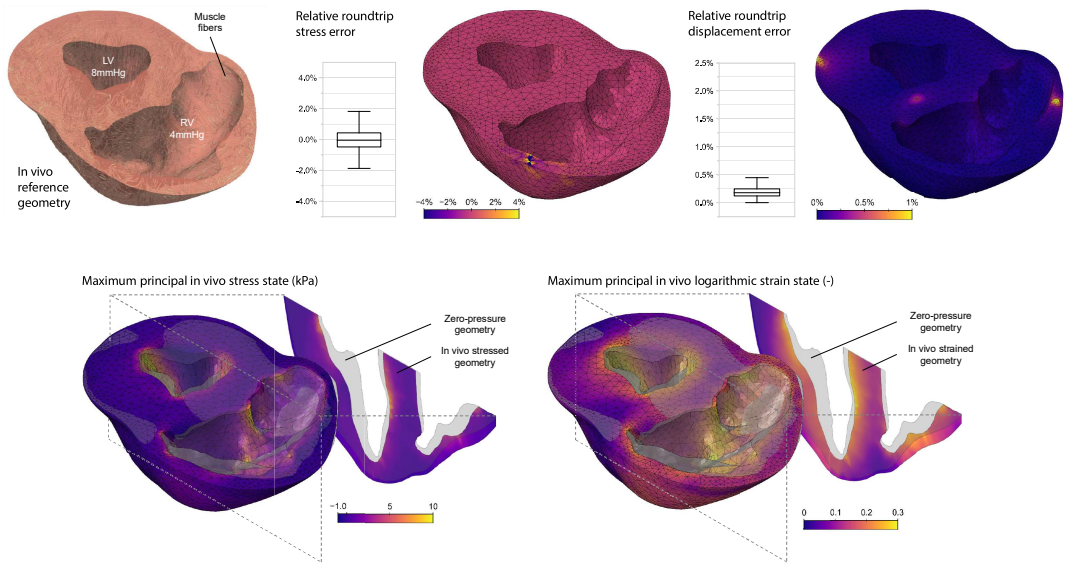

Figure 8.4: Inverse methodology accuracy assessment on a porcine biventricular model. (top left): MRI-based in vivo reference geometry with the DTMRI-deduced muscle fiber architecture incorporated leading to highly anisotropic hyperelastic tissue behavior. (top mid and right): Relative roundtrip stress and displacement error, showing the maximum error between the computed stress state and the roundtrip stress state, and the initial in vivo reference geometry and the roundtrip geometry respectively, coming from the forward inflation of the computed zero-pressure geometry. (bottom left and right): Computed in vivo stress state (maximum principal stress) and in vivo strain state (maximum principal strain) for the porcine biventricular model. A transversal slice shows the in vivo stress and strain state respectively throughout the tissue depth. The computed zero-pressure geometry is depicted in transparent gray.

the Dirichlet boundary condition was enforced (and in particularly at the nodes that are most distal (and thus the weakliest constrained) from the geometric center. The minimal and mean relative accuracy with respect to the displacement magnitude ended up being 99.6% and 99.8% respectively.

8.5 Applications

8.5.1 The in vivo stress state of a patient-specific AAA

A patient-specific abdominal aortic aneurysm (AAA) model (see Figure 8.5) was built based on an earlier study on the virtual deployment of a stent graft device in a patient-specific model [53]. The vessel lumen, thrombi and calcifications were segmented using *Mimics* (Materialise; Leuven, Belgium) from an anonymized pre-op computed tomography (CT) acquisition on a patient at the Ghent University Hospital. Although wall thickness could be extracted on some slices (around 3 pixels in width; in plane CT resolution =

0.782mm - 2mm slice thickness), this was not the case for all slices, especially in highly calcified zones. Consequently, wall thickness was assumed constant at 1.9mm. To create the finite element model, *pyFormex* (Ghent University, Gent, Belgium) was used to discretize the segmented geometry into 470,811 linear tetrahedral elements and 117,428 nodes, which introduced 352,284 degrees of freedom into the model (shown in Figure 8.5). The aortic and iliac artery and the intraluminal thrombi and calcifications show anisotropic hyperelastic behavior [89, 296] and isotropic hyperelastic behavior [215] respectively (constitutive parameters can be found in Table 8.1). The two intertwining families of collagen fibers are defined through the definition of 367,823 local fiber directions N_1 and N_2 (not shown in Figure 8.5). To fix the AAA in space, we applied homogeneously distributed Dirichlet boundary conditions at the geometric centers of the in- and outlets of the AAA model. The inverse computation took 68 minutes to compute the zero-pressure geometry (depicted in Figure 8.5 mid left) on the same computational infrastructure as before. The computed zero pressure state of the considered

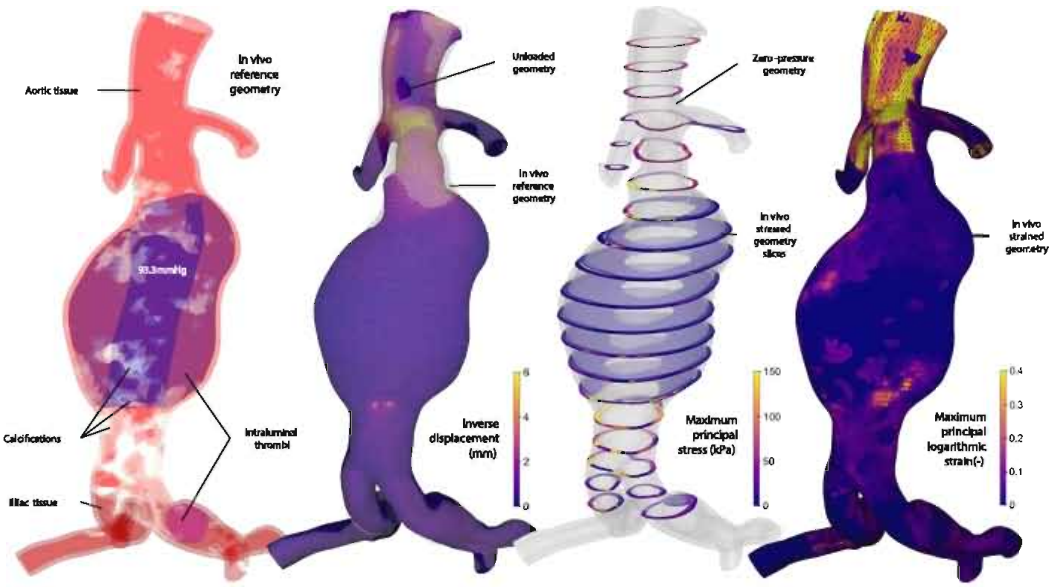

Figure 8.5: The in vivo stress and strain state of a patient-specific abdominal aortic aneurysm (AAA). (left): CT-based in vivo reference geometry including the aortic and iliac vessel lumen, calcified vessel tissue and two intraluminal thrombi each showing specific (anisotropic) hyperelastic tissue behavior. For clarity, the intertwining families of collagen fibers are not shown in the aortic and iliac vessel tissue. (mid left): Displacement inverse zero-pressure geometry computation, with the in vivo reference geometry depicted in transparent gray. (mid right): Computed in vivo stress state (maximum principal stress) for the AAA model shown in transmural slices. The computed zero-pressure geometry is depicted in transparent gray. (right): Computed in vivo strain state (maximum principal logarithmic strain) for the AAA model.

AAA model caused by the mean arterial pressure present during visualization (93.3 mmHg) is shown in Figure 8.5 (mid left) and in transparent gray in Figure 8.5 (mid right). The corresponding in vivo stress state is shown in transmural slices (to show the stress variation through the wall thickness) and the in vivo strain state on the full AAA model. The highest stresses and strains are present distal from the thrombi regions (up to 150kPa maximum principal stress – which is within the range reported for aortic tissue [142] – and 0.49 maximum principal nominal strain).

8.5.2 The in vivo stress state of the human heart

Modeling the entire heart as a whole is considered superior to studying the diseased subsystems in complete isolation [338]. Therefore, the 'Living Heart Project' has been developing an electrically excitable, deformable, hyperelastic, electroactive four-chamber human heart model connected to the external cardiovascular system via in- and outflow boundary conditions of viscous resistance type; the 'Living Human Heart Model' (LHHM) [14]. This Living Heart Project (LHP) is a translational research initiative to revolutionize cardiovascular science through realistic simulation, bringing cardiovascular researchers, educators, medical device developers, regulatory agencies, and practicing cardiologists together all around the world [197]. During a 6-month break from this doctoral research (October 2015 - March 2016), the author of this dissertation actively joined forces with the core development team within Dassault Systèmes Simulia Corporation which brings this LHHM to the community. Since then, the author became an active member of this LHP community. The underlying geometry of the LHHM finite element heart model was created from magnetic resonance images of a healthy, 21-year old, 50th percentile U.S. male (Zygote Media Group, Inc.; American Fork, Utah). Images were reconstructed from 0.75 mm thick slices using a medium soft-tissue kernel with retrospective electrocardiogram gating [380]. Data acquisition and reconstruction were performed during 70% diastole. The resulting anatomically accurate model, shown in Figure 8.6 (i) and (ii), includes all four chambers, the left and right atria and ventricles, connected by the four valves. The tricuspid and mitral valves connect the right and left atria to the right and left ventricles; the pulmonary and aortic valves connect the right and left ventricles to the pulmonary and systemic circulation. The major vessels including the aorta, the pulmonary arteries and the superior vena cava are included, together with the coronary arteries and some cardiac fat tissue. To create the finite element model, *Abaqus/CAE* was used to discretize this geometrical model into 598,862 linear tetrahedral elements and 140,160 nodes, which introduced 420,480 degrees of freedom into the model (shown in Figure 8.6 (iii)). The muscle fibers follow a complex helically wrapping architecture which alters with

depth throughout the cardiac wall. This myoarchitecture is implemented in the finite element model through the definition of 598,862 local fiber and sheet (cross-fiber) directions N_f and N_s [14, 358], which is depicted in Figure 8.6 (iv). We assumed the myocardial tissue to behave as nearly-incompressible, anisotropic and hyperelastic material (see Table 8.1). To fix the heart in space, we applied homogeneous Dirichlet boundary conditions at the geometric centers of the in- or outlets of all blood vessels. To prescribe different pressure values in each chamber, we model all valves in a fully closed state. The proposed methodology was used to solve the inverse problem of computing the human heart's in vivo loaded state, which is

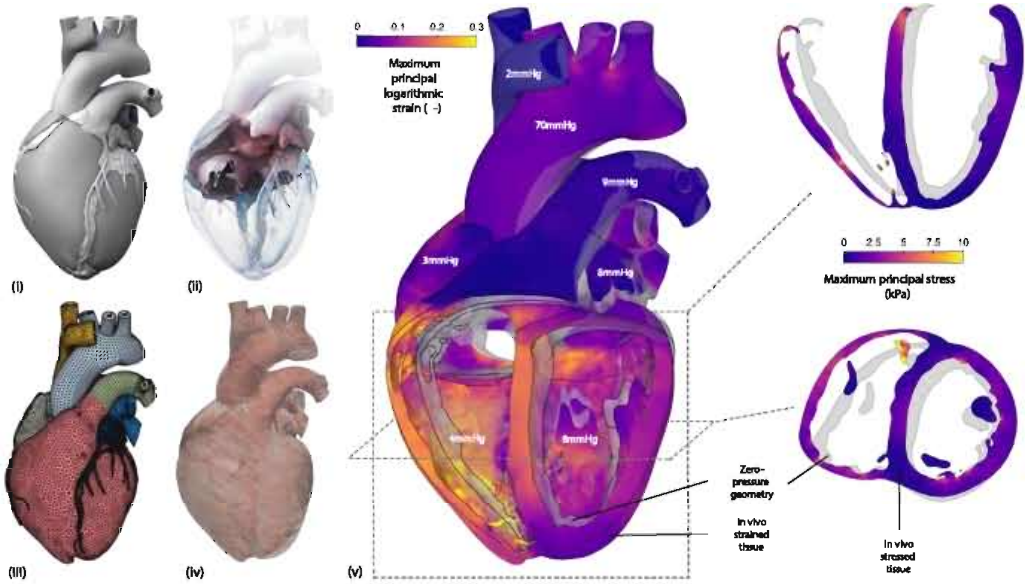

Figure 8.6: The in vivo stress and strain state of the human heart. Panel (i) illustrates the anatomic model created from computer tomography and magnetic resonance images of a healthy, 21-year old, 50th percentile U.S. male at 70% diastole. The model displays the characteristic anatomic features: the major vessels (the aortic arch, the pulmonary arteries and the superior vena cava), the two atria, the two ventricles, the coronary arteries and fat tissue. Panel (ii) illustrates the resulting geometric model's characteristic circulatory features: the tricuspid and mitral valves, which connect the right and left atria to the right and left ventricles; and the pulmonary and aortic valves, which connect the right and left ventricles to the pulmonary and systemic circulation. Both (i) and (ii) were adapted from (Zygote Media Group Inc. 2014). Panel (iii) illustrates the tetrahedral discretization of the heart's solid geometry into a finite element model in *Abaqus/CAE* with 598,862 linear tetrahedral elements and 140,160 nodes. This discretization introduces 420,480 degrees of freedom and 598,862 discrete fiber and sheet directions (see panel (iv)). Panel (v) depicts the computed zero pressure state (transparent gray) and in vivo strained state of the considered living human heart model caused by the depicted diastolic pressures present during visualization. The computed stress state of the ventricles is depicted separately in a short and long axis slice.

shown in Figure 8.6 (v). The inverse computation took 13 minutes on the aforementioned computational configuration. The computed zero pressure state of the considered living human heart model caused by the depicted diastolic pressures present during visualization is shown in transparent gray. The corresponding in vivo strain state is shown for the full heart model and shows significant strains throughout the whole heart. The ventricles, in particular, show maximum principal nominal in vivo strains up to 0.35. The corresponding ventricular in vivo stress state is shown in a short and long axis slice.

8.6 Discussion

The importance of in vivo stress state estimation for (patient-specific modeling of) biological tissues has been demonstrated in several areas. For abdominal aortic aneurysms (AAAs), new approaches to AAA rupture risk assessment, such as numerical biomechanics-based computation of patient-specific AAA wall stresses, quantified in e.g. the finite element analysis rupture index (FEARI) and the rupture potential index (RPI), can have a higher discriminatory value than the currently used aneurysm diameter [75]. An abundance of studies [22, 33, 54, 91, 212, 290, 328, 354, 374] have shown significant under- and overestimations of peak wall stress when the in vivo stress state was included which shows its (potential) importance in providing a more accurate AAA rupture risk assessment. For the myocardium, it was demonstrated that accounting for the tissue's in vivo stress state leads to softer and less anisotropic material properties which shows its significant impact on capturing the (realistic) mechanical response of the heart [247]. Wang et al. [352] recognized this need for in vivo stress state inclusion, but noted it was difficult to track the fiber structure during the inverse analysis. When studying mitral valve mechanics, Rausch et al. [284] demonstrated the high sensitivity of mitral leaflet stiffness estimations on prestrain. Providing a non-cardiovascular biomechanics example, we refer the reader to the works of Maas et al. [214] where the application of prestrain to the knee ligaments resulted in a stiffer response for the torque-rotation curve, higher strains on the medial collateral ligament, and higher contact stresses on the articular cartilage in the lateral compartment under valgus loading. All these cases demonstrate the necessity to include prestress and prestrain in computational models to obtain reasonable predictions of subsequent loading conditions of interest.

Apart from the methodology disclosed in this chapter, other techniques have been reported to restore the original geometry of a structure in absence of its loading state. These methods can be categorized into two groups, *iterative* and *direct* methodologies. In the first category, Raghavan

et al. [280] proposed an optimization framework for the parameter k in which the unknown zero-pressure geometry $\mathcal{B}_{0^{i'}}$ (see Figure 8.1) was approximated by $\boldsymbol{x} - k\boldsymbol{U}$, where $\boldsymbol{U}$ represents the nodal displacements that result from a single forward calculation in which the in vivo pressure load is applied on the in vivo measured deformed geometry $\boldsymbol{x}$. A similar strategy was proposed by Sellier [313, 314] who approached the unknown zero-pressure geometry $\mathcal{B}_{0^{i'}}$ by iteratively updating the reference configuration by subtracting the per node displacement vector $\boldsymbol{R}^i = \boldsymbol{\varphi}(\boldsymbol{X}^i) - \boldsymbol{x}$ between the updated deformed configuration and the target in vivo configuration $\boldsymbol{X}^{i+1} = \boldsymbol{X}^i - \alpha\boldsymbol{R}^i$ until a required error tolerance is reached between the updated deformed configuration and the target in vivo configuration. These schemes were reintroduced specifically for biomechanical problems in the so-called 'backward displacement method' by Bols et al. [22] and the 'pull-back algorithm' by Riveros et al. [290]. An adapted iterative scheme was also proposed by Zeinali et al. [373] where anisotropic material parameters of an in vivo stressed geometry were estimated to satisfy both the force equilibrium and physiological homeostatic conditions at a discrete number of approximation points throughout the geometry. The big advantage of these iterative schemes is that any FEA package which allows the user to output nodal locations of the updated deformed configuration can be exploited to solve the iterative forward problems. Apart from the straightforward implementation in combination with existing structural solvers, these iterative methodologies suffer from relatively high computational costs due to the need of running numerous forward approximation simulations in series. Moreover, these methodologies require iterative updates of the structural mesh's nodal coordinates, which renders the convergence rate and convergence radius highly dependent on both the initial mesh size and the iterative step size toward the next updated deformed configuration. To avoid an 'overshooted guess' of the undeformed geometry, where the mesh would be too distorted to lead to converged results in the next forward iterative simulation, the iterative step size must be chosen small enough. Small iterative step sizes however lead to high computational costs to compute the undeformed geometry which might still end up being outside the convergence radius for the chosen mesh quality. In our own experience, applying the backward displacement method [22] for some arterial bifurcation models (e.g. [56]) in combination with an iterative step size larger than $1/50^{\text{th}}$ of the total load (meaning we needed to perform at least 50 forward simulations) led to inverted forward displacements which rendered the deformed geometry mesh too distorted to get a converged solution in the next iterative forward simulation. Finding the appropriate mesh quality (even if a forward mesh sensitivity study proved the mesh quality to be adequate) in combination with the balance in iterative step size leads

to high computational costs, especially given that the choice of an optimal step size is very problem dependent. Recently, it has been demonstrated that Sellier's method with $\alpha = 1$ (as assumed in Sellier's original work, the backward displacement method [22] and the pull-back algorithm [290]) may result in suboptimal convergence rates and in some examples may fail altogether [285]. It was shown that the optimal α is problem dependent without means of a priori determination. Very recently, Rausch et al. [285] did however propose an augmented Sellier's method which promises increased convergence rates and radii which we did not yet investigate in more detail. Other iterative solution strategies calculated a prestressed and prestrained configuration without altering the imaging-derived geometry [54, 91, 92, 354]. These approaches involved iterative updates to the deformation gradient that generates the stresses in the reference configuration required to balance the applied loads. These strategies involved access to the deformation gradient, a task hardly compatible with the straightforward usage of commercial software [314], or the definition of an initial stress tensor field at the start of each iterative forward simulation, which is less obvious for most existing FEA codes, especially for anisotropic materials (let alone incompressible anisotropic hyperelastic materials such as arterial and myocardial tissue).

Direct methodologies on the other hand, even though still sensitive to initial mesh quality, do not suffer from large computational times or costs as they are a one shot method which admit a unique solution [314]. The typical arguments opposing these methodologies are cumbersome derivations of the formulation, that they are problem specific because the formulation is dependent on the material behavior, and that access to the finite element code is required, which is not trivial for commercial products. The approach proposed in this chapter addressed these issues and was based on the inverse elastostatics (IE) method. The finite element implementation of this IE problem was initially reported for isotropic materials [114, 115], subsequently extended to anisotropic Saint-Venant solids [113, 178] and finally extended to a family of anisotropic materials [67, 212]. For the implementation in general anisotropic solids, the equilibrium equations need to be written in the deformed configuration and the Cauchy stress defined as a function of the constitutive behavior. Lu et al. [212] solved the inverse problem in *Eulerian* form: their kinematics produce an inverse of the deformation gradient tensor $\boldsymbol{F}^{-1}$ and Eulerian representations of the governing constitutive equations were systematically derived. Focusing on an easy implementation of the methodology in existing commercial code, this paper proposed a modified IE approach in which a systematic derivation of the Eulerian equations was avoided. Although the equilibrium equations were written in the deformed configuration, the constitutive formulation was kept in terms of the right Cauchy Green strain tensor invariants (*Lagrangian* description). This implied

the need for algebraically inverting the deformation gradient tensor $\boldsymbol{F}^{-1}$ and for performing polar decompositions to rotate the fiber directions into an undeformed state. Consequently, this methodology allows the user to plug in any constitutive material model without the need to change the full formulation for each material specifically (modular). The constitutive models for human arterial tissue and myocardial tissue were implemented with two separate user subroutines to define anisotropic hyperelastic material behavior using the invariant formulation just like for classic forward simulations. Due to the modular algorithm design, this methodology can also be easily expanded towards any other inverse motion problem. In industrial design, for example, elastomeric parts need to be designed to have a specific deformed shape under a given load. Without having to rederive the whole formulation, we could compute the undeformed (to-be-manufactured) original shape of a reinforced rubber tire or gasket by a mere implementation of the corresponding constitutive material model.

The verification metrics reported in the arterial tube and porcine biventricular examples illustrate the viability of the proposed methodology. Comparing these accuracy metrics to other approaches would involve applying all other existing solution methods on these two models, which is beyond the scope of this study. Iterative methodologies, however, typically consider the approximated unloaded geometry to be converged when the last iteration led to an updated geometry which differs less than an initially set tolerance error from the reference geometry. Raghavan et al. [280] reported nodal displacement accuracy rates of 89.85%, 96.16% and 97.25% and roundtrip stress accuracy rates of 99.3%, 97.3% and 98.2% respectively for three isostropic hyperelastic AAA models. Compared to these metrics, our modified direct methodology scores at least as good, especially given that we included anisotropic fiber-embedded hyperelastic material behavior. This is in agreement with other literature [92] showing better accuracy of a direct inverse methodology compared to an iterative inverse methodology for isotropic materials. The inverse methodology even proved to be quite robust at higher in vivo pressures, as depicted in Figure 8.3.

The reported computation times for the verification and application cases demonstrate the computational efficiency of the proposed methodology. Again, comparing the computational efficiency of this methodology with iterative methodologies would involve a benchmark study involving all other methodologies, which is considered beyond this study's scope. Such a benchmark study would require all methodologies to lead to a converged solution, which is not guaranteed. As stated by Rausch et al. [285], iterative approaches have been successfully applied to problems in arterial mechanics but no information on convergence speed (and possible issues of slow

convergence or divergence) was given in those cases. In our own experience, inverse modeling of anisotropic multi-layered human tissue models (e.g [268]) with the 'backward incremental approach' by De Putter et al. [54] (see section 3.3.1) proved to have very slow convergence rates compared to the current direct methodology (50-fold; one case example). Upon building patient-specific solid tissue models based on in vivo data, we must note that even in the absence of externally applied loads, soft tissues are often not stress free. The remaining 'residual stresses', which result from tissue growth and remodeling, have an additional effect on the biomechanical accuracy of the models (see section 2.1.1.5). Moreover, we often do not know the exact material properties for each tissue (patient-)specifically. To incorporate and estimate these unknowns, it is important to note that the proposed unloading methodology could be integrated into a larger inverse framework, where not only the stress-free reference configuration is approximated, but also, based on image-based geometric data and measured in vivo loads, the material parameters [225, 285]. In that case, any increase in computational efficiency of the zero-pressure approach leads to an immense decrease in the full framework's computational cost.

In conclusion, a modified inverse elastostatic method was presented [†], which allowed for a straightforward implementation in commercial finite element code by slight modifications to the elements used for a forward analysis. The modular algorithm allows using any (anisotropic) hyperelastic tissue/material in an inverse motion analysis without the need to change and rederive the whole inverse formulation. Considering the applicability of the method to conduct imaged-based, in vivo analysis of permanently loaded biological organs, we calculated the prestressed and prestrained state of an in vivo patient-specific abdominal aortic aneurysm and living human heart model. The results of these computations are crucial in

[†] Only after having published this modified inverse elastostatics approach in the international peer-reviewed journal *Journal of the Mechanical Behavior of Biomedical Materials*, the author of this dissertation was notified about, and learned the existence of, the inverse elastostatics approach proposed by Joldes et al. [168]. Similar to our approach, Joldes et al. avoided an Eulerian derivation of the equilibrium equations and discretized the standard equilibrium equations to solve the inverse problem in a *Total Lagrangian* framework. However, compared to our approach, their methodology did not take into account anisotropic material behavior and computed the stiffness matrix differently. In comparison to our verification and application problems, their application examples were rather simple and were solved using an explicit instead of an implicit solution technique. Moreover, their approach was incorporated in dedicated in-house developed finite element analysis software, which is in strong contrast to our implementation into existing commercial finite element analysis software.

assessing the mechanosensory function and behavior and estimating possible failure, growth or remodeling of these organs correctly. The accuracy of the implemented methodology proved to be more than adequate, and in combination with the shown computational efficiency, this approach shows promise to be integrated in a larger inverse framework, where not only the stress-free configuration needs to be computed, but by extension also the material's constitutive parameters can be approximated based on in vivo geometry and load data [373]). We chose to implement the proposed methodology in the commercial FEA solver *Abaqus* but this methodology can be implemented in other FEA solvers as long as they provide access to the equilibrium equation definitions, more specifically through the definition of modified nodal residuals.

Conclusion

Gastro-intestinal and cardiovascular diseases continually challenge the vitality of societies, healthcare systems and economies worldwide. Consequently, it is being increasingly recognized that translation of fundamental insights on tissue physiology and function into clinical care holds immense diagnostic and prognostic potential. Fueled by the potential for significant clinical impact, this research work took important strides along a *road to translation* strewn with obstacles. Through the development of physics-based computational esophagus and heart models closely merged with (clinically available) data, this dissertation actively pursued computational soft tissue modeling to ultimately come to novel insights in gastroenterology and cardiology.

A patient-specific gastro-intestinal and cardiovascular simulation approach

Modeling the complex multiscale and multiphysical entity that describes the patient-specific esophagus or heart in a mathematical structure requires a realistic physics-based approximation of the underlying anatomical and physiological complexities.

With the development of non-invasive 3D imaging techniques, it has become increasingly feasible to develop computational models that accurately represent the *anatomy* and *tissue structure* of the intact esophagus and heart. Even with limited imaging data available, we managed to develop effective approaches to reconstruct patient-specific anatomies and tissue structures in finite element meshes (the virtual esophagus and (human and porcine) heart models in this work were built from low-resolution CT, magnetic resonance (MR) and ultrasound (US) imaging data respectively). More specifically, accurate 3D anatomical geometries of the subject-specific human esophagus, human heart and porcine heart were reconstructed through a *pyFormex* morphing procedure that integrated imaging-deduced geometrical information with trans-esophageal ultrasound thickness measurements and clinical report data (chapter 3), through a volume mesh generation from biventricular surface segmentations in *Mimics* and *Simpleware* (chapter 6)

and through a morphing procedure that maps ventricular template meshes to semi-automatically segmented endo- and epicardial left ventricular surfaces (chapter 7) respectively. To implement the tissue structure, a joint *VMTK-pyFormex* algorithm was developed to translate histological information on the arrangement of helically winding collagen fibers and circumferential/axial smooth muscle cells into the personalized esophagus model. The complex diffusion tensor magnetic resonance imaging (DT-MRI)-informed cardiomyocyte architecture was reconstructed using a Laplace-Dirichlet rule-based algorithm in *Abaqus* and *VTK*.

By taking into account histology, anisotropy and in vitro experimental testing data we characterized the tissue's complex non-linear *passive* behavior by means of appropriate constitutive relations. The corresponding strain energy functions were decomposed in multiple constituents that are interconnected with the underlying microstructure. For cardiac tissue, we followed Holzapfel et al.'s proposal to decompose the strain energy in isotropic matrix and anisotropic fiber, sheet and fiber-sheet constituents relating the constitutive law for cardiac tissue to the underlying laminar-sheet based microstructure [147] (chapter 5). In like manner, we proposed an esophageal deviatoric strain energy potential which constituted an isotropic matrix constituent, an anisotropic collagen fiber constituent and an anisotropic muscle cell constituent (chapter 3). Subsequently, the corresponding constitutive parameters were calibrated based on biaxial tensile testing data of ovine esophageal tissue [325] and triaxial shear testing data of human myocardial tissue [326]. This was done through optimization protocols that tune the constitutive parameter set until the best match between the experimentally measured and computationally predicted result of the conducted loading protocol on the considered tissue slab/cube is found. Based on cardiac in vivo compliance data, this calibration procedure was further extended to correct for the mismatch between ex vivo and subject-specific in vivo tissue behavior.

Although other soft tissues such as ligaments, tendons and skin predominantly entail passive behavior, gastro-intestinal and cardiovascular tissue intrinsically generate significant amounts of active tension to function. Nevertheless, this physiological behavior is not always accounted for in gastro-intestinal and cardiovascular modeling. Ignoring *active* tissue behavior should be avoided as an inaccurate assessment of the internal stress state undermines the diagnostic and prognostic power of soft tissue modeling. Hence, our esophageal tissue model was extended to incorporate the active tonicity and neurologically incited contractions using a phenomenological active fiber approach. For cardiac tissue, we described the tissue's contractile behavior through a time-varying elastance model which takes into account

the kinematic stretch state of the muscle cell (and sarcomeres) and the intercellular Ca^{2+} concentration (forming a multiphysical link with cardiac electrophysiology) [126]. Here, the mismatch between ex vivo measured and personal in vivo contractile behavior was corrected for through an optimization protocol that takes into account non-invasive, easily obtainable and clinically available ventricular stroke volume and longitudinal shortening measurements.

Similar to the active tissue behavior, personalized gastro-intestinal and cardiovascular models often ignore *prestress* which leads to erroneous assessments of the tissue's mechanical function. To correct for the in vivo stress state, this work took two different routes, one where we implemented an iterative forward approach [54] and one where we developed and implemented a novel modular inverse elastostatics methodology in commercial FEA software. Whereas both methods managed to compute the in vivo stress state of patient-specific gastro-intestinal and cardiovascular models, the novel modular inverse elastostatics methodology developed in chapter 8 shows great potential in robustness and efficiency, which is not always seen in iterative forward methodologies.

The tethering and/or constraining effect that (not explicitly modeled) surrounding structures or tissues have on the mechanical functioning of the developed model required careful consideration. This modeling aspect translates itself into defining appropriate *boundary conditions* to the model. Again, insufficient attention for this aspect in gastro-intestinal and cardiovascular modeling impairs model accuracy. Only by a meticulous assessment of the influence and the suitability of boundary conditions in close correlation with quantified in vivo tissue behavior (both on a global and local scale), we managed to make a substantiated choice for suitable in silico boundary conditions for the heart (chapter 6).

In the development of our virtual esophagus model, we attempted to bring the field of gastro-intestinal biomechanics up to speed with the more advanced field of cardiovascular biomechanics. To the best of our knowledge, only passive analytical or double-layered esophageal slice or axisymmetrical tube models were available in the literature when our research started [170, 180, 370, 371]. Through the inclusion of an active fiber contraction model, muscle layer tonicity, (sub)mucosal buckling and residual and pressure-induced stresses in a patient-specific pathological esophagus model, we significantly pushed the current state-of-the-art in esophageal modeling forward. For cardiac modeling, we brought forward new methodologies (e.g. subject-specific in vivo tissue response tuning, inverse elastostatics methodologies to retrieve pressure-induced in vivo stress state) to develop complex multiscale heart (ventricle) models considering

the limited availability of data that is typically present in a clinical context. Subsequently, these cardiac models were used to provide a previously unseen quantification of the predictive capacity of a stretch-driven cardiac growth law.

VALORIZATION OF COMPUTATIONAL TISSUE MECHANICS

The developed tools for, and advancements in, personalized gastro-intestinal and cardiovascular modeling serve multiple pathways to come to clinical impact. These will be discussed in the subsections below.

Diagnosis

The currently available non-invasive in vivo measurement techniques cannot readily measure important biomechanical quantities such as stress, stiffness and contractile work [25]. However, the developed soft tissue organ models provide a direct means to estimate these metrics of function and (patho)physiology on a patient-specific basis. It is strongly believed that such model-based biomarkers can be exploited for improved diagnosis and patient stratification [88, 130]. This work's personalization tools repeatedly tuned patient-specific model parameters, which on their own also serve as additional clinical quantities of interest. More specifically, the passive α and β mapping parameters evaluate myocardial stiffness, whilst the active in vivo tissue calibration for the T_{act} parameter provides a patient-specific quantification of myocardial contractility (chapter 5).

Therapy planning

The obtained mechanistic insights in organ function and physiology also serve more prognostic goals. In a virtual modeling environment, the outcome of different treatment strategies can easily be evaluated prior to the actual intervention. Predicting the outcome of different therapies provides a new way to improve personalized treatment efficacy [193]. Some successful examples of this are FEops HEARTguide^{TM} or HeartFlow®. For a long-term assessment of therapy outcomes, a legitimate understanding of the (mechanistic) stimuli that drive tissue to grow and/or remodel is still missing. Such fundamental knowledge can only be gathered through multiscale modeling in close correlation with clinical (animal) studies where invasive tissue samples can be collected. In chapter 7, we did just that. Using chronic porcine heart failure models, subject-specific multiscale cardiac simulations and machine learning techniques, we probed the hypothesis that end diastolic stretch serves as a mechanistic stimulus to drive eccentric myocardial hypertrophy.

Medical device design

Device-based treatment and therapy are playing an increasingly important role in the clinic [32, 49, 52, 137, 159, 216]. Computational modeling and simulation technology, with encouragement from regulatory agencies [78], starts to become an essential part of the design process paradigm for new devices. Through combined in vitro and in silico examinations of the design's performance, the risk for damage and fatigue can be extensively studied before the device enters the clinical trial. As such, the design process could be substantially sped up and made less expensive (e.g. less physical prototyping is needed). Moreover, these models also form an important alternative to animal testing.

Whereas these technologies mostly use computational mechanics to study device performance, damage and fatigue, the personalized simulation approach can leverage the clinical potential of computational modeling and simulation further. In chapter 4, we developed novel numerical models that accurately describe the mechanical behavior of polymeric braided fiber stents. To subsequently study how the device interacts with the organ's (esophageal) mechanics itself, the patient-specific in vivo stressed esophagus model was vital. Through virtual device implantation procedures that accurately simulate how the device is implanted/released in the patient's esophagus, we provide access to otherwise immeasurable metrics including in vivo performance, the tissue's internal peak stress state, contact pressures, etc. as shown in [52, 159, 163, 193, 286, 292, 312]. As such, these personalized in vivo organ models provide virtual testing environments that cannot be reproduced in vitro. Only through the provided increased understanding of the interaction between organ and device, we can start cross-correlating fine details on device design with clinical complications. In that sense, these models do not only serve R&D purposes for the device manufacturers. They also actuate the evolution towards safer and patient-tailored device-based treatment strategies.

Learning platform

The developed computational mechanics framework also provides both clinicians and engineers with a valuable virtual learning platform. For a doctor, these models can improve their understanding of the organ's anatomy and function and how certain interventions impact organ physiology. At the same time, the framework can be used to rehearse a procedure in silico, prior to the actual in vivo intervention. For engineers, these models also provide an interesting toolset to understand the multiscale and/or multiphysical subtleties and (technical) challenges of new clinical techniques (e.g. non-invasive ultrasound elastography [25] or cardiac resynchronization therapy [191]).

ROAD TO CLINICAL TRANSLATION: LIMITATIONS AND FUTURE PERSPECTIVES

Any application of soft tissue biomechanics that tends to realize translational potential in a clinical context needs to find a balance between the available data and the clinical question at hand. Where simplicity might be preferred to provide robustness and reliability, it typically comes at the cost of decreased accuracy. In contrast, complexity might yield additional fidelity but concurrently lead to uncertainty (due to non-uniqueness from the available data). For example, the cardiac contraction model in chapter 5 could be extended to take into account detailed subcellular mechanochemical events of cycling myosin crossbridges in the sarcomere [237]. While this might be an interesting approach for a fundamental research or prognostic study that needs to assess drug-induced effects on cardiac contractility, the model overshoots diagnostic medicine needs where a mere quantification of T_{act} could act as a biomarker to indicate or stratify heart disease. In essence, realizing translational potential requires careful consideration of the interplay between complexity and unique identifiability. Therefore, any model should be designed based on the needs of the clinical question it tries to answer and the available data.

Once required model complexity has been identified, the difficulty of appropriate model calibration and validation remains a point of concern. To extend these developments beyond the academic research territory further into the hospital, ever improving (non-invasive) imaging and image processing techniques (including newer techniques such as 4D MR or US (strain) imaging, DT-MRI, US backscatter tensor imaging, MR- or US-based shear wave elastography) will be vital and need to be further integrated in the personalized simulation approach. Take for example the uncertainty on tissue characterization which stemmed from the discrepancy that exists between ex vivo and in vivo tissue behavior on one hand and inter-subject/inter-pathology variability on the other hand. For now, we corrected for this mismatch in a two-stage passive tissue calibration procedure rooted on the availability of subject-specific compliance data. Due to the invasive character of pressure catheters [36, 99, 211], such data is however typically absent in a clinical context. Consequently, a translation of this calibration/tuning approach to the clinic hinges on new non-invasive tissue stiffness characterization techniques, where elastography shows promising results [25, 87, 219, 260, 272, 291] Similarly, the pending validation of our virtual esophageal model in part I requires 4D US or MR (strain) imaging data of the esophagus to be collected. Given these points, it becomes clear that the integration between modeling and image acquisition should start at

a much more fundamental level where clinicians, modeling engineers and industrial partners will have to work closer together [32].

As measuring living tissue behavior is, by nature, sparse and noisy, an elaborate characterization of tissue behavior should also quantify the uncertainty on any ex vivo or in vivo (being it invasive or non-invasive) measurement that is being fed into the model. Therefore, the probabilistic conduct that we disclosed in chapter 7 where uncertainty on model input gets quantified and propagated through the model to quantify uncertainty on model output, should be further expanded to other aspects of our personalized simulation approach. As data from multiple sources enters our modeling pathway at multiple stages, such a quantification will require some substantial additional fundamental research. Take the ex vivo tissue calibration for example. To quantify the uncertainty that this aspect of the modeling pathway entails, a significant amount of experimentally quantified multiscale responses of gastro-intestinal and cardiovascular tissue from multiple human subjects at various states of health and disease to various physiological loading conditions will need to be collected. Here, it is important to point out that the new hierarchical modeling, Bayesian interference, Gaussian progression, ... techniques developed in chapter 7 hold immense potential to interpret unevenly distributed data and to quantify the intrinsic uncertainties in experimental measurements. As such, these techniques can also guide strategies for adaptive sampling to efficiently explore the parameter space and maximize the information content of each measurement [301]. Only through a systematic switch from the current deterministic approaches to more probabilistic approaches, can we come to a much-needed statistical assessment of personalized tissue (patho)physiology and treatment efficacy assessments in the clinic.

List of Tables

3.1 Esophageal constitutive parameters 71
3.2 Thickness of each esophageal layer 73

4.1 Foreshortening recovery ratio calibration friction coefficient *EllaBD* stent model 97

5.1 Calibrated myocardial constitutive parameters 129
5.2 Active myocardial constitutive parameters 132

6.1 Kinematic BC heterogeneity in the literature 148
6.2 Studied boundary condition cases 152

7.1 Echocardiography and histology measurements during 8-week volume overload animal study 179
7.2 Second-stage passive in vivo myocardial tissue behavior calibration 182
7.3 Quantitative numerical and experimental myocyte lengthening evolution through time 189

8.1 Inverse elastostatic constitutive parameters 206

List of Figures

0.1 Health care applications of biomechanics 3

1.1 Kinematic description of deformation 10
1.2 Polar decomposition of the deformation gradient 11
1.3 Definition of Cauchy stress 14
1.4 Force equilibrium inside a solid body 17
1.5 Finite element approximation of the solid body 21
1.6 The quadrilateral finite element 23
1.7 Illustration of material nonlinearity of soft tissue associated with the gradual recruitment of collagen fibers. 24
1.8 Newton-Raphson method 25

2.1 Qualitative stress-strain comparison hard vs soft tissues 30
2.2 Qualitative stress-strain relationship illustration anisotropic myocardium and epicardium 31
2.3 Three standard viscoelastic models 37
2.4 Matarial user subroutine flowchart 41
2.5 Uniaxial tests 42
2.6 Biaxial tests 43
2.7 Triaxial tests 44
2.8 Opening angle experiment 45
2.9 Muscle tissues 47
2.10 Length-tension relationships of sarcomeres in skeletal muscle . . 48
2.11 The active-strain approach 50
2.12 Active stress dependence on stretch and calcium concentration for cardiac tissue 51
2.13 Kinematic growth 52
2.14 Constrained mixture model 55

3.1 The digestive system 62
3.2 Peristalsis 62
3.3 Esophageal histology 63

3.4 Distribution of collagen fibers within the submucosa 67
3.5 Arrangement and microstructure of smooth muscle cells in the esophagus 68
3.6 Esophageal constitutive material model fit 70
3.7 Segmentation of patient-specific esophagus 72
3.8 Patient-specific esophagus model 73
3.9 Experimental evidence of buckled state (sub)mucosa 74
3.10 Perturbation 'load' and corresponding buckling modes of the mucosa-submucosa 75
3.11 Double backward incremental approach to compute the in vivo stress state of the patient-specific esophagus 77
3.12 Esophageal in vivo stress state 79
3.13 Esophageal peristalsis 81

4.1 Esophageal strictures 88
4.2 Self-expanding esophageal stents 89
4.3 *EllaBD* stent 92
4.4 In vitro bench testing *EllaBD* stent 93
4.5 Finite element *EllaBD* stent model 94
4.6 In vitro degradation study *EllaBD* stent and stent fibers 96
4.7 Radial force calibration friction coefficient *EllaBD* stent model . 97
4.8 Numerical model validation throughout degradation process. . . 98
4.9 Virtual stent implantation procedure. 99
4.10 The in-silico esophagus-stent interaction. 99

5.1 Location and gross anatomy human heart 114
5.2 Blood pathway 115
5.3 Ventricular muscle thickness. 116
5.4 Cardiac wall structure 117
5.5 Heart Musculature 118
5.6 Microscopic anatomy of cardiac muscle 119
5.7 Sliding filament model of contraction 120
5.8 Excitation-contraction coupling in cardiac muscle cells. 120
5.9 Cardiac conduction system 122
5.10 Laminar-sheet based microstructure in myocardial tissue 124
5.11 Myocardial muscle and collagen fiber arrgangement unloaded, in tension and under compression 125
5.12 First-stage passive myocardial tissue response calibration 128
5.13 Frank-Starling effect in time-varying elastance model 132
5.14 High-resolution subject-specific porcine biventricular geometry 134
5.15 Living Heart Project's Human Heart geometry 135
5.16 An RCR-Windkessel circuit 138
5.17 Schematic illustration of the CircAdapt circulatory model 139

5.18 Chronic heart failure mechanisms 140
5.19 Kinematics-based multiscale cardiac growth modeling pathologies of diastolic and systolic heart failure on a full 4-chamber human heart model 142

6.1 TMRI-registered diastolic tissue displacement 150
6.2 From image data to patient-specific computational biventricular mesh 151
6.3 Schematic illustration of the studied boundary condition cases . 152
6.4 Open-loop LPN to incorporate hemodynamic effect arterial buffer 153
6.5 Solutions to the Laplace-Dirichlet scalar fields in the biventricular model. 155
6.6 LDRB-derived myofiber directions in the patient-specific BV model. 156
6.7 Second-stage passive and active myocardial tissue response calibration 158
6.8 Tagged MRI strain results 160
6.9 FEA computed systolic fiber strains 161
6.10 FEA vs TMRI strains BC case 5 161
6.11 FEA vs TMRI Cohen's d size effect 161
6.12 Influence BCs on global ventricular functioning 162
6.13 FEA case-to-case variance of diastolic maximal principal strains 163
6.14 FEA regional case-to-case variance of diastolic circumferential and radial strains 164
6.15 Statistical analysis regional case-to-case variance diastolic maximum principal strains 164

7.1 Multiscale model of cardiac growth 174
7.2 Evolution of end-diastolic volumes in response to left ventricular volume overload 180
7.3 Evolution of myocyte lengths in response to left ventricular volume overload 181
7.4 Evolution of myocyte widths in response to left ventricular volume overload 181
7.5 Second-stage passive myocardial tissue response calibration . . . 183
7.6 Sensitivity analysis of growth with respect to the growth speed τ 184
7.7 Regional, transmural, temporal, and inter-animal variations of growth in response to left ventricular overload 185
7.8 Simulation and experiment of chronic myocyte lengthening across the entire ventricular wall 186
7.9 Simulation and experiment of chronic myocyte lengthening across the endocardial wall 187

7.10 Simulation and experiment of chronic myocyte lengthening across the endocardial wall 188

8.1 Modified inverse elastostatics methodology schematic 205
8.2 Inverse methodology accuracy assessment on a curved arterial tube 207
8.3 Inverse methodology accuracy arterial tube in different pressure conditions 208
8.4 Inverse methodology accuracy on a porcine biventricular model 209
8.5 In vivo stress state of a patient-specific abdominal aortic aneurysm 210
8.6 In vivo stress state of the human heart 212

Bibliography

[1] J. Aguado-Sierra, A. Krishnamurthy, C. Villongco, *et al.*, "Patient-specific modeling of dyssynchronous heart failure: a case study", *Progress in Biophysics and Molecular biology*, vol. 107, no. 1, pp. 147–55, 2011.

[2] R. K. Amanfu and J. J. Saucerman, "Cardiac models in drug discovery and development: a review", *Crit Rev Biomed Eng*, vol. 39, no. 5, pp. 379–95, 2011.

[3] D. Ambrosi, G. Arioli, F. Nobile, *et al.*, "Electromechanical Coupling in Cardiac Dynamics: The Active Strain Approach", *SIAM Journal on Applied Mathematics*, vol. 71, no. 2, pp. 605–621, 2011.

[4] A. P. Antoniadis, P. Mortier, G. Kassab, *et al.*, "Biomechanical Modeling to Improve Coronary Artery Bifurcation Stenting", *Expert Review Document on Techniques and Clinical Implementation*, vol. 8, no. 10, pp. 1281–1296, 2015.

[5] E. M. Arruda and M. C. Boyce, "A three-dimensional constitutive model for the large stretch behavior of rubber elastic materials", *Journal of the Mechanics and Physics of Solids*, vol. 41, no. 2, pp. 389–412, 1993.

[6] T. Arts, K. D. Costa, J. W. Covell, *et al.*, "Relating myocardial laminar architecture to shear strain and muscle fiber orientation", *Am J Physiol Heart Circ Physiol*, vol. 280, no. 5, H2222–9, 2001.

[7] T. Arts, T. Delhaas, P. Bovendeerd, *et al.*, "Adaptation to mechanical load determines shape and properties of heart and circulation: the CircAdapt model", *American Journal of Physiology-Heart and Circulatory Physiology*, vol. 288, no. 4, H1943–H1954, 2005.

[8] L. Asner, M. Hadjicharalambous, R. Chabiniok, *et al.*, "Patient-specific modeling for left ventricular mechanics using data-driven boundary energies", *Computer Methods in Applied Mechanics and Engineering*, vol. 314, pp. 269–295, 2017.

[9] F. Auricchio, A. Constantinescu, M. Conti, *et al.*, "A computational approach for the lifetime prediction of cardiovascular balloon-expandable stents", *International Journal of Fatigue*, vol. 75, pp. 69–79, 2015.

[10] F. Auricchio, A. Constantinescu, M. Conti, *et al.*, "Fatigue of metallic stents: from clinical evidence to computational analysis", *Annals of Biomedical Engineering*, vol. 44, no. 2, pp. 287–301, 2016.

[11] F. Auricchio, M. Conti, M. De Beule, *et al.*, "Carotid artery stenting simulation: from patient-specific images to finite element analysis", *Medical engineering & physics*, vol. 33, no. 3, pp. 281–289, 2011.

[12] S. Baek, R. L. Gleason, K. R. Rajagopal, *et al.*, "Theory of small on large: potential utility in computations of fluid–solid interactions in arteries", *Computer Methods in Applied Mechanics and Engineering*, vol. 196, no. 31-32, pp. 3070–3078, 2007.

[13] B. Baillargeon, I. Costa, J. R. Leach, *et al.*, "Human Cardiac Function Simulator for the Optimal Design of a Novel Annuloplasty Ring with a Sub-valvular Element for Correction of Ischemic Mitral Regurgitation", *Cardiovasc Eng Technol*, vol. 6, no. 2, pp. 105–16, 2015.

[14] B. Baillargeon, N. Rebelo, D. D. Fox, *et al.*, "The living heart project: a robust and integrative simulator for human heart function", *European Journal of Mechanics-A/Solids*, vol. 48, pp. 38–47, 2014.

[15] S. Bargmann, B. Klusemann, J. Markmann, *et al.*, "Generation of 3D representative volume elements for heterogeneous materials: A review", *Progress in Materials Science*, vol. 96, pp. 322–384, 2018.

[16] J. D. Bayer, R. C. Blake, G. Plank, *et al.*, "A novel rule-based algorithm for assigning myocardial fiber orientation to computational heart models", *Annals of Biomedical Engineering*, vol. 40, no. 10, pp. 2243–54, 2012.

[17] T. Belytschko, W. K. Liu, B. Moran, *et al.*, "Nonlinear finite elements for continua and structures". John wiley & sons, 2013.

[18] E. Berberoglu, H. O. Solmaz, and S. Goktepe, "Computational modeling of coupled cardiac electromechanics incorporating cardiac dysfunctions", *European Journal of Mechanics a-Solids*, vol. 48, pp. 60–73, 2014.

[19] D. H. Bergel, "The visco-elastic properties of the arterial wall", Thesis, 1960.

[20] D. E. Bettendorff-Bakman, P. Schmid, P. P. Lunkenheimer, *et al.*, "Diastolic ventricular aspiration: a mechanism supporting the rapid filling phase of the human ventricles", *Journal of Theoretical Biology*, vol. 250, no. 4, pp. 581–92, 2008.

[21] G. Biglino, C. Capelli, J. Bruse, *et al.*, "Computational modelling for congenital heart disease: how far are we from clinical translation?", *Heart*, vol. 103, no. 2, pp. 98–103, 2017.

[22] J. Bols, J. Degroote, B. Trachet, *et al.*, "A computational method to assess the in vivo stresses and unloaded configuration of patient-specific blood vessels", *Journal of Computational and Applied Mathematics*, vol. 246, pp. 10–17, 2013.

[23] M.-A. Bray, S. P. Sheehy, and K. K. Parker, "Sarcomere alignment is regulated by myocyte shape", *Cell Motility*, vol. 65, no. 8, pp. 641–651, 2008.

[24] J. D. Brown, J. Rosen, Y. S. Kim, *et al.*, "In-vivo and in-situ compressive properties of porcine abdominal soft tissues", *Studies in Health Technology and Informatics*, pp. 26–32, 2003.

[25] A. Caenen, "A biomechanical analysis of shear wave elastography in pediatric heart models", PhD thesis, Faculty of Engineering, Ghent University, 2018.

[26] A. Caenen, M. Pernot, M. Peirlinck, *et al.*, "An in silico framework to analyze the anisotropic shear wave mechanics in cardiac shear wave elastography", *Physics in Medicine and Biology*, 2018.

[27] J. O. Campos, J. Sundnes, R. W. dos Santos, *et al.*, "Effects of left ventricle wall thickness uncertainties on cardiac mechanics", *Biomechanics and Modeling in Mechanobiology*, 2019.

[28] J. M. T. Canena, M. J. A. Liberato, R. A. N. Rio-Tinto, *et al.*, "A comparison of the temporary placement of 3 different self-expanding stents for the treatment of refractory benign esophageal strictures: a prospective multicentre study", *BMC Gastroenterology*, vol. 12, no. 1, p. 70, 2012.

[29] F. Cansız, H. Dal, and M. Kaliske, "An orthotropic viscoelastic material model for passive myocardium: theory and algorithmic treatment", *Computer Methods in Biomechanics and Biomedical Engineering*, vol. 18, no. 11, pp. 1160–1172, 2015.

[30] R. Carrick, L. Ge, L. C. Lee, *et al.*, "Patient-Specific Finite Element-Based Analysis of Ventricular Myofiber Stress After Coapsys: Importance of Residual Stress". 2012, vol. 93, pp. 1964–71.

[31] M. D. Cerqueira, N. J. Weissman, V. Dilsizian, *et al.*, "Standardized myocardial segmentation and nomenclature for tomographic imaging of the heart", *Circulation*, vol. 105, no. 4, pp. 539–542, 2002.

[32] R. Chabiniok, V. Y. Wang, M. Hadjicharalambous, *et al.*, "Multiphysics and multiscale modelling, data-model fusion and integration of organ physiology in the clinic: ventricular cardiac mechanics", *Interface Focus*, vol. 6, no. 2, p. 20 150 083, 2016.

[33] S. Chandra, V. Gnanaruban, F. Riveros, *et al.*, "A Methodology for the Derivation of Unloaded Abdominal Aortic Aneurysm Geometry With Experimental Validation", *Journal of Biomechanical Engineering*, vol. 138, no. 10, p. 101 005, 2016.

[34] C. Cherubini, S. Filippi, P. Nardinocchi, *et al.*, "An electromechanical model of cardiac tissue: Constitutive issues and electrophysiological effects", *Progress in Biophysics and Molecular Biology*, vol. 97, no. 2, pp. 562–573, 2008.

[35] C. Chiastra, W. Wu, B. Dickerhoff, *et al.*, "Computational replication of the patient-specific stenting procedure for coronary artery bifurcations: From OCT and CT imaging to structural and hemodynamics analyses", *Journal of Biomechanics*, vol. 49, no. 11, pp. 2102–2111, 2016.

[36] J. S. Choy, S. Leng, Y. Awakeem, *et al.*, "Mechanical stretch as stimulus for growth and remodeling in mitral regurgitation." *submitted for publication*, 2019.

[37] C.-J. Chuong and Y.-C. Fung, "Residual stress in arteries", in *Frontiers in biomechanics*. Springer, 1986, pp. 117–129.

[38] R. H. Clayton, O. Bernus, E. M. Cherry, *et al.*, "Models of cardiac tissue electrophysiology: Progress, challenges and open questions", *Progress in Biophysics and Molecular biology*, vol. 104, no. 1, pp. 22–48, 2011.

[39] K. D. Costa, Y. Takayama, A. D. McCulloch, *et al.*, "Laminar fiber architecture and three-dimensional systolic mechanics in canine ventricular myocardium", *American Journal of Physiology*, vol. 276, no. 2 Pt 2, H595–607, 1999.

[40] K. D. Costa, J. W. Holmes, and A. D. McCulloch, "Modelling cardiac mechanical properties in three dimensions", *Philosophical Transactions of the Royal Society of London A: Mathematical, Physical and Engineering Sciences*, vol. 359, no. 1783, pp. 1233–1250, 2001.

[41] F. H. C. Crick and A. F. W. Hughes, "The physical properties of cytoplasm: A study by means of the magnetic particle method Part I. Experimental", *Experimental Cell Research*, vol. 1, no. 1, pp. 37–80, 1950.

[42] F. Cuomo, S. Roccabianca, D. Dillon-Murphy, *et al.*, "Effects of age-associated regional changes in aortic stiffness on human hemodynamics revealed by computational modeling", *PLOS ONE*, vol. 12, no. 3, e0173177, 2017.

[43] E. Cutrì, M. Serrani, P. Bagnoli, *et al.*, "The cardiac torsion as a sensitive index of heart pathology: A model study", *Journal of the Mechanical Behavior of Biomedical Materials*, vol. 55, pp. 104–119, 2016.

[44] C. J. Cyron, J. S. Wilson, and J. D. Humphrey, "Constitutive formulations for soft tissue growth and remodeling", in *Biomechanics of Living Organs*. Elsevier, 2017, pp. 79–100.

[45] C. Darwin, "On the origin of species by means of natural selection, or preservation of favoured races in the struggle for life". London : John Murray, 1859, 1859.

[46] Dassault Systèmes Simulia Corp., "Abaqus Documentation". 2018.

[47] Dassault Systèmes Simulia Corp., "Abaqus Theory Guide". 2018.

[48] M. De Beule, S. Van Cauter, P. Mortier, *et al.*, "Virtual optimization of self-expandable braided wire stents", *Medical Engineering & Physics*, vol. 31, no. 4, pp. 448–53, 2009.

[49] M. De Beule, "Finite element stent design", Book, Faculty of Engineering, Ghent University, Ghent University, 2008.

[50] S. De Bock, F. Iannaccone, G. De Santis, *et al.*, "Our capricious vessels: The influence of stent design and vessel geometry on the mechanics of intracranial aneurysm stent deployment", *Journal of Biomechanics*, vol. 45, no. 8, pp. 1353–1359, 2012.

[51] S. De Bock, F. Iannaccone, G. De Santis, *et al.*, "Virtual evaluation of stent graft deployment: A validated modeling and simulation study", *Journal of the Mechanical Behavior of Biomedical Materials*, vol. 13, pp. 129–139, 2012.

[52] S. De Bock, "A (bio)mechanical analysis of stent grafts for the treatment of abdominal aortic aneurysms", PhD thesis, Faculty of Engineering, Ghent University, 2014.

[53] S. De Bock, I. Van Herzeele, F. Vermassen, *et al.*, "In vivo case study of the virtual deployment of a stent graft device", in *European Symposium on Vascular Biomaterials*, 2015.

[54] S. De Putter, B. J. B. M. Wolters, M. C. M. Rutten, *et al.*, "Patient-specific initial wall stress in abdominal aortic aneurysms with a backward incremental method", *Journal of Biomechanics*, vol. 40, no. 5, pp. 1081–1090, 2007.

[55] G. De Santis, M. Conti, B. Trachet, *et al.*, "Haemodynamic impact of stent-vessel (mal)apposition following carotid artery stenting: mind the gaps!", *Computer Methods in Biomechanics and Biomedical Engineering*, vol. 16, no. 6, pp. 648–59, 2013.

[56] D. De Wilde, B. Trachet, N. Debusschere, *et al.*, "Assessment of shear stress related parameters in the carotid bifurcation using mouse-specific FSI simulations", *Journal of Biomechanics*, vol. 49, no. 11, pp. 2135–2142, 2016.

[57] N. Debusschere, "Finite Element Modelling of Biodegradable Stents", Thesis, Faculty of Engineering, Ghent University, 2016.

[58] N. Debusschere, P. Segers, P. Dubruel, *et al.*, "A finite element strategy to investigate the free expansion behaviour of a biodegradable polymeric stent", *Journal of Biomechanics*, vol. 48, no. 10, pp. 2012–2018, 2015.

[59] N. Debusschere, P. Segers, P. Dubruel, *et al.*, "A Computational Framework to Model Degradation of Biocorrodible Metal Stents Using an Implicit Finite Element Solver", *Annals of Biomedical Engineering*, vol. 44, no. 2, pp. 382–390, 2016.

[60] I. Del-Canto, M. P. López-Lereu, J. V. Monmeneu, *et al.*, "Characterization of normal regional myocardial function by MRI cardiac tagging", *Journal of Magnetic Resonance Imaging*, vol. 41, no. 1, pp. 83–92, 2015.

[61] T. S. Denney, B. L. Gerber, and L. Yan, "Unsupervised reconstruction of a three-dimensional left ventricular strain from parallel tagged cardiac images", *Magnetic Resonance in Medicine*, vol. 49, no. 4, pp. 743–754, 2003.

[62] S. Dokos, B. H. Smaill, A. A. Young, *et al.*, "Shear properties of passive ventricular myocardium", *American Journal of Physiology-Heart and Circulatory Physiology*, vol. 283, no. 6, H2650–H2659, 2002.

[63] E. Dolan, L. Thijs, Y. Li, *et al.*, "Ambulatory arterial stiffness index as a predictor of cardiovascular mortality in the Dublin Outcome Study", *Hypertension*, vol. 47, no. 3, pp. 365–370, 2006.

[64] F. Dorri, P. F. Niederer, and P. P. Lunkenheimer, "A finite element model of the human left ventricular systole", *Computer Methods in Biomechanics and Biomedical Engineering*, vol. 9, no. 5, pp. 319–41, 2006.

[65] B. J. Doyle, R. A. Macrae, and P. R. Hoskins, "Measurement of the Mechanical Properties of Biological Tissues", in *Cardiovascular Biomechanics*, P. R. Hoskins, P. V. Lawford, and B. J. Doyle, Eds. Cham: Springer International Publishing, 2017, pp. 255–269.

[66] T. S. E. Eriksson, A. J. Prassl, G. Plank, *et al.*, "Influence of myocardial fiber/sheet orientations on left ventricular mechanical contraction", *Mathematics and Mechanics of Solids*, vol. 18, no. 6, pp. 592–606, 2013.

[67] V. D. Fachinotti, A. Cardona, and P. Jetteur, "Finite element modelling of inverse design problems in large deformations anisotropic hyperelasticity", *International Journal for Numerical Methods in Engineering*, vol. 74, no. 6, pp. 894–910, 2008.

[68] N. Famaey, J. Vander Sloten, and E. Kuhl, "A three-constituent damage model for arterial clamping in computer-assisted surgery", *Biomechanics and Modeling in Mechanobiology*, vol. 12, no. 1, pp. 123–36, 2013.

[69] N. Famaey, "Soft Tissue Damage Prevention in Surgery: An Experimental and Computational Framework with Application to Arterial Clamping", PhD, 2012.

[70] N. Famaey, H. Fehervary, J. Vastmans, *et al.*, "On the use of UMATs for fiber-reinforced hyperelastic materials", *(in press)*, 2019.

[71] N. Famaey, J. Vastmans, H. Fehervary, *et al.*, "Numerical simulation of arterial remodeling in pulmonary autografts", *ZAMM-Journal of Applied Mathematics and Mechanics/Zeitschrift für Angewandte Mathematik und Mechanik*, 2018.

[72] Y. Fan, H. Gregersen, and G. S. Kassab, "A two-layered mechanical model of the rat esophagus. Experiment and theory", *Biomedical Engineering Online*, vol. 3, no. 1, p. 40, 2004.

[73] H. Fehervary, "Planar Biaxial Testing of Soft Biological Tissues", PhD, 2018.

[74] M. A. Fernandez-Teran and J. M. Hurle, "Myocardial fiber architecture of the human heart ventricles", *The Anatomical Record*, vol. 204, no. 2, pp. 137–147, 1982.

[75] M. F. Fillinger, S. P. Marra, M. L. Raghavan, *et al.*, "Prediction of rupture risk in abdominal aortic aneurysm during observation: wall stress versus diameter", *Journal of Vascular Surgery*, vol. 37, no. 4, pp. 724–732, 2003.

[76] H. Finsberg, C. Xi, J. L. Tan, *et al.*, "Efficient estimation of personalized biventricular mechanical function employing gradient-based optimization", *International journal for numerical methods in biomedical engineering*, 2018.

[77] J. Fish and T. Belytschko, "A first course in finite elements", 2007.

[78] Food and Drug Administration, "Reporting of Computational Modeling Studies in Medical Device Submissions, Guidance for Industry and Food and Drug Administration Staff", U.S. Department of Health et al., Tech. Rep., 2016.

[79] N. Frey and E. N. Olson, "Cardiac Hypertrophy: The Good, the Bad, and the Ugly", *Annual Review of Physiology*, vol. 65, no. 1, pp. 45–79, 2003.

[80] M. K. Friedberg and A. N. Redington, "Right versus left ventricular failure: differences, similarities, and interactions", *Circulation*, vol. 129, no. 9, pp. 1033–1044, 2014.

[81] L. Fuccio, C. Hassan, L. Frazzoni, *et al.*, "Clinical outcomes following stent placement in refractory benign esophageal stricture: a systematic review and meta-analysis", *Endoscopy*, vol. 48, no. 02, pp. 141–148, 2016.

[82] Y.-C. Fung, "Mathematical representation of the mechanical properties of the heart muscle", *Journal of Biomechanics*, vol. 3, no. 4, pp. 381–404, 1970.

[83] Y.-C. Fung, "Biomechanics: mechanical properties of living tissues". Springer Science & Business Media, 2013.

[84] Y.-c. Fung, "Biomechanics : motion, flow, stress and growth". New York (N.Y.) : Springer, 1990.

[85] H. Gao, W. G. Li, L. Cai, *et al.*, "Parameter estimation in a Holzapfel–Ogden law for healthy myocardium", *Journal of Engineering Mathematics*, vol. 95, no. 1, pp. 231–248, 2015.

[86] H. Gao, H. Wang, C. Berry, *et al.*, "Quasi-static image-based immersed boundary-finite element model of left ventricle under diastolic loading", *Int J Numer Method Biomed Eng*, vol. 30, no. 11, pp. 1199–222, 2014.

[87] L. Gao, K. J. Parker, R. M. Lerner, *et al.*, "Imaging of the elastic properties of tissue—A review", *Ultrasound in Medicine & Biology*, vol. 22, no. 8, pp. 959–977, 1996.

[88] C. T. Gasser, "Biomechanical rupture risk assessment: a consistent and objective decision-making tool for abdominal aortic aneurysm patients", *AORTA Journal*, vol. 4, no. 2, p. 42, 2016.

[89] C. T. Gasser, R. W. Ogden, and G. A. Holzapfel, "Hyperelastic modelling of arterial layers with distributed collagen fibre orientations", *Journal of the royal society interface*, vol. 3, no. 6, pp. 15–35, 2006.

[90] T. A. Gaziano, "Reducing the growing burden of cardiovascular disease in the developing world", *Health affairs (Project Hope)*, vol. 26, no. 1, pp. 13–24, 2007.

[91] M. W. Gee, C. Reeps, H. H. Eckstein, *et al.*, "Prestressing in finite deformation abdominal aortic aneurysm simulation", *Journal of Biomechanics*, vol. 42, no. 11, pp. 1732–1739, 2009.

[92] M. W. Gee, C. Förster, and W. A. Wall, "A computational strategy for prestressing patient-specific biomechanical problems under finite deformation", *International Journal for Numerical Methods in Biomedical Engineering*, vol. 26, no. 1, pp. 52–72, 2010.

[93] L. Geerts, P. Bovendeerd, K. Nicolay, *et al.*, "Characterization of the normal cardiac myofiber field in goat measured with MR-diffusion tensor imaging", *Am J Physiol Heart Circ Physiol*, vol. 283, no. 1, H139–45, 2002.

[94] A. Gelman, "Prior distributions for variance parameters in hierarchical models", *Bayesian Analysis*, vol. 1, pp. 515–534, 2006.

[95] A. Gelman and J. Hill, "Data analysis using regression and multilevel/hierarchical models". Cambridge: Cambridge university press, 2006.

[96] M. Genet, L. C. Lee, B. Baillargeon, *et al.*, "Modeling Pathologies of Diastolic and Systolic Heart Failure", *Annals of Biomedical Engineering*, vol. 44, no. 1, pp. 112–127, 2016.

[97] M. Genet, L. C. Lee, R. Nguyen, *et al.*, "Distribution of normal human left ventricular myofiber stress at end diastole and end systole: a target for in silico design of heart failure treatments", *J Appl Physiol (1985)*, vol. 117, no. 2, pp. 142–52, 2014.

[98] M. Genet, L. Chuan Lee, L. Ge, *et al.*, "A Novel Method for Quantifying Smooth Regional Variations in Myocardial Contractility Within an Infarcted Human Left Ventricle Based on Delay-Enhanced Magnetic Resonance Imaging", *Journal of Biomechanical Engineering*, vol. 137, no. 8, pp. 081009-081009-8, 2015.

[99] M. Genet, M. K. Rausch, L. C. Lee, *et al.*, "Heterogeneous growth-induced prestrain in the heart", *Journal of Biomechanics*, vol. 48, no. 10, pp. 2080–2089, 2015.

[100] A. N. Gent, "A New Constitutive Relation for Rubber", *Rubber Chemistry and Technology*, vol. 69, no. 1, pp. 59–61, 1996.

[101] A. Gerbi, L. Dedè, and A. Quarteroni, "A monolithic algorithm for the simulation of cardiac electromechanics in the human left ventricle", *MOX report*, vol. 51, 2017.

[102] A. M. Gerdes, S. E. Kellerman, J. A. Moore, *et al.*, "Structural remodeling of cardiac myocytes in patients with ischemic cardiomyopathy", *Circulation*, vol. 86, no. 2, pp. 426–30, 1992.

[103] A. M. Gerdes and J. M. Capasso, "Structural remodeling and mechanical dysfunction of cardiac myocytes in heart failure", *Journal of Molecular and Cellular Cardiology*, vol. 27, no. 3, pp. 849–856, 1995.

[104] M. Gheorghiade, C. J. Larson, S. J. Shah, *et al.*, "Developing new treatments for heart failure: focus on the heart", *Circulation: Heart Failure*, vol. 9, no. 5, e002727, 2016.

[105] R. J. Gilbert, T. A. Gaige, R. Wang, *et al.*, "Resolving the three-dimensional myoarchitecture of bovine esophageal wall with diffusion spectrum imaging and tractography", *Cell and Tissue Research*, vol. 332, no. 3, pp. 461–468, 2008.

[106] A. S. Go, D. Mozaffarian, V. L. Roger, *et al.*, "Heart disease and stroke statistics - 2015 update", *Circulation*, vol. 129, no. 3, 2014.

[107] S. Göktepe, S. N. S. Acharya, J. Wong, *et al.*, "Computational modeling of passive myocardium", *International Journal for Numerical Methods in Biomedical Engineering*, vol. 27, no. 1, pp. 1–12, 2011.

[108] S. Göktepe, O. J. Abilez, and E. Kuhl, "A generic approach towards finite growth with examples of athlete's heart, cardiac dilation, and cardiac wall thickening", *Journal of the Mechanics and Physics of Solids*, vol. 58, no. 10, pp. 1661–1680, 2010.

[109] S. Göktepe, O. J. Abilez, K. K. Parker, *et al.*, "A multiscale model for eccentric and concentric cardiac growth through sarcomerogenesis", *Journal of Theoretical Biology*, vol. 265, no. 3, pp. 433–442, 2010.

[110] S. Göktepe and E. Kuhl, "Electromechanics of the heart: a unified approach to the strongly coupled excitation–contraction problem", *Computational Mechanics*, vol. 45, no. 2, pp. 227–243, 2010.

[111] S. Göktepe, A. Menzel, and E. Kuhl, "The generalized Hill model: A kinematic approach towards active muscle contraction", *Journal of the Mechanics and Physics of Solids*, vol. 72, pp. 20–39, 2014.

[112] A. Goriely and G. A. Maugin, "Five ways to model active processes in elastic solids: Active forces, active stresses, active strains, active fibers, and active metrics", *Mechanics Research Communications*, 2017.

[113] S. Govindjee and E. P. Kaspar, "Finite deformation inverse design modeling with temperature changes, axis-symmetry and anisotropy". Department of Civil Engineering, University of California, 1999.

[114] S. Govindjee and P. A. Mihalic, "Computational methods for inverse finite elastostatics", *Computer Methods in Applied Mechanics and Engineering*, vol. 136, no. 1, pp. 47–57, 1996.

[115] S. Govindjee and P. A. Mihalic, "Computational methods for inverse deformations in quasi-incompressible finite elasticity", *International Journal for Numerical Methods in Engineering*, vol. 43, no. 5, pp. 821–838, 1998.

[116] H. Gregersen and G. Kassab, "Biomechanics of the gastrointestinal tract", *Neurogastroenterology & Motility*, vol. 8, no. 4, pp. 277–297, 1996.

[117] H. Gregersen, G. S. Kassab, and Y. C. Fung, "The zero-stress state of the gastrointestinal tract: biomechanical and functional implications", *Digestive Diseases and Sciences*, vol. 45, no. 12, pp. 2271–81, 2000.

[118] H. Gregersen, "Biomechanics of the gastrointestinal tract: new perspectives in motility research and diagnostics". Springer Science & Business Media, 2003.

[119] H. Gregersen, T. C. Lee, S. Chien, *et al.*, "Strain distribution in the layered wall of the esophagus", *Journal of Biomechanical Engineering*, vol. 121, no. 5, pp. 442–448, 1999.

[120] H. Gregersen, D. Liao, and J. G. Brasseur, "The Esophagiome: concept, status, and future perspectives", *Annals of the New York Academy of Sciences*, vol. 1380, no. 1, pp. 6–18, 2016.

[121] H. Gregersen, J. Pedersen, and A. M. Drewes, "Deterioration of muscle function in the human esophagus with age", *Digestive Diseases and Sciences*, vol. 53, no. 12, pp. 3065–3070, 2008.

[122] J. A. Grogan, S. B. Leen, and P. E. McHugh, "Optimizing the design of a bioabsorbable metal stent using computer simulation methods", *Biomaterials*, vol. 34, no. 33, pp. 8049–8060, 2013.

[123] W. Grossman, "Cardiac hypertrophy: useful adaptation or pathologic process", *The American Journal of Medicine*, vol. 69, no. 4, pp. 576–584, 1980.

[124] W. Grossman, D. Jones, and L. P. McLaurin, "Wall stress and patterns of hypertrophy in the human left ventricle", *The Journal of clinical investigation*, vol. 56, no. 1, pp. 56–64, 1975.

[125] J. M. Guccione and A. D. McCulloch, "Mechanics of Active Contraction in Cardiac Muscle: Part I—Constitutive Relations for Fiber Stress That Describe Deactivation", *Journal of Biomechanical Engineering*, vol. 115, no. 1, pp. 72–81, 1993.

[126] J. M. Guccione, L. K. Waldman, and A. D. McCulloch, "Mechanics of Active Contraction in Cardiac Muscle: Part II—Cylindrical Models of the Systolic Left Ventricle", *Journal of Biomechanical Engineering*, vol. 115, no. 1, pp. 82–90, 1993.

[127] J. Guccione, A. D. McCulloch, and L. Waldman, "Passive Material Properties of Intact Ventricular Myocardium Determined From a Cylindrical Model". 1991, vol. 113, pp. 42–55.

[128] O. Gültekin, G. Sommer, and G. A. Holzapfel, "An orthotropic viscoelastic model for the passive myocardium: continuum basis and numerical treatment", *Computer Methods in Biomechanics and Biomedical Engineering*, vol. 19, no. 15, pp. 1647–1664, 2016.

[129] M. Hadjicharalambous, "Development of Patient-Specific Diastolic Models for the study of Dilated Cardiomyopathy", PhD thesis, 2016.

[130] M. Hadjicharalambous, L. Asner, R. Chabiniok, *et al.*, "Non-invasive Model-Based Assessment of Passive Left-Ventricular Myocardial Stiffness in Healthy Subjects and in Patients with Non-ischemic Dilated Cardiomyopathy", *Annals of Biomedical Engineering*, pp. 1–14, 2017.

[131] G. J. Hall and E. P. Kasper, "Comparison of element technologies for modeling stent expansion", *Journal of Biomechanical Engineering*, vol. 128, no. 5, pp. 751–6, 2006.

[132] D. Haskett, G. Johnson, A. Zhou, *et al.*, "Microstructural and biomechanical alterations of the human aorta as a function of age and location", *Biomechanics and Modeling in Mechanobiology*, vol. 9, no. 6, pp. 725–736, 2010.

[133] L. J. Healy, Y. Jiang, and E. W. Hsu, "Quantitative comparison of myocardial fiber structure between mice, rabbit, and sheep using diffusion tensor cardiovascular magnetic resonance", *Journal of cardiovascular magnetic resonance : official journal of the Society for Cardiovascular Magnetic Resonance*, vol. 13, no. 1, pp. 74–74, 2011.

[134] A. V. Hill, "The heat of shortening and the dynamic constants of muscle", *Proc. R. Soc. Lond. B*, vol. 126, no. 843, pp. 136–195, 1938.

[135] A. V. Hill, "First and last experiments in muscle mechanics". University Press, 1970.

[136] M. M. C. Hirdes, P. D. Siersema, P. G. A. van Boeckel, *et al.*, "Single and sequential biodegradable stent placement for refractory benign esophageal strictures: a prospective follow-up study", *Endoscopy*, vol. 44, no. 07, pp. 649–654, 2012.

[137] M. M. Hirdes, F. P. Vleggaar, M. de Beule, *et al.*, "In vitro evaluation of the radial and axial force of self-expanding esophageal stents", *Endoscopy*, vol. 45, no. 12, pp. 997–1005, 2013.

[138] M. M. Hirdes, F. P. Vleggaar, and P. D. Siersema, "Stent placement for esophageal strictures: an update", *Expert Review of Medical Devices*, vol. 8, no. 6, pp. 733–55, 2011.

[139] M. Hirdes, M. Peirlinck, M. De Beule, *et al.*, "Can we develop self-expandable metallic stents without consideration of mechanical properties? Reply", *Endoscopy*, vol. 46, no. 8, p. 716, 2014.

[140] M. Hirschvogel, M. Bassilious, L. Jagschies, *et al.*, "A monolithic 3D-0D coupled closed-loop model of the heart and the vascular system: Experiment-based parameter estimation for patient-specific cardiac mechanics", *International Journal for Numerical Methods in Biomedical Engineering*, vol. 33, no. 8, e2842, 2017.

[141] J. W. Holmes, "Candidate mechanical stimuli for hypertrophy during volume overload", *Journal of Applied Physiology: Respiratory, Environmental and Exercise Physiology*, vol. 97, no. 4, pp. 1453–1460, 2004.

[142] G. A. Holzapfel, T. C. Gasser, and R. W. Ogden, "A new constitutive framework for arterial wall mechanics and a comparative study of material models", *Journal of Elasticity*, vol. 61, no. 1-3, pp. 1–48, 2000.

[143] G. A. Holzapfel, "Nonlinear solid mechanics: a continuum approach for engineering science", *Meccanica*, vol. 37, no. 4, pp. 489–490, 2002.

[144] G. A. Holzapfel and B. Fereidoonnezhad, "Modeling of Damage in Soft Biological Tissues", in *Biomechanics of Living Organs*, Y. Payan and J. Ohayon, Eds. Oxford: Academic Press, 2017, pp. 101–123.

[145] G. A. Holzapfel, C. T. Gasser, and M. Stadler, "A structural model for the viscoelastic behavior of arterial walls: continuum formulation and finite element analysis", *European Journal of Mechanics-A/Solids*, vol. 21, no. 3, pp. 441–463, 2002.

[146] G. A. Holzapfel and T. C. Gasser, "A viscoelastic model for fiber-reinforced composites at finite strains: Continuum basis, computational aspects and applications", *Computer Methods in Applied Mechanics and Engineering*, vol. 190, no. 34, pp. 4379–4403, 2001.

[147] G. A. Holzapfel and R. W. Ogden, "Constitutive modelling of passive myocardium: a structurally based framework for material characterization", *Philosophical Transactions of the Royal Society of London A: Mathematical, Physical and Engineering Sciences*, vol. 367, no. 1902, pp. 3445–3475, 2009.

[148] G. A. Holzapfel and R. W. Ogden, "Constitutive modelling of arteries", in *Proceedings of the Royal Society of London A: Mathematical, Physical and Engineering Sciences*, vol. 466, The Royal Society, 2010, pp. 1551–1597.

[149] D. A. Hooks, K. A. Tomlinson, S. G. Marsden, *et al.*, "Cardiac Microstructure", *Implications for Electrical Propagation and Defibrillation in the Heart*, vol. 91, no. 4, pp. 331–338, 2002.

[150] P. R. Hoskins, P. V. Lawford, and B. J. Doyle, "Cardiovascular biomechanics". Springer, 2017.

[151] J. J. Hu, S. Baek, and J. D. Humphrey, "Stress–strain behavior of the passive basilar artery in normotension and hypertension", *Journal of Biomechanics*, vol. 40, no. 11, pp. 2559–2563, 2007.

[152] T. J. R. Hughes, "The finite element method: linear static and dynamic finite element analysis". Courier Corporation, 2012.

[153] J. D. Humphrey and K. R. Rajagopal, "A constrained mixture model for growth and remodeling of soft tissues", *Mathematical Models and Methods in Applied Sciences*, vol. 12, no. 03, pp. 407–430, 2002.

[154] J. D. Humphrey, "Continuum mechanics", in *Cardiovascular Solid Mechanics*. Springer, 2002, pp. 68–106.

[155] J. D. Humphrey and S. L. Delange, "An Introduction to Biomechanics". Springer, 2016.

[156] D. E. Hurtado, S. Castro, and A. Gizzi, "Computational modeling of non-linear diffusion in cardiac electrophysiology: A novel porous-medium approach", *Computer Methods in Applied Mechanics and Engineering*, vol. 300, pp. 70–83, 2016.

[157] J. M. Huyghe, D. H. van Campen, T. Arts, *et al.*, "The constitutive behaviour of passive heart muscle tissue: A quasi-linear viscoelastic formulation", *Journal of Biomechanics*, vol. 24, no. 9, pp. 841–849, 1991.

[158] F. Iannaccone, N. Debusschere, S. De Bock, *et al.*, "The influence of vascular anatomy on carotid artery stenting: A parametric study for damage assessment", *Journal of Biomechanics*, vol. 47, no. 4, pp. 890–898, 2014.

[159] F. Iannaccone, "Computer simulations in stroke prevention : design tools and strategies towards virtual procedure planning", PhD thesis, Faculty of Engineering, Ghent University, 2014.

[160] A. A. Inamdar and A. C. Inamdar, "Heart Failure: Diagnosis, Management and Utilization", *Journal of clinical medicine*, vol. 5, no. 7, p. 62, 2016.

[161] H. F. Inman and E. L. Bradley, "The overlapping coefficient as a measure of agreement between probability distributions and point estimation of the overlap of two normal densities", *Communications in Statistics - Theory and Methods*, vol. 18, no. 10, pp. 3851–3874, 1989.

[162] H. Isayama, Y. Nakai, Y. Toyokawa, *et al.*, "Measurement of radial and axial forces of biliary self-expandable metallic stents", *Gastrointestinal Endoscopy*, vol. 70, no. 1, pp. 37–44, 2009.

[163] P. de Jaegere, G. De Santis, R. Rodriguez-Olivares, *et al.*, "Patient-Specific Computer Modeling to Predict Aortic Regurgitation After Transcatheter Aortic Valve Replacement", *Jacc-Cardiovascular Interventions*, vol. 9, no. 5, pp. 508–512, 2016.

[164] R. Jasaityte and J. D'hooge, "Strain rate imaging: Fundamental principles and progress so far", *Imaging in Medicine*, vol. 2, no. 5, p. 547, 2010.

[165] M. R. Jedwab and C. O. Clerc, "A Study of the Geometrical and Mechanical-Properties of a Self-Expanding Metallic Stent Theory and Experiment", *Journal of Applied Biomaterials*, vol. 4, no. 1, pp. 77–85, 1993.

[166] C. Jiang, G. Liu, X. Han, *et al.*, "A smoothed finite element method for analysis of anisotropic large deformation of passive rabbit ventricles in diastole", *International journal for numerical methods in biomedical engineering*, vol. 31, no. 1, 2015.

[167] H. Jiang, D. Liao, J. Zhao, *et al.*, "Contractions Reverse Stress Softening in Rat Esophagus", *Annals of Biomedical Engineering*, vol. 42, no. 8, pp. 1717–1728, 2014.

[168] G. R. Joldes, A. Wittek, and K. Miller, "A Total Lagrangian based method for recovering the un-deformed configuration in finite elasticity", *Applied Mathematical Modelling*, vol. 39, no. 14, pp. 3913–3923, 2015.

[169] E. Jones, T. Oliphant, and P. Peterson, "SciPy: Open Source Scientific Tools for Python". 2014.

[170] W. Kajzer, M. Kaczmarek, and J. Marciniak, "Biomechanical analysis of stent–oesophagus system", *Journal of Materials Processing Technology*, vol. 162, pp. 196–202, 2005.

[171] J. Karády, I. Ntalas, B. Prendergast, *et al.*, "Transcatheter mitral valve replacement in mitral annulus calcification–"The art of computer simulation"", *Journal of Cardiovascular Computed Tomography*, 2018.

[172] N. Kawel-Boehm, A. Maceira, E. R. Valsangiacomo-Buechel, *et al.*, "Normal values for cardiovascular magnetic resonance in adults and children", *Journal of Cardiovascular Magnetic Resonance*, vol. 17, no. 1, p. 29, 2015.

[173] R. C. P. Kerckhoffs, J. Omens, and A. D. McCulloch, "A single strain-based growth law predicts concentric and eccentric cardiac growth during pressure and volume overload", *Mechanics Research Communications*, vol. 42, pp. 40–50, 2012.

[174] P. L. M. Kerkhof, "Characterizing Heart Failure in the Ventricular Volume Domain", *Clinical Medicine Insights. Cardiology*, vol. 9, no. Suppl 1, pp. 11–31, 2015.

[175] J. H. Kim, T. J. Kang, and W.-R. Yu, "Mechanical modeling of self-expandable stent fabricated using braiding technology", *Journal of Biomechanics*, vol. 41, no. 15, pp. 3202–3212, 2008.

[176] M. Kleiber, "Body size and metabolic rate", *Physiological Reviews*, vol. 27, no. 4, pp. 511–541, 1947.

[177] S. Klotz, I. Hay, M. L. Dickstein, *et al.*, "Single-beat estimation of end-diastolic pressure-volume relationship: a novel method with potential for noninvasive application", *American Journal of Physiology-Heart and Circulatory Physiology*, vol. 291, no. 1, H403–H412, 2006.

[178] M. Koishi and S. Govindjee, "Inverse design methodology of a tire", *Tire Science and Technology*, vol. 29, no. 3, pp. 155–170, 2001.

[179] J. Kortsmit, N. H. Davies, R. Miller, *et al.*, "The effect of hydrogel injection on cardiac function and myocardial mechanics in a computational post-infarction model", *Computer Methods in Biomechanics and Biomedical Engineering*, vol. 16, no. 11, pp. 1185–95, 2013.

[180] W. Kou, A. P. S. Bhalla, B. E. Griffith, *et al.*, "A fully resolved active musculo-mechanical model for esophageal transport", *arXiv preprint arXiv:1501.02010*, 2015.

[181] D. Kraft, "A software package for sequential quadratic programming", *Forschungsbericht- Deutsche Forschungs- und Versuchsanstalt fur Luft- und Raumfahrt*, 1988.

[182] A. Krishnamurthy, C. T. Villongco, J. Chuang, *et al.*, "Patient-Specific Models of Cardiac Biomechanics", *Journal of Computational Physics*, vol. 244, pp. 4–21, 2013.

[183] W. Kroon, T. Delhaas, T. Arts, *et al.*, "Computational modeling of volumetric soft tissue growth: application to the cardiac left ventricle", *Biomechanics and Modeling in Mechanobiology*, vol. 8, no. 4, pp. 301–309, 2009.

[184] V. Kumar, A. K. Abbas, and J. C. Aster, "Robbins and Cotran Pathologic Basis of Disease", 9th ed. Saunders Elsevier, 2010.

[185] B. Kuo and D. Urma, "Esophagus-anatomy and development", *GI Motility online*, 2006.

[186] P. Lamata, R. Casero, V. Carapella, *et al.*, "Images as drivers of progress in cardiac computational modelling", *Progress in Biophysics and Molecular biology*, vol. 115, no. 2-3, pp. 198–212, 2014.

[187] P. Lamata, S. Niederer, D. Nordsletten, *et al.*, "An accurate, fast and robust method to generate patient-specific cubic Hermite meshes", *Medical Image Analysis*, vol. 15, no. 6, pp. 801–13, 2011.

[188] S. Land, V. Gurev, S. Arens, *et al.*, "Verification of cardiac mechanics software: benchmark problems and solutions for testing active and passive material behaviour", in *Proc. R. Soc. A*, vol. 471, The Royal Society, 2015, p. 20 150 641.

[189] M. Landajuela, C. Vergara, A. Gerbi, *et al.*, "Numerical approximation of the electromechanical coupling in the left ventricle with inclusion of the Purkinje network", *International Journal for Numerical Methods in Biomedical Engineering*, vol. 0, no. 0, e2984, 2018.

[190] B. Laycock, M. Nikolić, J. M. Colwell, *et al.*, "Lifetime prediction of biodegradable polymers", *Progress in Polymer Science*, vol. 71, pp. 144–189, 2017.

[191] A. W. C. Lee, C. M. Costa, M. Strocchi, *et al.*, "Computational Modeling for Cardiac Resynchronization Therapy", *Journal of Cardiovascular Translational Research*, vol. 11, no. 2, pp. 92–108, 2018.

[192] J. D. Lee, S. Sasayama, Y. Kihara, *et al.*, "Adaptations of the left ventricle to chronic volume overload induced by mitral regurgitation in conscious dogs", *Heart and Vessels*, vol. 1, no. 1, pp. 9–15, 1985.

[193] L. C. Lee, M. Genet, A. B. Dang, *et al.*, "Applications of computational modeling in cardiac surgery", *Journal of Cardiac Surgery*, vol. 29, no. 3, pp. 293–302, 2014.

[194] L. C. Lee, G. S. Kassab, and J. M. Guccione, "Mathematical modeling of cardiac growth and remodeling", *Wiley Interdisciplinary Reviews: Systems Biology and Medicine*, vol. 8, no. 3, pp. 211–226, 2016.

[195] L. C. Lee, L. Ge, Z. Zhang, *et al.*, "Patient-specific finite element modeling of the Cardiokinetix Parachute® device: Effects on left ventricular wall stress and function". 2014, vol. 52.

[196] I. J. LeGrice, B. H. Smaill, L. Z. Chai, *et al.*, "Laminar structure of the heart: ventricular myocyte arrangement and connective tissue architecture in the dog", *American Journal of Physiology-Heart and Circulatory Physiology*, vol. 269, no. 2, H571–H582, 1995.

[197] S. Levine, T. Battisti, B. Butz, *et al.*, "Modeling congenital heart disease - engineering a patient-specific therapy", in, G. Butera, S. Schievano, G. Biglino, *et al.*, Eds. Springer Nature, 2019, ch. Dassault Systèmes' Living Heart Project, under review.

[198] D. Lewandowski, D. Kurowicka, and H. Joe, "Generating random correlation matrices based on vines and extended onion method", *Journal of Multivariate Analysis*, vol. 100, no. 9, pp. 1989–2001, 2009.

[199] G. Li, Y. Li, P. Lan, *et al.*, "Biodegradable weft-knitted intestinal stents: Fabrication and physical changes investigation in vitro degradation", *Journal of Biomedical Materials Research. Part A*, 2013.

[200] M. Li and J. G. Brasseur, "Non-steady peristaltic transport in finite-length tubes", *Journal of Fluid Mechanics*, vol. 248, pp. 129–151, 1993.

[201] D. H. Liao, J. B. Zhao, and H. Gregersen, "Gastrointestinal tract modelling in health and disease", *World Journal of Gastroenterology*, vol. 15, no. 2, pp. 169–76, 2009.

[202] D. Liao, J. B. Frokjaer, J. Yang, *et al.*, "Three-dimensional surface model analysis in the gastrointestinal tract", *World J Gastroenterol*, vol. 12, no. 18, pp. 2870–5, 2006.

[203] D. Liao, J. Zhao, Y. Fan, *et al.*, "Two-layered quasi-3D finite element model of the oesophagus", *Medical Engineering & Physics*, vol. 26, no. 7, pp. 535–43, 2004.

[204] D. Liao, J. Zhao, J. Yang, *et al.*, "The oesophageal zero-stress state and mucosal folding from a GIOME perspective", *World Journal of Gastroenterology*, vol. 13, no. 9, pp. 1347–51, 2007.

[205] D. Liao, Y. Fan, Y. Zeng, *et al.*, "Stress distribution in the layered wall of the rat oesophagus", *Medical engineering & physics*, vol. 25, no. 9, pp. 731–738, 2003.

[206] D. Liao, J. Zhao, and H. Gregersen, "Esophagus", in *Biomechanics of Living Organs*, Y. Payan and J. Ohayon, Eds. Oxford: Academic Press, 2017, pp. 147–167.

[207] D. Liao, J. Zhao, P. Kunwald, *et al.*, "Tissue softening of guinea pig oesophagus tested by the tri-axial test machine", *Journal of Biomechanics*, vol. 42, no. 7, pp. 804–810, 2009.

[208] D. H. S. Lin and F. C. P. Yin, "A multiaxial constitutive law for mammalian left ventricular myocardium in steady-state barium contracture or tetanus", *Journal of Biomechanical Engineering*, vol. 120, no. 4, pp. 504–517, 1998.

[209] D. H. Lin and F. C. Yin, "A multiaxial constitutive law for mammalian left ventricular myocardium in steady-state barium contracture or tetanus", *J Biomech Eng*, vol. 120, no. 4, pp. 504–17, 1998.

[210] H. Lombaert, J.-M. Peyrat, P. Croisille, *et al.*, "Human atlas of the cardiac fiber architecture: study on a healthy population", *IEEE Transactions on Medical Imaging*, vol. 31, no. 7, pp. 1436–1447, 2012.

[211] C. Lottrup, H. Gregersen, D. Liao, *et al.*, "Functional lumen imaging of the gastrointestinal tract", *Journal of Gastroenterology*, vol. 50, no. 10, pp. 1005–1016, 2015.

[212] J. Lu, X. Zhou, and M. L. Raghavan, "Computational method of inverse elastostatics for anisotropic hyperelastic solids", *International Journal for Numerical Methods in Engineering*, vol. 69, no. 6, pp. 1239–1261, 2007.

[213] J. Lumens, T. Delhaas, B. Kirn, *et al.*, "Three-Wall Segment (TriSeg) Model Describing Mechanics and Hemodynamics of Ventricular Interaction", *Annals of Biomedical Engineering*, vol. 37, no. 11, pp. 2234–2255, 2009.

[214] S. A. Maas, A. Erdemir, J. P. Halloran, *et al.*, "A general framework for application of prestrain to computational models of biological materials", *Journal of the Mechanical Behavior of Biomedical Materials*, vol. 61, no. Supplement C, pp. 499–510, 2016.

[215] A. Maier, M. W. Gee, C. Reeps, *et al.*, "Impact of calcifications on patient-specific wall stress analysis of abdominal aortic aneurysms", *Biomechanics and Modeling in Mechanobiology*, vol. 9, no. 5, pp. 511–521, 2010.

[216] D. Mancini and D. Burkhoff, "Mechanical device-based methods of managing and treating heart failure", *Circulation*, vol. 112, no. 3, pp. 438–48, 2005.

[217] D. L. Mann, D. P. Zipes, P. Libby, *et al.*, "Braunwald's heart disease: a textbook of cardiovascular medicine". Elsevier Health Sciences, 2014.

[218] S. Marchesseau, H. Delingette, M. Sermesant, *et al.*, "Fast parameter calibration of a cardiac electromechanical model from medical images based on the unscented transform", *Biomechanics and Modeling in Mechanobiology*, vol. 12, no. 4, pp. 815–831, 2013.

[219] Y. K. Mariappan, K. J. Glaser, and R. L. Ehman, "Magnetic resonance elastography: A review", *Clinical Anatomy*, vol. 23, no. 5, pp. 497–511, 2010.

[220] E. N. Marieb and K. Hoehn, "Anatomy and Physiology". Pearson Education, 2011, vol. 4th edition.

[221] G. A. Maugin, "Continuum mechanics through the twentieth century", *Springer, Berlin. doi*, vol. 10, pp. 978–94, 2013.

[222] S. Mayrand and N. E. Diamant, "Measurement of human esophageal tone in vivo", *Gastroenterology*, vol. 105, no. 5, pp. 1411–1420, 1993.

[223] L. A. McGill, P. F. Ferreira, A. D. Scott, *et al.*, "Relationship between cardiac diffusion tensor imaging parameters and anthropometrics in healthy volunteers", *Journal of cardiovascular magnetic resonance : official journal of the Society for Cardiovascular Magnetic Resonance*, vol. 18, no. 1, pp. 2–2, 2016.

[224] A. Menzel and E. Kuhl, "Frontiers in growth and remodeling", *Mechanics Research Communications*, vol. 42, pp. 1–14, 2012.

[225] A. Meoli, E. Cutrì, A. Krishnamurthy, *et al.*, "A multiscale model for the study of cardiac biomechanics in single-ventricle surgeries: a clinical case", *Interface Focus*, vol. 5, no. 2, 2015.

[226] M. Metra and J. R. Teerlink, "Heart failure", *The Lancet*, vol. 390, no. 10106, pp. 1981–1995, 2017.

[227] K. Miller, "Biomechanics of soft tissues", *Medical Science Monitor*, vol. 6, no. 1, MT158–MT167, 2000.

[228] L. S. Miller, J.-B. Liu, F. P. Colizzo, *et al.*, "Correlation of high-frequency esophageal ultrasonography and manometry in the study of esophageal motility", *Gastroenterology*, vol. 109, no. 3, pp. 832–837, 1995.

[229] R. K. Mittal, B. Padda, V. Bhalla, *et al.*, "Synchrony between circular and longitudinal muscle contractions during peristalsis in normal subjects", *American Journal of Physiology-Gastrointestinal and Liver Physiology*, vol. 290, no. 3, G431–G438, 2006.

[230] D. S. Molony, E. G. Kavanagh, P. Madhavan, *et al.*, "A Computational Study of the Magnitude and Direction of Migration Forces in Patient-specific Abdominal Aortic Aneurysm Stent-Grafts", *European Journal of Vascular and Endovascular Surgery*, vol. 40, no. 3, pp. 332–339, 2010.

[231] P. Morais, B. Heyde, D. Barbosa, *et al.*, "Cardiac motion and deformation estimation from tagged MRI sequences using a temporal coherent image registration framework", in *International Conference on Functional Imaging and Modeling of the Heart*, Springer, 2013, pp. 316–324.

[232] P. Morais, A. Marchi, J. A. Bogaert, *et al.*, "Cardiovascular magnetic resonance myocardial feature tracking using a non-rigid, elastic image registration algorithm: assessment of variability in a real-life clinical setting", *Journal of Cardiovascular Magnetic Resonance*, vol. 19, no. 1, p. 24, 2017.

[233] P. Mortier, "Computer Modelling of Coronary Bifurcation Stenting", PhD thesis, Faculty of Engineering, Ghent University, 2009.

[234] R. L. Moss and D. P. Fitzsimons, "Frank-Starling Relationship", *Circulation Research*, vol. 90, no. 1, pp. 11–13, 2002.

[235] J. S. Mousavi and S. Avril, "Patient-specific stress analyses in the ascending thoracic aorta using a finite-element implementation of the constrained mixture theory", *Biomechanics and Modeling in Mechanobiology*, vol. 16, no. 5, pp. 1765–1777, 2017.

[236] C. D. Murray, "The Physiological Principle of Minimum Work: II. Oxygen Exchange in Capillaries", *Proceedings of the National Academy of Sciences of the United States of America*, vol. 12, no. 5, pp. 299–304, 1926.

[237] S.-I. Murtada, J. D. Humphrey, and G. A. Holzapfel, "Multiscale and Multiaxial Mechanics of Vascular Smooth Muscle", *Biophysical Journal*, vol. 113, no. 3, pp. 714–727, 2017.

[238] S.-I. Murtada, M. Kroon, and G. A. Holzapfel, "A calcium-driven mechanochemical model for prediction of force generation in smooth muscle", *Biomechanics and Modeling in Mechanobiology*, vol. 9, no. 6, pp. 749–762, 2010.

[239] P. Nardinocchi and L. Teresi, "On the Active Response of Soft Living Tissues", *Journal of Elasticity*, vol. 88, no. 1, pp. 27–39, 2007.

[240] M. P. Nash and P. J. Hunter, "Computational Mechanics of the Heart", *Journal of elasticity and the physical science of solids*, vol. 61, no. 1, pp. 113–141, 2000.

[241] M. P. Nash and A. V. Panfilov, "Electromechanical model of excitable tissue to study reentrant cardiac arrhythmias", *Progress in Biophysics and Molecular Biology*, vol. 85, no. 2, pp. 501–522, 2004.

[242] A. N. Natali, E. L. Carniel, and H. Gregersen, "Biomechanical behaviour of oesophageal tissues: material and structural configuration, experimental data and constitutive analysis", *Medical engineering & physics*, vol. 31, no. 9, pp. 1056–1062, 2009.

[243] M. A. Nicosia, J. G. Brasseur, J.-B. Liu, *et al.*, "Local longitudinal muscle shortening of the human esophagus from high-frequency ultrasonography", *American Journal of Physiology-Gastrointestinal and Liver Physiology*, vol. 281, no. 4, G1022–G1033, 2001.

[244] S. A. Niederer and N. P. Smith, "The role of the Frank-Starling law in the transduction of cellular work to whole organ pump function: a computational modeling analysis", *PLoS Computational Biology*, vol. 5, no. 4, e1000371, 2009.

[245] S. A. Niederer, K. S. Campbell, and S. G. Campbell, "A short history of the development of mathematical models of cardiac mechanics", *Journal of Molecular and Cellular Cardiology*, vol. 127, pp. 11–19, 2019.

[246] S. Niederer, K. Rhode, R. Razavi, *et al.*, "The importance of model parameters and boundary conditions in whole organ models of cardiac contraction", in *International Conference on Functional Imaging and Modeling of the Heart*, Springer, 2009, pp. 348–356.

[247] A. Nikou, S. M. Dorsey, J. R. McGarvey, *et al.*, "Effects of using the unloaded configuration in predicting the in vivo diastolic properties of the heart", *Computer Methods in Biomechanics and Biomedical Engineering*, vol. 19, no. 16, pp. 1714–1720, 2016.

[248] D. Noble, "Modeling the heart–from genes to cells to the whole organ", *Science*, vol. 295, no. 5560, pp. 1678–1682, 2002.

[249] D. R. Nolan and J. P. McGarry, "On the compressibility of arterial tissue", *Annals of Biomedical Engineering*, vol. 44, no. 4, pp. 993–1007, 2016.

[250] O. Nordbo, P. Lamata, S. Land, *et al.*, "A computational pipeline for quantification of mouse myocardial stiffness parameters", *Computers in Biology and Medicine*, vol. 53, pp. 65–75, 2014.

[251] J. P. Nuutinen, C. Clerc, and P. Tormala, "Theoretical and experimental evaluation of the radial force of self-expanding braided bioabsorbable stents", *Journal of Biomaterials Science-Polymer Edition*, vol. 14, no. 7, pp. 677–687, 2003.

[252] S. Obara, S. Hayashi, A. Hazama, *et al.*, "Correlation between augmentation index and pulse wave velocity in rabbits", *Journal of Hypertension*, vol. 27, no. 2, pp. 332–340, 2009.

[253] J. Ochola, M. Peirlinck, I. Peeters, *et al.*, "Feasibility of reinforcing suture repaired tendon using a tubular braided fabric", in preparation.

[254] R. W. Ogden, "Nearly isochoric elastic deformations: Application to rubberlike solids", *Journal of the Mechanics and Physics of Solids*, vol. 26, no. 1, pp. 37–57, 1978.

[255] R. W. Ogden, "Large deformation isotropic elasticity–on the correlation of theory and experiment for incompressible rubberlike solids", *Proc. R. Soc. Lond. A*, vol. 326, no. 1567, pp. 565–584, 1972.

[256] J. Ohayon, D. Ambrosi, and J.-L. Martiel, "Hyperelastic Models for Contractile Tissues: Application to Cardiovascular Mechanics", in *Biomechanics of Living Organs*. Elsevier, 2017, pp. 31–58.

[257] J. H. Omens, "Stress and strain as regulators of myocardial growth", *Progress in Biophysics and Molecular biology*, vol. 69, no. 2-3, pp. 559–572, 1998.

[258] J. H. Omens and Y.-C. Fung, "Residual strain in rat left ventricle", *Circulation Research*, vol. 66, no. 1, pp. 37–45, 1990.

[259] G. K. B. Ong and R. K. Freeman, "Endoscopic management of esophageal leaks", *Journal of thoracic disease*, vol. 9, no. Suppl 2, S135–S145, 2017.

[260] J. Ophir, S. K. Alam, B. Garra, *et al.*, "Elastography: Ultrasonic estimation and imaging of the elastic properties of tissues", *Proceedings of the Institution of Mechanical Engineers, Part H: Journal of Engineering in Medicine*, vol. 213, no. 3, pp. 203–233, 1999.

[261] L. H. Opie, "Heart physiology: from cell to circulation". Lippincott Williams & Wilkins, 2004.

[262] L. H. Opie, P. J. Commerford, B. J. Gersh, *et al.*, "Controversies in ventricular remodelling", *The Lancet*, vol. 367, no. 9507, pp. 356–367, 2006.

[263] A. Palit, S. K. Bhudia, T. N. Arvanitis, *et al.*, "Computational modelling of left-ventricular diastolic mechanics: effect of fibre orientation and right-ventricle topology", *Journal of Biomechanics*, vol. 48, no. 4, pp. 604–12, 2015.

[264] A. Palit, P. Franciosa, S. K. Bhudia, *et al.*, "Passive diastolic modelling of human ventricles: Effects of base movement and geometrical heterogeneity", *Journal of Biomechanics*, vol. 52, pp. 95–105, 2017.

[265] A. F. Peery, S. D. Crockett, A. S. Barritt, *et al.*, "Burden of Gastrointestinal, Liver, and Pancreatic Diseases in the United States", *Gastroenterology*, vol. 149, no. 7, 1731–1741.e3, 2015.

[266] M. Peirlinck, "Design of biodegradable esophageal stents", Master Thesis, 2013.

[267] M. Peirlinck, M. De Beule, P. Segers, *et al.*, "A modular inverse elastostatics approach to resolve the pressure-induced stress state for in vivo imaging based cardiovascular modeling", *Journal of the Mechanical Behavior of Biomedical Materials*, vol. 85, pp. 124–133, 2018.

[268] M. Peirlinck, N. Debusschere, F. Iannaccone, *et al.*, "An in silico biomechanical analysis of the stent–esophagus interaction", *Biomechanics and Modeling in Mechanobiology*, vol. 17, no. 1, pp. 111–131, 2018.

[269] M. Peirlinck, K. L. Sack, P. De Backer, *et al.*, "Kinematic boundary conditions substantially impact in silico ventricular function", *International Journal for Numerical Methods in Biomedical Engineering*, vol. 35, no. 1, e3151, 2019.

[270] M. Peirlinck, F. Sahli Costabal, K. L. Sack, *et al.*, "Using machine learning to characterize heart failure across the scales", *Biomechanics and Modeling in Mechanobiology*, 2019, in press.

[271] P. Perdikaris, *Gaussian processes. A hands-on tutorial.* 2017.

[272] M. Pernot, M. Couade, P. Mateo, *et al.*, "Real-Time Assessment of Myocardial Contractility Using Shear Wave Imaging", *Journal of the American College of Cardiology*, vol. 58, no. 1, pp. 65–72, 2011.

[273] S. Pezzuto and D. Ambrosi, "Active contraction of the cardiac ventricle and distortion of the microstructural architecture", *International journal for numerical methods in biomedical engineering*, vol. 30, no. 12, pp. 1578–1596, 2014.

[274] S. Pezzuto, D. Ambrosi, and A. Quarteroni, "An orthotropic active–strain model for the myocardium mechanics and its numerical approximation", *European Journal of Mechanics-A/Solids*, vol. 48, pp. 83–96, 2014.

[275] A. V. S. Ponnaluri, L. E. Perotti, D. B. Ennis, *et al.*, "A viscoactive constitutive modeling framework with variational updates for the myocardium", *Computer Methods in Applied Mechanics and Engineering*, vol. 314, pp. 85–101, 2017.

[276] A. V. S. Ponnaluri, "Cardiac Electromechanics Modeling and Validation", PhD thesis, 2018.

[277] P. Pouderoux, S. Lin, and P. J. Kahrilas, "Timing, propagation, coordination, and effect of esophageal shortening during peristalsis", *Gastroenterology*, vol. 112, no. 4, pp. 1147–1154, 1997.

[278] J. L. Puckett, V. Bhalla, J. Liu, *et al.*, "Oesophageal wall stress and muscle hypertrophy in high amplitude oesophageal contractions", *Neurogastroenterology & Motility*, vol. 17, no. 6, pp. 791–799, 2005.

[279] A. Quarteroni, T. Lassila, S. Rossi, *et al.*, "Integrated Heart—Coupling multiscale and multiphysics models for the simulation of the cardiac function", *Computer Methods in Applied Mechanics and Engineering*, vol. 314, pp. 345–407, 2017.

[280] M. L. Raghavan, B. Ma, and M. F. Fillinger, "Non-invasive determination of zero-pressure geometry of arterial aneurysms", *Annals of Biomedical Engineering*, vol. 34, no. 9, pp. 1414–1419, 2006.

[281] M. Raissi, P. Perdikaris, and G. Karniadakis, "Numerical Gaussian Processes for Time-Dependent and Nonlinear Partial Differential Equations", *SIAM Journal on Scientific Computing*, vol. 40, no. 1, A172–A198, 2018.

[282] M. Raissi, P. Perdikaris, and G. E. Karniadakis, "Machine learning of linear differential equations using Gaussian processes", *Journal of Computational Physics*, vol. 348, pp. 683–693, 2017.

[283] M. K. Rausch, A. Dam, S. Göktepe, *et al.*, "Computational modeling of growth: systemic and pulmonary hypertension in the heart", *Biomechanics and Modeling in Mechanobiology*, vol. 10, no. 6, pp. 799–811, 2011.

[284] M. K. Rausch, N. Famaey, T. O. Shultz, *et al.*, "Mechanics of the mitral valve", *Biomechanics and Modeling in Mechanobiology*, vol. 12, no. 5, pp. 1053–1071, 2013.

[285] M. K. Rausch, M. Genet, and J. D. Humphrey, "An augmented iterative method for identifying a stress-free reference configuration in image-based biomechanical modeling", *Journal of Biomechanics*, vol. 58, pp. 227–231, 2017.

[286] M. K. Rausch, A. M. Zöllner, M. Genet, *et al.*, "A virtual sizing tool for mitral valve annuloplasty", *International Journal for Numerical Methods in Biomedical Engineering*, vol. 33, no. 2, e02788, 2017.

[287] A. Repici, F. P. Vleggaar, C. Hassan, *et al.*, "Efficacy and safety of biodegradable stents for refractory benign esophageal strictures: the BEST (Biodegradable Esophageal Stent) study", *Gastrointestinal Endoscopy*, vol. 72, no. 5, pp. 927–934, 2010.

[288] J. C. Reynolds, "The Netter collection of medical illustrations: Digestive System: Part I-The Upper Digestive Tract". Elsevier Health Sciences, 2016.

[289] A. M. Riddell, D. C. Davies, W. H. Allum, *et al.*, "High-Resolution MRI in Evaluation of the Surgical Anatomy of the Esophagus and Posterior Mediastinum", *American Journal of Roentgenology*, vol. 188, no. 1, W37–W43, 2007.

[290] F. Riveros, S. Chandra, E. A. Finol, *et al.*, "A pull-back algorithm to determine the unloaded vascular geometry in anisotropic hyperelastic AAA passive mechanics", *Annals of Biomedical Engineering*, vol. 41, no. 4, pp. 694–708, 2013.

[291] B. Robert, R. Sinkus, J.-L. Gennisson, *et al.*, "Application of DENSE-MR-elastography to the human heart", *Magnetic Resonance in Medicine*, vol. 62, no. 5, pp. 1155–1163, 2009.

[292] G. Rocatello, N. El Faquir, G. De Santis, *et al.*, "Patient-Specific Computer Simulation to Elucidate the Role of Contact Pressure in the Development of New Conduction Abnormalities After Catheter-Based Implantation of a Self-Expanding Aortic Valve", *Circulation: Cardiovascular Interventions*, vol. 11, no. 2, e005344, 2018.

[293] J. C. L. Rodrigues, A. M. Amadu, A. G. Dastidar, *et al.*, "Comprehensive characterisation of hypertensive heart disease left ventricular phenotypes", *Heart*, vol. 102, no. 20, pp. 1671–1679, 2016.

[294] R. Rodríguez-Cantano, J. Sundnes, and M. E. Rognes, "Uncertainty in cardiac myofiber orientation and stiffnesses dominate the variability of left ventricle deformation response", *International Journal for Numerical Methods in Biomedical Engineering*, vol. 35, no. 5, e3178, 2019.

[295] E. K. Rodriguez, A. Hoger, and A. D. McCulloch, "Stress-dependent finite growth in soft elastic tissues", *Journal of Biomechanics*, vol. 27, no. 4, pp. 455–467, 1994.

[296] J. F. Rodríguez, C. Ruiz, M. Doblaré, *et al.*, "Mechanical stresses in abdominal aortic aneurysms: influence of diameter, asymmetry, and material anisotropy", *Journal of Biomechanical Engineering*, vol. 130, no. 2, p. 021 023, 2008.

[297] K. L. Sack, "Biological tissue mechanics with fibres modelled as one dimensional Cosserat continua: applications to cardiac tissue in healthy and diseased states", Master's thesis, 2014.

[298] K. L. Sack, N. H. Davies, J. M. Guccione, *et al.*, "Personalised computational cardiology: Patient-specific modelling in cardiac mechanics and biomaterial injection therapies for myocardial infarction", *Heart Failure Reviews*, vol. 21, no. 6, pp. 815–826, 2016.

[299] K. L. Sack, E. Aliotta, D. B. Ennis, *et al.*, "Construction and Validation of Subject-Specific Biventricular Finite-Element Models of Healthy and Failing Swine Hearts From High-Resolution DT-MRI", *Frontiers in Physiology*, vol. 9, no. 539, 2018.

[300] K. L. Sack, L.-C. Lee, J. M. Guccione, *et al.*, "Population-Based Myofibre Assignment: The Importance of Longitudinal Variation in Subject-Specific Cardiac Models", in *22nd Congress of the European Society of Biomechanics*, 2016.

[301] F. Sahli Costabal, J. S. Choy, K. L. Sack, *et al.*, "Multiscale characterization of heart failure", *Acta Biomaterialia*, 2019.

[302] F. Sahli Costabal, "Multi-scale modeling of cardiac arrhythmias", PhD thesis, 2019.

[303] F. Sahli Costabal, K. Matsuno, J. Yao, *et al.*, "Machine learning in drug development: Characterizing the effect of 30 drugs on the QT interval using Gaussian process regression, sensitivity analysis, and uncertainty quantification", *Computer Methods in Applied Mechanics and Engineering*, vol. 348, pp. 313–333, 2019.

[304] J. Sainte-Marie, D. Chapelle, R. Cimrman, *et al.*, "Modeling and estimation of the cardiac electromechanical activity", *Computers & Structures*, vol. 84, no. 28, pp. 1743–1759, 2006.

[305] K. S. Saladin, C. A. Gan, and H. N. Cushman, "Anatomy & Physiology: The Unity of Form and Function." 8th ed. New York, NY: McGraw-Hill, 2018.

[306] J. Salvatier, T. V. Wiecki, and C. Fonnesbeck, "Probabilistic programming in Python using PyMC3", *PeerJ Computer Science*, vol. 2, e55, 2016.

[307] H. Sandler and T. Dodge Harold, "Left Ventricular Tension and Stress in Man", *Circulation Research*, vol. 13, no. 2, pp. 91–104, 1963.

[308] S. Sasayama, J. Ross J., D. Franklin, *et al.*, "Adaptations of the left ventricle to chronic pressure overload", *Circulation Research*, vol. 38, no. 3, pp. 172–8, 1976.

[309] O. V. Savinova and A. M. Gerdes, "Myocyte Changes in Heart Failure", *Heart Failure Clinics*, vol. 8, no. 1, pp. 1–6, 2012.

[310] A. Scatteia, A. Baritussio, and C. Bucciarelli-Ducci, "Strain imaging using cardiac magnetic resonance", *Heart Failure Reviews*, vol. 22, no. 4, pp. 465–476, 2017.

[311] H. Schmid, M. P. Nash, A. A. Young, *et al.*, "Myocardial Material Parameter Estimation—A Comparative Study for Simple Shear", *Journal of Biomechanical Engineering*, vol. 128, no. 5, pp. 742–750, 2006.

[312] C. Schultz, R. Rodriguez-Olivares, J. Bosmans, *et al.*, "Patient-specific image-based computer simulation for the prediction of valve morphology and calcium displacement after TAVI with the medtronic CoreValve and the Edwards SAPIEN valve", *EuroIntervention*, vol. 11, no. 9, pp. 1044–1052, 2016.

[313] M. Sellier, "Optimal process design in high-precision glass forming", *International Journal of Forming Processes*, vol. 9, no. 1, p. 61, 2006.

[314] M. Sellier, "An iterative method for the inverse elasto-static problem", *Journal of Fluids and Structures*, vol. 27, no. 8, pp. 1461–1470, 2011.

[315] M. Sermesant, P. Moireau, O. Camara, *et al.*, "Cardiac function estimation from MRI using a heart model and data assimilation: Advances and difficulties", *Medical Image Analysis*, vol. 10, no. 4, pp. 642–656, 2006.

[316] M. Sermesant, J. M. Peyrat, P. Chinchapatnam, *et al.*, "Toward patient-specific myocardial models of the heart", *Heart Fail Clin*, vol. 4, no. 3, pp. 289–301, 2008.

[317] *Servier Medical Art, licensed under a Creative Common Attribution 3.0 Generic License. http://smart.servier.com/.*

[318] M. Shams, M. Destrade, and R. W. Ogden, "Initial stresses in elastic solids: constitutive laws and acoustoelasticity", *Wave Motion*, vol. 48, no. 7, pp. 552–567, 2011.

[319] C. Shanahan, S. A. M. Tofail, and P. Tiernan, "Viscoelastic braided stent: Finite element modelling and validation of crimping behaviour", *Materials and Design*, vol. 121, pp. 143–153, 2017.

[320] P. Sharma, R. Kozarek, and G. Practice Parameters Committee of American College of, "Role of esophageal stents in benign and malignant diseases", *American Journal of Gastroenterology*, vol. 105, no. 2, 258–73, quiz 274, 2010.

[321] M. J. Shelley, "The dynamics of microtubule/motor-protein assemblies in biology and physics", *Annual Review of Fluid Mechanics*, vol. 48, pp. 487–506, 2016.

[322] O. A. Smiseth, H. Torp, A. Opdahl, *et al.*, "Myocardial strain imaging: how useful is it in clinical decision making?", *European Heart Journal*, vol. 37, no. 15, pp. 1196–1207, 2015.

[323] D. P. Sokolis, "Strain-energy function and three-dimensional stress distribution in esophageal biomechanics", *Journal of Biomechanics*, vol. 43, no. 14, pp. 2753–64, 2010.

[324] D. P. Sokolis, "Structurally-motivated characterization of the passive pseudo-elastic response of esophagus and its layers", *Computers in Biology and Medicine*, vol. 43, no. 9, pp. 1273–85, 2013.

[325] G. Sommer, A. Schriefl, G. Zeindlinger, *et al.*, "Multiaxial mechanical response and constitutive modeling of esophageal tissues: Impact on esophageal tissue engineering", *Acta Biomaterialia*, vol. 9, no. 12, pp. 9379–91, 2013.

[326] G. Sommer, A. J. Schriefl, M. Andrä, *et al.*, "Biomechanical properties and microstructure of human ventricular myocardium", *Acta Biomaterialia*, vol. 24, pp. 172–192, 2015.

[327] V. Sørhus, "Auxotonic Loading of the Cardiac Muscle: Experiments and Model Simulations", 2000.

[328] L. Speelman, E. M. H. Bosboom, G. W. H. Schurink, *et al.*, "Initial stress and nonlinear material behavior in patient-specific AAA wall stress analysis", *Journal of Biomechanics*, vol. 42, no. 11, pp. 1713–1719, 2009.

[329] A. J. M. Spencer, "Continuum theory of the mechanics of fibre-reinforced composites". Springer, 1984, vol. 282.

[330] J. Stålhand, A. Klarbring, and G. A. Holzapfel, "Smooth muscle contraction: Mechanochemical formulation for homogeneous finite strains", *Progress in Biophysics and Molecular biology*, vol. 96, no. 1, pp. 465–481, 2008.

[331] E. A. Stavropoulou, Y. F. Dafalias, and D. P. Sokolis, "Biomechanical and histological characteristics of passive esophagus: experimental investigation and comparative constitutive modeling", *Journal of Biomechanics*, vol. 42, no. 16, pp. 2654–63, 2009.

[332] S. F. C. Stewart, E. G. Paterson, G. W. Burgreen, *et al.*, "Assessment of CFD performance in simulations of an idealized medical device: results of FDA's first computational interlaboratory study", *Cardiovascular Engineering and Technology*, vol. 3, no. 2, pp. 139–160, 2012.

[333] K. Sun, N. Stander, C.-S. Jhun, *et al.*, "A computationally efficient formal optimization of regional myocardial contractility in a sheep with left ventricular aneurysm", *Journal of Biomechanical Engineering*, vol. 131, no. 11, p. 111 001, 2009.

[334] D. W. Thompson, "On growth and form", *On growth and form.*, 1942.

[335] M. J. Thubrikar and F. Robicsek, "Pressure-induced arterial wall stress and atherosclerosis", *The Annals of Thoracic Surgery*, vol. 59, no. 6, pp. 1594–1603, 1995.

[336] A. Tottrup, A. Forman, N. Uldbjerg, *et al.*, "Mechanical properties of isolated human esophageal smooth muscle", *American Journal of Physiology-Gastrointestinal and Liver Physiology*, vol. 258, no. 3, G338–G343, 1990.

[337] N. Townsend, L. Wilson, P. Bhatnagar, *et al.*, "Cardiovascular disease in europe: epidemiological update 2016", *European Heart Journal*, vol. 37, no. 42, pp. 3232–3245, 2016.

[338] N. A. Trayanova, "Whole-heart modeling: applications to cardiac electrophysiology and electromechanics", *Circulation Research*, vol. 108, no. 1, pp. 113–28, 2011.

[339] N. A. Trayanova and P. M. Boyle, "Advances in modeling ventricular arrhythmias: from mechanisms to the clinic", *Wiley Interdisciplinary Reviews: Systems Biology and Medicine*, vol. 6, no. 2, pp. 209–24, 2014.

[340] A. Tsamis, A. Cheng, T. C. Nguyen, *et al.*, "Kinematics of cardiac growth: In vivo characterization of growth tensors and strains", *Journal of the Mechanical Behavior of Biomedical Materials*, vol. 8, pp. 165–177, 2012.

[341] M. J. Uitdehaag, P. D. Siersema, M. C. Spaander, *et al.*, "A new fully covered stent with antimigration properties for the palliation of malignant dysphagia: a prospective cohort study", *Gastrointestinal Endoscopy*, vol. 71, no. 3, pp. 600–5, 2010.

[342] T. P. Usyk, R. Mazhari, and A. D. McCulloch, "Effect of laminar orthotropic myofiber architecture on regional stress and strain in the canine left ventricle", *Journal of Elasticity*, vol. 61, no. 1-3, pp. 143–164, 2000.

[343] L. M. Van Bortel, S. Laurent, P. Boutouyrie, *et al.*, "Expert consensus document on the measurement of aortic stiffness in daily practice using carotid-femoral pulse wave velocity", *Journal of Hypertension*, vol. 30, no. 3, pp. 445–448, 2012.

[344] V. Vavourakis, Y. Papaharilaou, and J. A. Ekaterinaris, "Coupled fluid–structure interaction hemodynamics in a zero-pressure state corrected arterial geometry", *Journal of Biomechanics*, vol. 44, no. 13, pp. 2453–2460, 2011.

[345] B. A. Venkatesh, S. Donekal, K. Yoneyama, *et al.*, "Regional myocardial functional patterns: Quantitative tagged magnetic resonance imaging in an adult population free of cardiovascular risk factors: The multi-ethnic study of atherosclerosis (MESA)", *Journal of Magnetic Resonance Imaging*, vol. 42, no. 1, pp. 153–159, 2015.

[346] B. D. Vermeulen and P. D. Siersema, "Esophageal Stenting in Clinical Practice: an Overview", *Current treatment options in gastroenterology*, vol. 16, no. 2, pp. 260–273, 2018.

[347] G. E. Villadsen, J. Storkholm, H. Zachariae, *et al.*, "Oesophageal pressure–cross-sectional area distributions and secondary peristalsis in relation to subclassification of systemic sclerosis", *Neurogastroenterology & Motility*, vol. 13, no. 3, pp. 199–210, 2001.

[348] A. Vogel, L. Rakotomanana, and D. P. Pioletti, "Viscohyperelastic Strain Energy Function", in *Biomechanics of Living Organs*, Y. Payan and J. Ohayon, Eds. Oxford: Academic Press, 2017, pp. 59–78.

[349] T. Wakatsuki, J. Schlessinger, and E. L. Elson, "The biochemical response of the heart to hypertension and exercise", *Trends in Biochemical Sciences*, vol. 29, no. 11, pp. 609–617, 2004.

[350] J. C. Walker, M. B. Ratcliffe, P. Zhang, *et al.*, "MRI-based finite-element analysis of left ventricular aneurysm", *American Journal of Physiology-Heart and Circulatory Physiology*, vol. 289, no. 2, H692–H700, 2005.

[351] H. M. Wang, H. Gao, X. Y. Luo, *et al.*, "Structure-based finite strain modelling of the human left ventricle in diastole", *International journal for numerical methods in biomedical engineering*, vol. 29, no. 1, pp. 83–103, 2013.

[352] H. M. Wang, X. Y. Luo, H. Gao, *et al.*, "A modified Holzapfel-Ogden law for a residually stressed finite strain model of the human left ventricle in diastole", *Biomechanics and Modeling in Mechanobiology*, vol. 13, no. 1, pp. 99–113, 2014.

[353] V. Y. Wang, P. M. F. Nielsen, and M. P. Nash, "Image-based predictive modeling of heart mechanics", *Annual Review of Biomedical Engineering*, vol. 17, pp. 351–383, 2015.

[354] H. Weisbecker, D. M. Pierce, and G. A. Holzapfel, "A generalized prestressing algorithm for finite element simulations of preloaded geometries with application to the aorta", *International journal for numerical methods in biomedical engineering*, vol. 30, no. 9, pp. 857–872, 2014.

[355] J. F. Wenk, L. Ge, Z. Zhang, *et al.*, "A coupled biventricular finite element and lumped-parameter circulatory system model of heart failure", *Computer Methods in Biomechanics and Biomedical Engineering*, vol. 16, no. 8, pp. 807–18, 2013.

[356] E. Wilkins, L. Wilson, K. Wickramasinghe, *et al.*, "European cardiovascular disease statistics 2017", 2017.

[357] C. M. Witzenburg and J. W. Holmes, "A Comparison of Phenomenologic Growth Laws for Myocardial Hypertrophy", *Journal of Elasticity*, vol. 129, no. 1, pp. 257–281, 2017.

[358] J. Wong and E. Kuhl, "Generating fibre orientation maps in human heart models using Poisson interpolation", *Computer Methods in Biomechanics and Biomedical Engineering*, vol. 17, no. 11, pp. 1217–1226, 2014.

[359] K. C. L. Wong, L. Wang, H. Zhang, *et al.*, "Meshfree implementation of individualized active cardiac dynamics", *Computerized Medical Imaging and Graphics*, vol. 34, no. 1, pp. 91–103, 2010.

[360] World Health Organization, "Fact Sheet on Cardiovascular Diseases (CVDs).", no. 317, 2017.

[361] P. Wriggers, "Nonlinear finite element methods". Springer Science & Business Media, 2008.

[362] M.-T. Wu, W.-Y. I. Tseng, M.-Y. M. Su, *et al.*, "Diffusion tensor magnetic resonance imaging mapping the fiber architecture remodeling in human myocardium after infarction", *Circulation*, vol. 114, no. 10, pp. 1036–1045, 2006.

[363] C. Xi, C. Latnie, X. Zhao, *et al.*, "Patient-specific computational analysis of ventricular mechanics in pulmonary arterial hypertension", *Journal of Biomechanical Engineering*, vol. 138, no. 11, p. 111 001, 2016.

[364] I. Yamada, K. Hikishima, N. Miyasaka, *et al.*, "Diffusion-tensor MRI and tractography of the esophageal wall ex vivo", *Journal of Magnetic Resonance Imaging*, vol. 40, no. 3, pp. 567–576, 2014.

[365] J. Yang, J. Zhao, D. Liao, *et al.*, "Biomechanical properties of the layered oesophagus and its remodelling in experimental type-1 diabetes", *Journal of Biomechanics*, vol. 39, no. 5, pp. 894–904, 2006.

[366] M. Yang and L. A. Taber, "The possible role of poroelasticity in the apparent viscoelastic behavior of passive cardiac muscle", *Journal of Biomechanics*, vol. 24, no. 7, pp. 587–597, 1991.

[367] W. Yang, T. C. Fung, K. S. Chian, *et al.*, "3D Mechanical properties of the layered esophagus: experiment and constitutive model", *Journal of Biomechanical Engineering*, vol. 128, no. 6, pp. 899–908, 2006.

[368] W. Yang, T. C. Fung, K. S. Chian, *et al.*, "Directional, regional, and layer variations of mechanical properties of esophageal tissue and its interpretation using a structure-based constitutive model", *Journal of Biomechanical Engineering*, vol. 128, no. 3, pp. 409–18, 2006.

[369] W. Yang, T. C. Fung, K. S. Chian, *et al.*, "Viscoelasticity of esophageal tissue and application of a QLV model", *Journal of Biomechanical Engineering*, vol. 128, no. 6, pp. 909–16, 2006.

[370] W. Yang, T. C. Fung, K. S. Chian, *et al.*, "Instability of the two-layered thick-walled esophageal model under the external pressure and circular outer boundary condition", *Journal of Biomechanics*, vol. 40, no. 3, pp. 481–90, 2007.

[371] W. Yang, T. C. Fung, K. S. Chian, *et al.*, "Three-dimensional finite element model of the two-layered oesophagus, including the effects of residual strains and buckling of mucosa", *Proc Inst Mech Eng H*, vol. 221, no. 4, pp. 417–26, 2007.

[372] M. Yoshida, E. Sho, H. Nanjo, *et al.*, "Weaving hypothesis of cardiomyocyte sarcomeres: discovery of periodic broadening and narrowing of intercalated disk during volume-load change", *The American journal of pathology*, vol. 176, no. 2, pp. 660–678, 2010.

[373] S. Zeinali-Davarani, L. G. Raguin, D. A. Vorp, *et al.*, "Identification of in vivo material and geometric parameters of a human aorta: toward patient-specific modeling of abdominal aortic aneurysm", *Biomechanics and Modeling in Mechanobiology*, vol. 10, no. 5, pp. 689–699, 2011.

[374] J. E. Zelaya, S. Goenezen, P. T. Dargon, *et al.*, "Improving the Efficiency of Abdominal Aortic Aneurysm Wall Stress Computations", *PLOS ONE*, vol. 9, no. 7, e101353, 2014.

[375] Z. Zhang, A. Tendulkar, K. Sun, *et al.*, "Comparison of the Young-Laplace law and finite element based calculation of ventricular wall stress: implications for postinfarct and surgical ventricular remodeling", *The Annals of thoracic surgery*, vol. 91, no. 1, pp. 150–156, 2011.

[376] S. Zhao, X. C. Liu, and L. Gu, "The impact of wire stent fabrication technique on the performance of stent placement", *Journal of Medical Devices*, vol. 6, no. 1, p. 011 007, 2012.

[377] Y. Zhou, S. Giffard-Roisin, M. D. Craene, *et al.*, "A Framework for the Generation of Realistic Synthetic Cardiac Ultrasound and Magnetic Resonance Imaging Sequences from the same Virtual Patients", *IEEE Transactions on Medical Imaging*, vol. PP, no. 99, pp. 1–1, 2018.

[378] O. C. Zienkiewicz and R. L. Taylor, "The finite element method for solid and structural mechanics". Elsevier, 2005.

[379] A. M. Zöllner, O. J. Abilez, M. Böl, *et al.*, "Stretching Skeletal Muscle: Chronic Muscle Lengthening through Sarcomerogenesis", *PLOS ONE*, vol. 7, no. 10, e45661, 2012.

[380] Zygote Media Group Inc., "Zygote Solid 3d Heart Generations I & II Development Report. Technical Development of 3D Anatomical Systems", Report, 2014.